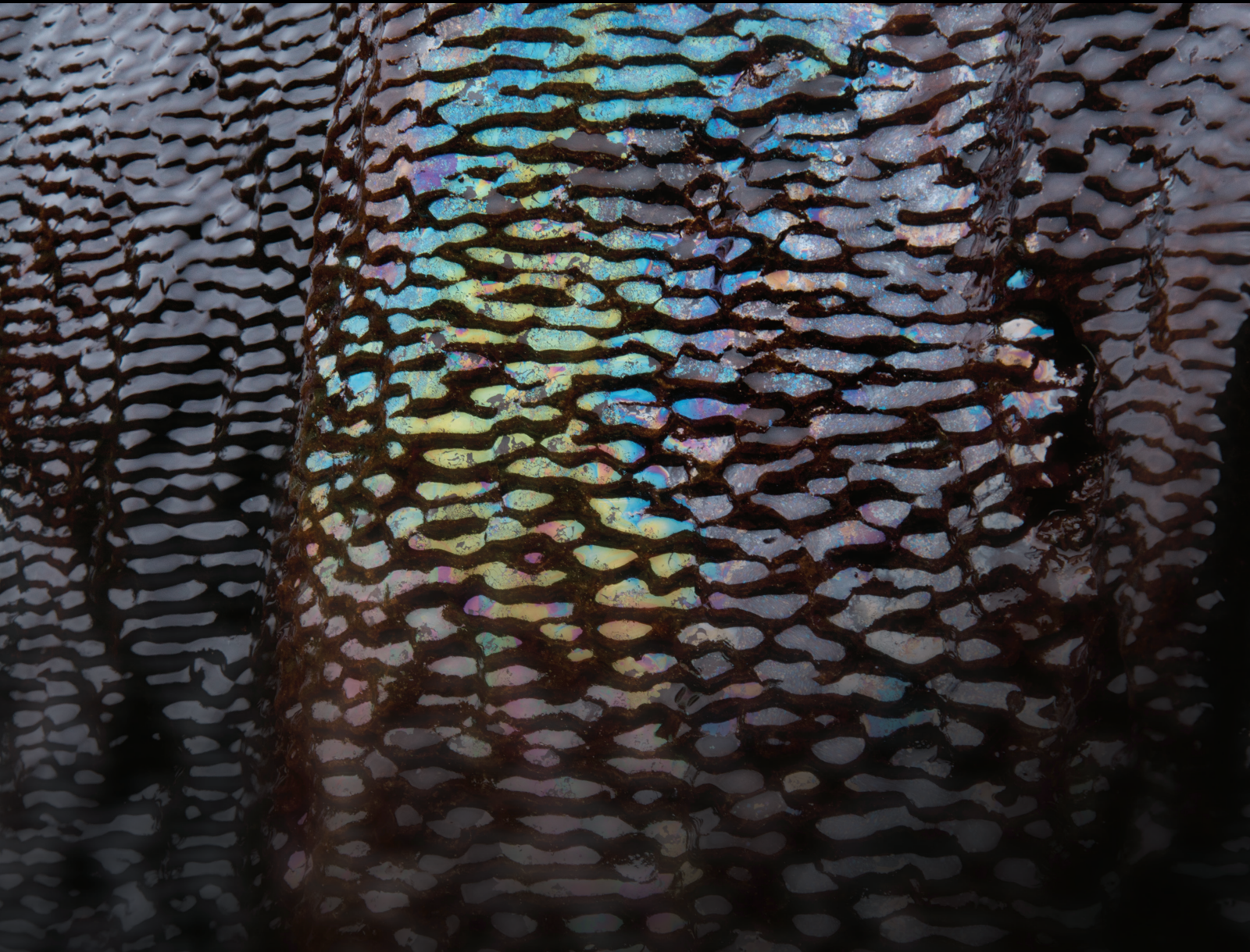


Contribution of Pore-Scale Approach to Macroscale Geofluids Modelling in Porous Media

Lead Guest Editor: Emanuele Romano

Guest Editors: Joaquín Jiménez-Martínez, Andrea Parmigiani, Xiangzhao Kong, and Ilenia Battiato





**Contribution of Pore-Scale Approach
to Macroscale Geofluids Modelling in
Porous Media**

**Contribution of Pore-Scale Approach
to Macroscale Geofluids Modelling in
Porous Media**

Lead Guest Editor: Emanuele Romano

Guest Editors: Joaquín Jiménez-Martínez, Andrea Parmigiani,
Xiangzhao Kong, and Ilenia Battiato



Copyright © 2019 Hindawi. All rights reserved.

This is a special issue published in "Geofluids." All articles are open access articles distributed under the Creative Commons Attribution License, which permits unrestricted use, distribution, and reproduction in any medium, provided the original work is properly cited.

Editorial Board

Carmine Apollaro, Italy
Baojun Bai, USA
Maurizio Barbieri, Italy
Julien Bourdet, Australia
Andrea Brogi, Italy
David A. Butterfield, USA
Mauro Cacace, Germany
Isabelle Chambefort, New Zealand
Shengnan Nancy Chen, Canada
Paola Cianfarra, Italy
Daniele Cinti, Italy
Timothy S. Collett, USA
Nicoló Colombani, Italy
Mercè Corbella, Spain
Henrik Drake, Sweden
Lionel Esteban, Australia
Cinzia Federico, Italy
Paulo Fonseca, Portugal
Francesco Frondini, Italy
Paolo Fulignati, Italy
Paola Gattinoni, Italy
Mauro Giudici, Italy

Fausto Grassa, Italy
Salvatore Inguaggiato, Italy
Francesco Italiano, Italy
Jaewon Jang, Republic of Korea
Luchao Jin, USA
Shinsuke Kawagucci, Japan
Karsten Kroeger, New Zealand
Cornelius Langenbruch, USA
Huazhou Li, Canada
Liangping Li, USA
Marcello Liotta, Italy
Stefano Lo Russo, Italy
Constantinos Loupasakis, Greece
Lin Ma, USA
Paolo Madonia, Italy
Fabien Magri, Germany
Andrew H. Manning, USA
Micòl Mastrocicco, Italy
John A. Mavrogenes, Australia
Agnes Mazot, New Zealand
Yuan Mei, Australia
Jean-Luc Michelot, France

Ferenc Molnar, Finland
Julie K. Pearce, Australia
Daniele Pedretti, Italy
Marco Petitta, Italy
Christophe Renac, France
Reza Rezaee, Australia
Mohammad Sarmadivaleh, Australia
Christian Siebert, Germany
Ricardo L. Silva, Canada
Ondra Sracek, Czech Republic
Andri Stefansson, Iceland
Pietro Teatini, Italy
Svetlana G. Tessalina, Australia
Rene Therrien, Canada
Umberta Tinivella, Italy
Tivadar M. Tóth, Hungary
Zhenjiang You, Australia
Keni Zhang, China
Ye Zhang, USA
Ling-Li Zhou, Ireland

Contents

Contribution of Pore-Scale Approach to Macroscale Geofluids Modelling in Porous Media

Emanuele Romano , Joaquín Jiménez-Martínez, Andrea Parmigiani, Xiang-Zhao Kong , and Ilenia Battiato

Editorial (4 pages), Article ID 6305391, Volume 2019 (2019)

Impact of Synthetic Porous Medium Geometric Properties on Solute Transport Using Direct 3D Pore-Scale Simulations

Paolo Roberto Di Palma , Nicolas Guyennon , Andrea Parmigiani, Christian Huber, Falk Heße, and Emanuele Romano

Research Article (13 pages), Article ID 6810467, Volume 2019 (2019)

Permeability Estimation Based on the Geometry of Pore Space via Random Walk on Grids

Tongchao Nan , Jichun Wu , Kaixuan Li, and Jianguo Jiang 

Research Article (10 pages), Article ID 9240203, Volume 2019 (2019)

Study on Reasonable Energy Supplement Time of Tight Sandstone Oil Reservoirs with Rock Compressibility Stress Sensitivity

Tian Xiaofeng , Tan Xianhong, Tian Ji, Li Nan, Yuan Zhongchao, and Liang Bin

Research Article (6 pages), Article ID 6293041, Volume 2018 (2019)

A Fluid-Solid Coupling Mathematical Model of Methane Driven by Water in Porous Coal

Bingxiang Huang and Weiyong Lu 

Research Article (17 pages), Article ID 7049830, Volume 2018 (2019)

The Visual and Quantitative Study of the Microoccurrence of Irreducible Water at the Pore and Throat System in a Low-Permeability Sandstone Reservoir by Using Microcomputerized Tomography

Xiaoyu Gu, Chunsheng Pu , Hai Huang, Nasir Khan, Jing Liu, Yanlong He, Cheng Jing, Feifei Huang, and Aojiang Qi

Research Article (14 pages), Article ID 6062475, Volume 2018 (2019)

Effect of Pore-Scale Mineral Spatial Heterogeneity on Chemically Induced Alterations of Fractured Rock: A Lattice Boltzmann Study

Hossein Fazeli , Ravi Patel, and Helge Hellevang

Research Article (28 pages), Article ID 6046182, Volume 2018 (2019)

Quantify the Pore Water Velocity Distribution by a Celerity Function

Wei Shao, Ye Su , Zongji Yang , Xieyao Ma, and Jakub Langhammer

Research Article (19 pages), Article ID 1054730, Volume 2018 (2019)

Upscaling Strategies of Porosity-Permeability Correlations in Reacting Environments from Pore-Scale Simulations

Nikolaos I. Prasianakis , Michael Gatschet, Aida Abbasi, and Sergey V. Churakov

Research Article (8 pages), Article ID 9260603, Volume 2018 (2019)

Fluid Interfaces during Viscous-Dominated Primary Drainage in 2D Micromodels Using Pore-Scale SPH Simulations

Rakulan Sivanesapillai and Holger Steeb 

Research Article (13 pages), Article ID 8269645, Volume 2018 (2019)

Editorial

Contribution of Pore-Scale Approach to Macroscale Geofluids Modelling in Porous Media

Emanuele Romano ¹, Joaquín Jiménez-Martínez,² Andrea Parmigiani,³
Xiang-Zhao Kong ⁴ and Ilenia Battiato⁵

¹Water Research Institute, National Research Council of Italy, Area della Ricerca-Roma 1, via Salaria km 29, 300-00015 Montelibretti, Italy

²Subsurface Environmental Processes Group, Eawag and ETH Zurich, Zurich, Switzerland

³Institute of Geochemistry and Petrology, ETH Zurich, Clausiusstrasse 25, 8092 Zurich, Switzerland

⁴Geothermal Energy and Geofluids Group, Institute of Geophysics, ETH Zurich, 8092 Zurich, Switzerland

⁵Energy Resources Engineering, Stanford University, 450 Serra Mall, Stanford, CA 94305, USA

Correspondence should be addressed to Emanuele Romano; romano@irsa.cnr.it

Received 28 April 2019; Accepted 28 April 2019; Published 22 May 2019

Copyright © 2019 Emanuele Romano et al. This is an open access article distributed under the Creative Commons Attribution License, which permits unrestricted use, distribution, and reproduction in any medium, provided the original work is properly cited.

1. Motivations and Background

Understanding the fundamental mechanisms of fluid flows and reactive transport in natural systems is a major challenge for several fields of Earth sciences (e.g., hydrology, soil science, and volcanology) and geo/environmental engineering (CO₂ sequestration, NAPLS contamination, geothermal energy, and oil and gas reservoir exploitation).

The hierarchical structures of natural system (e.g., heterogeneity of geological formations) as well as the different behavior of single and multiphase fluids at the pore-scale coupled with the nonlinearity of underlying reactive processes necessitates investigating these aspects at the scale at which they physically occur, the scale of pore and fractures.

Recent improvements in pore-scale computational modelling, together with the development of noninvasive microscopic imaging technology and the latest microfluidic technics are allowing the vast field of porous and fractured media research to benefit of major advances due to (1) an improved understanding and description of pore-scale mechanisms and (2) the ability of thinking in terms of coupled processes.

The contributions collected in this special issue, although far from constituting a comprehensive picture of the “pore-scale world,” however offer a good example of the potentialities

of such an approach to investigate a wide range of processes usually observed at macroscale, but whose underlying physical and chemical processes take place at microscale.

2. Contents of the Special Issue

While a number of different porous media and chemical-physical processes have been investigated in the papers collected in this special issue, we think that there is a common point shared by all the contributions: the attempt to assess sound criteria to upscale information. Even if not always explicitly stated, all studies try to answer the following question: which kind of information we should collect at microscale to improve our understanding and therefore forecasting of processes observed at macroscale?

In the following, a short presentation of each contribution is given.

- (1) “Fluid Interfaces during Viscous-Dominated Primary Drainage in 2D Micromodels Using Pore-Scale SPH Simulations” by R. Sivanapillai and H. Steeb. Authors adopt a pore-scale hydrodynamic direct numerical approach to investigate viscous-dominated two-phase flow. In particular, simulations of primary drainage in partially wettable 2D porous media of particulate

- microstructure at large capillary numbers have been performed. Numerical results indicate that the characteristic length of the capillary dispersion zone increases with the heterogeneity of the microstructure.
- (2) “*Upscaling Strategies of Porosity-Permeability Correlations in Reacting Environments from Pore-Scale Simulations*” by N. I. Prasianakis et al. The paper focuses on one of the still open challenges in geochemically reacting environments, i.e., the modeling and upscaling of porosity and permeability changes due to mineral dissolution and precipitation processes. Permeability-porosity correlations, extracted after fitting known type of relationships, are highly nonlinear and strongly dependent on the magnitude of Péclet and Damköhler numbers. The authors finally discuss the challenges of upscaling while curbing computational costs.
 - (3) “*Quantify the Pore Water Velocity Distribution by a Celerity Function*” by W. Shao et al. Fluid flow velocities within porous media show a widely heterogeneous distribution with the coexistence of high velocities, also call preferential paths, and low velocity regions or stagnations zones. W. Shao et al. propose to quantify the pore water velocity distribution from a celerity function. They showed that the proposed function can assist in investigating subsurface flow and tracer transport, both in fully and partially saturated conditions, and the kinematic ratio could be used to predict the first arrival time of a conservative tracer.
 - (4) “*Effect of Pore-Scale Mineral Spatial Heterogeneity on Chemically Induced Alterations of Fractured Rock: A Lattice Boltzmann Study*” by H. Fazeli et al. Authors investigate the pore-scale porosity-permeability relationship during mineral dissolution reactions in a multiminerale fracture with a focus on a well-mixed and a banded structure, using lattice-Boltzmann methods. Authors identify a degraded zone in the well-mixed structures due to the dissolution of fast-dissolving minerals, and a comb-tooth zone in the banded structures. They finally conclude that besides the contribution of geometry structures, the porosity-permeability relationship greatly relies on the values of Péclet and Damköhler numbers.
 - (5) “*The Visual and Quantitative Study of the Microoccurrence of Irreducible Water at the Pore and Throat System in a Low-Permeability Sandstone Reservoir by Using Microcomputerized Tomography*” by X. Gu et al. With 3D tomographic imaging on a low permeable sandstone after a displacement of brine with oil, authors observed that the irreducible water (wetting phase) tends to accumulate in the throat system as water films, leading to a significant cutoff of drainage channels of oil. While the remaining irreducible water spreads in the corners of the pore system, these water blobs are primarily linked through a water film. These findings advance the understandings on irreducible water microbehaviors.
 - (6) “*A Fluid-Solid Coupling Mathematical Model of Methane Driven by Water in Porous Coal*” by B. Huang and W. Lu. The mathematical coupling of multiphase flow and adsorption-desorption processes within porous media is of extraordinary complexity. The fluid-solid model proposed by B. Huang and W. Lu has demonstrated its potential in reproducing experimental result of water-driven methane in porous coal.
 - (7) “*Study on Reasonable Energy Supplement Time of Tight Sandstone Oil Reservoirs with Rock Compressibility Stress Sensitivity*” by T. Xiaofeng et al. T. Xiaofeng et al. Proposes a new method to estimate the energy supplement time (i.e., the time when it is convenient to supply energy for extraction because the natural energy is going to decrease) in an oil reservoir. Such an approach, validated on experimental data, takes into account at the pore scale of both threshold pressure gradient and rock compressibility stress sensitivity, demonstrating that the latter cannot be neglected.
 - (8) “*Permeability Estimation Based on the Geometry of Pore Space via Random Walk on Grids*” by T. Nan et al. The characterization of hydraulic properties is always challenging because of its strong dependence on geometry and topology. In this special issue, T. Nan et al. introduce a method to estimate permeability based on the geometry of pore space via random walks on grids. This method overcomes difficulties found by widely used approaches such as “walk on spheres” or “walk on cubes.” In comparison with Green’s functions for simple geometries and computational fluid-flow dynamics for complex geometries, the proposed method is invaluable in the estimation of permeability from digitalized porous media.
 - (9) “*Impact of Synthetic Porous Medium Geometric Properties on Solute Transport Using Direct 3D Pore-Scale Simulations*” by P. R. Di Palma et al. The study proposes a systematic analysis of the relationships between geometric features of the porous media, as defined in the context of Minkowski functionals, and transport processes through direct simulations of fluid flow and advection-diffusion of a nonreactive solute in synthetically generated 3D media. The study finds that the advective transport is primarily affected by the first and second Minkowski functional, while effective diffusion scales as the inverse of the tortuosity squared.

3. Next Challenges

We believe that in the next future, advances in understanding physical and chemical processes occurring in porous media will take advantage from the superposition of approaches

able to collect information at different scales, from nano to macro. Such a multiscale approach will be favoured by the increasingly performing imaging techniques, as well as by the increasing computational power allowing for a number of “numerical experiments” much larger than in the past.

Therefore, to conclude this short Editorial, we wish to suggest some “research challenges” that may be addressed in the next future.

(1) *Scale Translation in Multiphase Reactive Systems.*

Notwithstanding the progress made in forward predictions of flow and reactive transport in porous media over the past decades, the achievement of a seamless predictive understanding of the system response at the macroscale (be it Darcy or field scale) from pore-scale processes appears still elusive, especially when the scale disparity between adjacent models increases (e.g., from pore scale to Darcy scale versus from pore scale to field scale) [1]. Such challenges are further amplified in reactive multiphase systems, where the complex distribution of phases, as well as the inherent instability of the interfaces separating them, undermine the very foundation of some of the upscaling methods classically employed to build effective medium models [2, 3]. Despite the ubiquity of multiphase flows in geologic media, current modelling efforts are still based on postulated multiphase Darcy’s equations, whose limitations have been ostensibly highlighted by numerous studies, and alternative physics-based formulations [4, 5] are still slow to penetrate common wisdom. This can greatly affect one’s ability to properly model reaction rates, distribution of contaminants and resources (gas and oil), nutrient cycling, etc., in multiphase systems. Moving away from parametrization of effective models toward estimation of effective properties from pore-scale models in a bottom-up framework requires the development of holistic approaches which combine rigorous upscaling, numerical simulations, experiments, and, last but not least, data analytics tools, while ensuring that predictive errors remain bounded by formal upscaling errors. The originally parallel paths between big data analytics and physics-based models must now intersect to generate the longed leap-frog improvement in predictive understanding of systems dominated by a tyranny of scales like porous media.

(2) *Validation with 4D Experiments.* Challenges should also be focused on validation of numerical predictions [6] on pore-scale processes using well-controlled laboratory experiments [7, 8]. It has been extremely difficult to visualize 3D time-series (i.e., 4D) data during laboratory experiments that investigate reactive transport through a porous and/or fractured medium at sufficient spatial and temporal resolutions, because the processes of interest occur (deep) inside the medium of interest. Thanks to fast evolution of nondestructive and noninvasive

instrumentation and detectors as well as the development of ultrafast imaging procedures, a micrometer to nanometer resolution is becoming affordable even during tracking of very rapid dynamic processes in porous media. The real-time tracking of pore-scale multiphase reactive transport processes enables confirmation/validation/reexamination of known mechanisms and reveal/discover unknown mechanisms, offering parametrization of the existing models and establishment of novel approaches to include the newly discovered mechanisms.

(3) *Fluid-Biofilm Interactions in Porous Media.* Processes of biofilm formation play a fundamental role in several natural phenomena, as well as in technological applications, ranging from bioreactors, to permeable reactive barriers, to medical systems. Biofilm growth is a stepwise complex process from attachment and adaptation to detachment of cells and biofilm fragments whose evolution is affected by and at the same time affects fluid dynamics features at the pore scale [9]. Such a strong interaction between biological processes and microfluidics is very far from being understood. Insights for a deeper comprehension of the mechanisms (mechanical and biological) involved in the biofilm growth can arise from a multidisciplinary approach involving (1) laboratory microfluidic experiments under flow controlled conditions [10], (2) noninvasive imaging methods for assessing the biomass evolution [11], and (3) 3D numerical models [12] coupling biofilm growth and pore-scale fluid dynamics models [13].

Conflicts of Interest

The guest editors declare that they have no conflicts of interest or private agreements with companies.

Acknowledgments

We sincerely thank Paolo Roberto Di Palma for supporting the editorial work in this special issue.

*Emanuele Romano
Joaquín Jiménez-Martínez
Andrea Parmigiani
Xiang-Zhao Kong
Ilénia Battiato*

References

- [1] P. de Anna, J. Jiménez-Martínez, H. Tabuteau et al., “Mixing and reaction kinetics in porous media: an experimental pore scale quantification,” *Environmental Science & Technology*, vol. 48, no. 1, pp. 508–516, 2014.
- [2] J. Jiménez-Martínez, P. de Anna, H. Tabuteau, R. Turuban, T. Le Borgne, and Y. Méheust, “Pore-scale mechanisms for the enhancement of mixing in unsaturated porous media and implications for chemical reactions,” *Geophysical Research Letters*, vol. 42, no. 13, pp. 5316–5324, 2015.

- [3] J. Jiménez-Martínez, T. Le Borgne, H. Tabuteau, and Y. Méheust, “Impact of saturation on dispersion and mixing in porous media: photo-bleaching pulse injection experiments and shear-enhanced mixing model,” *Water Resources Research*, vol. 53, no. 2, pp. 1457–1472, 2017.
- [4] D. Picchi and I. Battiato, “The impact of pore-scale flow regimes on upscaling of immiscible two-phase flow in porous media,” *Water Resources Research*, vol. 54, no. 9, pp. 6683–6707, 2018.
- [5] D. Picchi and I. Battiato, “Relative permeability scaling from pore-scale flow regimes,” *Water Resources Research*, vol. 55, 2019.
- [6] A. Parmigiani, P. Di Palma, S. Leclaire, F. Habib, and X.-Z. Kong, “Characterization of transport-enhanced phase separation in porous media using a lattice-Boltzmann method,” *Geofluids*, vol. 2019, 2019.
- [7] M. Ahkami, T. Roesgen, M. O. Saar, and X.-Z. Kong, “High-resolution Temporo-ensemble PIV to resolve pore-scale flow in 3D-printed fractured porous media,” *Transport in Porous Media*, pp. 1–17, 2018.
- [8] M. Nooraiepour, H. Fazeli, R. Miri, and H. Hellevang, “Effect of CO₂ phase states and flow rate on salt precipitation in shale caprocks—a microfluidic study,” *Environmental Science & Technology*, vol. 52, no. 10, pp. 6050–6060, 2018.
- [9] C. D. Persat, M. K. Nadell, F. Kim et al., “The mechanical world of bacteria,” *Cell*, vol. 161, no. 5, pp. 988–997, 2015.
- [10] Y. Yawata, J. Nguyen, R. Stocker, and R. Rusconi, “Microfluidic studies of biofilm formation in dynamic environments,” *Journal of Bacteriology*, vol. 198, no. 19, pp. 2589–2595, 2016.
- [11] M. Carrel, M. A. Beltran, V. L. Morales et al., “Biofilm imaging in porous media by laboratory X-ray tomography: combining a non-destructive contrast agent with propagation-based phase-contrast imaging tools,” *PLoS One*, vol. 12, no. 7, article e0180374, 2017.
- [12] P. R. Di Palma, N. Guyennon, F. Hesse, and E. Romano, “Porous media flux sensitivity to pore-scale geostatistics: a bottom-up approach,” *Advances in Water Resources*, vol. 102, pp. 99–110, 2017.
- [13] M. Benioug, F. Golfier, C. Oltéan, M. A. Buès, T. Bahar, and J. Cuny, “An immersed boundary-lattice Boltzmann model for biofilm growth in porous media,” *Advances in Water Resources*, vol. 107, pp. 65–82, 2017.

Research Article

Impact of Synthetic Porous Medium Geometric Properties on Solute Transport Using Direct 3D Pore-Scale Simulations

Paolo Roberto Di Palma ¹, Nicolas Guyennon ¹, Andrea Parmigiani,² Christian Huber,³ Falk Heße,⁴ and Emanuele Romano¹

¹National Research Council of Italy, Water Research Institute, Area della Ricerca di Roma 1-Montelibretti, Strada Provinciale 35d, km 0.7 Montelibretti Roma, Italy

²Institute of Geochemistry and Petrology, ETH Zurich, Clausiusstrasse 25, CH-8092 Zurich, Switzerland

³Department of Earth, Environmental and Planetary Sciences, Brown University, Providence, 02912 RI, USA

⁴Department of Computational Hydrosystems Helmholtz, Centre for Environmental Research, UFZ Permoserstr. 15 04318 Leipzig, Germany

Correspondence should be addressed to Nicolas Guyennon; guyennon@irsa.cnr.it

Received 17 July 2018; Revised 30 November 2018; Accepted 22 January 2019; Published 3 April 2019

Academic Editor: Andri Stefansson

Copyright © 2019 Paolo Roberto Di Palma et al. This is an open access article distributed under the Creative Commons Attribution License, which permits unrestricted use, distribution, and reproduction in any medium, provided the original work is properly cited.

Transport processes in porous media have been traditionally studied through the parameterization of macroscale properties, by means of volume-averaging or upscaling methods over a representative elementary volume. The possibility of upscaling results from pore-scale simulations, to obtain volume-averaging properties useful for practical purpose, can enhance the understanding of transport effects that manifest at larger scales. Several studies have been carried out to investigate the impact of the geometric properties of porous media on transport processes for solute species. However, the range of pore-scale geometric properties, which can be investigated, is usually limited to the number of samples acquired from microcomputed tomography images of real porous media. The present study takes advantage of synthetic porous medium generation to propose a systematic analysis of the relationships between geometric features of the porous media and transport processes through direct simulations of fluid flow and advection-diffusion of a non-reactive solute. Numerical simulations are performed with the lattice Boltzmann method on synthetic media generated with a geostatistically based approach. Our findings suggest that the advective transport is primarily affected by the specific surface area and the mean curvature of the porous medium, while the effective diffusion coefficient scales as the inverse of the tortuosity squared. Finally, the possibility of estimating the hydrodynamic dispersion coefficient knowing only the geometric properties of porous media and the applied pressure gradient has been tested, within the range of tested porous media, against advection-diffusion simulations at low Reynolds ($<10^{-1}$) and Peclet numbers ranging from 10^1 to 10^{-2} .

1. Introduction

A quantitative relation between the structure of porous media and its effect on solute transport is fundamental to our understanding of groundwater contamination dynamics and the development of pollutant remediation strategies [1]. Transport processes in porous media have been traditionally studied through the parametrization of macroscale properties (e.g., hydraulic conductivity or hydrodynamic dispersion

coefficients) by means of volume-averaging or upscaling methods over a representative elementary volume.

However, these upscaling approaches are not valid when considering length scales on the order of a single pore or the complexity of processes (i.e., physical, chemical, and biological) that take place at the pore scale [2]. Developing averaging approaches from the pore-scale approach can provide further information on the macroscopic medium properties and then enhance the understanding of transport

effects which exhibit at a greater scale (e.g., field or laboratory scale) [3–6].

The development of digital image processing led to a large expansion of the quantitative analyses of rock and soil structure. Various tomographic techniques are nowadays available for a three-dimensional non-invasive visualization of structural properties with a spatial resolution down to microns [7–11]. Even with the availability of these techniques, the cost of imaging limits the number of samples that can be analyzed [12]. As an alternative, a statistical approach to generate media with given imposed structural features can be a cost-effective means for producing large numbers of realizations that represent those features of natural samples deemed relevant. The two approaches that are commonly used to generate synthetic porous media can be divided into statistical models (e.g., multipoint statistics and autocorrelation functions) and object-based methods, where geometrical objects are randomly placed in a domain to simulate diagenesis processes [8].

The well-established use of pore-scale approach consists of estimating averaged properties, such as permeability through direct single-phase fluid flow simulations [6, 13–18] and relative permeability for multiphase fluid flows [4, 19–22]. Recently, some authors focused on the relationship between velocity distribution and pore structure [23–28] as well as transport processes [2, 24, 29–36].

The present research is aimed at analyzing the relationships between geometric features of different porous media and transport processes through direct simulations of fluid flow and advection-diffusion of non-reactive solute using the lattice Boltzmann method (LBM). The LBM is selected for its ability to easily model different phenomena and its suitability to be parallelized and to exploit the computing power of HPC systems [37]. The question we address here is which geometric properties of the porous media control fluid flow and solute transport? In order to perform a sensitivity analysis on a wide class of porous microstructures, multiple synthetic porous media are generated using a geostatistical approach. We also consider two available sandpack samples (<https://www.imperial.ac.uk/earth-science/research/research-groups/perm/research/pore-scale-modelling/micro-ct-images-and-networks/>, last access 16/01/2019) to compare results for synthetic and natural porous media. The choice of sandpack images is motivated because alluvial aquifers are the most commonly contaminated systems [1]. Each porous medium is described by the Minkowski functionals: porosity, specific surface area, mean curvature, and Euler characteristic [38].

2. Materials and Methods

To identify the dominant pore-scale parameters that control the transport of non-reactive solutes, LBM simulations (Section 2.2) are run over synthetic porous media and micro-CT images of sandpicks (Section 2.1). A specific simulation setup is designed to first consider separately the impact of advective and diffusive transport (Section 2.3). Our objective is to reduce the number of variables to consider

for the advection-diffusion simulations, which are subsequently carried out on a selection of porous media. In fact, a full sensitivity analysis between the correlation lengths (ξ) set for the generation model, the Minkowski functionals for porous media characterizations (porosity (ϕ), specific surface area (SSA), mean curvature (MC), and Euler number (χ_V)), and tortuosity (τ) over different transport regimes would require a computational effort that goes beyond our current capacity. Finally, the metrics used to quantify the simulation results over the selected parameters are described in Section 2.4.

Acronyms and abbreviations adopted throughout the paper are summarized in Supplementary Material S3.

2.1. 3D Porous Medium. The procedure to generate the porous media is described in details in Di Palma et al. [23]. Here, we only summarize the main steps as follows: (i) the 3D domain and resolution of the porous medium are set; (ii) the geostatistical model is assigned, setting the type of semivariogram (exponential and Gaussian) and the correlation length ξ . Pore-scale variability (i.e., for multiple length scale) is neglected; (iii) a 3D Gaussian random field (zero mean and variance of 1) following the assigned spatial autocorrelation function (semivariogram) is generated with the *TFracGen* code [39]; (iv) a threshold is imposed to the normal cumulated distribution function to obtain an indicator field of pores and grains with an assigned target porosity ϕ ; and (v) the spatial autocorrelation of the generated indicator field is estimated by fitting the Matérn covariance model [40, 41] as a function of the smoothness parameter ν_m and the associated practical range. This step is necessary as the transformation of a Gaussian field into an indicator field does not preserve the characteristics of the spatial autocorrelation [12, 42]. The resulting smoothness parameters of the Matérn model for the porous media generated by exponential and Gaussian variograms are $\nu_m = 0.35$ and $\nu_m = 1.2$, respectively. These values are consistent with the findings of Di Palma et al. [23]. However, for the sake of simplicity, we refer for the rest of the paper to EXX and GXX to porous media generated by exponential and Gaussian functions, respectively, where XX refers to the correlation length of each medium.

In this work, each porous medium is generated at a spatial resolution of $10 \mu\text{m}$ for a domain size of 3 mm^3 , resulting in a number of voxels equal to 300^3 . A greater calculation domain would have involved a huge computational cost, especially for advection-diffusion simulations. Porous media are generated in a range between 3% and 11% of the ratio correlation length over domain size to guarantee a suitable balance between the spatial resolution impact on short correlation lengths and the representativeness of porous medium generation for great correlation lengths compared to domain size [23]. It is worth stressing that the synthetic porous media are isotropic (i.e., show only one independent length scale) and statistically homogeneous. We are aware that this modeling assumption constitutes a limitation of our approach, e.g., for sedimentary porous media that often show pronounced anisotropy between the horizontal and vertical directions. However, we think that this is justified by the reduction of

the numbers of descriptors required to describe each medium. Such limitation does not significantly affect the interpretability of our results.

In order to compare the analysis of the synthetic porous media with real samples, we performed additionally flow and solute transport simulations on two different sandpacks (i.e., F42C and LV60A) with the same spatial resolution of $10\ \mu\text{m}$ and 300^3 voxels, whose micro-CT images are available from the pore-scale modelling Consortium of Imperial College (https://figshare.com/articles/F42C_sandstone/1189261, https://figshare.com/articles/LV60A_sandpack/1153795, last access 15/01/2019). Both the X-ray scanned sandpack media have been verified to be isotropic and homogenous [17].

To describe the spatial characteristics of the generated porous media, we adopted the four Minkowski functionals and the tortuosity. The Minkowski functionals provide a detailed description of the geometric characteristics of a porous medium and are widely used in mathematical morphology [12, 38]. We briefly summarize the general definitions for each of them but refer interested readers to Vogel et al. [38] for a complete treatment of the Minkowski functional.

The first functional is the porosity:

$$\phi = \frac{V_{\text{voids}}}{V}, \quad (1)$$

defined as the volume of the voids V_{voids} over the total volume of the medium (V).

The second functional is the specific surface area, as the interstitial surface area of the voids and solids:

$$\text{SSA} = \frac{A_s}{V}, \quad (2)$$

where A_s is the surface area of the grains.

The third functional is the mean curvature (MC) representing a measure of the average pore size of the sample over the total volume:

$$\text{MC} = \frac{W_1}{V}. \quad (3)$$

Here, W_1 is related to the mean width and is defined as the mean value of the distance between a pair of parallel support planes [12, 43].

Finally, the fourth functional is the total curvature, also known as the Euler number that measures the connectivity of the pore space. This is more easily defined by Vogel [38, 44, 45] as a topological parameter:

$$\chi_V = \frac{N - C + H}{V}, \quad (4)$$

where N are the isolated objects, C are interconnected regions or loops, and H are the completely enclosed cavities. Broadly speaking, a negative χ_V corresponds to high pore space connectivity [45].

We calculate the tortuosity following the definition of hydraulic tortuosity in Clennell [46] as $\tau = (L_e/L)$, L_e being

the average length of the fluid paths and L is the straight-line length in the direction of flow [46]. L_e is obtained from steady-state flow simulations by counting the number of streamlines passing through the porous medium. Streamlines are calculated using MATLAB® function “stream3,” which is based on an explicit Euler integration of the ordinary differential equation $(\dot{x}(t), \dot{y}(t), \dot{z}(t)) = (u(x(t), y(t), z(t)), v(x(t), y(t), z(t)), w(x(t), y(t), z(t)))$ for a given set of starting points $(x(t=0), y(t=0), z(t=0))$, where u , v , and w represent the components of the velocity.

In our 3D media, the porosity ϕ and correlation length ξ are imposed in the generation process, whereas the Minkowski functionals and tortuosity are calculated after the porous medium realization and fluid flow simulations, respectively.

The imposed geometric properties of the generated porous media and associated nomenclature (ID) are reported in Table 1, together with the corresponding estimated geometric properties for the scanned samples.

Figure 1 shows the geometric descriptors of the generated and scanned porous media (both imposed or calculated using the Minkowski functionals). The dispersion of imposed properties is by construction regularly distributed over the imposed ranges of correlation length and porosity, including both micro-CT sandpacks (Figure 1(a)). The SSA values of the EXX are approximately two or three times greater than those of the GXX and almost independent of the porosity. Moreover, the SSA values of the micro-CT are closer to the GXX than to the EXX (Figure 1(b)). On the other hand, the SSA variability introduced by the investigated range of generated pore size is similar to that of EXX and GXX (Figure 1(c)). The dependence of the mean curvature (MC) on correlation length (Figure 1(d)) is similar to the dependence of the specific surface area (SSA) on the porosity (Figure 1(e)) while these two functionals appear correlated (Figure 1(f)). This implies that the two semivariogram models (Gaussian and exponential) adopted for synthetic generation lead to different average pore sizes for the same imposed correlation length.

The Euler number χ_V values (Figures 1(g)–1(j)) are consistent with literature data for similar porous media [38], showing overall negative values, except for one sample. A good correlation is found between χ_V and SSA (Figure 1(i)), similar to the second versus the third Minkowski functional (Figure 1(f)). Indeed, the Euler number and the mean curvature seem to be correlated (Figure 1(j)). The highest values of the χ_V for the media generated using the exponential semivariogram model and the lowest correlation lengths (e.g., upper left black triangles in Figure 1(g)) are due to the presence of many isolated small structures, which result in a massive inflation of the connectivity. The issue is an artifact of the binarization procedure, which can be avoided by using a finer spatial resolution for the exponential semivariogram model or a dedicated postprocessing routine.

A principal component analysis has been carried out on the set of descriptors presented in Figure 1 (not shown here). The loads of the first PCA component confirm the strong relationship among SSA, MC, and χ_V , whereas the second PCA component is mostly explained by the tortuosity and

TABLE 1: Characteristics of generated and scanned porous media used for numerical simulations.

	Exponential model media					Gaussian model media					X-ray scanned sandpack media	
ID	E09	E15	E21	E27	E33	G09	G15	G21	G27	G33	F42C	LV60A
ξ (mm)	0.1	0.2	0.2	0.3	0.3	0.1	0.2	0.2	0.3	0.3	0.16	0.125
ϕ (-)	0.30/0.325/0.35/0.375/0.40					0.30/0.325/0.35/0.375/0.40					0.33	0.38

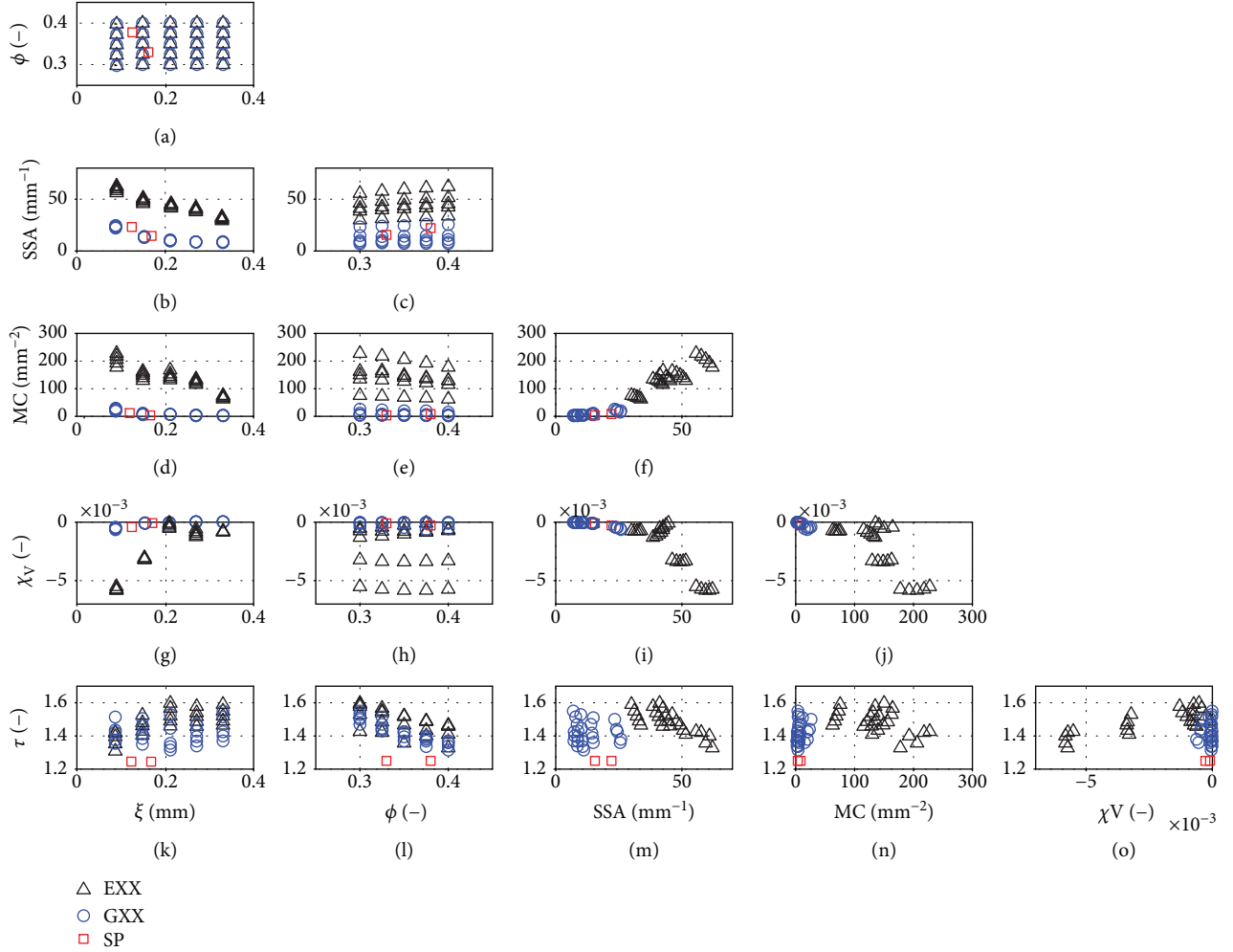


FIGURE 1: Relationships between values of correlation length (ξ), Minkowski functionals—porosity (ϕ), specific surface area (SSA), mean curvature (MC) and Euler number (χ_V)—and tortuosity τ for generated (black triangles and blue circles) and scanned porous media (SP) as red squares used for numerical simulations. Porous media generated by exponential and Gaussian functions are named EXX and GXX, respectively, where XX refers to the correlation length of each medium.

the third by the pore size and the porosity. 95% of the variance can be explained by these first three PCA components. It is worth noting that, in contrast to the other geometric parameters, the micro-CT sandpack tortuosity is systematically lower than that of the synthetic media (Figures 1(k)–1(o)). Such a feature is not explained by the geometric characteristics captured by the variogram (or related to it), or by the first three Minkowski functionals. It is probably due to the limitations of variogram-based generators. As the name implies, such methods can generate

random fields with a specified mean and variogram function, which are their one-point and two-point statistics, respectively. Higher order statistics can, by definition, not be reproduced, limiting the range of possible structures that such methods can produce (see, e.g., [47]). One particular feature that cannot be directly reproduced, and is often discussed in the literature, is the presence of long-ranging highly-connected flow paths [48]. Within the scope of our study, we do not consider this a major issue, since such long-range structures are hardly present at the pore scale. This

notion is confirmed by our analysis, since the porous media generated using the Gaussian random fields are described effectively by the Minkovsky functionals and show properties comparable to the real media.

2.2. Lattice Boltzmann Method. The lattice Boltzmann method is a computational fluid dynamics technique that solves fluid flow and transport processes within complex structures such as porous media [37, 49, 50]. The mainstay of the LBM is the discretized Boltzmann equation (or lattice Boltzmann equation), which is based on kinetic theory and describes the streaming and collision of particles. The macroscopic variables are defined along each node of the computational domain as moments of the particle distribution function $f_i(\mathbf{x}, t)$, which interact locally following simple microscopic laws. The LBM allows us to model several physical phenomena by means of different particle distribution functions, which are properly coupled to reproduce the process of interest (i.e., advection and diffusion within the single-phase fluid flow). Here, two particle distribution functions for fluid hydrodynamic $f_i(\mathbf{x}, t)$ and concentration field $g_i(\mathbf{x}, t)$ are used and a one-way coupling (the velocity of the fluid is used to calculate the advective term of equation S2.4 in Supplementary Materials) is adopted, since the transport of a non-reactive solute does not affect the fluid flow (Parmigiani et al., 2009). In LBM, all dimensional units are expressed in lattice units and, conventionally, lattice spacing and time step are unitary. More details about the lattice Boltzmann algorithm are given in Supplementary Material S1.

2.3. Numerical Simulation Setup. Numerical simulations for both flow and transport are carried out using *Palabos* [51], an open-source software for computational fluid dynamics based on the LBM. All calculations are performed on the cluster facility *Euler* at ETH Zurich. Initial and boundary conditions for all simulations are summarized in Figure 2.

Incompressible viscous flow is simulated directly through the pore space of the porous media by solving the Lattice Boltzmann equation for fluid flow. The fluid flow is driven by a fixed pressure gradient imposed along the z direction at the inlet (higher pressure at $z = 0$) and the outlet of the domain (lower pressure at $z = L$). Periodic boundary conditions are applied to the other edges of the computational domain. The solid-liquid interfaces along the grain boundaries are treated as a no-slip condition ($\mathbf{u} = 0$), where \mathbf{u} is the local fluid velocity. Simulations run until the fluid flow reaches a steady state (Figure 2(a)).

For diffusion simulations, no pressure gradient is applied and we assume for each run an initially homogenous concentration in a subdomain (i.e., $C_{\text{ini}}(50 \leq x \leq 250, 50 \leq y \leq 250, 50 \leq z \leq 250) = 1$) and a concentration equals to 0 otherwise. A fixed null concentration is assigned at the inlet ($C_{\text{inlet}}(0 \leq x \leq 300, 0 \leq y \leq 300, z = 0) = 0$) and the outlet ($C_{\text{outlet}}(0 \leq x \leq 300, 0 \leq y \leq 300, z = L) = 0$) of the domain, while periodic boundaries are set at the other faces (Figure 2(b)).

Finally, to simulate the combined solute advection and diffusion process, the solute transport simulation is

initiated after the fluid flow reaches a steady state. The advection-diffusion simulations use the same initial conditions as the diffusion simulations, but a Dirichlet boundary condition for the concentration is assigned at the inlet face of the domain ($C_{\text{inlet}}(0 \leq x \leq 300, 0 \leq y \leq 300, z = 0) = 0$) and a Neumann boundary condition ($\partial C / \partial z = 0$) with a second-order finite difference scheme [52] is assigned to the outlet ($0 \leq x \leq 300, 0 \leq y \leq 300, z = L$). Periodic boundary conditions are set as in the previous diffusive simulations (Figure 2(c)).

2.4. Quantitative Descriptors of the Simulated Processes

2.4.1. Descriptors of Flow Simulations. To describe the flow features, the Reynolds number is calculated as follows:

$$\text{Re} = \frac{\bar{U}_z \cdot (\pi/\text{SSA})}{\nu}, \quad (5)$$

where ν is the kinematic viscosity of the fluid (assumed constant). Following Mostaghimi et al. (2016, [16]), we use the ratio π/SSA as the characteristic length scale. This choice is motivated since the specific surface area is readily computed for each medium. It represents a proper descriptor of the sample as it is directly related to the viscous forces acting at the fluid-rock interface. \bar{U}_z is the average seepage velocity along the main flow direction, calculated using the passing streamlines through the porous medium having a length that exceeds the domain side:

$$\bar{U}_z = \frac{\sum_{s=1}^N \sum_{i=1}^{L_s} \mathbf{u}_z(x_i, y_i, z_i)}{N}, \quad (6)$$

where L_s is the length of each streamline and N the number of streamlines passing through the porous media.

The calculation of the seepage velocity suffers from the underestimation that may occur when the porosity is used in lieu of the effective porosity, because the latter is unknown [23]. However, given the porosity range (between 0.3 and 0.4), the homogeneity, and relatively narrow pore size distribution of the media, we expect the effective and true porosity to closely match for each medium. Hereafter, the porosity will therefore be used in lieu of the effective porosity.

Finally, we use the original formula of Kozeny-Carman that provides a simple model to relate permeability to most of the descriptors discussed above:

$$k = \frac{\phi^3}{\beta \tau^2 \text{SSA}^2}, \quad (7)$$

where β is a geometric factor (also called Kozeny constant) and depends on the shape of the cross sections of the channels. The original value of the Kozeny constant equals to 5, even if generally accepted literature values of β range from 2 for circular pores and 3 for flat cracks [46] to 10 [53].

2.4.2. Geometrical Control on Solute Diffusive Transport. In the diffusion simulations, we compute for each time t the

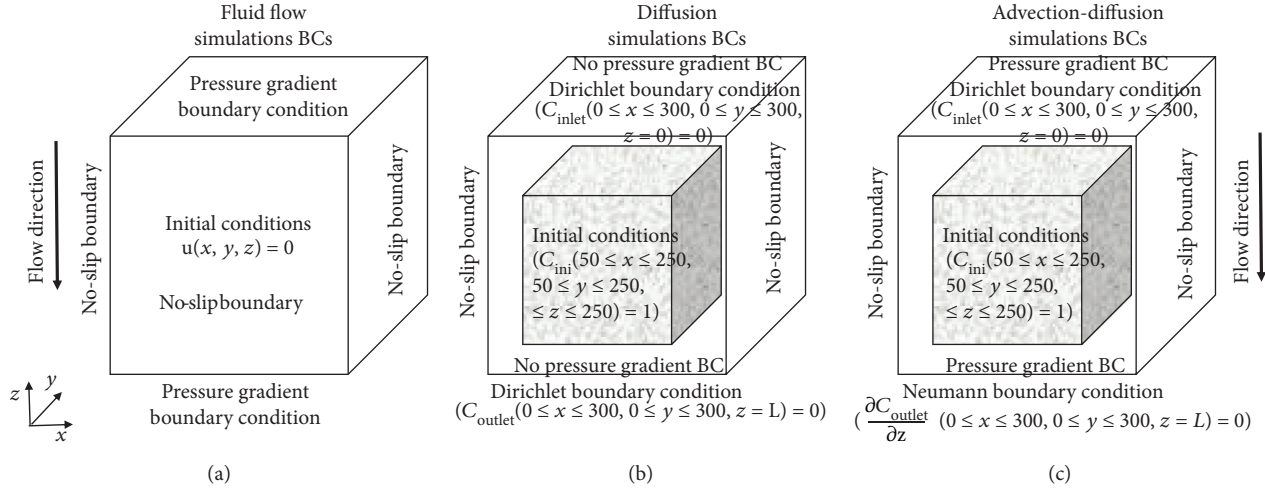


FIGURE 2: Schematic representation of the boundary conditions and initial conditions imposed for fluid flow (a), diffusion simulations (b), and advection-diffusion (c).

normalized solute mass within the computational spatial domain as follows:

$$\frac{M_{\text{in}}(t)}{M_0} = \frac{\sum_{i=1}^{N_x} \sum_{j=1}^{N_y} \sum_{k=1}^{N_z} C(x_i, y_j, z_k, t)}{M_0}, \quad (8)$$

where $M_0 = \sum_{i=1}^{N_x} \sum_{j=1}^{N_y} \sum_{k=1}^{N_z} C(x_i, y_j, z_k, t=0)$. This ratio quantifies the fraction of solute lost over time for the volume of porous medium initially occupied by the solute. By virtue of the initial conditions, this ratio is equal to 1 at $t=0$ and decreases accordingly to the efficiency of the diffusive solute transport of each medium. In order to analyze the diffusion simulations for all porous media, we compared the time t^* necessary for each sample to reach a selected cutoff of the initial mass, set at 10%.

The time t^* is compared with the effective diffusion coefficient D_{eff} , which is different from the molecular bulk diffusion coefficient. Several theoretical and empirical laws are proposed in the literature, mostly based on relationships that include either porosity and tortuosity combined or the tortuosity only [54–57]. We test the following relationships:

$$D_{\text{eff}} = \begin{cases} \frac{1}{\tau^2} D_m, \\ \frac{\phi}{\tau} D_m, \\ \frac{\phi}{\tau^2} D_m. \end{cases} \quad (9)$$

These different relationships vary depending on the spatial scale of investigation. For example, considering a macroscopic description of the effective diffusion coefficient requires both tortuosity and porosity. However, at the microscopic scale, the porosity is generally not considered [58]. There is no clear agreement on linear or quadratic dependence on the tortuosity [55, 56].

2.4.3. Geometrical Control on Combined Advective-Diffusive Solute Transport. We perform the advection-diffusion simulations over a range of transport regimes, from diffusion to advection dominated. These simulations are characterized by the Peclet (Pe) number, comparing diffusive and advective flux and being defined as the product of Reynolds and Schmidt numbers ($Sc = \nu/D_m$). We test three different Sc number values, i.e., 320, 32, and 3.2, obtained by varying the magnitude of the molecular diffusivity D_m to avoid flow field variations due to kinematic viscosity of the fluid and to obtain faster simulations without affecting the transport process.

The pressure gradient for all advection-diffusion simulations is fixed to 1.5 Pa/mm. Consequently, the Re number for each porous medium differs slightly because of the actual value of SSA and seepage velocity (\bar{U}_z). The advection-diffusion simulations are carried out over a range of Pe values from 10^1 to 10^{-2} for 9 samples selected over the initial 52: the two scanned samples and 7 synthetic media.

We calculate the hydrodynamic dispersion coefficient using the method of temporal moments [59–62]. The dispersion coefficient is estimated from the first three temporal moments of the concentration breakthrough curves at the outlet of the computational domain. The n^{th} temporal moment of a concentration distribution at the location $z=L$ is defined as follows:

$$M_n = \int_0^{\infty} t^n c(x, y, z=L, t) dt. \quad (10)$$

We also define the second central moment as $M_{2c} = M_2 - (M_1)^2/M_0$. The longitudinal dispersion coefficient is given by

$$D_L = \frac{z^2 M_{2c} (M_0)^2}{2(M_1)^3}. \quad (11)$$

Then, we compare the values of D_L/D_m computed through equation (11) with typical relationship used to estimate D_L , as the following function of the Peclet number:

$$\frac{D_L}{D_m} = \frac{1}{\tau^2} + \text{Pe}^\alpha, \quad (12)$$

where the exponent α varies from 1 to 2. Here, we used $\alpha = 1.2$ accordingly to Mostaghimi et al. [16] and Icardi et al. [36].

3. Results and Discussion

In this section, the influence of the porous medium structure on fluid flow (Section 3.1) and solute diffusion (Section 3.2) is analyzed for all generated porous media as well as the two scanned sandpacks, while advection-diffusion simulations (Section 3.3) are described for nine samples selected among all porous media.

3.1. Fluid Flow Simulations. Figure 3 illustrates the pore-scale fluid flow for two of the generated porous media (Figures 3(a) and 3(b)) and the two sandpack samples (Figures 3(c) and 3(d)). The porous media EXX exhibit a very rough pore surface, whereas the GXX media show a smoother pore surface. The low velocities clearly define a creeping flow regime ($\text{Re} \ll 1$). For a detailed discussion about semivariogram functions adopted in the geostatistical model, we address the interested readers to Di Palma et al. [23].

Figure 4 shows the behavior of the seepage velocity with respect to the various geometric parameters analyzed. The seepage velocity relation to the pore size and porosity is approximately linear for each set of the two semivariogram models (Figures 4(a) and 4(b)). As pointed out in a previous study [23], the difference between the two semivariogram models is clear (velocities differ by two orders of magnitude), whereas the variations of porosity result in a vertical shift of the linear dispersion. The seepage velocity versus SSA displays a slightly nonlinear, inverse relation (Figure 4(c)), almost independent of the porosity. A 2nd-degree polynomial function has been fitted to highlight the relation between the seepage velocity and the SSA (the corresponding coefficient of determination R^2 is shown on the plot). The dependence of the seepage velocity on the MC (Figure 4(d)) appears clearer than its dependence on the SSA, the coefficient of determination being higher. This finding is quite intuitive, meaning how high velocities, which are responsible for the average flow rate, are controlled by the shape/size of channels passing through [26, 28].

The trend between the Euler number and the seepage velocity (Figure 4(e)) shows a behavior similar to $\bar{U}_z(\text{MC})$ (Figure 4(d)). It means that the mean curvature and the Euler number provide similar information when describing the seepage velocity, even if the former is preferable because of its physical significance compared to the connectivity information provided by χ_V that is purely topological.

Finally, the seepage velocity as a function of either tortuosity (Figure 4(f)) or porosity and tortuosity (Figures 4(g) and 4(h)) well identifies the generated porous media and

the scanned samples in two subsets, although the values appear slightly scattered.

It is interesting to relate the computed seepage velocity to the permeability calculated using the Kozeny-Carman equation (equation (7)). The clear linear correlation among the generated media (i.e., black triangles and blue circles in Figure 5) suggests the proper combination of parameters governing the seepage velocity in the tested porous media. The wide range of permeability values also highlights the wide range explored through the two end-member semivariogram models. The values obtained for the sandpack samples (i.e., red squares) fall within the range of values obtained for the GXX porous media. The specific surface area represents the most sensitive parameter in the KC equation. Indeed, the porosities are identical for both semivariogram models; tortuosity varies over a limited range of values, whereas the SSA of EXX media is approximately two or three times greater than that of the GXX.

Because of the linearity between calculated seepage velocity and KC permeability, we can estimate the geometric factor (β) in equation (7) simply as the ratio of the imposed pressure gradient for all the fluid flow simulations over the slope of the fitting line. We obtain a Kozeny constant equals to 5.13, very similar to Carman's finding [46, 63].

The analysis of the results for the advective flow shows that the SSA and the MC can be considered the most important/leading proxies of the advective flow. However, according to equation (7), the only specific surface area is not able to describe the linear relation between the seepage velocity and imposed pressure gradient (essentially the permeability), but it needs to be combined with the porosity and tortuosity to provide the best relationship ($R^2 = 0.99$). On the contrary, the permeability at the REV scale can be represented by the solely mean curvature, although with a small degradation of the performance ($R^2 > 0.90$).

3.2. Diffusion Simulations. We analyze the behavior of the solute diffusive transport over time (equation (8)) and with the time t^* as a metric for the efficiency of the diffusion process (Section 2.4.2). In analogy to the analysis of the seepage velocity, each Minkowski functional is plotted against t^* (Figure 6). Figures 6(a)–6(e) did not show a clear correlation with t^* . However, it is worth to note how the porosity is a good descriptor within each model adopted to generate porous media.

A common relationship can be observed when considering the inverse tortuosity (Figure 6(f)), with the exception of the porous media having the lowest correlation length (i.e., the upper right black triangles). This behavior results from a limited spatial resolution for the lowest correlation length. Excluding such realizations, a 2nd-degree polynomial function has been fitted and the corresponding coefficient of determination R^2 is shown on the plot to highlight the relation between the time t^* and the inverse of the tortuosity squared. Finally, introducing the porosity in the descriptor (Figures 6(g) and 6(h)) splits the diffusive response accordingly to the two correlation models, in line with the results presented in Figure 6(a). In the following, the $1/\tau^2$ is considered as a unique proxy of the diffusive flow.

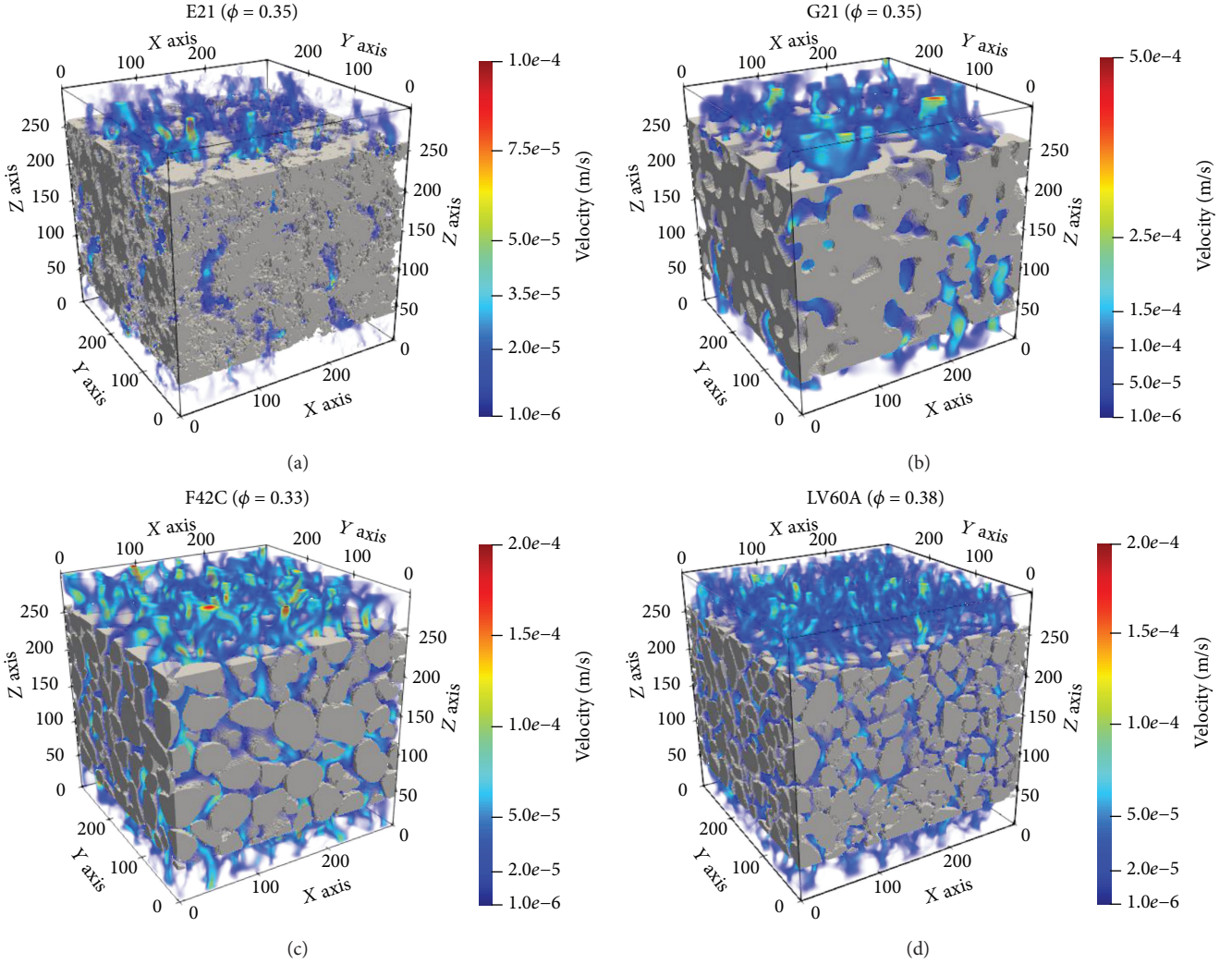


FIGURE 3: Visualization of porous medium structures and fluid flow streamlines. (a) and (b) are two generated media with $\xi = 0.21$ mm and $\phi = 0.35$, whereas (c) and (d) are the scanned sandpacks with estimated $\xi = 0.16$ mm and $\phi = 0.33$ (F42C) and $\xi = 0.125$ mm and $\phi = 0.38$ (LV60A).

3.3. Advection-Diffusion Simulations. The analysis of seepage velocity and time t^* suggests that two pore-scale geometrical properties can be selected as proxies to describe either the advective or the diffusive transport (i.e., MC and $1/\tau^2$). This allows reducing the number of descriptors to only two. This two-parameter space is shown in Figure 7. It is worth noting that the selected media do not correspond exactly to the outermost points of this parameter space because the extreme values of generated porous media highlight different uncertainty issues: one related to low space resolution (i.e., EXX with lowest ξ corresponding to the highest MC values) and the second one to the unrepresentativeness of the domain length compared to the correlation length (i.e., GXX with highest ξ corresponding to the lowest MC values).

The results of the advection-diffusion simulations provide information that can be used to infer transport parameters at the REV scale. We estimate the hydrodynamic

dispersion coefficient from the concentration breakthrough curves of each run using temporal moments (equation (11)) and compare them with published relationships (equation (12)). The Peclet number is estimated directly using the geometric properties of the porous media, where the seepage velocity is inferred from the KC formula, as validated in the previous section:

$$Pe = \frac{\bar{U}_z(\pi/SSA)}{D_m} = \frac{\pi\phi^2}{\beta\tau^2SSA^3D_mt} \frac{dP}{L}. \quad (13)$$

Figure 8 shows the calculated longitudinal dispersion normalized by the molecular diffusivity for each simulation. We find a good match between the values calculated by the temporal moments and the relationship based on the geometric properties entering the definition of the Peclet number. Associated uncertainty has been estimated through the

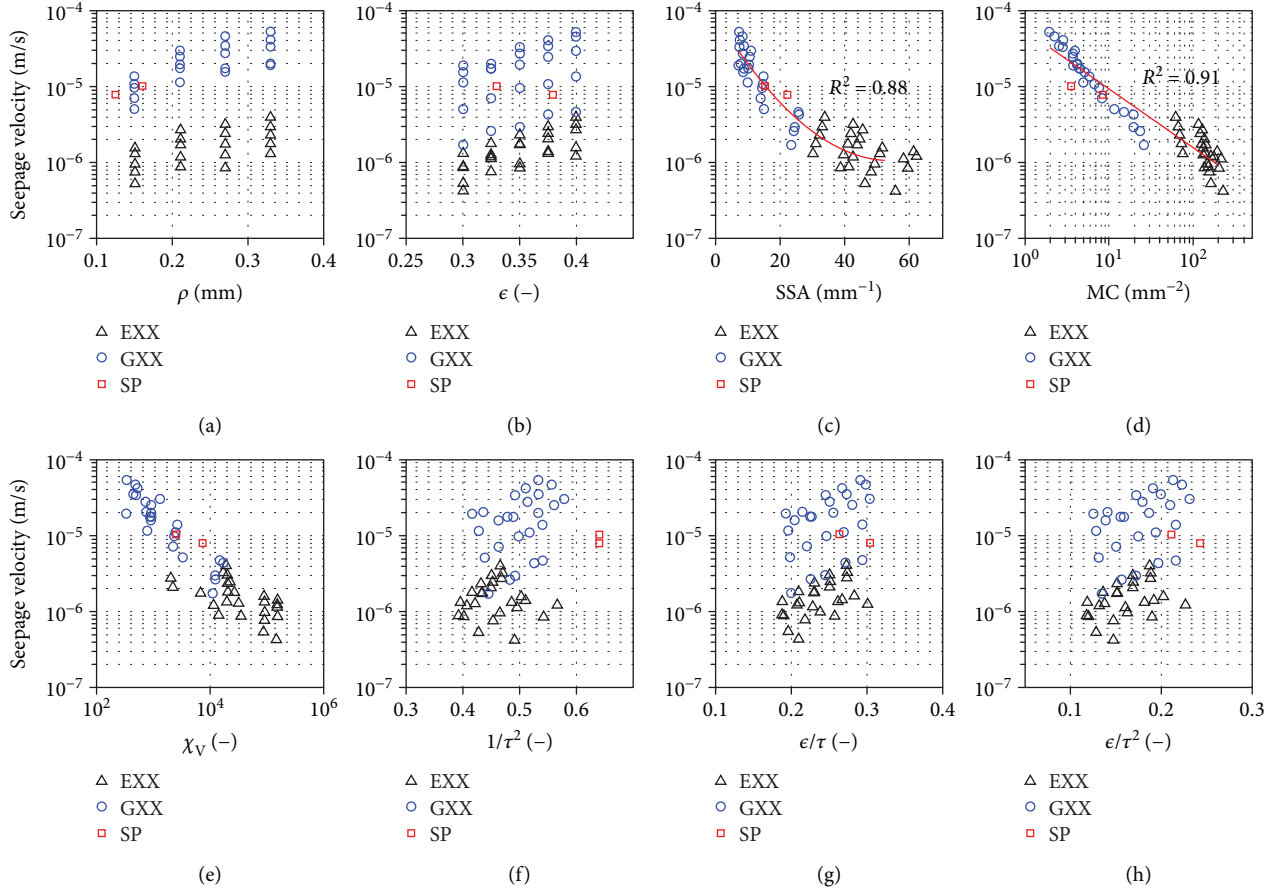


FIGURE 4: Seepage velocity as a function of correlation length (ξ), Minkowski functionals—porosity (ϕ), specific surface area (SSA), mean curvature (MC), and Euler number (χ_v)—and literature relationships for effective diffusivity, $1/\tau^2$, τ^2/τ , and ϕ/τ^2 , respectively, for generated porous media (black triangles and blue circles for exponential (EXX) and Gaussian (GXX) variogram models, respectively) and scanned sandpicks (SP) (red squares). The coefficient of determination (R^2) associated with the fitting functions for the SSA and MC (red lines) is reported in (c, d).

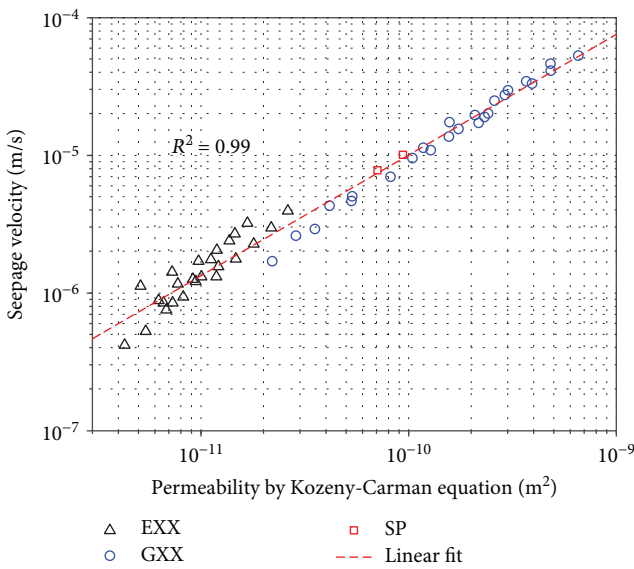


FIGURE 5: Seepage velocity as function of permeability. Porous media generated by exponential and Gaussian variogram models are named EXX and GXX (black triangles and blue circles, respectively).

symmetric mean absolute percentage error (SMAPE) defined as follows:

$$SMAPE = \frac{100}{n} \sum_{i=1}^n \frac{|X - Y|}{(|X| + |Y|)/2}, \quad (14)$$

resulting in a value equal to 43%. The uncertainty decreases for increasing Pe (30% for $Pe > 10^{-1}$). In case of diffusion-dominant process, the mechanical dispersion vanishes and the effective diffusivity can be calculated by fitting the concentration breakthrough curves with analytical expressions. The shift from high to low Pe, at the same conditions of imposed pressure gradient, is a straightforward consequence of the SSA range of the porous media, highlighting again the impact of this geometric feature.

The good estimation of the longitudinal dispersion through the temporal moments confirms the validity of Fickian transport regime for the investigated porous media, as also reported in Bijeljic et al. [30] and Icardi et al. [36] that used realistic packed geometries comparable to our synthetic media. The non-Fickian behavior shows up in more complex porous media, such as carbonate and sandstone rock,

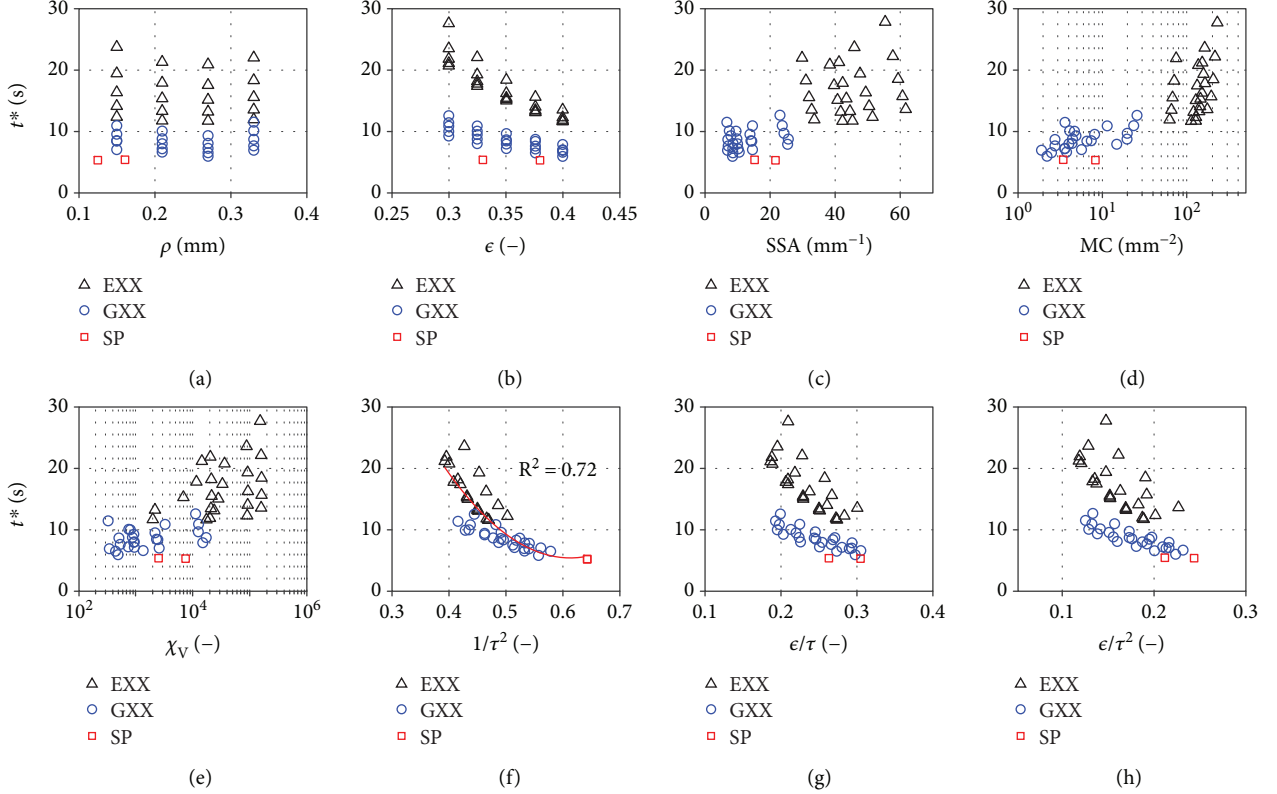


FIGURE 6: t^* as a function of correlation length (ξ), Minkowski functionals—porosity (ϕ), specific surface area (SSA), mean curvature (MC), and Euler number (χ_V)—and literature relationships for effective diffusivity, $1/\tau^2$, ϕ/τ , and ϕ/τ^2 , respectively, for generated porous media (black triangles and blue circles for exponential (EXX) and Gaussian (GXX) variogram models, respectively) and scanned sandpicks (SP) (red squares). The coefficient of determination (R^2) associated to the fitting functions for the MC (red lines) is reported in (f).

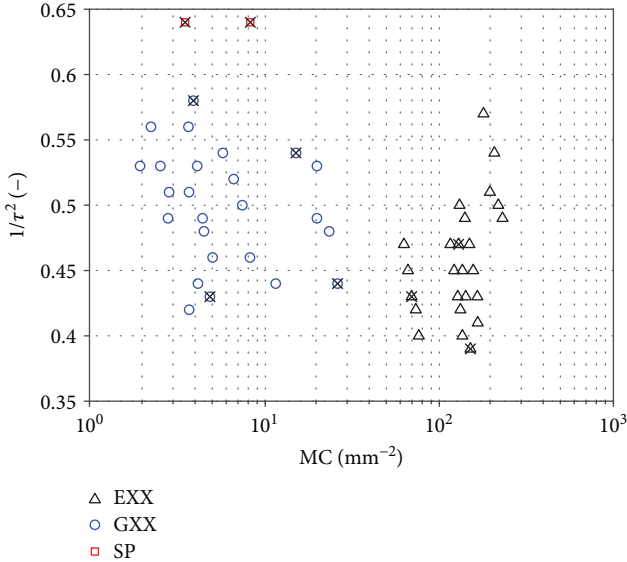


FIGURE 7: Parameter space of MC and $1/\tau^2$ for all generated porous media and CT image sandpick samples, obtained after fluid flow and diffusion simulations. Crossed markers indicate the sample selected for the advection-diffusion simulations.

in which the solute experiences a very wide range of transit times across pores of a very different size [29, 30, 34]. Moreover, the non-Fickian behavior is more evident under high advection-dominant transport [32].

One possible limit to the application of our findings to natural media lies in the assumption of geostatistical homogeneity of the generated porous media, which could prevent the extension of our results to porous media that exhibit multiple length scales and/or anisotropy. Future works should focus on the ability to generate realistic media displaying either or both heterogeneity and anisotropy. We do anticipate two different approaches to address this challenge. First, one could keep the present workflow but amend the procedure adopted in this paper by one additional transformation that allows for varying degrees of tortuosity (similar to the approach by [48]). Second, one could switch to the use of generators able to directly reproduce multipoint statistics [64, 65].

4. Conclusions

This study investigates the impact of various porous medium geometric descriptors on the transport of non-reactive solutes. To that end, we performed pore-scale flow and transport simulations on 3D synthetic porous media and micro-CT images of sandpicks using the lattice Boltzmann method. Synthetic porous media are generated with a geostatistically

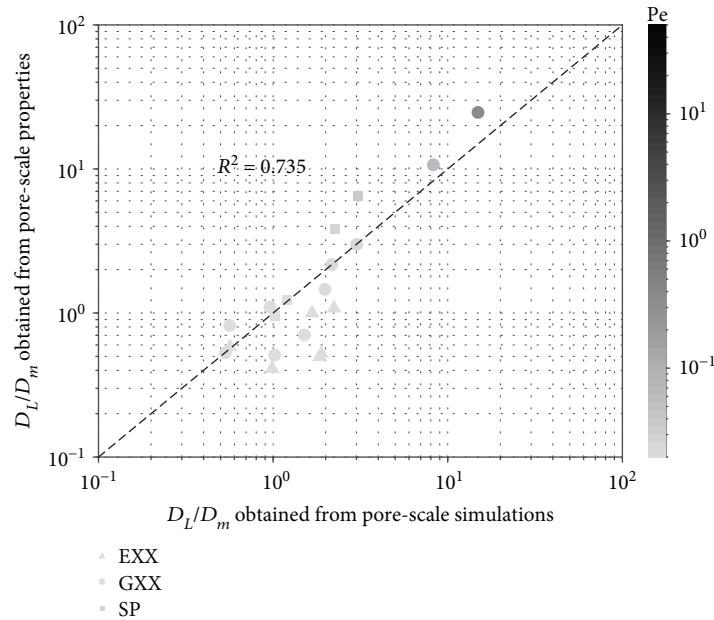


FIGURE 8: Comparison between the hydrodynamic dispersion coefficients calculated from the advection-diffusion simulation using equation (11) and the dispersion coefficients obtained from Mostaghimi et al. [16] and Icardi et al. [36] and defined in equation (12).

based approach, where the pore-scale characteristics are described by semivariogram models with a specified correlation length.

We carried out a sensitivity analysis over different synthetic porous medium features to identify proxies that best describe advective and diffusive transport. Our findings suggest that the advective flow is primarily affected by the second and third Minkowski functionals (specific surface area and mean curvature). However, according to the Kozeny-Carman equation, macroscopic permeability necessitates three pore-scale parameters to be estimated (porosity, tortuosity, and specific surface area), while similar results can be obtained using the only mean curvature as proxy.

Results of the diffusion simulations show that the effective diffusion coefficient scales as the inverse of the tortuosity squared.

Finally, we tested the possibility to estimate the hydrodynamic dispersion coefficients using only the geometric properties of porous media and the applied pressure gradient. Such estimates from pore-scale geometric features have been compared with the coefficients calculated through the temporal moment method from the advection-diffusion simulations with Peclet numbers ranging from 10^{-2} to 10^1 . We concluded, for the range of tested porous media, that an estimation of the hydrodynamic dispersion can be obtained from pore-scale properties: considering all tested Peclet numbers, the uncertainty of hydrodynamic dispersion is equal to 43%, when compared with that obtained from advection-diffusion simulations. Limiting such estimation to simulations characterized by $Pe > 10^{-1}$, uncertainty decreases to 30%.

Data Availability

The micro-CT images of sandpacks used to support the findings of this study have been deposited in the Figshare digital

repository (<https://www.imperial.ac.uk/earth-science/research/research-groups/perm/research/pore-scale-modelling/micro-ct-images-and-networks/>). The generated porous media and simulation results used to generate figures are available upon request via e-mail to the first author.

Additional Points

Highlights. (i) We perform pore-scale flow simulations on synthetic porous media and micro-CT images. (ii) Advective transport is primarily affected by the second and third Minkowski functionals. (iii) Diffusive transport is a function of the inverse of the squared tortuosity. (iv) Hydrodynamic dispersion coefficients are estimated using geometric properties.

Conflicts of Interest

The authors declare that there is no conflict of interest regarding the publication of this paper.

Supplementary Materials

The details/description of the lattice Boltzmann method for single-phase fluid flow and non-reactive advection-diffusion simulations and the set of parameters used in this work. (*Supplementary Materials*)

References

- [1] J. W. Delleur, *The Handbook of Groundwater Engineering*, CRC press, 2006.
- [2] M. Rolle and P. K. Kitanidis, "Effects of compound-specific dilution on transient transport and solute breakthrough: a pore-scale analysis," *Advances in Water Resources*, vol. 71, pp. 186–199, 2014.

- [3] A. Guadagnini, M. J. Blunt, M. Riva, and B. Bijeljic, "Statistical scaling of geometric characteristics in millimeter scale natural porous media," *Transport in Porous Media*, vol. 101, no. 3, pp. 465–475, 2014.
- [4] Z. Liu, A. Herring, C. Arns, S. Berg, and R. T. Armstrong, "Pore-scale characterization of two-phase flow using integral geometry," *Transport in Porous Media*, vol. 118, no. 1, pp. 99–117, 2017.
- [5] C. Noiriel, P. Gouze, and B. Madé, "3D analysis of geometry and flow changes in a limestone fracture during dissolution," *Journal of Hydrology*, vol. 486, pp. 211–223, 2013.
- [6] T. D. Scheibe, W. A. Perkins, M. C. Richmond et al., "Pore-scale and multiscale numerical simulation of flow and transport in a laboratory-scale column," *Water Resources Research*, vol. 51, no. 2, pp. 1023–1035, 2015.
- [7] H. Andrä, N. Combaret, J. Dvorkin et al., "Digital rock physics benchmarks—part II: computing effective properties," *Computers & Geosciences*, vol. 50, pp. 33–43, 2013.
- [8] M. J. Blunt, B. Bijeljic, H. Dong et al., "Pore-scale imaging and modelling," *Advances in Water Resources*, vol. 51, pp. 197–216, 2013.
- [9] T. Bultreys, W. De Boever, and V. Cnudde, "Imaging and image-based fluid transport modeling at the pore scale in geological materials: a practical introduction to the current state-of-the-art," *Earth-Science Reviews*, vol. 155, pp. 93–128, 2016.
- [10] C. J. Werth, C. Zhang, M. L. Brusseau, M. Oostrom, and T. Baumann, "A review of non-invasive imaging methods and applications in contaminant hydrogeology research," *Journal of Contaminant Hydrology*, vol. 113, no. 1–4, pp. 1–24, 2010.
- [11] D. Wildenschild and A. P. Sheppard, "X-ray imaging and analysis techniques for quantifying pore-scale structure and processes in subsurface porous medium systems," *Advances in Water Resources*, vol. 51, pp. 217–246, 2013.
- [12] J. D. Hyman and C. L. Winter, "Stochastic generation of explicit pore structures by thresholding Gaussian random fields," *Journal of Computational Physics*, vol. 277, pp. 16–31, 2014.
- [13] J. T. Fredrich, A. A. DiGiovanni, and D. R. Noble, "Predicting macroscopic transport properties using microscopic image data," *Journal of Geophysical Research: Solid Earth*, vol. 111, no. B3, 2006.
- [14] M. Singh and K. K. Mohanty, "Permeability of spatially correlated porous media," *Chemical Engineering Science*, vol. 55, no. 22, pp. 5393–5403, 2000.
- [15] Y. Gao, X. Zhang, P. Rama et al., "Calculating the anisotropic permeability of porous media using the lattice Boltzmann method and X-ray computed tomography," *Transport in Porous Media*, vol. 92, no. 2, pp. 457–472, 2012.
- [16] P. Mostaghimi, B. Bijeljic, and M. Blunt, "Simulation of flow and dispersion on pore-space images," *SPE Journal*, vol. 17, no. 4, pp. 1131–1141, 2012.
- [17] P. Mostaghimi, M. J. Blunt, and B. Bijeljic, "Computations of absolute permeability on micro-CT images," *Mathematical Geosciences*, vol. 45, no. 1, pp. 103–125, 2013.
- [18] A. Ghassemi and A. Pak, "Pore scale study of permeability and tortuosity for flow through particulate media using Lattice Boltzmann method," *International Journal for Numerical and Analytical Methods in Geomechanics*, vol. 35, no. 8, pp. 886–901, 2011.
- [19] P. Lehmann, M. Berchtold, B. Ahrenholz et al., "Impact of geometrical properties on permeability and fluid phase distribution in porous media," *Advances in Water Resources*, vol. 31, no. 9, pp. 1188–1204, 2008.
- [20] A. Q. Raeini, M. J. Blunt, and B. Bijeljic, "Modelling two-phase flow in porous media at the pore scale using the volume-of-fluid method," *Journal of Computational Physics*, vol. 231, no. 17, pp. 5653–5668, 2012.
- [21] A. Q. Raeini, M. J. Blunt, and B. Bijeljic, "Direct simulations of two-phase flow on micro-CT images of porous media and upscaling of pore-scale forces," *Advances in Water Resources*, vol. 74, pp. 116–126, 2014.
- [22] D. Zhang, K. Papadikis, and S. Gu, "A lattice Boltzmann study on the impact of the geometrical properties of porous media on the steady state relative permeabilities on two-phase immiscible flows," *Advances in Water Resources*, vol. 95, pp. 61–79, 2016.
- [23] P. R. Di Palma, N. Guyennon, F. Heße, and E. Romano, "Porous media flux sensitivity to pore-scale geostatistics: a bottom-up approach," *Advances in Water Resources*, vol. 102, pp. 99–110, 2017.
- [24] P. K. Kang, P. de Anna, J. P. Nunes, B. Bijeljic, M. J. Blunt, and R. Juanes, "Pore-scale intermittent velocity structure underpinning anomalous transport through 3-D porous media," *Geophysical Research Letters*, vol. 41, no. 17, pp. 6184–6190, 2014.
- [25] M. Matyka, J. Golembiewski, and Z. Koza, "Power-exponential velocity distributions in disordered porous media," *Physical Review E*, vol. 93, no. 1, article 013110, 2016.
- [26] M. Siena, M. Riva, J. D. Hyman, C. L. Winter, and A. Guadagnini, "Relationship between pore size and velocity probability distributions in stochastically generated porous media," *Physical Review E*, vol. 89, no. 1, article 013018, 2014.
- [27] M. Wang, Y. F. Chen, G. W. Ma, J. Q. Zhou, and C. B. Zhou, "Influence of surface roughness on nonlinear flow behaviors in 3D self-affine rough fractures: lattice Boltzmann simulations," *Advances in Water Resources*, vol. 96, pp. 373–388, 2016.
- [28] P. de Anna, B. Quaife, G. Biros, and R. Juanes, "Prediction of the low-velocity distribution from the pore structure in simple porous media," *Physical Review Fluids*, vol. 2, no. 12, article 124103, 2017.
- [29] B. Bijeljic, P. Mostaghimi, and M. J. Blunt, "Insights into non-Fickian solute transport in carbonates," *Water Resources Research*, vol. 49, no. 5, pp. 2714–2728, 2013.
- [30] B. Bijeljic, A. Raeini, P. Mostaghimi, and M. J. Blunt, "Predictions of non-Fickian solute transport in different classes of porous media using direct simulation on pore-scale images," *Physical Review E*, vol. 87, no. 1, article 013011, 2013.
- [31] M. Dentz, T. Le Borgne, A. Englert, and B. Bijeljic, "Mixing, spreading and reaction in heterogeneous media: a brief review," *Journal of Contaminant Hydrology*, vol. 120–121, pp. 1–17, 2011.
- [32] M. Dentz, M. Icardi, and J. J. Hidalgo, "Mechanisms of dispersion in a porous medium," *Journal of Fluid Mechanics*, vol. 841, pp. 851–882, 2018.
- [33] P. R. Di Palma, A. Parmigiani, C. Huber, N. Guyennon, and P. Viotti, "Pore-scale simulations of concentration tails in heterogeneous porous media," *Journal of Contaminant Hydrology*, vol. 205, pp. 47–56, 2017.

- [34] F. Gjetvaj, A. Russian, P. Gouze, and M. Dentz, "Dual control of flow field heterogeneity and immobile porosity on non-Fickian transport in Berea sandstone," *Water Resources Research*, vol. 51, no. 10, pp. 8273–8293, 2015.
- [35] D. L. Hochstetler, M. Rolle, G. Chiogna, C. M. Haberer, P. Grathwohl, and P. K. Kitanidis, "Effects of compound-specific transverse mixing on steady-state reactive plumes: insights from pore-scale simulations and Darcy-scale experiments," *Advances in Water Resources*, vol. 54, pp. 1–10, 2013.
- [36] M. Icardi, G. Boccardo, D. L. Marchisio, T. Tosco, and R. Sethi, "Pore-scale simulation of fluid flow and solute dispersion in three-dimensional porous media," *Physical Review E*, vol. 90, no. 1, article 013032, 2014.
- [37] S. Succi, *The Lattice Boltzmann Equation: for Fluid Dynamics and Beyond*, Oxford University Press, 2001.
- [38] H. J. Vogel, U. Weller, and S. Schlüter, "Quantification of soil structure based on Minkowski functions," *Computers & Geosciences*, vol. 36, no. 10, pp. 1236–1245, 2010.
- [39] F. Heße, V. Prykhodko, S. Schlüter, and S. Attinger, "Generating random fields with a truncated power-law variogram: a comparison of several numerical methods," *Environmental Modelling & Software*, vol. 55, pp. 32–48, 2014.
- [40] B. Matérn, *Spatial Variation: Stochastic Models and Their Application to Some Problems in Forest Surveys and Other Sampling Investigations*, Statens skogsforskningsinstitut, 1960.
- [41] B. Minasny and A. B. McBratney, "The Matérn function as a general model for soil variograms," *Geoderma*, vol. 128, no. 3–4, pp. 192–207, 2005.
- [42] O. Dubrule, "Indicator variogram models: do we have much choice?," *Mathematical Geosciences*, vol. 49, no. 4, pp. 441–465, 2017.
- [43] F. D. E. Latief, B. Biswal, U. Fauzi, and R. Hilfer, "Continuum reconstruction of the pore scale microstructure for Fontainebleau sandstone," *Physica A: Statistical Mechanics and its Applications*, vol. 389, no. 8, pp. 1607–1618, 2010.
- [44] H. J. Vogel, "Topological characterization of porous media," in *Morphology of Condensed Matter*, pp. 75–92, Springer, Berlin, Heidelberg, 2002.
- [45] K. Wu, M. I. J. van Dijke, G. D. Couples et al., "3D stochastic modelling of heterogeneous porous media—applications to reservoir rocks," *Transport in Porous Media*, vol. 65, no. 3, pp. 443–467, 2006.
- [46] M. B. Clennell, "Tortuosity: a guide through the maze," *Geological Society, London, Special Publications*, vol. 122, no. 1, pp. 299–344, 1997.
- [47] N. Linde, P. Renard, T. Mukerji, and J. Caers, "Geological realism in hydrogeological and geophysical inverse modeling: a review," *Advances in Water Resources*, vol. 86, pp. 86–101, 2015.
- [48] B. Zinn and C. F. Harvey, "When good statistical models of aquifer heterogeneity go bad: a comparison of flow, dispersion, and mass transfer in connected and multivariate Gaussian hydraulic conductivity fields," *Water Resources Research*, vol. 39, no. 3, 2003.
- [49] T. Krüger, H. Kusumaatmaja, A. Kuzmin, O. Shardt, G. Silva, and E. M. Viggien, *The Lattice Boltzmann Method: Principles and Practice*, Springer, Cham, Switzerland, 2017.
- [50] M. C. Sukop and D. T. Thorne, *Lattice Boltzmann Modeling: an Introduction for Geoscientists and Engineers*, Springer, 2006.
- [51] J. Latt, "Palabos, parallel lattice Boltzmann solver," 2009, January 2019, <http://www.palabos.org>.
- [52] C. Huber, B. Shafei, and A. Parmigiani, "A new pore-scale model for linear and non-linear heterogeneous dissolution and precipitation," *Geochimica et Cosmochimica Acta*, vol. 124, pp. 109–130, 2014.
- [53] A. Koponen, M. Kataja, and J. Timonen, "Permeability and effective porosity of porous media," *Physical Review E*, vol. 56, no. 3, pp. 3319–3325, 1997.
- [54] N. Epstein, "On tortuosity and the tortuosity factor in flow and diffusion through porous media," *Chemical Engineering Science*, vol. 44, no. 3, pp. 777–779, 1989.
- [55] B. Ghanbarian, A. G. Hunt, R. P. Ewing, and M. Sahimi, "Tortuosity in porous media: a critical review," *Soil Science Society of America Journal*, vol. 77, no. 5, p. 1461, 2013.
- [56] L. Shen and Z. Chen, "Critical review of the impact of tortuosity on diffusion," *Chemical Engineering Science*, vol. 62, no. 14, pp. 3748–3755, 2007.
- [57] J. Van Brakel and P. M. Heertjes, "Analysis of diffusion in macroporous media in terms of a porosity, a tortuosity and a constrictivity factor," *International Journal of Heat and Mass Transfer*, vol. 17, no. 9, pp. 1093–1103, 1974.
- [58] M. Matyka, A. Khalili, and Z. Koza, "Tortuosity-porosity relation in porous media flow," *Physical Review E*, vol. 78, no. 2, article 026306, 2008.
- [59] E. E. Adams and L. W. Gelhar, "Field study of dispersion in a heterogeneous aquifer: 2. Spatial moments analysis," *Water Resources Research*, vol. 28, no. 12, pp. 3293–3307, 1992.
- [60] O. A. Cirpka and P. K. Kitanidis, "Characterization of mixing and dilution in heterogeneous aquifers by means of local temporal moments," *Water Resources Research*, vol. 36, no. 5, pp. 1221–1236, 2000.
- [61] M. N. Goltz and P. V. Roberts, "Using the method of moments to analyze three-dimensional diffusion-limited solute transport from temporal and spatial perspectives," *Water Resources Research*, vol. 23, no. 8, pp. 1575–1585, 1987.
- [62] L. Pang, M. Goltz, and M. Close, "Application of the method of temporal moments to interpret solute transport with sorption and degradation," *Journal of Contaminant Hydrology*, vol. 60, no. 1–2, pp. 123–134, 2003.
- [63] P. C. Carman, "Fluid flow through granular beds," *Chemical Engineering Research and Design*, vol. 75, pp. S32–S48, 1997.
- [64] L. Y. Hu and T. Chugunova, "Multiple-point geostatistics for modeling subsurface heterogeneity: a comprehensive review," *Water Resources Research*, vol. 44, no. 11, 2008.
- [65] G. Mariethoz and S. Lefebvre, "Bridges between multiple-point geostatistics and texture synthesis: review and guidelines for future research," *Computers & Geosciences*, vol. 66, pp. 66–80, 2014.

Research Article

Permeability Estimation Based on the Geometry of Pore Space via Random Walk on Grids

Tongchao Nan , Jichun Wu , Kaixuan Li, and Jianguo Jiang 

Department of Hydrosociences, School of Earth Sciences and Engineering, Nanjing University, Nanjing 210093, China

Correspondence should be addressed to Tongchao Nan; tcnan@nju.edu.cn and Jichun Wu; jcwu@nju.edu.cn

Received 25 May 2018; Revised 13 September 2018; Accepted 1 October 2018; Published 8 January 2019

Guest Editor: Joaquín Jiménez-Martínez

Copyright © 2019 Tongchao Nan et al. This is an open access article distributed under the Creative Commons Attribution License, which permits unrestricted use, distribution, and reproduction in any medium, provided the original work is properly cited.

In the literature, the mean penetration depth (MPD) calculated by “walk on spheres” or “walk on cubes” was used to quickly estimate the intrinsic permeability of digitized porous media. However, these two methods encounter difficulties such as irregular boundaries and the determination of arrivals at a boundary. In this study, an MPD method that is based on a more flexible “random walk on grid” (WOG) is explored. Moreover, the accurate MPDs for the pores of simple shapes are derived with Green’s functions to validate the WOG-based MPD. The results suggested that MPDs based on Green’s functions and WOG are consistent with each other; the factor C in the permeability expression is slightly dependent on roundness of the cross sections and is approximately 1.125 on average, according to analytical and numerical results. In a synthetic complex pore, the permeability estimated by WOG is comparable to, but greater than, the estimate based on the pore-scale dynamics simulation in COMSOL.

1. Introduction

Permeability, which is a measure of the ability of a porous material to allow fluid to pass through it, is one of the most important properties of geologic formations to hydrogeologists, petrophysicists, and other geologic fluid researchers. Since permeability (or hydraulic conductivity) greatly influences the fluid movements and flow fields of groundwater, it is generally the fundamental factor in all groundwater-related problems, such as groundwater exploitation, surface-groundwater interaction, contaminant transport, agricultural irrigation, and site selection for radioactive waste disposal [1, 2].

As a macroscopic parameter of formations, permeability is closely related to pore microstructures. In addition to the direct measurement of samples, indirect measurement is also important for different environmental and technological applications. Some studies have been devoted to establishing the relationship between microscopic geometry and macroscopic permeability by theoretical models and numerical calculations [3–8], which are becoming increasingly valuable for the growing availability of microscopic tomographic data,

such as nuclear magnetic resonance, X-ray microtomography, and scanning-electron-microscopic imaging ([9–12]; among many others).

For pores of some of the simplest geometries, the permeability can be calculated by the exact solution to the Poiseuille flow equation. For example, in a straight tube of circle-shaped cross sections, one obtains $k = R^2/8$ by combining three equations: $Q = (\pi R^4/8\mu)(\Delta P/L)$ (Hagen-Poiseuille law), $Q = K(\Delta P/\rho g L)\pi R^2$ (Darcy’s law), and $K = k(\rho g/\mu)$ (relation between permeability and conductivity) (see, e.g., [13]). For tubes of elliptical cross sections, $k = a^2 b^2/[4(a^2 + b^2)]$, where a and b are the semiaxes [14]; similar results are available for several other shapes [15, 16]. For media of higher complexity, for example, $k = c_K(n^3/(1-n)^2)d^2$ in a packed bed of solids, where d is the mean grain diameter, n is the porosity, and c_K is a parameter that is dependent on cross-sectional geometry [6, 17, 18].

However, more powerful tools are required in media of general microstructure. By analyzing diffusion processes in porous media, Torquato [8] linked the permeability tensor of the media to a so-called trapping constant, which is not easy to evaluate and thus is not practical. However, the idea

of using diffusion or Brownian processes to reflect the properties of porous media is useful. Based on the Brownian motion model and the Debye-Brinkman equation (see, e.g., [19]), Hwang et al. [5] found that the mean penetration depth (MPD, denoted by D), which is the expected depth that a Brownian motion can enter before reaching solid surface for the first time, is a good measure of the permeability of the medium and suggested that $k = D^2$. Simonov and Mascagni [7] took porosity into account and suggested that $k = C_{SM} n D^2$, where n is the porosity and c_{SM} is a factor. They estimated $C_{SM} = k/nD^2 \approx 6.63$ by using the Poiseuille law-based permeability $k = 0.0351d^2$ in an ideal, straight pore of the square cross section with a side length that is equal to d , and $n = 0.5$. It is still not clear whether $k = C_{SM} n D^2$ is also valid for pores of other geometries. Sabelfeld [20] used a spectral projection method to avoid the numerical calculation on overlapping discs and spheres which, however, applies to simplified pore surfaces and is unsuitable for real media with rough surfaces.

The equations above are all in a quadratic form; i.e., $k = CL^2$, where L is some type of characteristic length (e.g., hydraulic radius, mean pore size, mean grain diameter, or MPD), and the coefficient C may depend on the cross section and/or porosity ([13]; and references therein).

If one uses MPD as the characteristic length, the coefficient C may depend on both cross-section shape and porosity. The influence of porosity on C was also investigated by Simonov and Mascagni [7] using “walk on cubes” and “walk on spheres.” However, “walk on cubes” is only suitable for voids of polyhedron and is inefficient for curly boundaries [21]. “Walk on spheres” has difficulty in determining exactly when and where the random walk ends at a boundary. The difficulty leads to significant error and generates some bias (Milstein and Tretyakov 1999; Deaconu and Lejay 2006). To avoid these problems, in this study, we extend the MPD method by using a more flexible “random walk on grid” (WOG), which is able to easily determine the arrival at boundaries and handle irregular surfaces, including cambering, narrow gaps, and wedge outs.

To validate the effectiveness of the WOG-based MPD method and to investigate the extent of C 's dependence on the roundness of pore cross sections, we derived the theoretical values of MPD and C using Green's function in the pores of several basic geometries and compared them to their WOG-based counterparts. Simonov and Mascagni [7] realized the possible weak dependence of C on the cross-sectional geometry of void space, but they did not investigate the problem further. Here, the dependence is investigated through C derived by Green's functions, as well as the C estimated by WOG.

To date, the permeability calculated by the MPD method has not been verified in a porous medium against dynamic simulation or experimental results in the literature. A synthetic porous sample is constructed for permeability estimation using COMSOL simulation and the WOG-based MPD method.

The paper is organized as follows: In Section 2, the MPD method based on WOG and Green's functions, as well as

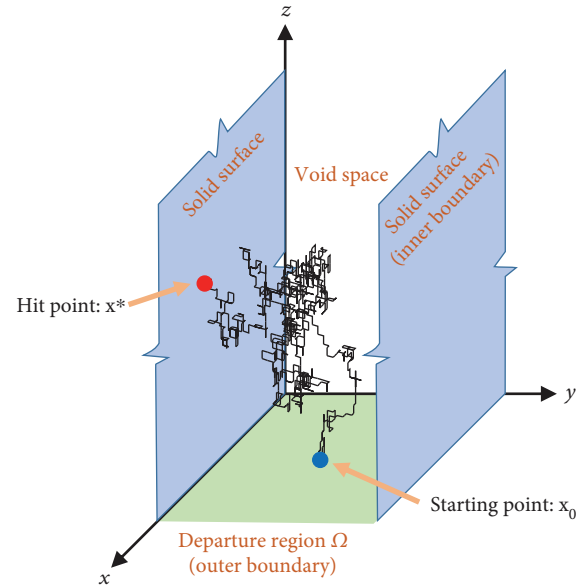


FIGURE 1: A diagram of random walk in void space. The outer boundary is the face of the medium; the inner boundary consists of the void-solid interface. Black line shows the path of a random walk realization.

COMSOL simulation, is introduced. In Section 3, the results of the MPD estimation in simple pores of different geometries are reported, and the factor C is calibrated for each geometry. Furthermore, the average C factor is used to estimate the permeability of a synthetic pore, and the result is verified by a COMSOL model. In Section 4, the results are discussed and conclusions are drawn.

2. Methodology

2.1. Mean Penetration Depth (MPD) and MPD Calculation via Green's Function. Given a porous medium, let a Brownian motion initiate at \mathbf{x}' (denoted by $\mathbf{x}_0 = \mathbf{x}'$) on its outer boundary plane (say, $z = 0$; Figure 1) and enter the medium until the walker hits a solid surface (i.e., the inner boundary, represented by blue surfaces in Figure 1) at a random position, \mathbf{x}^* . The depth of the hit point relative to the outer boundary plane (i.e., $z(\omega)$; ω is the ensemble index) is called the penetration depth of the Brownian motion, denoted by $l(\mathbf{x}', \omega)$. The mean penetration depth (MPD) is the ensemble mean of the penetration depths in Monte Carlo experiments, starting from an area on the outer boundary (termed “departure region” Ω , i.e., the green area in Figure 1), i.e., $D_B = \langle 1/S \int_{\mathbf{x}' \in \Omega} l(\mathbf{x}', \omega) d\mathbf{x}' \rangle$, where $\langle \rangle$ stands for expectation with respect to the ensemble index ω , D_B denotes the MPD estimated by the Brownian motion (or random walk), and S is the area of Ω .

In fact, the Brownian motion in void space, as mentioned above, is a diffusion process that is reflected back to void space at the outer boundary and is killed at the inner boundary. Given a starting point $\mathbf{x}_0 = \mathbf{x}'$, the spatial density $c(\mathbf{x} | \mathbf{x}')$

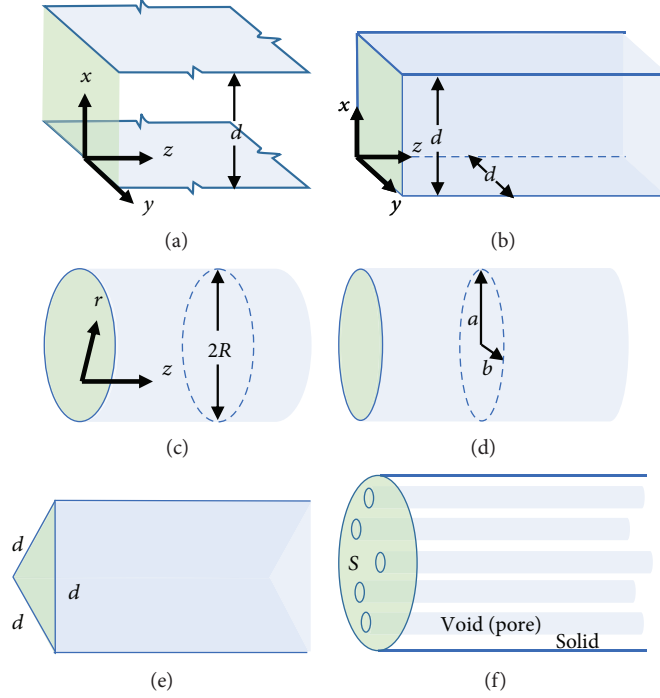


FIGURE 2: Void spaces (a) between parallel planes and in straight tubes of (b) a square cross section; (c) a circular cross section; (d) an elliptic cross section; and (e) an equilateral triangular cross section. (f) An ideal porous medium sample consisting of solid and many straight pores. The green area indicates the outer boundary.

(i.e., mean times of occurrence in space) of the diffusion satisfies the following equation:

$$\Delta c(\mathbf{x} | \mathbf{x}') + \delta(\mathbf{x} - \mathbf{x}') = 0, \quad (1a)$$

$$c(\mathbf{x} | \mathbf{x}') = 0, \quad \mathbf{x} \in \Gamma, \quad (1b)$$

$$\frac{\partial c(\mathbf{x} | \mathbf{x}')}{\partial \mathbf{n}_e} = 0, \quad \mathbf{x} \in \Omega, \quad (1c)$$

where $\mathbf{x}' = (x', y', z') \in \Omega$ and $\mathbf{x} = (x, y, z)$, δ is the Dirac function, and \mathbf{n}_e is the vector normal to outer boundary Ω . Equation (1b) is the absorbing boundary at the void-solid interface Γ . Equation (1c) is the reflection (no-flux) boundary at the departure region Ω (outer boundary).

One may notice that (1) is actually a Green's function problem. Its solution $c(\mathbf{x} | \mathbf{x}')$ is the Green's function of the following Poisson equation:

$$\Delta u(\mathbf{x}) = -f(\mathbf{x}), \quad (2a)$$

$$\text{Dirichlet boundary at } \Gamma, \quad (2b)$$

$$\text{Neumann boundary at } \Omega. \quad (2c)$$

For some simple geometries, the analytical expressions of $c(\mathbf{x} | \mathbf{x}')$ can be found or easily derived from the libraries of Green's functions in the literature (e.g., Cole et al. [22]). When $c(\mathbf{x} | \mathbf{x}')$ is known, the probability distribution of the

hit point \mathbf{x}^* at the inner boundary can be expressed as (see, e.g., Deaconu and Lejay [23])

$$p(\mathbf{x}^* | \mathbf{x}_0 = \mathbf{x}') = -\frac{\partial c(\mathbf{x}^* | \mathbf{x}')}{\partial \mathbf{n}}, \quad \mathbf{x}^* \in \Gamma, \quad (3)$$

where \mathbf{n} is the vector normal to Γ and pointing to solid. Hence, the penetration depth and MPD can be calculated via $c(\mathbf{x} | \mathbf{x}')$. That is, the penetration depth of point \mathbf{x}' is $l_e(\mathbf{x}') = \langle l(\mathbf{x}', \omega) \rangle = -\int_{\Gamma} z (\partial c(\mathbf{x} | \mathbf{x}') / \partial \mathbf{n})|_{\mathbf{x} \in \Gamma} d\mathbf{x}$, which will be further averaged on the departure region Ω to calculate the MPD, i.e.,

$$D_G = \frac{1}{S} \int_{\mathbf{x}' \in \Omega} l_e(\mathbf{x}') d\mathbf{x}' = -\frac{1}{S} \int_{\mathbf{x}' \in \Omega} d\mathbf{x}' \int_{\Gamma} z \frac{\partial c(\mathbf{x} | \mathbf{x}')}{\partial \mathbf{n}}|_{\mathbf{x} \in \Gamma} d\mathbf{x}, \quad (4)$$

where S is the area of Ω .

We consider the pores of three simple geometries for which Green's function $c(\mathbf{x} | \mathbf{x}')$ is available, i.e., parallel planes, straight square, and circular tubes (Figures 2(a)–2(c)). Here, we used the “isoperimetric ratio” φ as a measure of the pore cross-sectional shape. $\varphi = l_c^2/A$ is used to measure how greatly the shape differs from a circle, where l_c is the length of a curve (perimeter) and A is the corresponding area. φ has a minimum value 4π for the circle and higher values for all other shapes [24]. For parallel planes $\varphi = \infty$, since the length of planes is infinite and the plane distance d is finite;

for the square cross section, $\varphi = (4d)^2/d^2 = 16$; for the equilateral triangle, $\varphi = (3d)^2/(\sqrt{3}d^2/4) = 12\sqrt{3} \approx 20.8$; for the ellipse with semiaxes a and b ($a \geq b$), $4\pi \leq \varphi < \infty$ and $\varphi \approx 15.0$ as $a = 2b$.

For parallel planes of distance d (Figure 2(a)), the corresponding Green's function is expressed as [22]

$$c(x, z | x', z' = 0) = \frac{2}{\pi} \sum_{n=1}^{\infty} \frac{1}{n} e^{-n\pi z/d} \sin\left(\frac{n\pi x}{d}\right) \sin\left(\frac{n\pi x'}{d}\right). \quad (5)$$

Applying Equation (4), we obtain the MPD based on Green's function, i.e.,

$$D_G = 7\zeta(3) \frac{d}{\pi^3} \approx 0.2714d, \quad (6)$$

where $\zeta(\bullet)$ is the zeta function and the subscript "G" stands for Green's function. For straight tubes of square cross sections (with side-length d , Figure 2(b)), Green's function is

$$c(x, y, z | x', y', z' = 0) = \frac{4}{\pi d} \sum_{m=1}^{\infty} \sum_{n=1}^{\infty} \frac{\exp\left(-\left(\pi\sqrt{n^2 + m^2}z\right)/d\right)}{\sqrt{n^2 + m^2}} \cdot \sin\left(\frac{m\pi x}{d}\right) \sin\left(\frac{m\pi x'}{d}\right) \cdot \sin\left(\frac{n\pi y}{d}\right) \sin\left(\frac{n\pi y'}{d}\right), \quad (7)$$

and the MPD based on Green's function is

$$D_G = \frac{16d}{\pi^5} \sum_{m=1}^{\infty} \sum_{n=1}^{\infty} \frac{1}{n^2(n^2 + m^2)^{3/2}} [1 - (-1)^m][1 - (-1)^n]^2 \approx \frac{16d}{\pi^5} \cdot 3.2535 = 0.1701d. \quad (8)$$

For straight tubes of circular cross sections (with radius R , Figure 2(c)), Green's function is written as

$$c(r, z | r', z' = 0) = \frac{1}{\pi R} \sum_{m=1}^{\infty} \frac{1}{\beta_m J_1^2(\beta_m)} \cdot \exp\left(-\frac{\beta_m z}{R}\right) J_0\left(\frac{\beta_m r}{R}\right) J_0\left(\frac{\beta_m r'}{R}\right). \quad (9)$$

The MPD based on Green's function is

$$D_G = 4R \sum_{m=1}^{\infty} \frac{1}{\beta_m^3} \approx 0.3235R, \quad (10)$$

where J_0 and J_1 are Bessel functions (of zeroth and first orders) of the first kind; β_m is the m -th root of $J_0(\beta_m) = 0$.

No analytical Green's functions are found for the remaining examples in Figure 2; therefore, the numerical simulation of the Brownian motion will be used to directly estimate the MPD.

Taking into account the impact of porosity, let us consider a porous medium consisting of many straight tubes (Figure 2(f)), whose porosity n is not equal to 1. For simplicity, assume that all of the pores are the same. Recall that k represents the permeability of a single pore, D_B is the MPD with respect to a single pore, and $k = CD_B^2$. One may note that the permeability of such a medium is

$$k_b = nk = nCD_B^2, \quad (11)$$

where "b" stands for bunch. Let D_b be the effective MPD after being averaged on the whole area S ; it is obvious that $D_b = nD_B + (1-n) \cdot 0 = nD_B$. Let $k_b = C_b D_b^2$. Then, $nk = C_b n^2 D_b^2$, i.e., $C_b = (k/n)/D_b^2$. Recall (C is the factor for porosity $n = 1$), one has $C_b = C/n$. Thus,

$$k_b = \frac{CD_b^2}{n}, \quad (12)$$

which is valid for media comprising uniform straight tubes. We will check this formula in the next section to test its applicability. The impact of tortuosity on permeability is not discussed but can be considered by some empirical equations in the literature (e.g., [13]).

2.2. Random Walk on Grid (WOG). Green's functions are accessible to only limited, simple geometries and are not practical for general pores. Thus, one has to rely on the numerical simulation of the Brownian motion or random walk. To simulate a Brownian motion in the medium, here we employ a random walk on grid (WOG) due to its ease in determining hit occurrences and its flexibility of irregular inner boundaries. In homogeneous void space, WOG is equivalent to a simple lattice random walk. Here, implementation of WOG is only briefly introduced in Figure 3. In step (a), the domain can be discretized with a regular/irregular block-/point-centered grid. In this study, we use regular block-centered grids; i.e., each node represents a block or cell of the same size. In step (b), given that the distances from the current node to the neighboring nodes in six directions (i.e., x_{\pm} , y_{\pm} , and z_{\pm}) are Δx_{\pm} , Δy_{\pm} , and Δz_{\pm} in the Cartesian coordinate and that $p_{x_{\pm}}$, $p_{y_{\pm}}$, and $p_{z_{\pm}}$ denote the probability that the walker moves from the current node to six neighboring nodes, the probability of the neighboring node in x_+ direction can be estimated as

$$p_{x_+} = \frac{1/\Delta x_+}{(1/\Delta x_+) + (1/\Delta x_-) + (1/\Delta y_+) + (1/\Delta y_-) + (1/\Delta z_+) + (1/\Delta z_-)}, \quad (13)$$

which is similar for other directions. If the grid is nonuniform, the probabilities are location-dependent and

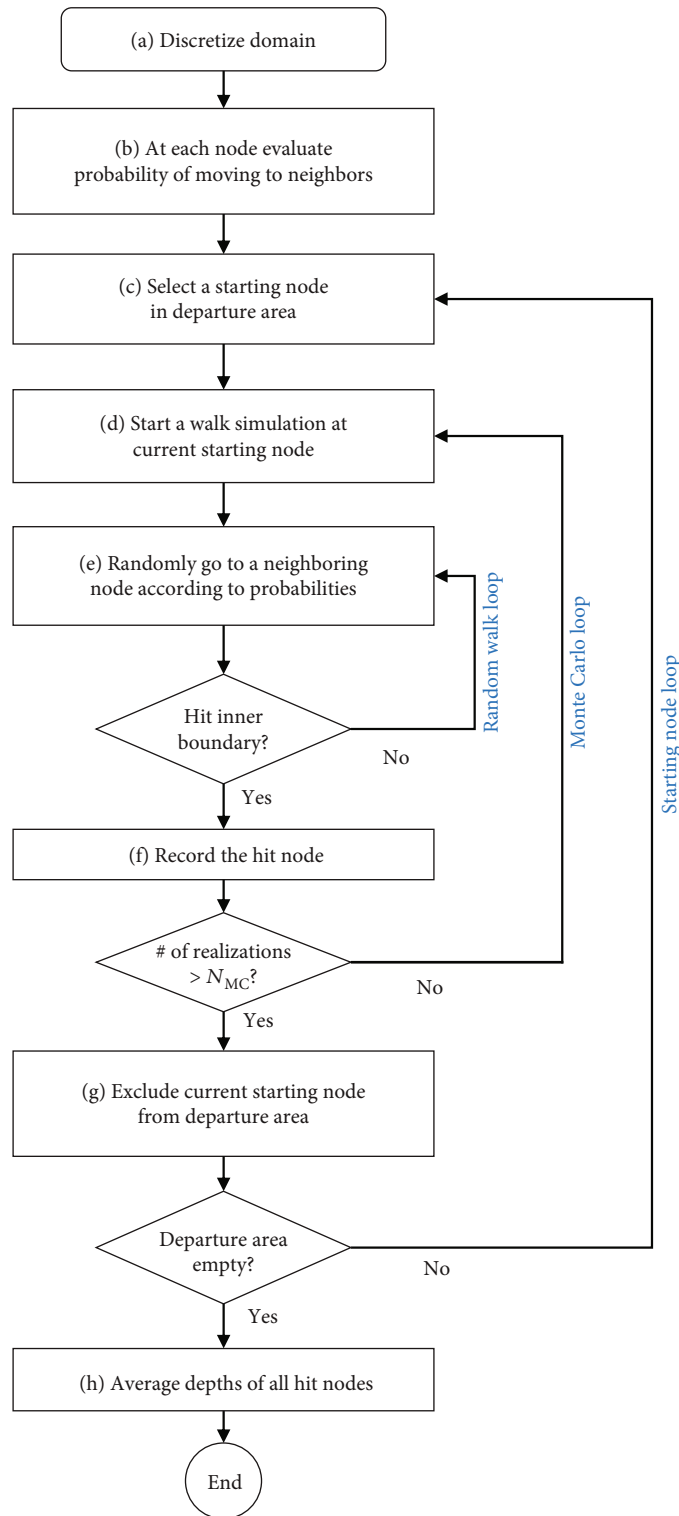


FIGURE 3: A flowchart of the MPD estimation via WOG.

direction-dependent. The probabilities to neighbors at all nodes are calculated and stored before random walks are simulated. In step (c), every node \mathbf{x}' in the departure area will be selected to serve as the starting node in the Monte Carlo loop for N_{MC} times (Figure 3). After completion of the Monte Carlo loop, the node will be excluded from the

departure area and will not be used again in the following simulation. If the original departure area contains N_S nodes after discretization, a random walk will be simulated for $N_S \times N_{MC}$ times, and the number of hit nodes is $N_S \times N_{MC}$ in total. Note that each realization of the random walk has an uncertain number of steps (in the random walk loop),

TABLE 1: Permeability, MPD, and C factor estimated by WOG and Green’s function for voids of simple geometries.

Void shape	Reference length	Theoretical k^*	MPD D_B^c	MPD D_G^{\ddagger}	C_B^c	C_G^{\ddagger}	φ^e
Parallel plane (Figure 2(a))	Plane distance d	$\frac{d^2}{12}$	$0.2763d$	$0.2714 d$	1.091	1.131	∞
Square (Figure 2(b))	Side-length d	$0.0351d^2$	$0.1751d$	$0.1701 d$	1.145	1.123	16
Circle (Figure 2(c))	Radius R	$\frac{R^2}{8}$	$0.3318R$	$0.3235 R$	1.135	1.194	4π
Ellipse (Figure 2(d))	Semiaxes: a, b	$a^2 \frac{b^2}{4} (a^2 + b^2)$	$0.4210 b$ (as $a = 2b$)	—	1.128	—	$4\pi \sim \infty$ (15 as $a = 2b$)
Equilateral triangle (Figure 2(e))	Side-length d	$\frac{d^2}{80}$	$0.1054 d$	—	1.125	—	$12\sqrt{3}$

*Theoretical k is obtained according to pressure drops and theoretical flow rates in Drazin and Norman [25]. cD_B is the MPD estimated by random walk on grid (WOG); $C_B = k/D_B^2$. $^{\ddagger}D_G$ is the MPD evaluated by Green’s function $c(\mathbf{x} | \mathbf{x}')$ by Equations (6), (8), and (10); $C_G = k/D_G^2$. $^e\varphi$ according to Berger [24].

and the location of its hit node is also uncertain before the realization is complete. When all of the nodes in the original departure area have served as starting nodes, the simulation procedure ends and the depths of all hit nodes will be averaged to estimate the MPD. More details of WOG algorithms and the superiority of WOG over “walk on cubes” and “walk on spheres” can be found in Nan and Wu [21].

We evaluated the permeability in the pores of some simple geometries, including parallel planes and void of square, circular, elliptic, and equilateral triangular cross sections (Figures 3(a)–3(e)). For the void space of these shapes, the theoretical expressions of permeability also exist (Table 1). In all of these pores, the porosities are all equal to 1. Factor C can be estimated using $C_B = k/D_B^2$ in each case after D_B is estimated by WOG.

2.3. COMSOL Simulation. COMSOL is a general-purpose platform software for modeling engineering problems. It is able to simulate multiple physical processes and models, including the flow of fluid. In this study, we use COMSOL to solve the steady-state Stokes flow in the pore space. The void-solid interface is treated as a no-slip boundary. The prescribed pressure boundaries are imposed onto two opposite faces of the parallelepiped and no-flux boundaries onto the other four lateral faces (due to the symmetry of the medium).

3. Results

3.1. MPD and C Factor Estimation. Table 1 reports the summary results in our investigation of simple pores, including the theoretical permeability k , the MPD and factor C estimated by WOG (D_B and C_B), and the MPD and C estimated by the three Green’s functions (D_G and C_G). First, it can be seen that D_B is slightly larger than D_G (if available) in all three cases. This suggests that D_B tends to slightly overestimate the real MPD (D_G), which may lead to a limited overestimation of the permeability (6%). Such a bias may result from spatial discretization, which is further explored in the sensitivity tests below. Second, the largest C value (1.194) is only 9% larger than the smallest C value (1.091). That is, the estimated values of C are more or less the same.

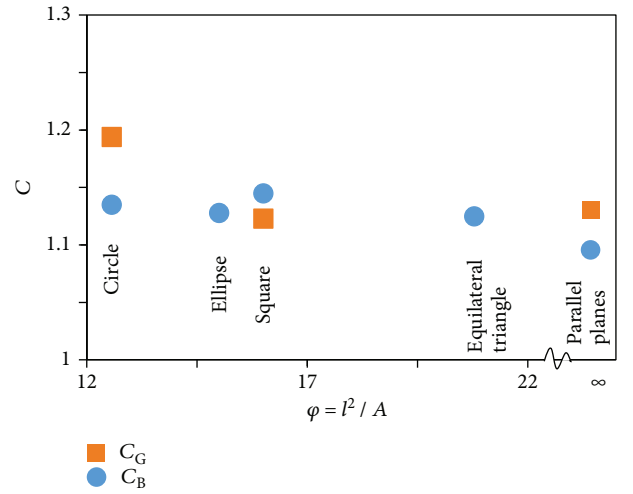


FIGURE 4: The isoperimetric ratio φ versus factor C ($a = 2b$ for ellipse case).

The average value for five cross-sectional shapes is approximately 1.125. Figure 4 shows the C value versus the isoperimetric ratio φ . The smaller φ is, the closer the shape is to being circular. It seems that there is no remarkable relationship between φ and C , which means that the dependence of C on the roundness of the cross section is quite weak.

In Hwang et al. [5], C was simply assumed to be 1, leading to the relationship $k = D^2$. However, our results from both numerical simulation and Green’s function, as shown above, indicate that the factor $C \approx 1.125$ on average rather than 1. Thus, the previous relation $k = D^2$ underestimates the permeability by 10% or so compared to that of $k = 1.125D^2$.

To investigate the sensitivity of the MPD estimates to the ensemble size, N_{MC} in Monte Carlo experiments, and grid discretization length Δ , we estimate the values of MPD for parallel planes using five different values of Δ (10^{-3} mm, 3×10^{-3} mm, 10^{-2} mm, 3×10^{-2} mm, and 10^{-1} mm) and nine different N_{MC} values (10^2 , 3×10^2 , 10^3 , 3×10^3 , 10^4 , 3×10^4 , 10^5 , 3×10^5 , and 10^6). $N_{MC} = 10^4$ when Δ is changed. Furthermore, $\Delta = 10^{-2}$ mm when N_{MC} is changed. The resulting

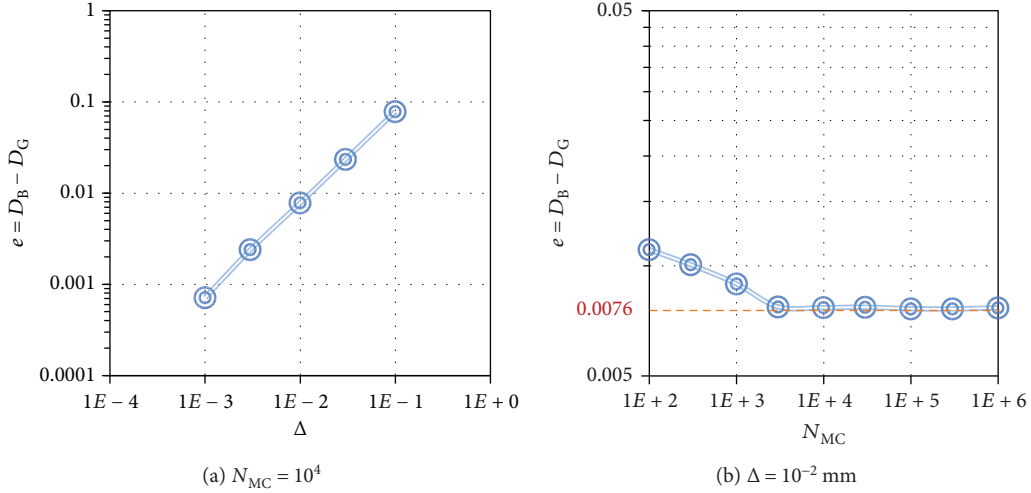


FIGURE 5: Sensitivity tests of the MPD estimates to discretization the length Δ and ensemble size N_{MC} .

errors ($e = D_B - D_G$) of MPD are reported in Figure 5. In Figure 5(a), it is found that the error e has the same order of magnitude as that of Δ (i.e., $e \propto O(\Delta)$) and continues decreasing as the grid becomes finer. Figure 5(b) illustrates the two-regime behavior of the error e with respect to N_{MC} . That is, when $N_{MC} < 10^4$, the error decreases with the increase in N_{MC} ; when $N_{MC} > 10^4$, the error stabilizes at approximately 0.0076 (close to the error of $\Delta = 10^{-2}$ mm, $N_{MC} = 10^4$), which means that when $\Delta = 10^{-2}$ mm, the increase of realizations will not improve the accuracy of estimates remarkably once $N_{MC} > 10^4$. The discretization error is dominant compared to the sampling error in Monte Carlo simulation. The MPD estimates seem to be sensitive to the discretization length.

3.2. Permeability Validation in a More Complex Medium. In this section, we predict the permeability of a given porous medium using a WOG-based MPD method. Meanwhile, COMSOL is used to solve the steady-state Stokes flow in the pore and estimate the permeability using the dynamics method to verify the MPD method.

Although there are geometric models available for isotropic random porous media (see, e.g., [26]), a synthetic ideal porous medium (Figure 6) is used here so that we can reconstruct the void space precisely in both the WOG and COMSOL simulations and minimize the model error. The void space is generated by removing tightly placed spheres of same size from a cuboid. To reduce the computational cost, we cut a representative volume (red-edge prism in Figure 6) from the medium, which contained a pore with enough length (Figure 7). The radius of each sphere is $d/2$. d is sufficiently small so that the requirement of Stokes flow can be easily satisfied in the following dynamic simulation. In the COMSOL simulation, we let $d = 1$ mm. The porosity of the medium was $n = (8 - 4\pi/3)/8 = 0.476$.

For simulating the Brownian motion with WOG, we established a grid of size $100 \times 100 \times 300$ in the space. The number of Monte Carlo realizations was $N_{MC} = 10^4$ for each starting point. Figure 8 shows the locations where the

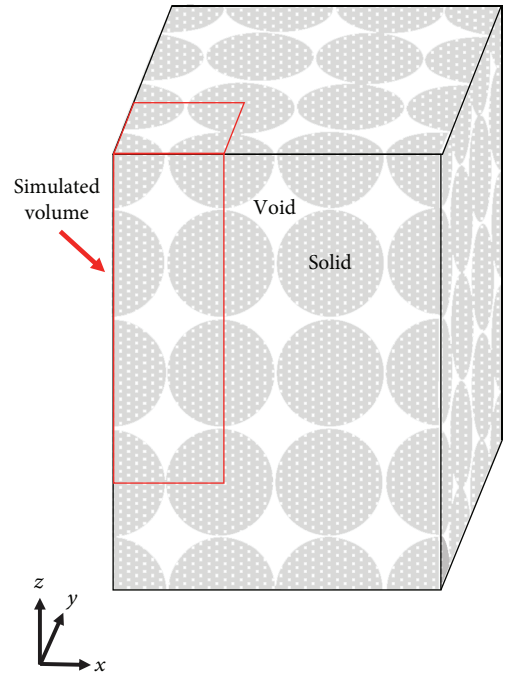


FIGURE 6: A synthetic porous medium consisting of solid spheres of equal radius (1 mm) and void.

Brownian motion stops (note that the Brownian motion starts at the bottom surface). The starting points within the solid immediately lead to stopping and, thus, are excluded. The estimated MPD is $D_B = 0.07591d$. Here, we use the average value of $C = 1.125$. The predicted permeability by MPD is $k_b = nCD_B^2 = 0.476 \times 1.125 \times 0.07591^2 d^2 \approx 3.09 \times 10^{-3} d^2$.

In a dynamic simulation via COMSOL software, we let $d = 1$ mm, the length in z direction $L_z = 3$ mm, the pressure difference $\Delta P = 0.1$ Pa between the top and bottom faces, the dynamic viscosity of water $\mu = 1.002 \times 10^{-3}$ Pa \cdot s at 20°C , and the sample cross-sectional area $S = d^2$. The void-solid interface is set to be a no-slip boundary (gray faces in

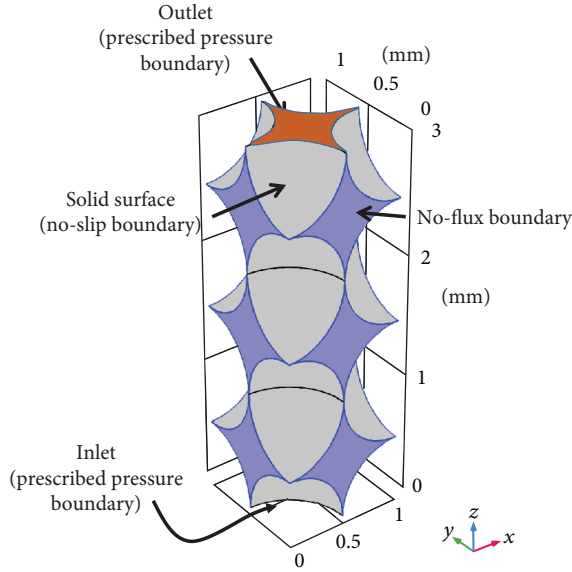


FIGURE 7: A void space formed among equal-sized solid spheres. The top face (red) is the outlet, and the bottom face (hidden) is the inlet; all the lateral planes (blue) are no-flow boundaries; the spherical faces (gray) are interfaces between the void and solid and are treated as a no-slip boundary in dynamic simulation.

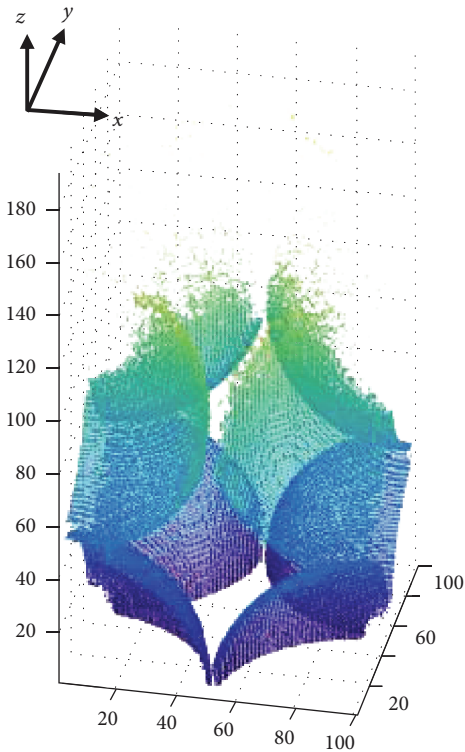


FIGURE 8: Locations where the simulated Brownian motions stop, i.e., points on the surfaces of the void-solid interface on the $100 \times 100 \times 300$ grid. The colors from blue to green-yellow indicate the increasing z values.

Figure 7). The blue lateral faces are cut sections of the void, which are treated as a no-flux boundary due to the void symmetry within the entire medium.

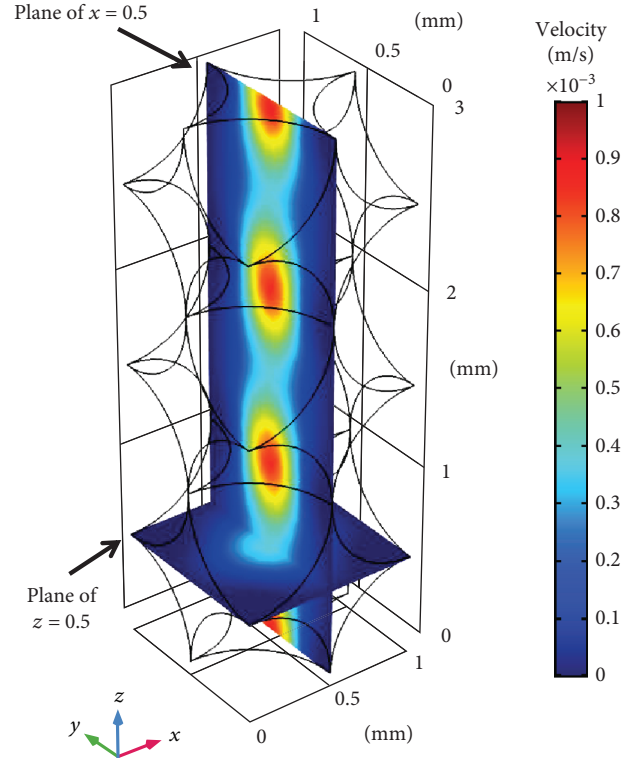


FIGURE 9: The magnitude of velocity on planes of $x = 0.5$ mm and $z = 0.5$ mm solved by COMSOL.

The velocity field is briefly shown in Figure 9, with two slices at planes of $x = 0.5$ and $z = 0.5$. The maximum velocity is approximately 8.4×10^{-5} m/s, and the Reynolds number is 0.093, which is much smaller than 1 (satisfying the requirement of Stokes flow). For the simulated steady-state flow, we found that the flowrate at the outlet was $Q = 8.3552 \times 10^{-11}$ m³/s. Since $Q = k_b (\Delta P / \mu L_z) S$, then $k_b = (Q/S) (\mu L_z) / \Delta P = 2.52 \times 10^{-9}$ m² = $2.52 \times 10^{-3} d^2$. Recall that the permeability estimated by MPD, as calculated above, is $k_b = 3.09 \times 10^{-3} d^2$, which is approximately 23% larger than that estimated by the COMSOL simulation and means that the MPD method here also overestimates the permeability by 1/4.

To explore the impact of Reynolds number to permeability estimated by COMSOL, we calculated permeability estimates using different pressure drops ($\Delta P = 10^{-4}, 10^{-3}, 10^{-2}, 10^{-1}, 1, 10, \text{ and } 100$ Pa). The results are shown in Figure 10. It was found that when $\Delta P < 1$ Pa (Reynolds number < 0.94), the permeability estimate stabilized and was insensitive to the Reynolds number.

4. Discussion and Conclusions

The effectiveness of the WOG-based MPD method was tested in this study via two approaches, i.e., comparing the MPD to Green's function results and comparing the permeability to the results of dynamic simulation. First, the results of the MPD estimated by WOG are quite close to those based on Green's functions in three cases (Figures 2(a)–2(c)) and its

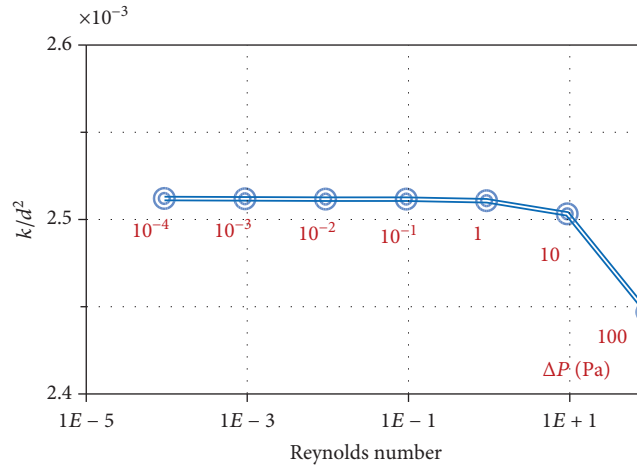


FIGURE 10: The permeability (normalized by d^2) for the different Reynolds numbers. The corresponding values of pressure drop ΔP are also shown in red (in Pa).

relative errors were less than 5%. We found that WOG estimates the MPD with good accuracy when compared to the theoretical MPD in the simple pores (although WOG still overestimates the MPD slightly, <6%). Second, the permeability of the synthetic porous medium as estimated by the WOG-based MPD method was compared with that estimated by the COMSOL simulation. To the best of our knowledge, this is the first time that an MPD estimate of the permeability was compared with the permeability estimated by a dynamic model in a “complex” porous medium. Our results suggested that the MPD-based estimate of permeability was approximately 1/4 larger than the dynamics-based estimate, which contrasts the accuracy in the pores of the simple geometries above. The deviation may result from a dramatic change in the void cross-sectional area and in the singularities generated by the tangent spheres.

While factor C was taken as 1 in the literature, we found that in pores of several geometries, the factor $C \approx 1.125$ on average using both the WOG simulation and Green’s function. Factor C depends on the cross-sectional shape very weakly. The largest C value (1.194) is only 9% larger than the smallest C value (1.091). After analyzing the plot of the C value against a shape parameter φ (isoperimetric ratio), it was found that there is no remarkable relationship between φ and C , which means that the dependence of C on the cross-sectional shape is quite weak.

In sensitivity tests of MPD to discretization of the length Δ and ensemble size N_{MC} , it was found that the error of MPD estimates has the same order of magnitude as that of Δ . If $\Delta > 10^{-3}$ mm, the sampling error is negligible as long as $N_{MC} > 10^4$.

When the pressure drop is sufficiently small ($\Delta P < 1$ Pa, Reynolds number < 0.94), the flow in the dynamic simulation is Stokes flow, and the permeability estimate stabilizes and is insensitive to the Reynolds number.

In summary, the effectiveness of the permeability estimation using the WOG-based MPD was validated using Green’s functions in simple pores and dynamic simulation in a complex pore. It was found that the WOG-based MPD method is

quite accurate in simple pores and overestimates the permeability in the complex pore. It was shown that the dependence of the factor C on cross-sectional geometry is very limited, and the average C value can be used. The discretization error and the Monte Carlo sampling error both result in errors in MPD estimation.

Data Availability

The datasets generated during and/or analysed during the current study are available from the corresponding author on reasonable request.

Conflicts of Interest

The authors declare that they have no conflicts of interest.

Acknowledgments

This work is funded by the National Key Research and Development Program of China (Grant No. 2016YFC040281000), the National Natural Science Foundation of China (Grant No. 41602250), and the Fundamental Research Funds for the Central Universities (Grant No. 0206-14380032).

References

- [1] T. Nan, K. Li, J. Wu, and L. Yin, “Assessment of groundwater exploitation in an aquifer using the random walk on grid method: a case study at Ordos, China,” *Hydrogeology Journal*, vol. 26, no. 5, pp. 1669–1681, 2018.
- [2] T.-C. J. Yeh, R. Khaleel, and K. Carrol, *Flow through Heterogeneous Geologic Media*, Cambridge University Press, Cambridge, UK, 2015.
- [3] L. Andersson, A. C. Jones, M. A. Knackstedt, and L. Bergstrom, “Permeability, pore connectivity and critical pore throat control of expandable polymeric sphere templated macroporous alumina,” *Acta Materialia*, vol. 59, no. 3, pp. 1239–1248, 2011.

- [4] D. A. Coker and S. Torquato, "Simulation of diffusion and trapping in digitized heterogeneous media," *Journal of Applied Physics*, vol. 77, no. 3, pp. 955–964, 1995.
- [5] C.-O. Hwang, J. A. Given, and M. Mascagni, "On the rapid estimation of permeability for porous media using Brownian motion paths," *Physics of Fluids*, vol. 12, no. 7, pp. 1699–1709, 2000.
- [6] J. Kozeny, "Über Kapillare Leitung der Wasser in Boden," *Royal Academy of Science, Vienna, Proc. Class I*, vol. 136, pp. 271–306, 1927.
- [7] N. A. Simonov and M. Mascagni, "Random walk algorithms for estimating effective properties of digitized porous media," *Monte Carlo Methods and Applications*, vol. 10, no. 3–4, pp. 599–608, 2004.
- [8] S. Torquato, "Relationship between permeability and diffusion-controlled trapping constant of porous media," *Physical Review Letters*, vol. 64, no. 22, pp. 2644–2646, 1990.
- [9] B. Abbasi, H. X. Ta, B. Muhunthan, S. Ramezani, N. Abu-Lail, and T. H. Kwon, "Modeling of permeability reduction in bioclogged porous sediments," *Journal of Geotechnical and Geoenvironmental Engineering*, vol. 144, no. 4, 2018.
- [10] F. Benavides, R. Leiderman, A. Souza, G. Carneiro, and R. Bagueira, "Estimating the surface relaxivity as a function of pore size from NMR T2 distributions and microtomographic images," *Computers & Geosciences*, vol. 106, pp. 200–208, 2017.
- [11] J. R. Izzo, A. S. Joshi, K. N. Grew et al., "Nondestructive reconstruction and analysis of SOFC anodes using X-ray computed tomography at Sub-50 nm resolution," *Journal of the Electrochemical Society*, vol. 155, no. 5, pp. B504–B508, 2008.
- [12] J. Ohser, C. Ferrero, O. Wirjadi, A. Kuznetsova, J. Dull, and A. Rack, "Estimation of the probability of finite percolation in porous microstructures from tomographic images," *International Journal of Materials Research*, vol. 103, no. 2, pp. 184–191, 2012.
- [13] J. Bear, *Dynamics of Fluids in Porous Media*, Dover, 1972.
- [14] G. K. Batchelor, *An Introduction to Fluid Dynamics*, Cambridge University Press, 2000.
- [15] J. Boussinesq, "Mémoire sur l'influence des Frottements dans les Mouvements Réguliers des Fluids," *Journal de Mathématiques Pures et Appliquées*, vol. 13, no. 2, pp. 377–424, 1868.
- [16] J. Proudman, "IV. Notes on the motion of viscous liquids in channels," *The London, Edinburgh, and Dublin Philosophical Magazine and Journal of Science*, vol. 28, no. 163, pp. 30–36, 1914.
- [17] P. C. Carman, "Fluid flow through granular beds," *Transactions of the Institution of Chemical Engineers*, vol. 15, pp. 150–166, 1937.
- [18] P. C. Carman, *Flow of Gases through Porous Media*, Butterworths, London, 1956.
- [19] F. W. Wiegand, *Fluid Flow through Porous Macromolecular Systems*, Springer-Verlag, Berlin Heidelberg, 1980.
- [20] K. K. Sabelfeld, "A stochastic spectral projection method for solving PDEs in domains composed by overlapping discs, spheres, and half-spaces," *Applied Mathematics and Computation*, vol. 219, no. 10, pp. 5123–5139, 2013.
- [21] T. Nan and J. Wu, "Random walk path solution to groundwater flow dynamics in highly heterogeneous aquifers," *Journal of Hydrology*, vol. 563, pp. 543–559, 2018.
- [22] K. D. Cole, J. V. Beck, A. Haji-Sheikh, and B. Litkouhi, *Heat Conduction Using Green's Functions*, CRC Press, 2nd edition, 2011.
- [23] M. Deaconu and A. Lejay, "A random walk on rectangles algorithm," *Methodology and Computing in Applied Probability*, vol. 8, pp. 135–151, 2006.
- [24] M. Berger, *Geometry Revealed: a Jacob's Ladder to Modern Higher Geometry*, Springer-Verlag, Berlin Heidelberg, 2010.
- [25] P. G. Drazin and R. Norman, *The Navier-Stokes Equations: a Classification of Flows and Exact Solutions*, Cambridge University Press, 2006.
- [26] H. Hermann and A. Elsner, "Geometric models for isotropic random porous media: a review," *Advances in Materials Science and Engineering*, vol. 2014, Article ID 562874, 16 pages, 2014.

Research Article

Study on Reasonable Energy Supplement Time of Tight Sandstone Oil Reservoirs with Rock Compressibility Stress Sensitivity

Tian Xiaofeng , Tan Xianhong, Tian Ji, Li Nan, Yuan Zhongchao, and Liang Bin

CNOOC Research Institute Ltd., Beijing 100028, China

Correspondence should be addressed to Tian Xiaofeng; txf5160@163.com

Received 20 May 2018; Revised 5 August 2018; Accepted 2 September 2018; Published 20 December 2018

Guest Editor: Emanuele Romano

Copyright © 2018 Tian Xiaofeng et al. This is an open access article distributed under the Creative Commons Attribution License, which permits unrestricted use, distribution, and reproduction in any medium, provided the original work is properly cited.

A-HBR field is a tight sandstone oil reservoir with a threshold pressure gradient and a rock compressibility stress sensitivity. However, no existing approach could predict reasonable energy supplement time considering both of them. Therefore, in this paper, rock compressibility stress sensitivity experiments are conducted. Then, a new approach is presented. This approach considers the correlation of rock compressibility and formation pressure. And the formation pressure is different from the development time and distance to oil well. The study suggests that the energy supplement time is later when the original rock compressibility is larger. The energy supplement time is earlier when the rock compressibility is more severe. A-HBR field's reasonable energy supplement time is 83 days when considering the effect of rock compressibility stress sensitivity. It is much earlier than that when not considering the effect of rock compressibility stress sensitivity.

1. Introduction

A-HBR field is an overpressured tight sandstone oil reservoir. The depth of the reservoir is 3760 m. The average porosity is 12%. The average permeability is 32 mD. The oil viscosity is 0.4 mPa·s. The original formation pressure is 50 MPa. Tight oil reservoirs have obvious threshold pressure gradient characters [1–3] and rock compressibility stress sensitivity characters [4–7]. The formation water is going to salt out and solution gas is going to get out from the oil if formation pressure decreases fast. As a result, oil production decreases [8–11]. Therefore, it is key to use natural energy as much as possible and replenish formation energy timely for A-HBR field.

Zhang [12] presented an approach to calculate energy supplement time considering the effect of threshold pressure gradient on drainage radius. However, this approach does not take the pressure distribution into account. Based on the Zhang's approach, Chen et al. presented an approach considering the effect of threshold pressure gradient on pressure distribution [13]. Numerical simulation also could

consider both of threshold pressure gradient and rock compressibility stress sensitivity [14–16]. However, numerical simulation takes longer time and is harder to conduct.

However, no existing approach could predict reasonable energy supplement time considering both threshold pressure gradient and rock compressibility stress sensitivity [12, 13, 17–19]. Therefore, this paper comes up with a new approach considering the effect of threshold pressure gradient and rock compressibility stress sensitivity.

2. Rock Compressibility Stress Sensitivity Experiment of A-HBR Field

The rock compressibility stress sensitivity experiments were conducted. The cores comes from A-HBR field, and the basic parameters are shown in Table 1. Experimental process is shown in Figure 1. The experimental method refers to the standard SY/T 5815-2008. The effective stress is designed to be 2.76, 5.52, 8.27, 10.34, 13.79, 20.68, 27.58, 34.47, and 55.16 MPa, respectively. The experimental results are shown in Figure 2. It is found that the rock compressibility stress

TABLE 1: Basic parameters of cores in rock compressibility stress sensitivity experiments.

Number	Depth (m)	ϕ (%)	K (mD)	C_{ro} ($\times 10^{-3}$ MPa $^{-1}$)
A	3773.72	12.6	37.6	7.8
B	3743.7	12.4	8.0	11
C	3727.36	11.5	35.2	7.6
D	3786.49	11.0	42.1	11
E	3775.76	10.6	40.3	7.4

sensitivity of A-HBR field is severe from Figure 2. The rock compressibility decreases by 90 percent when the effective stress increases from 2.76 MPa to 55.16 MPa. The correlation of rock compressibility and effective stress is obtained from the experimental results (1).

It is found that rock compressibility and effective stress show a good exponential relationship. Rock compressibility is the pore volume reduction per effective stress. When effective stress is small, pore volume is large and pore is easy to press. When effective stress increases, pore volume decreases and rock becomes tight. Thus, pore volume is harder to press and per effective stress results in less pore volume reduction. As a result, rock compressibility is less when effective stress increases [5, 20].

$$C_r = C_{ro} \cdot 4.3434\sigma_{\text{eff}}^{-1.097}, \quad (1)$$

where C_r is rock compressibility when the effective stress is σ_{eff} , MPa $^{-1}$; C_{ro} is original rock compressibility, MPa $^{-1}$; σ_{eff} is effective stress, $\sigma_{\text{eff}} = p_{\text{over}} - p$, MPa; p_{over} is overburden formation pressure, MPa; and p is formation pressure, MPa.

3. Reservoir Engineering Approach to Predict Reasonable Energy Supplement Time

The rock compressibility of A-HBR field is stress sensitive. As a result, the location with different distances to oil well has different rock compressibilities (Figure 3). The elastic cumulative oil production, where the distance is r from the oil well, is shown in (2) according to the matter balance principle.

$$dV_o = C_f(\sigma_{\text{eff}})(p_e - p(r))dV_f, \quad (2)$$

where V_o is the elastic cumulative oil production, m 3 ; C_f is the composite compressibility, $C_f = \phi(C_o + C_r(\sigma_{\text{eff}}))$, MPa $^{-1}$; ϕ is the porosity; C_o is the oil compressibility, MPa $^{-1}$; C_r is the rock compressibility, MPa $^{-1}$; V_f is the drainage volume of the oil well, $dV_f = 2\pi rh \cdot dr$, m 3 ; r is the distance to the oil well, m; h is the net pay, m; p_e is original formation pressure, MPa; and $p(r)$ is the formation pressure where the distance to the oil well is r , MPa.

The threshold pressure gradient greatly affects the pressure distribution in tight sandstone oil reservoirs. The elastic cumulative oil production is the max in tight sandstone oil reservoirs when formation pressure gradient equals the

threshold pressure gradient. The formation pressure distribution is shown in

$$p(r) = p_{wf} + \frac{(p_e - p_{wf}) - G(r_e - r_w)}{\ln(r_e/r_w)} \ln\left(\frac{r}{r_w}\right) + G(r_e - r_w), \quad (3)$$

where p_{wf} is the bottom hole pressure, MPa; G is threshold pressure gradient, MPa/m; r_e is the drainage radius, m; and r_w is the well diameter, m.

At the same location, the formation pressure decreases in development. As a result, the rock compressibility decreases (Figure 3) because of the stress sensitivity. Integrating (2) with respect to formation pressure and distance yields the elastic cumulative oil production in drainage volume (4).

$$V_o = \int_{p_b}^{p_e} \int_{r_w}^{r_e} 2\pi rh \cdot C_f(r)(p_e - p(r))drdp, \quad (4)$$

where r_w is the well diameter, m, and r_e the is drainage radius, m.

The controlled reserves per well is shown in (5) if the well space is r_e .

$$N_o = \left(\frac{\pi r_e^2 \cdot h \cdot \phi \cdot S_{oi}}{B_{oi}} \right), \quad (5)$$

where N_o is the controlled reserves per well, m 3 ; ϕ is the porosity; S_{oi} is the original oil saturation; and B_{oi} is the formation volume factor.

The oil production per well is shown in (6) if the oil recovery rate equals a .

$$q = \frac{aN_o}{t}, \quad (6)$$

where q is the oil production rate, m 3 /d; a is the oil recovery rate; and t is the production days per year, days.

Substituting (1) and (3) into (4) yields the elastic cumulative oil production. Substituting (5) into (6) yields the oil production rate. The reasonable energy supplement time is obtained when the elastic cumulative oil production divides the oil production rate:

$$t_b = \frac{V_o}{q}, \quad (7)$$

where t_b is the energy supplement time, days.

4. Verification

Numerical simulation could consider both threshold pressure gradient and rock compressibility stress sensitivity. Therefore, numerical simulation helps to verify the new approach, and commercial software Eclipse E100 is used. The numerical model is shown in Figure 4. The numerical model basic parameters are shown in Table 2. The threshold pressure gradient is shown in (8) [1]. Comparing to the

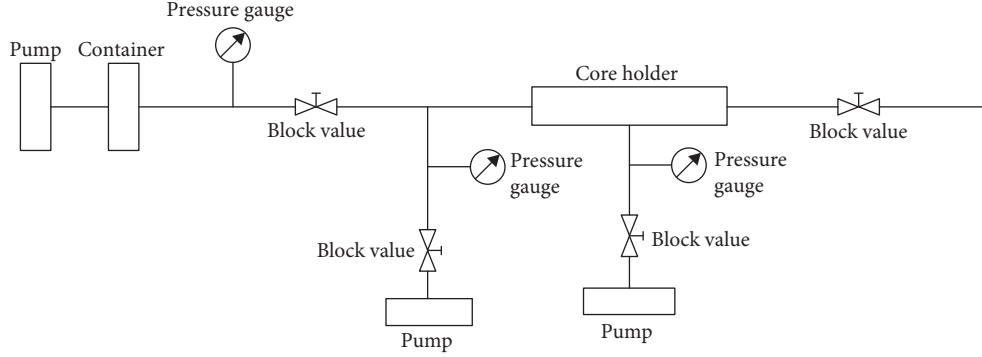


FIGURE 1: Rock compressibility stress sensitivity experimental process.

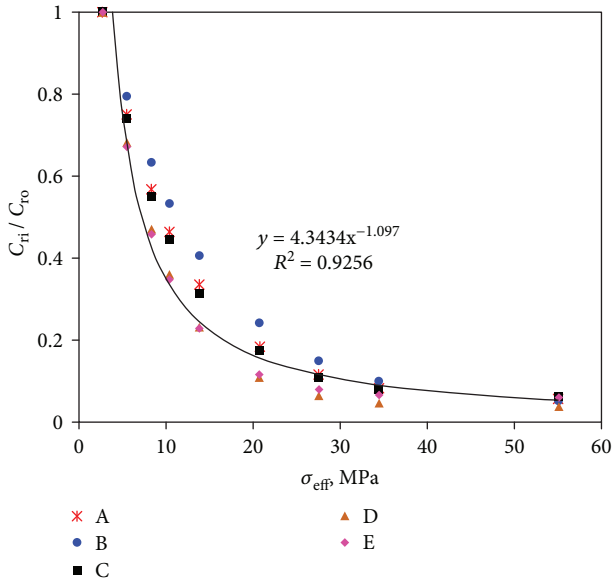


FIGURE 2: Rock compressibility stress sensitivity experimental results.

formation pressure distribution of numerical model and the new approach, the new approach results have a great agreement with numerical model results (Figure 5). And the error of elastic oil recovery is less than 1% (Table 3).

$$G = 0.075K^{-1.12}, \quad (8)$$

where G is the threshold pressure gradient, MPa/m, and K is the permeability, mD.

5. Sensitivity Analysis

5.1. Original Rock Compressibility. Original rock compressibility ranges from 0.0074 MPa^{-1} to approximately 0.011 MPa^{-1} (Table 1). Therefore, the effect of original rock compressibility on energy supplement time is studied. The basic parameters in the new approach is shown in Table 2. It is found that the original rock compressibility and energy supplement time have a good linear relationship (Figure 6). The average rock compressibility is larger in elastic development when the original rock compressibility is larger. As a

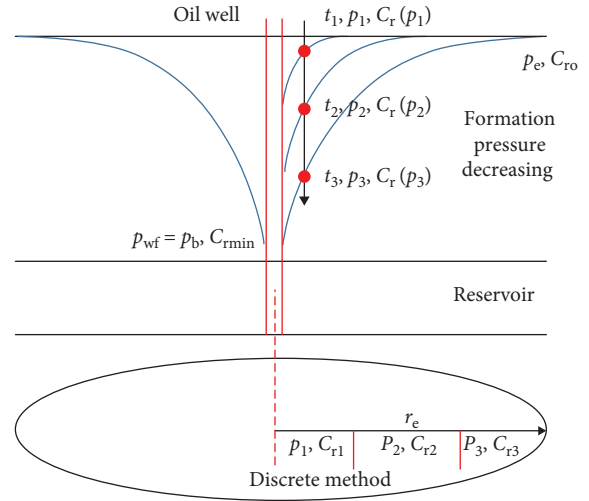


FIGURE 3: Rock compressibility distribution.

result, formation pressure decreases slower and energy supplement time is later.

5.2. Rock Compressibility Reduction. The rock compressibility reduction is different, although the effective stress is the same (Figure 2). Therefore, the effect of rock compressibility reduction on energy supplement time is studied. The basic parameters in the new approach is shown in Table 2. It is found that rock compressibility reduction and energy supplement time have a good logarithmic relationship (Figure 7). The average rock compressibility is larger in elastic development when the rock compressibility reduction is less. As a result, formation pressure decreases slower and energy supplement time is later.

6. Application

Existing approach and this new approach are used to predict energy supplement time of A-HBR field. Basic data of the field is shown in Table 4. From Table 4, it is found that formation pressure decreases faster considering rock compressibility stress sensitivity (Figure 8). In order to avoid gas degassing from oil and oil rate decreasing, energy supplement time should be 86% earlier than not taking the effect of rock compressibility stress sensitivity into account.

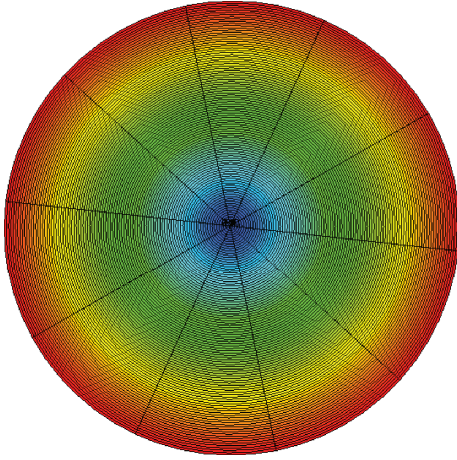


FIGURE 4: Numerical model.

TABLE 2: Basic parameters of numerical model.

Parameters	Value
Grid number	$100 \times 10 \times 10$
Grid size	$1 \text{ m} \times 36^\circ \times 1 \text{ m}$
Porosity, %	10.6
Permeability, mD	20
Net pay, m	10
Original pressure, MPa	55
Drainage radius, m	1000
Fluid viscosity, mPa·s	0.4
Formation volume factor	1.6
Original rock compressibility, $\times 10^{-3} \text{ MPa}^{-1}$	8.9
Fluid compressibility, $\times 10^{-4} \text{ MPa}^{-1}$	4.5
Oil recovery rate, %	1

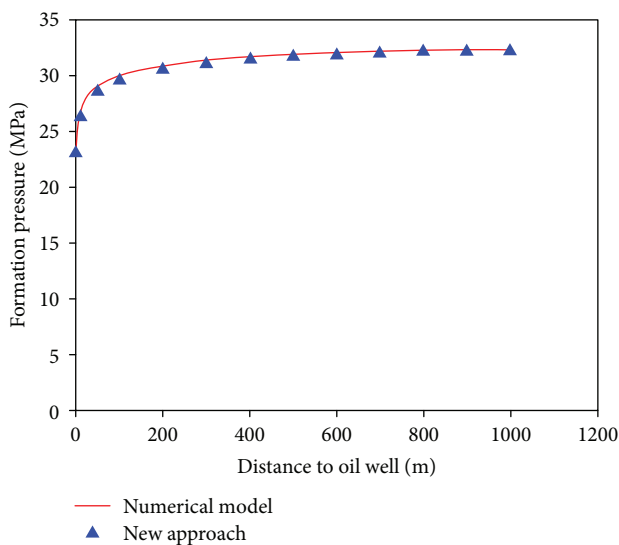


FIGURE 5: Verification of formation pressure distribution.

TABLE 3: Error of the new approach.

Method	Elastic cumulative oil production (m^3)	Elastic oil recovery (%)	Energy supplement time (d)	Average formation pressure (MPa)
Numerical model	5111	0.25	81	53.0
New approach	5136	0.25	81	53.3
Error (%)	0.48	0.43	0.39	0.59

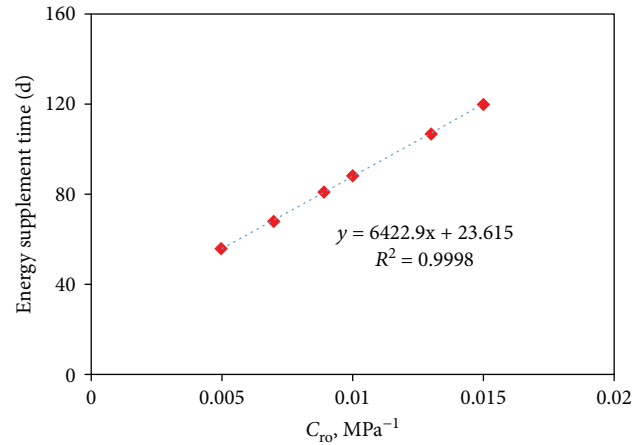


FIGURE 6: Energy supplement time vs original rock compressibility.

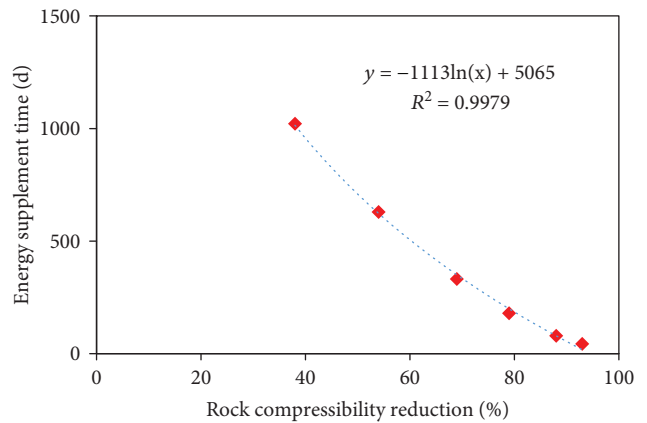


FIGURE 7: Energy supplement time vs rock compressibility reduction.

7. Conclusions

- (1) From experimental results, it is found that A-HBR field has obvious rock compressibility stress sensitivity. The rock compressibility and effective stress have a good power relationship
- (2) A new approach is presented to predict energy supplement time of tight sandstone oil reservoirs. This new approach takes threshold pressure gradient and rock compressibility stress sensitivity into account

TABLE 4: Basic data of A-HBR field.

Field	h (m)	φ (%)	K (mD)	μ_o (mPa·s)	B_o	p_b (MPa)	C_{ro} ($\times 10^{-3}$ MPa $^{-1}$)	Energy supplement time (d)	
								Existing approach (2)	The new approach
A-HBR	13	12	33	0.4	1.6	20	8.9	589	83

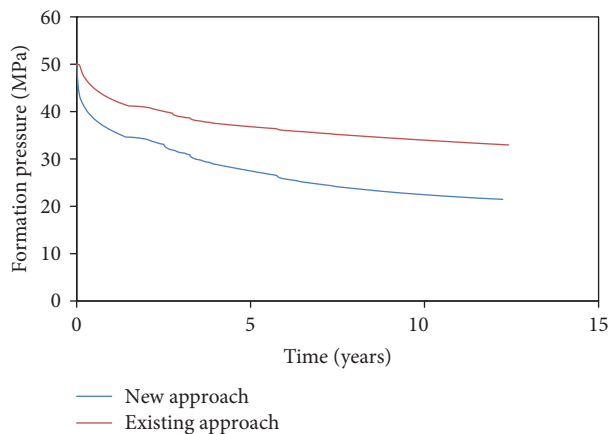


FIGURE 8: Formation pressure comparison of the existing approach and the new approach.

- (3) The formation pressure decreases more slowly, and elastic recovery is larger if the original rock compressibility is larger. As a result, the energy supplement time is later. The formation pressure decreases faster and elastic recovery is smaller if the rock compressibility reduction is larger. As a result, the energy supplement time is earlier
- (4) The energy supplement time of A-HBR is 83 days considering the effect of rock compressibility stress sensitivity. It is 86% earlier than the energy supplement time of not taking the effect of rock compressibility stress sensitivity into account

Data Availability

The data used to support the findings of this study are available from the corresponding author upon request.

Conflicts of Interest

The authors declare that they have no conflicts of interest.

References

- [1] B. Q. Zeng, L. S. Cheng, and F. Hao, "Experiment and mechanism analysis on threshold pressure gradient with different fluids," in *Nigeria Annual International Conference and Exhibition*, Tinapa-Calabar, Nigeria, August 2010.
- [2] R. Gao, X. Wang, M. Che, C. Bo, and H. Chunming, "The fractures optimization method with the threshold pressure of multistage fracturing in tight oil reservoir," in *SPE Reservoir Characterisation and Simulation Conference and Exhibition*, Abu Dhabi, UAE, May 2017.
- [3] Y. L. Zhao, L. H. Zhang, Z. X. He, and B. N. Zhang, "Productivity for horizontal wells in low-permeability reservoir with oil/water two-phase flow," *Mathematical Problems in Engineering*, vol. 2014, Article ID 364678, 9 pages, 2014.
- [4] R. Smith, K. Bard, and R. Colmenares, "Non-linear rock compressibility in the Naricual and Los Jabillos formations, El Furrial Field, Venezuela," in *SPE Latin American and Caribbean Petroleum Engineering Conference*, Buenos Aires, Argentina, March 2001.
- [5] G. P. da Silva Jr., D. R. Franco, G. C. Stael et al., "Petrophysical studies of North American carbonate rock samples and evaluation of pore-volume compressibility models," *Journal of Applied Geophysics*, vol. 123, pp. 256–266, 2015.
- [6] D. Davudov and R. G. Moghanloo, "Impact of pore compressibility and connectivity loss on shale permeability," *International Journal of Coal Geology*, vol. 187, pp. 98–113, 2018.
- [7] H. X. Wang, Y. Song, H. F. Fang, Y. J. Li, and Y. X. Xie, "Transforming laws of rock compressibility," *Journal of Oil and Gas Technology*, vol. 29, no. 1, pp. 42–44, 2007.
- [8] Z. Y. Wu, K. Li, and T. C. Li, "Water injection development and stable production technology in Ansai extra low permeability oilfield," in *International Oil and Gas Conference and Exhibition in China*, Beijing, China, November 2000.
- [9] D. Denney, "Characterization of water injection in low-permeability rock using sandstone micromodels," *Journal of Petroleum Technology*, vol. 56, no. 5, pp. 71–72, 2004.
- [10] L. M. Surguchev, N. H. Giske, and L. Kollbotn, "Cyclic water injection improves oil production in carbonate reservoir," in *Abu Dhabi International Petroleum Exhibition and Conference*, Abu Dhabi, UAE, November 2008.
- [11] B. Haynes, A. Abdemawla, and S. G. L. Stromberg, "Impact of pore volume compressibility on recovery from depletion drive and miscible gas injection in South Oman," in *SPE Annual Technical Conference and Exhibition*, Denver, CO, USA, September 2008.
- [12] X. L. Zhang, "Calculation of natural depletion oil recovery for low permeability reservoirs," *Journal of Liaoning Technical University (Natural Science)*, vol. 33, no. 5, pp. 633–636, 2014.
- [13] M. F. Chen, M. Zhao, M. Wang, G. Jian, and S. Jianhu, "Study on reasonable energy supplement timing for low permeability and high saturation reservoirs," *Fault-Block Oil & Gas Field*, vol. 21, no. 4, pp. 463–466, 2014.
- [14] J. Akande and J. P. Spivey, "Considerations for pore volume stress effects in over-pressured shale gas under controlled drawdown well management strategy," in *SPE Canadian Unconventional Resources Conference*, Calgary, Alberta, Canada, October 2012.
- [15] H. Pu, G. F. Wang, and Y. X. Li, "Reservoir simulation study on improvement of waterflooding effect for a naturally fractured low permeability field in Daqing, China: a successful case," in *SPE Middle East Oil and Gas Show and Conference*, Manama, Bahrain, March 2009.
- [16] A. Graue, R. Moe, and B. A. Baldwin, "Comparison of numerical simulations and laboratory waterfloods with in-situ saturation imaging of fractured blocks of reservoir

- rocks at different wettabilities,” in *SPE International Petroleum Conference and Exhibition in Mexico*, Villahermosa, Mexico, February 2000.
- [17] X. Q. Xie, H. Q. Jiang, Q. Z. Wang, T. Liu, and W. Zhang, “Discussion on pressure-sensitivity effect and water-flooding timing in low-permeability reservoir,” *Acta Petrolei Sinica*, vol. 30, no. 4, pp. 574–577, 2009.
- [18] X. L. Zhang and J. Q. Zhang, “Calculation method of natural depletion oil recovery for micro-fractured low permeability reservoirs,” *Xinjiang Petroleum Geology*, vol. 32, no. 4, pp. 409–411, 2011.
- [19] X. L. Zhang, X. P. Li, Y. Zhao, and D. Luo, “Calculation of elastic recovery for abnormal high pressure and low permeability reservoir,” *Reservoir Evaluation and Development*, vol. 3, no. 2, pp. 34–37, 2011.
- [20] G. L. P. D. Oliveira, M. A. R. Ceia, R. M. Missagia et al., “Pore volume compressibilities of sandstones and carbonates from helium porosimetry measurements,” *Journal of Petroleum Science and Engineering*, vol. 137, pp. 185–201, 2016.

Research Article

A Fluid-Solid Coupling Mathematical Model of Methane Driven by Water in Porous Coal

Bingxiang Huang and Weiyong Lu 

State Key Laboratory of Coal Resources and Safe Mining, China University of Mining and Technology, Xuzhou, Jiangsu 221116, China

Correspondence should be addressed to Weiyong Lu; 489698551@qq.com

Received 30 April 2018; Revised 14 July 2018; Accepted 25 July 2018; Published 16 September 2018

Academic Editor: Joaquín Jiménez-Martínez

Copyright © 2018 Bingxiang Huang and Weiyong Lu. This is an open access article distributed under the Creative Commons Attribution License, which permits unrestricted use, distribution, and reproduction in any medium, provided the original work is properly cited.

The existence of the water-driven-methane effect in gassy coal has been verified by field tests and laboratory experiments. However, a water-driven-methane mathematical model that considers methane adsorption and desorption has not yet been established. Based on the water-driven-methane process, a fluid-solid coupling mathematical model of methane driven by water is established. The model's reliability is verified by the results of a water-driven-methane physical experiment and by using a solution of the COMSOL Multiphysics software. The space-time distribution regularities of the pore pressure, water-methane two-phase saturation, and pore pressure gradient in the water-driven-methane process are analysed. The results reveal the following. (1) The water-driven-methane fluid-solid coupling mathematical model for porous coal is reliable. (2) In the water-driven-methane process, there is an increasing zone and a decreasing zone of pore pressure in the coal sample. The increasing zone of pore pressure is closest to the side of the water inlet, and its area gradually decreases. The decreasing zone of pore pressure is closest to the side of the methane outlet, and its area gradually increases. Over time, the methane pressure in the increasing zone of pore pressure first increases and then decreases, and the methane pressure in the decreasing zone of pore pressure continuously decreases. The change (increase or decrease) rate of the methane pressure gradually decreases from both ends towards the middle of the coal sample. (3) The curve of the water saturation over time changes from a lower concave curve to a straight line, while the curve of the methane saturation with time changes from an upper convex curve to a straight line. The methane saturation in the decreasing zone of pore pressure is greater than that in the increasing zone of pore pressure. Over time, the water saturation of a specific point in space continuously increases while its methane saturation continuously decreases. Both of the increase rate of the water saturation and the decrease rate of the methane saturation gradually reduce over time. (4) The pore pressure gradient along the driving direction first decreases and then increases. The decreasing zone of the pore pressure gradient is located in the increasing zone of pore pressure, and the increasing zone of the pore pressure gradient is located in the decreasing zone of pore pressure. Over time, the pore pressure gradient at the side of the water inlet increases, and its increase rate decreases. The pore pressure gradient at the side of the methane outlet decreases, and its decrease rate decreases. The rate of increase in the pore pressure gradient at the side of the water inlet is greater than the rate of decrease in the pore pressure gradient at the side of the methane outlet.

1. Introduction

During the process of water injection or hydraulic fracturing in gassy coal, the methane concentration of the airflow in the roadway clearly increases. This phenomenon is known as the water-driven-methane effect [1]. The existence of this phenomenon has been shown in laboratory experiments. The effect has both advantages and disadvantages in production

practice. On the one hand, it can provide new ideas and technology for the exploitation of coalbed gas, and the hydraulic measures are used to eliminate methane outbursts. On the other hand, it can increase the methane concentration of the airflow in the roadway in addition to the methane content and methane pressure of the local region in the coal seam, which is detrimental to the prevention of coal and methane outbursts and methane explosions [2–7]. In fact, the negative

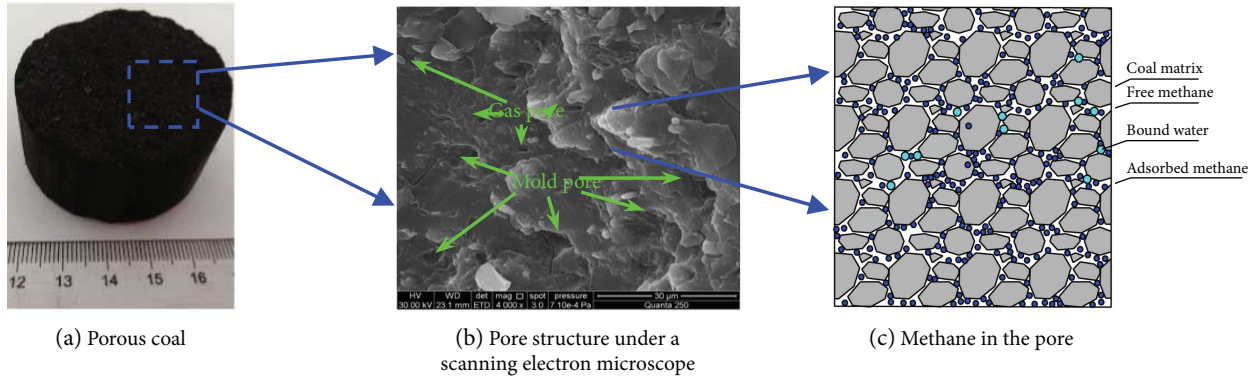


FIGURE 1: Methane distribution in porous coal.

effect of the water-driven-methane process has always existed, but it has not been an obvious cause of a disaster and has not attracted the attention of fieldworkers and researchers. With an increase in the exploitation depth of coal seam gas and coal resources, the positive and negative impacts of the water-driven-methane effect have become more and more obvious [8, 9]. However, at present, a mathematical model considering the effect of methane adsorption and desorption in coal has not been established to describe the water-driven-methane effect in coal. Therefore, during the water-driven-methane process, the distribution regularities of water and methane saturation in addition to the pore pressure and its gradient are still not clear. Therefore, to describe the water-driven-methane process accurately, a mathematical model should be established. Based on this mathematical model, the distribution regularities of water and methane saturation and of the pore pressure and its gradient can be analysed. A more comprehensive and in-depth understanding of the effect of this process will be useful for making the best use of this phenomenon's advantages and overcoming its disadvantages.

At present, a mathematical model has been established to describe water-gas or water-oil two-phase driving processes in conventional porous medium reservoirs [10–12]. Of course, coal rock masses are also porous media. The water-driven-methane process in a coal rock mass also belongs to water-gas two-phase flow in porous media. However, the effect of methane adsorption and desorption in coal is significantly different from that of the water-driven-gas process in coal rock masses and conventional porous media. During the processes of water drainage, decreasing pressure, and desorption of coalbed methane, there is a stage of water-gas two-phase flow. A coupled fluid-solid mathematical model that considers the effects of methane adsorption and desorption has already been established to describe this stage, but it still cannot be directly used to describe the water-driven-methane process in coal because of the following reasons. (1) The coupled fluid-solid model of coalbed methane drainage is used to describe the process of water-methane two-phase flow with a decrease in the water pressure and adsorbed coalbed methane becoming free coalbed methane. However, a coupled fluid-solid model of methane driven by water is required to describe the process of driving out methane in

coal by the injected water, which is injected into the coal. The boundary conditions of the above two processes are different. In addition, the injected water will also cause an increase in methane pressure, resulting in the transformation of free methane to adsorbed methane. (2) For the coupled fluid-solid mathematical models of coalbed methane drainage, some equations are only listed but not solved, and for the other equations, only the numerical solutions are offered. However, the reliability of these mathematical models has not been verified. Furthermore, these models primarily study the evolution regularities of reservoir permeability and methane production but rarely address the distribution regularities of water-methane two-phase saturation and of the pore pressure and its gradient [13–15].

To clarify the distribution regularities of water-methane two-phase saturation and the pore pressure and the mechanism of the pore pressure gradient in the water-driven-methane process, pure porous coal rock without fractures is selected in this study, thereby excluding the effects of fractured structures. Based on the elastic theory of porous media, the principle of effective stress, the principle of methane adsorption and desorption, and the principle of conservation of mass and Darcy's law, a coupled fluid-solid mathematical model of methane driven by water is established. This model considers the effect of coalbed methane adsorption and desorption, the deformation field of the coal rock mass, and the seepage field of water and methane. The reliability of the mathematical model is verified by physical experiments of artificially suppressed briquette coal. On the basis of the mathematical model, a further study is developed on the distribution regularities of water-methane two-phase saturation and the pore pressure and the mechanism of the pore pressure gradient. Scientific understanding is provided for the water-driven-methane process in the porous coal.

2. Conceptual Model

Porous coal rock (Figure 1(a)) is characterized by a pore structure of air pores and mold pores and similar structures (Figure 1(b)), which can provide space for free methane and adsorbed methane (Figure 1(c)) [16–18]. In a porous coal rock, there are many interconnected pores, which can be regarded as the migration channels of fluid [19, 20].

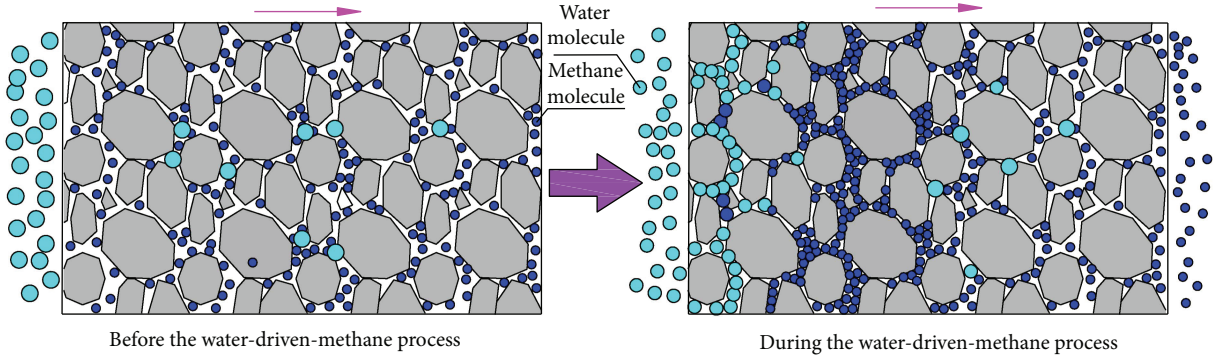


FIGURE 2: Conceptual model of methane driven by water in porous coal rock.

Before methane is driven by water, there are primarily methane and a small amount of bound water (Figure 1(c)) in the pores of coal rock. The pressure is regarded as the initial pore pressure. During the water-driven-methane process, pressure water will flow along the pore channel [21–24]. This breaks the original mechanical equilibrium in the coal sample, and the stress is redistributed again. The methane pressure will rise at a distance from the water injection position. The water drives the methane in the pore to move forward in the pore channel until the methane is expelled from the coal rock mass. At the same time, the pore space of methane is also occupied by water [1]. The pore space occupied by water forms the water zone, but a certain amount of methane remains in the water zone. The pore space occupied by methane forms the gas zone, and there is also a small amount of bound water in the gas zone. According to the above process, a conceptual model of methane driven by water in porous coal rock (Figure 2) is constructed in this study.

3. Mathematical Model

3.1. Basic Assumptions. The mathematical model is established based on the following six basic assumptions:

- (1) The water-methane two-phase flow is an immiscible system, and the solubility of methane in water is not considered in the model.
- (2) The temperature in the seepage field is a constant, and the water, methane, and rock strata are in a state of thermal equilibrium.
- (3) Methane is an ideal gas. The flow of water and methane in porous coal is both characterized by laminar flow and obeys Darcy's law.
- (4) Porous coal rock is homogeneous and isotropic. Its solid skeletons and pores are compressible, and the deformation of porous coal rock is elastic and small.
- (5) The influences of capillary pressure and gravity are considered in the mathematical model.
- (6) Only the water-driven-methane effect is considered, and the water-displaced-methane effect is ignored.

3.2. Basic Equations

3.2.1. The Equations of the Stress Field. The free coalbed methane and water in the coal can transfer fluid pressure. When methane is adsorbed on the surface of the coal, the surface tension of the coal decreases, resulting in the expansion of the volume. However, when the methane is desorbed from the coal surface, its volume shrinks. The above differences have prompted scholars to supplement the Terzaghi's effective pressure principle to adapt to the deformation of coal, which is rich in adsorbed coalbed methane. Based on the elastic theory of porous media, the constitutive equation of the coal body considering the effect of methane adsorption and desorption is as follows [14]:

$$\varepsilon_{ij} = \underbrace{\frac{1}{2G}\sigma_{ij} - \left(\frac{1}{6G} - \frac{1}{9K}\right)\sigma_{kk}\delta_{ij}}_{\text{Geostress strain}} + \underbrace{\frac{\alpha_p}{3K}p\delta_{ij}}_{\text{Pore pressure strain}} + \underbrace{\frac{\varepsilon_a}{3}\delta_{ij}}_{\text{Adsorption swelling strain}}, \quad (1)$$

in which

$$\begin{aligned} G &= \frac{E}{2(1+\nu)}, \\ \sigma_{kk} &= \sigma_{11} + \sigma_{22} + \sigma_{33}, \\ \alpha_p &= \frac{1-K}{K_s}, \\ K &= \frac{2G(1+\nu)}{3(1-2\nu)} = \frac{E}{3(1-2\nu)}, \\ K_s &= \frac{E_s}{1-2\nu}, \\ \varepsilon_a &= \varepsilon_g V_g = \varepsilon_g \frac{V_L p_g}{p_g + P_L}, \\ p &= S_w p_w + S_g p_g, \end{aligned} \quad (2)$$

where G is the shear modulus, E is the elastic modulus, ν is Poisson's ratio, σ_{kk} represents the components of the normal stress, p is the pore pressure, $\alpha (\leq 1)$ is Biot's effective stress

coefficient, K is the volume modulus of coal rock, K_s is the volume modulus of a coal rock skeleton, E_s is the elastic modulus of a coal rock skeleton, δ_{ij} is the Kronecker symbol (when i is equal to j , δ_{ij} is 1; when i is unequal to j , δ_{ij} is 0), ε_s is the adsorption strain of the methane, ε_g is the adsorption strain coefficient of the methane, P_L is the Langmuir pressure constant, V_L is the Langmuir volume constant, S_w is the water saturation, p_w is the pore pressure of water, S_g is the methane saturation, and p_g is the pore pressure of methane.

According to the theory of elastic mechanics, the relation between strain and displacement is

$$\varepsilon_{ij} = \frac{1}{2} (u_{i,j} + u_{j,i}). \quad (3)$$

From the condition of static equilibrium, the following can be obtained:

$$\sigma_{i,j,j} + F_i = 0. \quad (4)$$

Substituting (1), (2), and (3) into (4), the modified Navier balance equation (5) with the displacement as the fundamentally unknown quantity and with the coupling term included can be obtained.

$$Gu_{i,j,j} + (G + \lambda)u_{j,j,i} - \alpha_p p_i - K\varepsilon_{a,i} + F_i = 0, \quad (5)$$

where u_i is the displacement along the i direction and F_i is the volume force along the i direction ($i = x, y, z$).

3.2.2. Mass Conservation Equation. There are adsorbed methane and free methane in coal. The methane, which is initially adsorbed on the internal surface of matrix pores, becomes free-phase methane due to the reduction in pore pressure. On the contrary, with the increase in the pore pressure, the free-phase methane can become adsorbed methane.

The total methane can be calculated by

$$m_g = m_y + m_x, \quad (6)$$

where m_y is the free methane and m_x is the adsorbed methane.

The free methane content m_y can be calculated by the following:

$$m_y = \rho_g \varphi_{nw}, \quad (7)$$

where ρ_g is the density of methane and φ_{nw} is the porosity of coal rock.

By regarding the methane as an original gas, the relationship between its density and pressure can be expressed as follows:

$$\rho_g = \beta p_g, \quad (8)$$

where p_g is the methane pressure (Pa), $\beta = M_g/RT$ is the compression coefficient ($\text{kg}/(\text{m}^3 \cdot \text{Pa})$), M_g is the molecular weight of methane (kg/mol), R is the ideal gas constant ($3.814 \text{ kJ}/(\text{mol} \cdot \text{K})$), and T is the absolute temperature (K).

According to (8) and (9), the density of methane can be calculated by

$$\rho_g = \frac{p_g}{p_0} \rho_0, \quad (9)$$

where p_0 is the pressure under standard conditions (101325 Pa) and ρ_0 is the density of methane under standard conditions ($0.717 \text{ kg}/\text{m}^3$).

The adsorbed methane content m_x satisfies the Langmuir formula, whose corresponding equation is

$$m_x = \frac{ab\beta p_0 \rho_c}{1 + bp_g} p_g, \quad (10)$$

where a is the ultimate adsorption capacity of the methane (m^3/kg), b is the adsorption equilibrium constant of the methane (Pa^{-1}), and ρ_c is the density of coal (kg/m^3).

According to the principle of mass conservation, the mass continuity equation of a fluid is expressed as follows:

$$\frac{\partial m_i}{\partial t} + \nabla \cdot (\rho_i \cdot u_i) = 0, \quad (11)$$

$$u_i = -\lambda_i (\nabla p_i + \rho_i g \nabla D), \quad (12)$$

where i represents w or g , where w is a water phase and g is a methane phase; m_i is the mass of an i -phase fluid (kg/m^3); ρ_i is the mass of an i -phase fluid (kg/m^3); u_i is the average velocity of an i -phase fluid (m/s); K is the absolute permeability of the coal (m^2); $\lambda_i = K k_{r,i}/\mu_i$ is the conductivity of an i -phase fluid; $k_{r,i}$ is the relative permeability of an i -phase fluid; μ_i is the dynamic viscosity of an i -phase fluid ($\text{Pa} \cdot \text{s}$); and D is the height of the coordinate system (m).

By regarding the methane as a compressible fluid and the water as an incompressible fluid, with the union of (1), (2), (3), (4), (5), (6), (7), (8), (9), (10), (11), and (12), the mass continuity equation of the methane and water can be separately expressed as follows:

$$\begin{aligned} & \beta p_g S_g \frac{\partial \varphi}{\partial t} + \varphi \beta p_g \frac{\partial S_g}{\partial t} + \left(\varphi \beta S_g + \frac{ab\beta p_0 \rho_c}{(1 + bp_g)^2} \right) \frac{\partial p_g}{\partial t} \\ & - \nabla \cdot \left[\beta p_g \lambda_g (\nabla p_g + \rho_g g \nabla D) \right] \\ & = 0, \frac{\partial (\varphi S_w)}{\partial t} - \nabla \cdot [\lambda_w (\nabla p_w + \rho_w g \nabla D)] \\ & = \varphi \frac{\partial S_w}{\partial t} + S_w \frac{\partial \varphi}{\partial t} - \nabla \cdot [\lambda_w (\nabla p_w + \rho_w g \nabla D)] = 0. \end{aligned} \quad (13)$$

For a further simplification, (13) can be separately expressed as follows:

$$\begin{aligned} \varphi \frac{\partial S_w}{\partial t} - \nabla \cdot [\lambda_w (\nabla p_w + \rho_w g \nabla D)] &= -S_w \frac{\partial \varphi}{\partial t}, \\ \varphi \beta p_g \frac{\partial S_g}{\partial t} + \left(\varphi \beta S_g + \frac{ab\beta p_0 \rho_c}{(1 + bp_g)^2} \right) \frac{\partial p_g}{\partial t} \\ - \nabla \cdot [\beta p_g \lambda_g (\nabla p_g + \rho_g g \nabla D)] &= -\beta p_g S_g \frac{\partial \varphi}{\partial t}. \end{aligned} \quad (14)$$

3.2.3. Level Set Transport Equation. The level set method, firstly proposed by Osher and Sethian, is a numerical method for solving the two-phase flowing equations including the surface tension phase. It can be utilized to simulate the water-driven-gas process. To understand the dynamic change characteristics of water and gas two-phase flow, the method has the advantages of convenience, visualization, and the like. The level set equation is written as follows [25]:

$$\frac{\partial \phi}{\partial t} + u \cdot \nabla \phi = \gamma \nabla \cdot \left(\varepsilon \nabla \phi - \phi (1 - \phi) \frac{\nabla \phi}{|\nabla \phi|} \right), \quad (15)$$

where ϕ is a contour line of the water-gas two-phase interface, γ is the reinitialization parameter in the solution of the equation, u is the velocity of the fluid, ε is the thickness of the water-gas interface, and t is the time of water and gas flow.

To avoid the instability of the numerical calculation, the density and viscous property parameters of the fluid in the vicinity of the interface need to be smoothed. The smoothing method of the level set equation describes the changes in the density and dynamic viscosity in the process of water-gas two-phase flow with the level set function, and the corresponding equations are

$$\begin{aligned} \rho(\phi) &= \rho_g + (\rho_w - \rho_g)\phi, \\ \mu(\phi) &= \mu_g + (\mu_w - \mu_g)\phi, \end{aligned} \quad (16)$$

where ρ_w and ρ_g are the densities of water and gas (kg/m^3), respectively, and μ_w and μ_g are the dynamic viscosities of water and methane (Pa·s), respectively.

3.2.4. Dynamic Model of Porosity and Permeability. Methane migration is determined by the porosity and permeability of coal rock, which are a bridge between the stress field and seepage field. Both of these key parameters are closely related to the stress and inherent material properties of coal rock.

Porous coal rock is porous media. Its porosity is influenced by the pore pressure and matrix expansion/contraction caused by methane adsorption/desorption. Considering the

combined effect of the pore pressure and matrix expansion/contraction, the dynamic model of porosity can be written as follows [26, 27]:

$$\varphi = \frac{1}{1 + S} [\varphi_0 (1 + S_0) + \alpha (S - S_0)], \quad (17)$$

in which

$$\begin{aligned} S &= \frac{\varepsilon_v + p}{K_s - \varepsilon_a}, \\ S &= \frac{\varepsilon_{v0} + p_0}{K_s - \varepsilon_{a0}}, \\ \varepsilon_v &= \varepsilon_x + \varepsilon_y + \varepsilon_z, \end{aligned} \quad (18)$$

where φ is the initial porosity of coal rock; ε_v is the volume strain of coal rock; ε_x , ε_y , and ε_z are the volume strain in the x , y , and z directions, respectively; K_s is the volume modulus of the coal skeleton; and the index 0 is the initial value of the corresponding parameter.

The absolute permeability of porous media is also influenced by the in situ stress. The dynamic model of absolute permeability can be expressed as follows [28, 29]:

$$K = \frac{K_0}{1 + \varepsilon_v} \left[1 + \frac{\varepsilon_v - \Delta p (1 - \varphi_0) / K_s}{\varphi_0} \right]^3, \quad (19)$$

where K_0 is the initial permeability of the porous media.

Capillary pressure curves are used by the Brooks and Corey-Burdine model to calculate the relative permeability of a fluid in porous media. Based on the Brooks and Corey-Burdine model, the relative permeabilities of water and methane in porous coal rock are a function of the water saturation. The corresponding expressions are as follows [30]:

$$\begin{aligned} k_{r,w} &= k_{r,w0} \left(\frac{S_w - S_{r,w}}{1 - S_{r,w} - S_{r,g}} \right)^{3+2/\lambda}, \\ k_{r,g} &= k_{r,g0} \left(1 - \frac{S_w - S_{r,w}}{1 - S_{r,w} - S_{r,g}} \right)^2 \left[1 - \left(\frac{S_w - S_{r,w}}{1 - S_{r,w} - S_{r,g}} \right)^{1+2/\lambda} \right], \end{aligned} \quad (20)$$

where $k_{r,w0}$ is the relative permeability of the water phase endpoints, $k_{r,g0}$ is the relative permeability of the gas phase endpoint, $S_{r,w}$ is the residual saturation of the water phase, $S_{r,g}$ is the residual saturation of the gas phase, and λ is a parameter that represents the pore structure characteristics of porous media.

When the parameter λ of the Brooks and Corey-Burdine model is 1, the calculated relative permeability curves of water and methane are consistent with the results of the unsteady method experiment, as shown in Figure 3 [31].

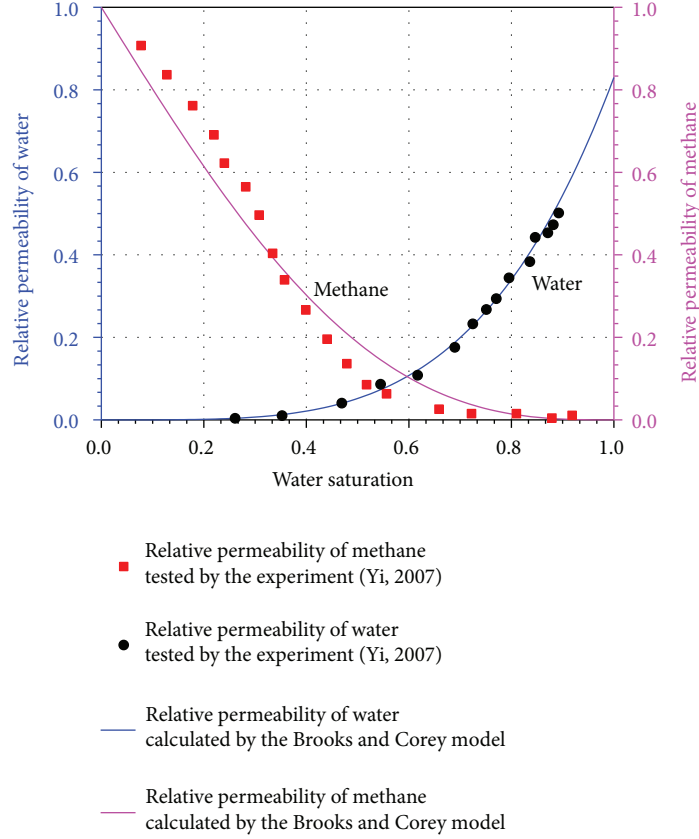


FIGURE 3: The permeability of water and methane in porous coal rock.

3.2.5. Capillary Equation. When the two immiscible fluids of water and gas flow into the pore channel, a meniscus-shaped interface between the water and methane is formed. The pressure on both sides of the interface is discontinuous. The difference in the pressure is called the capillary force, and the corresponding expression is

$$p_{cgw} = p_g - p_w, \quad (21)$$

where p_{cgw} is the capillary force, p_g is the methane pressure, and p_w is the water pressure.

3.2.6. Saturation Equation. In saturated porous media, the effective pores are all filled with water and gas. This process is described by the saturation equation:

$$S_g + S_w = 1. \quad (22)$$

3.3. Geometric Model and Boundary Conditions. After water enters the coal rock from the borehole, it will drive the methane forward along the pore channels in the coal rock. The boundary and initial conditions corresponding to the physical model are as follows:

$$\begin{aligned} p_w &= p_w(t), & \partial\Omega \text{ inlet surface,} \\ p_g &= p_{g0}, & \partial\Omega \text{ outlet surface,} \end{aligned}$$

$$\begin{aligned} n \cdot \rho_w [-\lambda_w (\nabla p_w + \rho_w g \nabla D)] &= 0, & \partial\Omega \text{ side of the cylinder,} \\ n \cdot \rho_g [-\lambda_g (\nabla p_g + \rho_g g \nabla D)] &= 0, & \partial\Omega \text{ side of the cylinder,} \\ p &= p_0, & \partial\Omega. \end{aligned} \quad (23)$$

4. Experimental Verification of the Model

4.1. Experiment of Methane Driven by Water in Porous Coal Rock

4.1.1. Experimental System. Based on the principle of methane displaced by water, a pseudo three-axial experimental system of water-methane displacement (Figure 4) is developed. This experimental system can simulate the process of displacing methane by water under the conditions of axial and confining pressures on a cylindrical coal sample with a diameter of 50 mm and a height of 100 mm. The experimental system comprises an axial and confining pressure loading system, a water injection system, a gas injection system, and displaced gas collection and measurement devices. The principle and real objective of the water-methane displacement device are shown in the blue rectangular dashed frame in Figure 4. The axial pressure is loaded by the hydraulic jack at the bottom of the water-methane displacement device, and the confining pressure is applied by injecting hydraulic oil into the annular space. The water pressure loading is controlled by a four-channel, electrohydraulic servo control

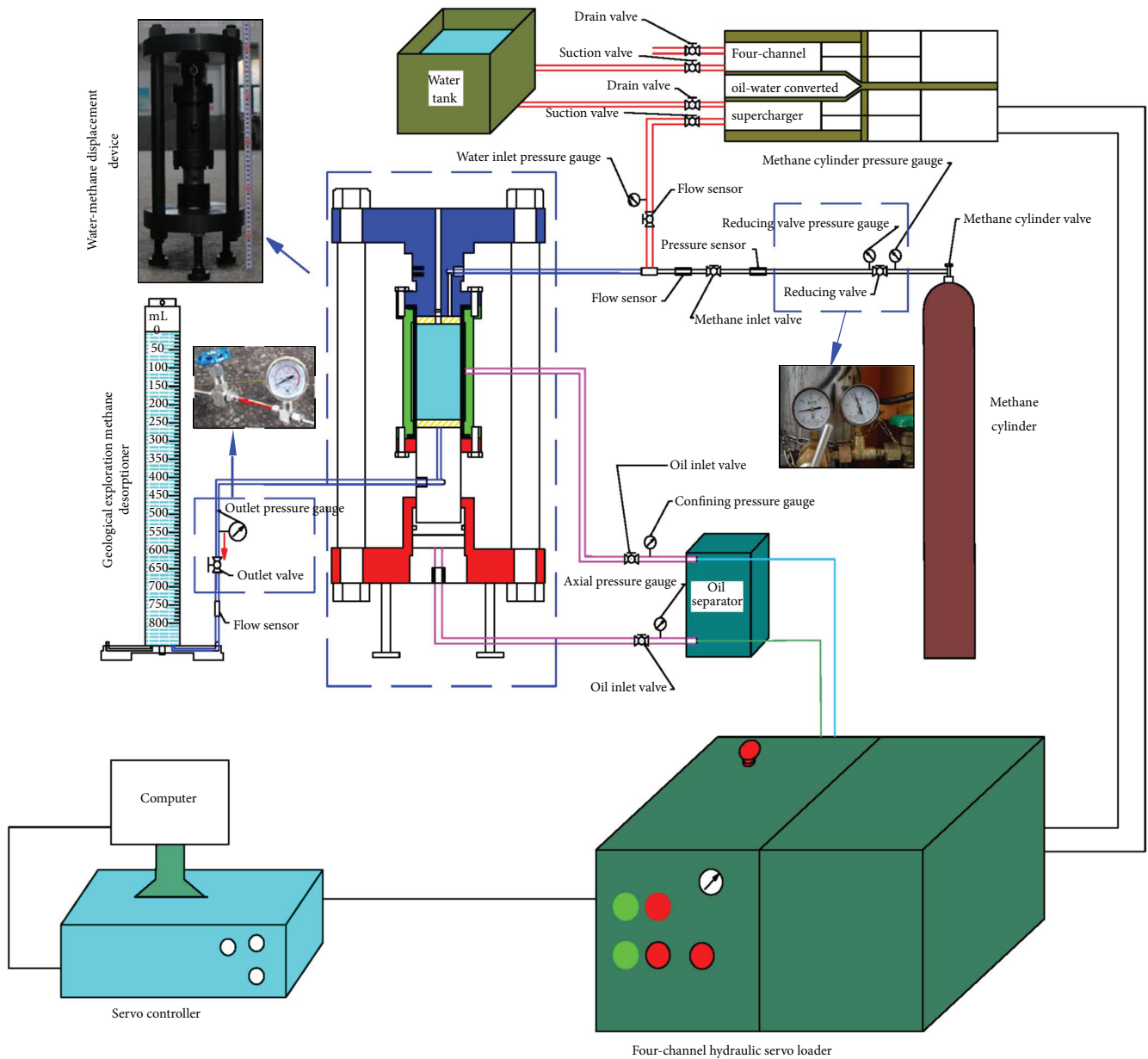


FIGURE 4: Experimental system of methane displacement by water.

system based on the MOOG valve. The pressure of the gas circuit system is adjusted using the pressure release valve at the outlet of the methane cylinders. The collection and volumetric measurement of the displaced methane are completed with the help of a geological exploration methane desorption instrument.

4.1.2. *Preparation of the Briquette Coal.* Briquette coal is formed from coal powder under the pressure provided by a rigid pressure testing machine, and the internal structure of the briquette coal is porous. To avoid the influence of discrete factors such as joints and fissures, the briquette coal can be an ideal porous coal. The preparation processes used for the briquette coal in this paper (Figure 5) are as follows. First, sieve out the coal powder with diameters of 0.3~0.45 mm with a

sifter (Figure 5(a)). Mix the coal powder and water to achieve a mass ratio of 10:1, and then put the coal-water mixture into the mold (Figure 5(b)). Exert a pressure of 100 MPa (Figure 5(b)) on the coal-water mixture with a rigid pressure testing machine. After ejection (Figure 5(c)), a briquette coal sample with a diameter of 50 mm and a height of 100 mm is produced (Figure 5(d)).

4.1.3. *Experimental Process.* The processes of the water-displaced-methane experiment are as follows. (1) Load the axial and confining pressures. An axial pressure of 2 MPa and a confining pressure of 1 MPa are simultaneously applied at loading rates of 0.2 MPa/s and 0.1 MPa/s, respectively. Then, maintain the axial pressure of 2 MPa and the confining pressure of 1 MPa for 5 minutes. (2) Vent the air. Open the

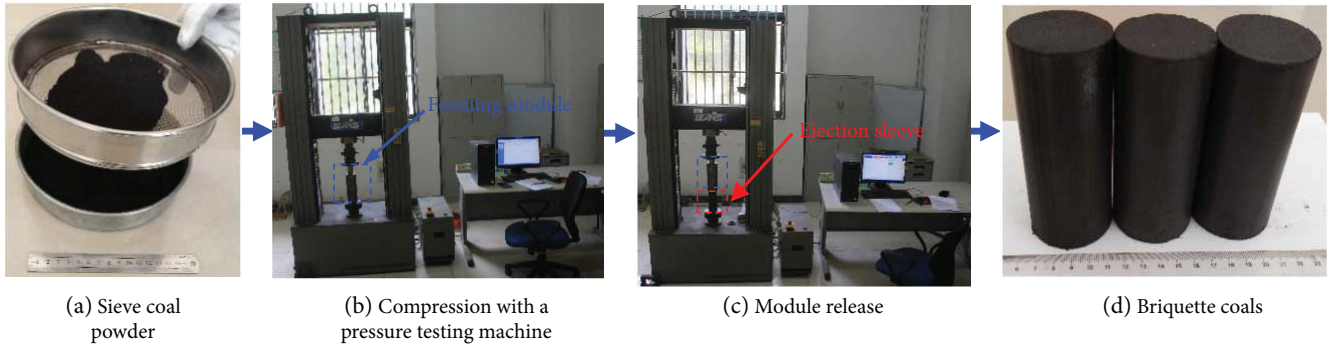


FIGURE 5: Preparation process of the briquette coal samples.

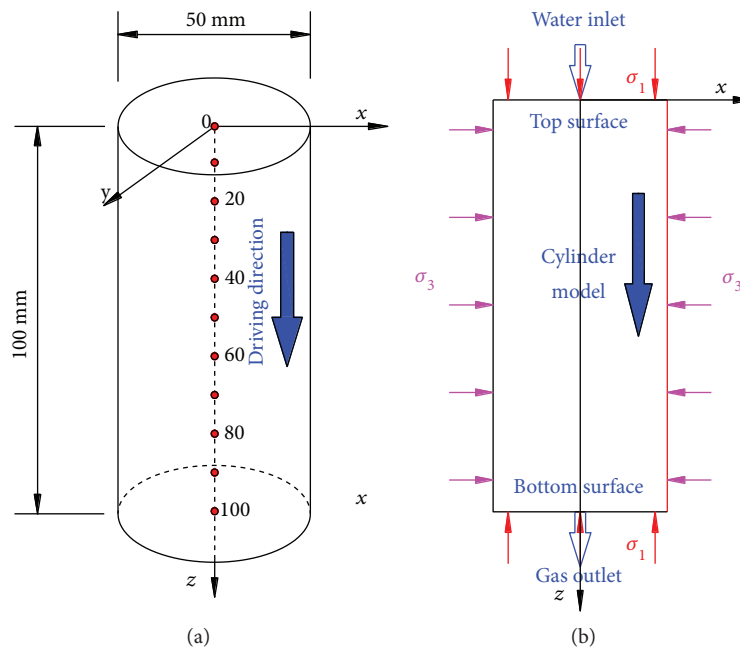


FIGURE 6: Schematic diagram of the geometric model (a) and imposed constraints (b).

intake and outlet valves and collect the gas at the outlet. When the methane concentration of the collected gas is close to 100%, it is believed that the air in the experimental system has been vented out. Then, close the outlet valve. (3) Achieve methane adsorption and desorption equilibrium. Open the cylinder and inlet valves and control the output pressure of the cylinder by adjusting the pressure-reducing valve. The coal sample finally arrives at a state of adsorption and desorption equilibrium, and the corresponding methane pressure is 0.5 MPa. (4) Drive the methane by water injection. Close the gas inlet valve, and open the gas outlet and water inlet valves. Maintain a water pressure of 0.7 MPa, and inject water into the coal sample. Collect the methane displaced by water until no further methane is released.

4.2. Calculation of the Mathematical Model

4.2.1. Geometrical Model. A cylindrical model with a diameter of 50 mm and a height of 100 mm (Figure 6(a)) is adopted in this numerical simulation. To facilitate the monitoring and

analysis of the related parameters of the postprocessing model, the water-displaced-methane direction is flagged as the positive direction of the z -axis, along which nine monitoring points are separately distributed at the locations of 10 mm, 20 mm, 30 mm, 40 mm, 50 mm, 60 mm, 70 mm, 80 mm, and 90 mm from the top of the cylinder. At the same time, the axis of the cylinder is selected as the monitoring line. Water enters the coal sample from its top and drives the methane in the coal forward. The side of the cylinder is an impermeable boundary, the upper surface is the water inlet, and the lower surface is the methane outlet. In the water-displaced-methane process, the loading conditions of the axial and confining pressures are shown in Figure 6(b).

4.2.2. Determining the Parameters of the Numerical Simulation. The process of solving the equations using the COMSOL Multiphysics software is actually a recurrence of a physical process. The recurrence of a physical process needs to be built on the basis of a series of reasonable parameters.

TABLE 1: Parameters of the numerical simulation.

Symbol	Physical significance	Value	Unit
E	Elastic modulus of the coal rock	2713	MPa
E_s	Elastic modulus of the coal skeleton	8469	MPa
ν	Poisson's ratio of the coal rock	0.32	1
φ_0	Initial porosity	0.09	1
μ_{nw}	Dynamic viscosity of the methane	$1.84e-5$	Pa-s
μ_w	Dynamic viscosity of the water	$1.01e-3$	Pa-s
ρ_s	Density of the coal skeleton	1470	kg/m ³
ρ_w	Density of water	1000	kg/m ³
K_0	Absolute permeability of the coal rock	$2e-17$	m ²
a	Langmuir ultimate adsorption capacity of the methane	0.036	m ³ /kg
b	Langmuir adsorption equilibrium constant of the methane	3.304	MPa
$S_{r,w}$	Bound water saturation	0.2	1
$S_{r,g}$	Residual methane saturation	0.1	1
$k_{r,w0}$	Relative permeability of the water endpoint	0.83	1
$k_{r,g0}$	Relative permeability of the methane endpoint	1	1
P_{g0}	Outlet pressure	0.1	MPa
P_0	Initial pore pressure	0.5	MPa

Only in this way can the solution of the equations converge and the recurrence of the physical process succeed. To ensure that the numerical simulation is similar to the real physical experiment, the real physical parameters of the experimental briquette coal sample are used in the numerical calculation to the farthest extent possible. The relevant parameters used in this numerical simulation are shown in Table 1.

4.3. Comparisons of the Experiment and Numerical Calculation Results. The methane driven by water is mainly free methane in the coal. The free methane includes the original free methane (black line in Figure 7) and the desorbed methane from the adsorbed methane (magenta line in Figure 7). When pressure water enters the pores of the coal, the free methane in the pores will be driven forward along the seepage direction of the pressure water. As more water enters the pores, additional methane is driven by the water. It can be seen from Figure 7 that, during the initial 20 min, the collected methane volume of the water-displaced-methane experiment is significantly higher than the value calculated by the mathematical model; however, from 20 min to 60 min, the collected methane volumes of the experiment and numerical calculation gradually converge. In an hour, the collected methane volume of the water-displaced-methane experiment is 1.4 percent higher than that of the numerical calculation. This is because after water enters the coal, both the free methane in the pores and the free methane from the adsorbed methane displaced by water are driven out at the same time. Although only a small volume of the methane is displaced by water, its existence is confirmed by the experiment [1, 32–35]. Currently, the methane displaced by water cannot be quantitatively calculated by the

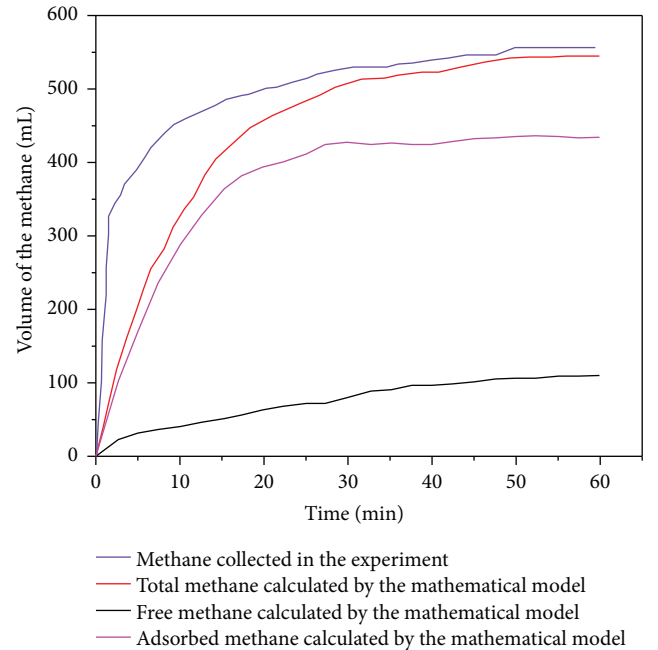


FIGURE 7: Change in the methane volume over time.

mathematical formula. In this paper, the mathematical model also lacks a quantitative expression of the methane volume. This is the reason for the subtle difference between the experimental and calculation results. Overall, the results indicate that the mathematical model of the methane driven by water is basically reliable and can be used to predict the methane volume in the water-driven-methane process.

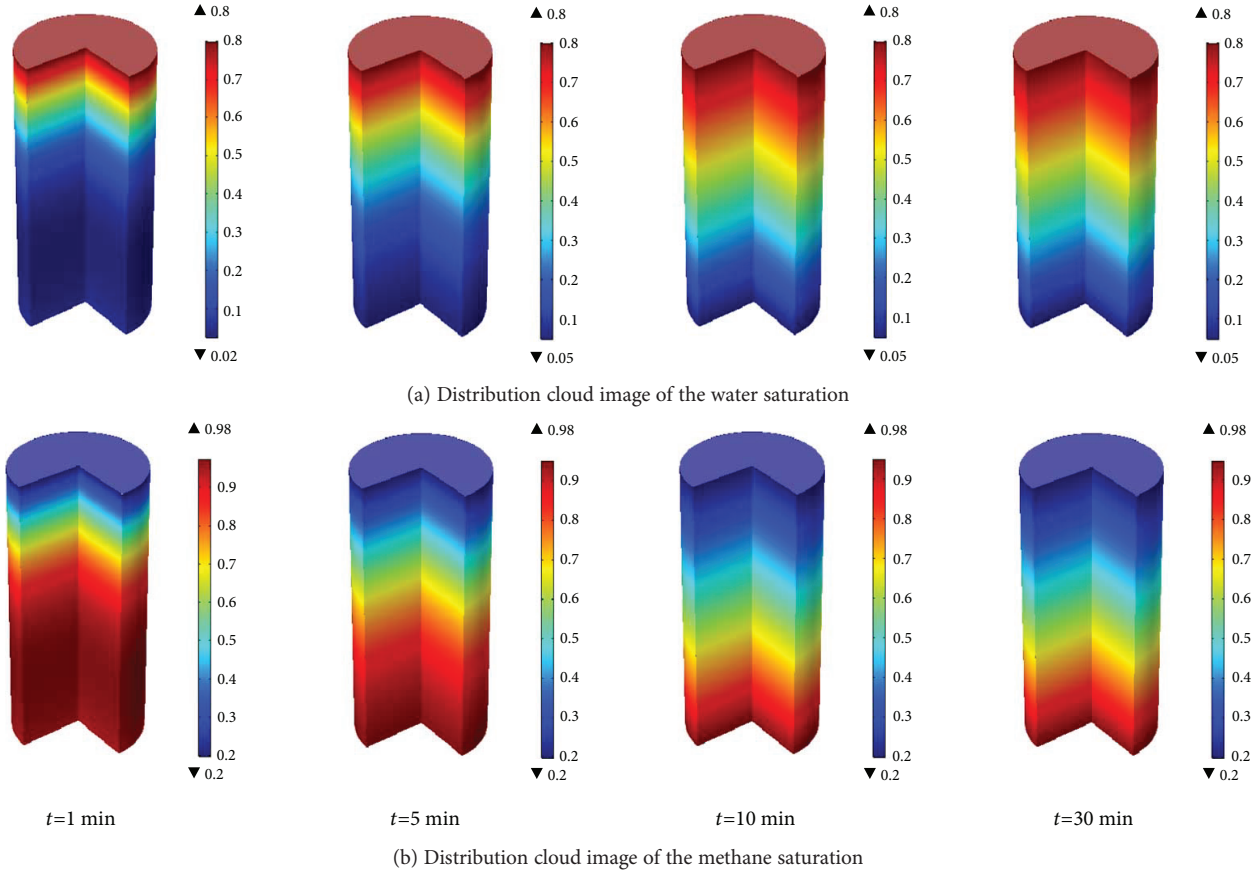


FIGURE 8: Space-time distribution of the water-methane two-phase saturation.

5. The Regularities of Methane Driven by Water

5.1. Space-Time Distribution Regularities of the Water-Methane Two-Phase Saturation

5.1.1. Visualization of the Space-Time Distribution of the Water-Methane Two-Phase Saturation along the Driving Direction. In the water-driven-methane process, the dynamic processes of the spatial distributions of water and methane saturations can be shown clearly by a saturation cloud image. The spatial distributions of the water and methane saturations at the four moments of 1 min, 5 min, 10 min, and 30 min are shown in Figure 8. The following can be seen from Figure 8. (1) When water enters the pores, the methane cannot be expelled completely, and there is residual methane in the pores of the coal rock. The residual methane saturation is set as 0.2 in the numerical simulation, so the maximum water saturation is 0.8. When the water saturation of the coal sample reaches 0.8, it is believed that the pores in this area have been saturated with water. (2) There is bound water in the coal sample. With the existence of bound water, the pores in the coal rock cannot be completely filled with methane. Therefore, the saturation of bound water in the coal sample is set as 0.05, and the maximum methane saturation is 0.95.

The results shown in Figure 8 are in agreement with the preset parameters of the mathematical model, which indicates indirectly the feasibility and reliability of the mathematical

model. With the help of the COMSOL Multiphysics software, the visualization of the water-driven-methane behaviours can be realized. This contributes to the semiquantitative and semi-quantitative research on the visualization of the space-time distribution of water-methane two-phase saturation.

5.1.2. Space-Time Distribution of the Water-Methane Two-Phase Saturation on the Axial Monitoring Line along the Driving Direction. When the pressure water is injected into the coal sample, more and more space is occupied by water. Meanwhile, the methane at that point is driven forward by water, resulting in a decrease in the space occupied by methane. Because the sum of the water and methane saturation at any space point is 1, the change regularities of the water and methane saturations at any point in space are opposite to one another. In other words, the water saturation is greater and the methane saturation is smaller, which is closer to the water inlet end. It can be seen from Figure 9. (1) In the same position, the water saturation increases with an increase in time (e.g., the water saturation at the 20 mm position increases from 0.05 to 0.65 within 30 minutes), but the methane saturation decreases over time (e.g., the methane saturation at the 20 mm position decreases from 0.95 to 0.35 within 30 minutes). Meanwhile, the increase rate of the water saturation decreases gradually, and the decrease rate of the methane saturation decreases gradually as well. The increase rate of the spatial distribution of the water saturation in 1~5 min is

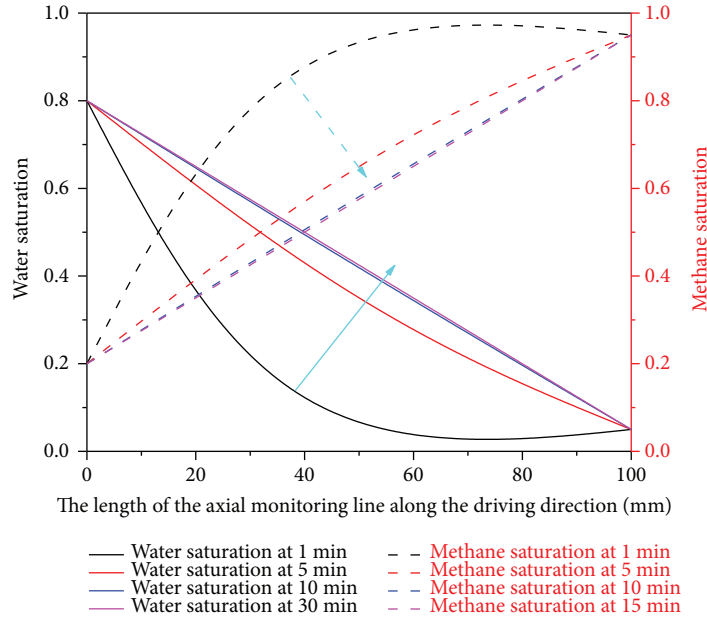


FIGURE 9: Space-time distribution curve of the water-methane two-phase saturation along the driving direction.

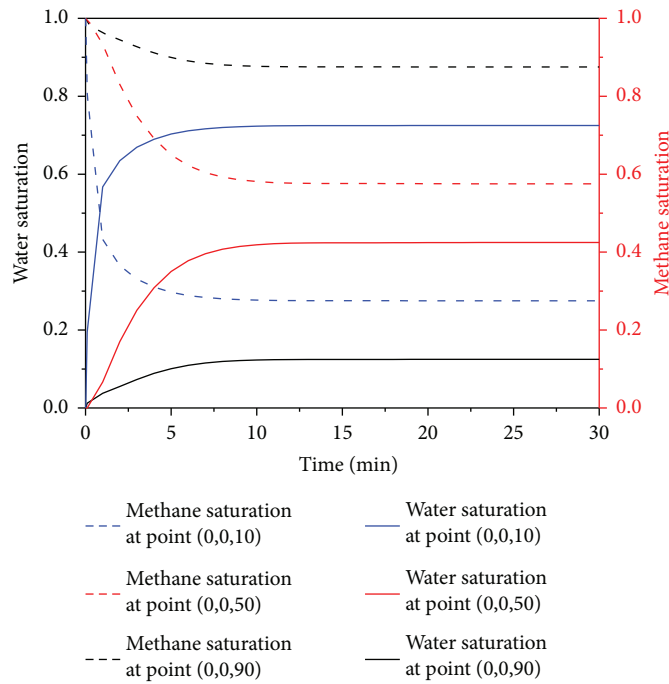


FIGURE 10: Space-time distribution curve of the water-methane two-phase saturation at the axial monitoring points along the driving direction.

larger than that in 10~30 min. (2) At the same time, the water saturation along the driving direction is continuously decreasing within the change interval from 0.05 to 0.8, and the methane saturation shows a continuous increase within the change interval from 0.2 to 0.95. (3) Over time, the curve of the water saturation changes from a lower concave curve to a straight line, and the curve of the methane saturation changes from an upper convex curve to a straight line. It is shown that with the continuous water-driven-methane

process, the water saturation along the driving direction shows a linear increase and the methane saturation shows a linear decrease.

5.1.3. *Space-Time Distribution of the Water-Methane Two-Phase Saturation at the Axial Monitoring Points along the Driving Direction.* It can be seen from Figure 10 and Table 2 that the space-time distribution regularities of the water saturation are as follows. (1) For the same point in

TABLE 2: Space-time distribution of the water-methane two-phase saturation at the axial monitoring points.

Time (min)	Monitoring point (mm)					
	10		50		90	
	Water	Methane	Water	Methane	Water	Methane
0	0.05	0.95	0.05	0.95	0.05	0.95
5	0.703	0.297	0.350	0.650	0.101	0.899
10	0.723	0.277	0.419	0.581	0.123	0.877
15	0.725	0.275	0.424	0.576	0.125	0.875

space, the water saturation first presents a nearly linear increase to a certain value and then remains stable. This is because, over time, water continues to flow into the coal sample, resulting in a continuous increase in the water saturation. However, the pore space at this point is limited. When the pore space is completely occupied by water, the water saturation at that point gradually becomes saturated and reaches a stable value. (2) The increased values of the water saturation at 10 m at 0~5 min, 5~10 min, and 10~15 min are, respectively, 0.653, 0.02, and 0.002, which indicates that the increase in the rate of water saturation gradually reduces over time. The changes in the water saturation at the 50 m and 90 m positions follow the same regularities as that at the 10 m position.

It can be seen from Figure 10 that the space-time regularities of the methane saturation are as follows. (1) For the same point in space, the methane saturation first presents a nearly linear decrease to a certain value and then remains stable. This is because, over time, pressure water enters the coal sample, drives the methane out from the coal sample, and occupies the pore space of the methane. However, the total pore space of the coal has a certain value. With an increase in the water entering the coal sample, the pore space occupied by water gradually increases and the pore space occupied by methane gradually decreases. When the pore space occupied by water in the coal sample tends to be stable, the pore space occupied by the methane will eventually stabilize. (2) The decreasing values of the methane saturation at the 10 m position at 0~5 min, 5~10 min, and 10~15 min are 0.653, 0.02, and 0.002, respectively. This indicates that, over time, the decreasing rate of methane saturation gradually reduces. The changes in the methane saturation at the 50 m and 90 m positions follow the same regularities as that at the 10 m position. (3) At the same time, the methane saturation is lower, which is closer to the water inlet. This is because the water injection volume at a specific time is certain. The closer to the water inlet, the greater the pore space occupied by water and the lower the pore space occupied by methane.

5.2. Space-Time Distribution Regularities of the Pore Pressure

5.2.1. Space-Time Distribution of the Pore Pressure along the Driving Direction. The following can be seen from Figure 11. (1) The initial pore pressure in the coal sample is 0.5 MPa. However, in the water-driven-methane process, the pore pressure in the coal sample is no longer 0.5 MPa.

This indicates that, in the water-driven-methane process, the pore pressure in the coal sample is redistributed. Compared with the initial pore pressure of 0.5 MPa, the maximum pore pressure after redistribution is 0.7 MPa and the minimum pore pressure after redistribution is 0.1 MPa. This shows that there is only a range of increasing zones of pore pressure caused by the transmission of water pressure. (2) Using the initial pore pressure of 0.5 MPa as the dividing line, the coal sample can be divided into an increasing zone and a decreasing zone of pore pressure, as shown by the dotted lines with arrows in Figure 11. Over time, the increasing zone of pore pressure gradually decreases, but the decreasing zone of pore pressure gradually increases. (3) As the water-driven-methane process continues, the pore pressure along the driving direction gradually decreases. This is because the water pressure at the inlet is 0.7 MPa and the atmospheric pressure at the outlet is 0.1 MPa. The pore pressure in the coal is continuous from 0.7 MPa to 0.1 MPa, as shown in the cloud image of the pore pressure in Figure 11. (4) For the same point in space, the methane pressure in the coal sample gradually decreases over time. This is because the free methane in the coal sample is driven by water, resulting in a decrease in the free methane content and the methane pressure in the coal sample.

By combining the space-time distribution regularities of the pore pressure with the space-time distribution regularities of the water-methane two-phase saturation, it is concluded that the methane saturation in the decreasing zone of pore pressure is greater than that in the increasing zone of pore pressure. That is, the free methane content in the decreasing zone of pore pressure is greater than that in the increasing zone of pore pressure. This is because, in the increasing zone of pore pressure, some free methane is driven to the decreasing zone of pore pressure and some free methane is converted into adsorption methane. The free methane in the decreasing zone of pore pressure includes the free methane driven by water from the increasing zone of pore pressure, the original free methane in the region, and the free methane desorbed from the adsorbed methane.

5.2.2. Space-Time Distribution of the Pore Pressure on the Axial Line along the Driving Direction. The following can be seen from Figure 12 and Table 3. (1) The initial pore pressure in the coal sample is 0.5 MPa, and thus the initial pore pressure at each space point in the coal sample is 0.5 MPa. When the pressure water enters the coal sample, the free methane in the pores is driven forward and the pore pressure along the driving direction is redistributed. Therefore, the pore pressures at 10 mm, 20 mm, 30 mm, 40 mm, and 50 mm are all greater than the initial pore pressure, indicating that these points in space are located in the increasing zone of pore pressure. However, the pore pressures at 60 mm, 70 mm, 80 mm, and 90 mm are less than the initial pore pressure, indicating that these points in space are located in the decreasing zone of pore pressure. That is, the increasing zone of pore pressure is distributed closer to the water inlet end, and the decreasing zone of pore pressure is distributed closer to the methane outlet end. This is because the water inlet end is closer to

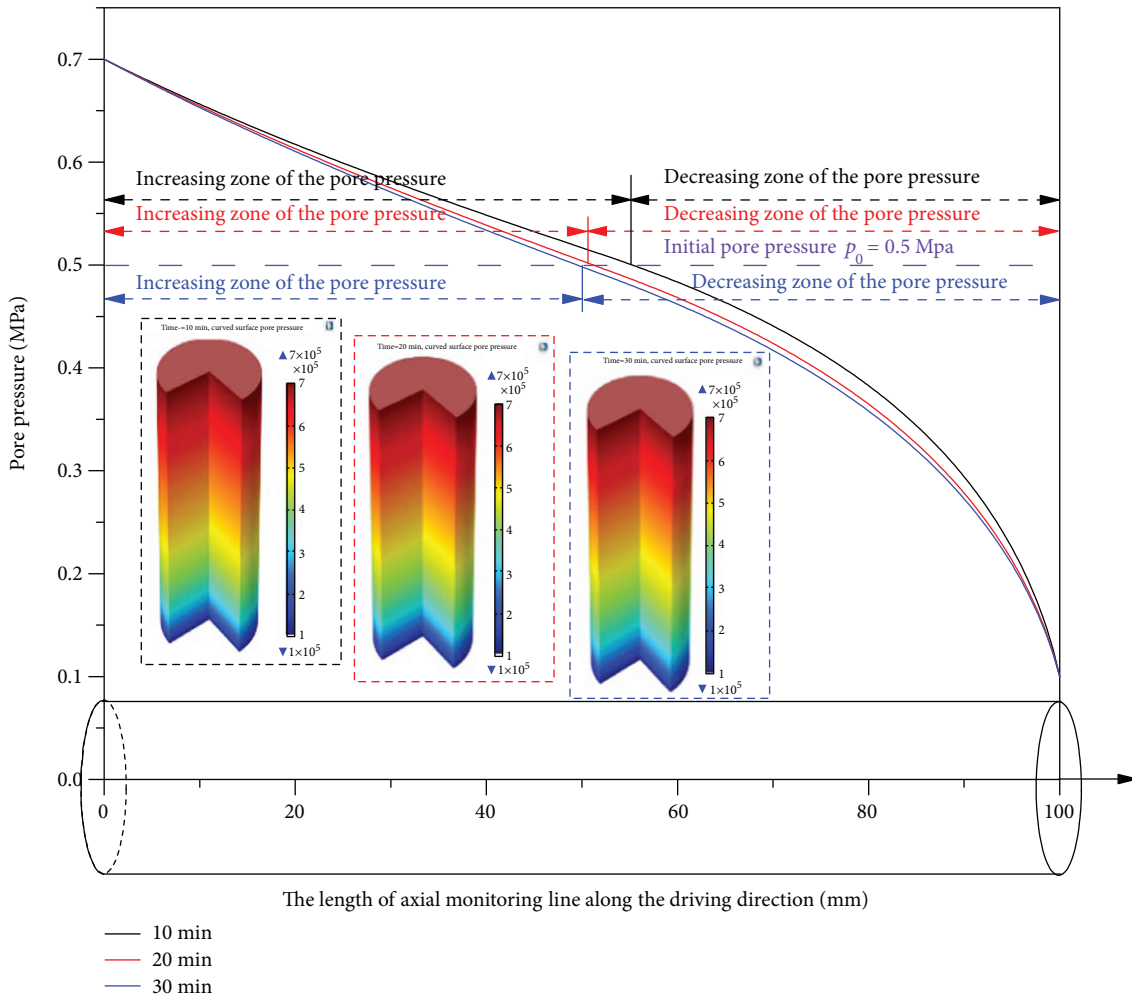


FIGURE 11: Space-time curve and cloud image of the pore pressure on the axial monitoring line along the driving direction.

a high-pressure source of 0.7 MPa, and the methane outlet end is closer to a low-pressure source of 0.1 MPa. (2) Over time, the pore pressure in the increasing zone first increases and then decreases, but the pore pressure in the decreasing zone decreases continuously. (3) At the beginning of the water-driven-methane process, the change (increase or decrease) rate of the pore pressure decreases from both ends to the middle of the coal sample. This is because the two ends of the coal sample are close to a high- or low-pressure source, which creates a pressure difference from the initial pore pressure. At the beginning of the water-driven-methane process, to realize the continuous distribution of the pore pressure in the coal sample, it is necessary to overcome this pressure difference in order to realize the connection and transition of the pore pressure in the coal sample.

5.3. Space-Time Distribution of the Pore Pressure Gradient along the Driving Direction. The following can be seen from Figure 13 and Table 4. (1) When time is constant, the pore pressure gradient on the monitoring line first decreases and then increases. The decreasing zone of the pore pressure gradient is located in the increasing zone of pore pressure, and the increasing zone of the pore pressure gradient is located

in the decreasing zone of pore pressure. (2) At the time of 30 minutes, the pore pressure gradient at the methane outlet end is 7~9 times greater than that at the water inlet end. This indicates that the pore pressure gradient at the side of the methane outlet is greater than that at the side of the water inlet. This is because the pressure difference of 0.4 MPa between the initial pore pressure and the atmospheric pressure is greater than the difference of 0.1 MPa between the water pressure and the initial pore pressure. (3) Over time, the pore pressure gradient at the side of the water inlet increases, but the rate of increase decreases. For example, the rate of increase of 0.183 MPa/m in the pore pressure gradient at 10~20 min is greater than the rate of increase of 0.141 MPa/m in the pressure gradient at 20~30 min. (4) Over time, the pore pressure gradient at the side of the methane outlet decreases, and the rate of decrease decreases as well. For example, the rate of increase of 5.515 MPa/m in the pore pressure gradient at 10~20 min is greater than the rate of increase of 1.76 MPa/m in the pressure gradient at 20~30 min. (5) The rate of increase in the pore pressure gradient at the water inlet is less than the rate of decrease in the pore pressure gradient at the methane outlet.

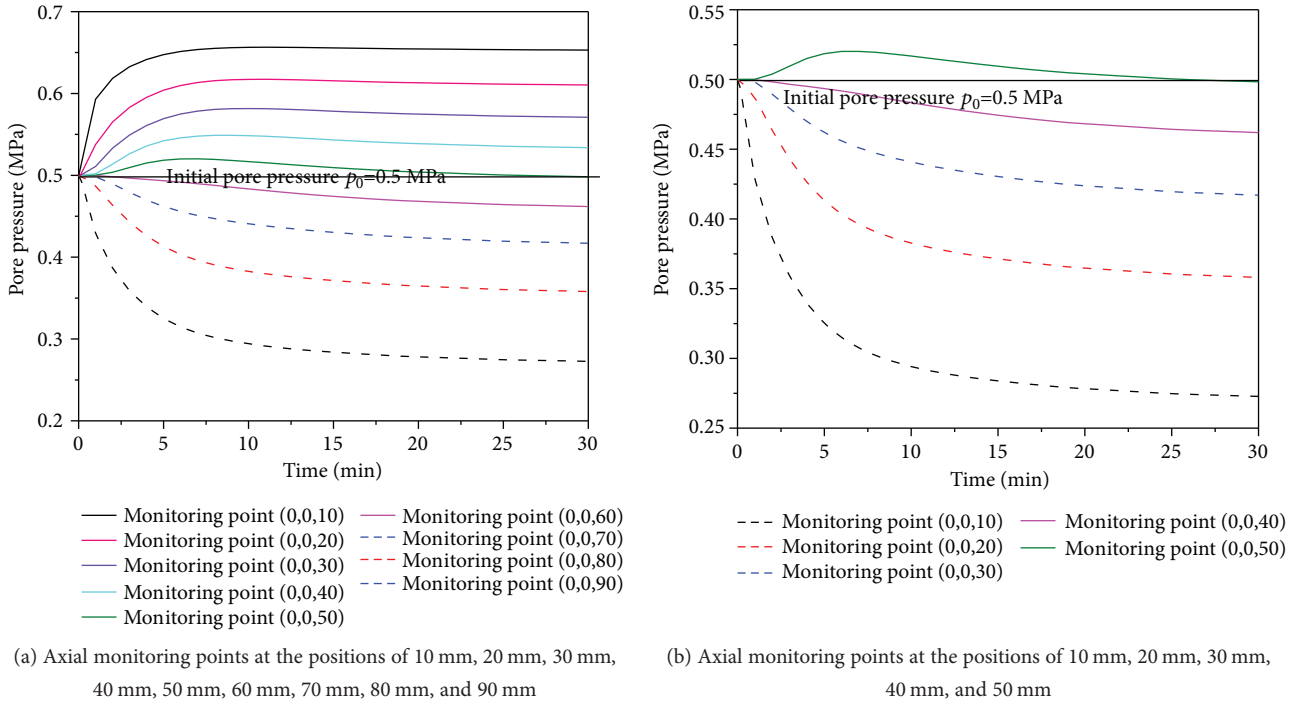


FIGURE 12: Space-time distribution curves of the pore pressure at the axial monitoring points along the driving direction.

TABLE 3: Space-time distribution of the pore pressure at the axial monitoring points.

Time (min)	Monitoring point (mm)								
	10 Pore pressure (MPa)	20 Pore pressure (MPa)	30 Pore pressure (MPa)	40 Pore pressure (MPa)	50 Pore pressure (MPa)	60 Pore pressure (MPa)	70 Pore pressure (MPa)	80 Pore pressure (MPa)	90 Pore pressure (MPa)
0	0.500	0.500	0.500	0.500	0.500	0.500	0.500	0.500	0.500
5	0.648	0.604	0.569	0.542	0.519	0.493	0.462	0.413	0.325
10	0.656	0.617	0.582	0.548	0.517	0.483	0.441	0.383	0.294
15	0.656	0.616	0.578	0.543	0.509	0.474	0.430	0.371	0.284
20	0.654	0.613	0.575	0.539	0.504	0.468	0.424	0.365	0.278

6. Conclusions

- (1) Based on the conceptual model of methane driven by water in porous coal rock, with the effect of methane adsorption and desorption considered, a fluid-solid coupling mathematical model of methane driven by water is established in this paper. The accuracy and reliability of the mathematical model have been verified by the results of the water-driven-methane experiment in a briquette coal sample.
- (2) With the help of the COMSOL Multiphysics software, visualization of the space-time distribution of water-methane two-phase saturation can be realized. The curve of the water saturation over time changes from a lower concave curve to a straight line, while the curve of the methane saturation with time changes from an upper convex curve to a straight

line. Meanwhile, both of the increase rate of the water saturation and the decrease rate of the methane saturation gradually reduce over time.

- (3) In the water-driven-methane process, the pore pressure of the coal sample is redistributed. The maximum pore pressure is the water pressure at the side of the water inlet, and the minimum pore pressure is the atmospheric pressure at the side of the methane outlet. The pore pressure decreases along the driving direction. Using the initial pore pressure as the dividing line, the coal sample can be divided into an increasing zone and a decreasing zone of pore pressure. The increasing zone of pore pressure is close to the side of the water inlet, and the decreasing zone of pore pressure is close to the methane outlet. The increasing zone of pore pressure gradually decreases, and the decreasing zone of pore pressure gradually

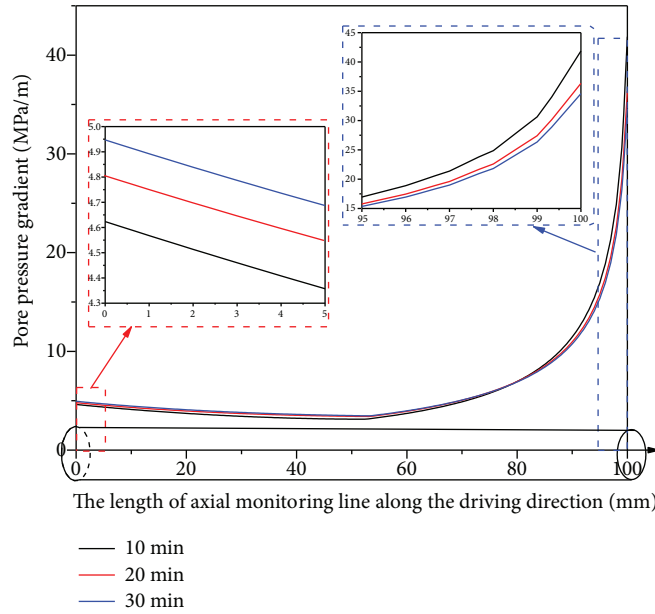


FIGURE 13: Space-time distribution of the pore pressure gradient along the driving direction.

TABLE 4: Space-time distribution of the pore pressure gradient at the axial monitoring points.

Time (min)	Monitoring point (mm)											
	0	10	20	30	40	50	60	70	80	90	100	
	Pore pressure (MPa/m)											
10	4.623	4.119	3.720	3.422	3.225	3.135	3.719	4.893	6.946	11.455	41.869	
20	4.806	4.325	3.966	3.704	3.526	3.423	3.930	5.049	6.944	10.963	36.354	
30	4.947	4.460	4.091	3.817	3.622	3.497	3.981	5.071	6.899	10.751	34.594	

increases. Over time, the pore pressure in the increasing zone of pore pressure first increases and then decreases, and the pore pressure in the decreasing zone of pore pressure continuously decreases. The change (increase or decrease) rate of the pore pressure in the coal sample gradually decreases from both ends towards the middle of the coal sample.

- (4) The pore pressure gradient decreases first and then increases along the driving direction. The decreasing zone of the pore pressure gradient is located in the increasing zone of pore pressure, and the increasing zone of the pore pressure gradient is located in the decreasing zone of pore pressure. In the water-driven-methane process, the distribution of the pore pressure gradient is influenced by the difference between the initial pore pressure and the atmospheric pressure at the side of the methane outlet and the difference between the water pressure at the side of the water inlet and the initial pore pressure. When the pressure difference between the first two is greater than that between the latter two, the pore pressure gradient at the side of the methane outlet is greater than that at the side of the water inlet. Over time,

the pore pressure gradient at the side of the water inlet increases, and its rate of increase decreases. The pore pressure gradient at the side of the methane outlet decreases, and its rate of decrease also decreases. The rate of increase in the pore pressure gradient at the side of the water inlet is greater than the rate of decrease in the pore pressure gradient at the side of the methane outlet.

Data Availability

The data used to support the findings of this study are available from the corresponding author upon request.

Conflicts of Interest

The authors declare that they have no conflicts of interest.

Acknowledgments

The financial support for this work, provided by the National Key Research and Development Program of China (no. 2017YFC0603001), the National Science Fund for Excellent Young Scholars (no. 51522406), and the Fundamental

Research Funds for the Central Universities (China University of Mining and Technology) (no. 2015XKZD04), is gratefully acknowledged.

References

- [1] B. Huang, Q. Cheng, and S. Chen, "Phenomenon of methane driven caused by hydraulic fracturing in methane-bearing coal seams," *International Journal of Mining Science and Technology*, vol. 26, no. 5, pp. 919–927, 2016.
- [2] Y. Ma, Y. Cheng, Z. Liu, and F. Cai, "Improvement of drainage gas of steep gassy coal seam with underground hydraulic fracture stimulation: a case in Huainan, China," *International Journal of Oil, Gas and Coal Technology*, vol. 13, no. 4, pp. 391–406, 2016.
- [3] X. Xia, K. Lin, X. Lu et al., "Study of the effects of hydraulic fracturing at different dip angles for the development of coalbed methane: a case study in the southeast part of Qinshui Basin, China," *International Journal of Oil, Gas and Coal Technology*, vol. 14, no. 1/2, pp. 186–200, 2017.
- [4] Y. Lu, Z. Yang, X. Li, J. Han, and G. Ji, "Problems and methods for optimization of hydraulic fracturing of deep coal beds in China," *Chemistry and Technology of Fuels and Oils*, vol. 51, no. 1, pp. 41–48, 2015.
- [5] J. Xu, C. Zhai, and L. Qin, "Mechanism and application of pulse hydraulic fracturing in improving drainage of coalbed methane," *Journal of Natural Gas Science and Engineering*, vol. 40, no. 4, pp. 79–90, 2017.
- [6] H. Zhang, Y. Cheng, Q. Liu et al., "A novel in-seam borehole hydraulic flushing gas extraction technology in the heading face: enhanced permeability mechanism, gas flow characteristics, and application," *Journal of Natural Gas Science and Engineering*, vol. 46, no. 10, pp. 498–514, 2017.
- [7] L. Yanwei, W. Qian, C. Wenxue, L. Mingju, and H. Mitri, "Enhanced coalbed gas drainage based on hydraulic flush from floor tunnels in coal mines," *International Journal of Mining, Reclamation and Environment*, vol. 30, no. 1, pp. 37–47, 2016.
- [8] F. Yan, B. Lin, C. Zhu et al., "A novel ECBM extraction technology based on the integration of hydraulic slotting and hydraulic fracturing," *Journal of Natural Gas Science and Engineering*, vol. 22, no. 1, pp. 571–579, 2015.
- [9] X. G. Zhang, P. G. Ranjith, M. S. A. Perera, A. S. Ranathunga, and A. Haque, "Gas transportation and enhanced coalbed methane recovery processes in deep coal seams: a review," *Fuel*, vol. 30, no. 11, pp. 8832–8849, 2016.
- [10] Z. Liu and H. Wu, "Pore-scale modeling of immiscible two-phase flow in complex porous media," *Applied Thermal Engineering*, vol. 93, no. 1, pp. 1394–1402, 2016.
- [11] J. Liu, J. G. Wang, F. Gao, Y. Ju, X. Zhang, and L. C. Zhang, "Flow consistency between non-Darcy flow in fracture network and nonlinear diffusion in matrix to gas production rate in fractured shale gas reservoirs," *Transport in Porous Media*, vol. 111, no. 1, pp. 97–121, 2016.
- [12] A. Basu, M. J. Boyd, and P. McConchie, "Numerical modelling of two phase flow of gas and water during drainage of a coal seam," *International Journal of Mine Water*, vol. 7, no. 4, pp. 27–42, 1988.
- [13] J. Liu, "Simulation of coal-bed methane and water two-phase fluid-solid coupling flow," in *ISRM International Symposium/2nd Asian Rock Mechanics Symposium (ISRM 2001-2nd ARMS)*, Beijing, China, 2001 http://xueshu.baidu.com/s?wd=paperuri%3A%282e06c1c106802a97301d8ebc58415eea%29&filter=sc_long_sign&tn=SE_xueshuource_2kduw22v&sc_vurl=http%3A%2F%2Fwww.onepetro.org%2Fconference-paper%2FISRM-ARMS2-2001-077&ie=utf-8&sc_us=2708211531915967481.
- [14] S. Li, C. Fan, J. Han, M. Luo, Z. Yang, and H. Bi, "A fully coupled thermal-hydraulic-mechanical model with two-phase flow for coalbed methane extraction," *Journal of Natural Gas Science and Engineering*, vol. 33, no. 7, pp. 324–336, 2016.
- [15] S. K. Chen, T. H. Yang, and C. H. Wei, "Displacement mechanism of the two-phase flow model for water and gas based on adsorption and desorption in coal seams," in *International Symposium on Multi-field Coupling Theory of Rock and Soil Media and Its Applications*, Chengdu, China, 2010 <http://www.wanfangdata.com.cn/details/detail.do?type=conference&id=WFHYXW399133>.
- [16] H. Liu, J. Mou, and Y. Cheng, "Impact of pore structure on gas adsorption and diffusion dynamics for long-flame coal," *Journal of Natural Gas Science and Engineering*, vol. 22, no. 1, pp. 203–213, 2015.
- [17] L. Si, Z. Li, Y. Yang et al., "Experimental investigation for pore structure and CH₄ release characteristics of coal during pulverization process," *Energy & Fuels*, vol. 31, no. 12, pp. 14357–14366, 2017.
- [18] S. Hou, X. Wang, X. Wang, Y. Yuan, S. Pan, and X. Wang, "Pore structure characterization of low volatile bituminous coals with different particle size and tectonic deformation using low pressure gas adsorption," *International Journal of Coal Geology*, vol. 183, no. 1, pp. 1–13, 2017.
- [19] H. Guo, Y. Cheng, T. Ren et al., "Pulverization characteristics of coal from a strong outburst-prone coal seam and their impact on gas desorption and diffusion properties," *Journal of Natural Gas Science and Engineering*, vol. 33, no. 7, pp. 867–878, 2016.
- [20] H. Guo, Y. Cheng, L. Yuan, L. Wang, and H. Zhou, "Unsteady-state diffusion of gas in coals and its relationship with coal pore structure," *Energy & Fuels*, vol. 30, no. 9, pp. 7014–7024, 2016.
- [21] J. Wu, J. Wang, J. Liu et al., "Moisture removal mechanism of low-rank coal by hydrothermal dewatering: physicochemical property analysis and DFT calculation," *Fuel*, vol. 187, no. 1, pp. 242–249, 2017.
- [22] L. Wang, E. T. Chen, S. Liu et al., "Experimental study on the effect of inherent moisture on hard coal adsorption-desorption characteristics," *Adsorption*, vol. 23, no. 5, pp. 723–742, 2017.
- [23] Y. Wen, J. Liao, X. Liu, F. Wei, and L. Chang, "Removal behaviors of moisture in raw lignite and moisturized coal and their dewatering kinetics analysis," *Drying Technology*, vol. 35, no. 1, pp. 88–96, 2017.
- [24] Z. Zhang, "Structure and dynamics in brown coal matrix during moisture removal process by molecular dynamics simulation," *Molecular Physics*, vol. 109, no. 3, pp. 447–455, 2011.
- [25] J. Shaikh, A. Sharma, and R. Bhardwaj, "On comparison of the sharp-interface and diffuse-interface level set methods for 2D capillary or/and gravity induced flows," *Chemical Engineering Science*, vol. 176, no. 2, pp. 77–95, 2018.
- [26] Q. Q. Liu, Y. P. Cheng, W. Li, and W. Zhao, "Mathematical model of coupled gas flow and coal deformation process in low-permeability and first mined coal seam," *Chinese Journal of Rock Mechanics and Engineering*, vol. 34, no. 1, pp. 2749–2758, 2015.

- [27] C. J. Fan, S. Li, M. K. Luo, Z. Yang, H. Zhang, and S. Wang, "Deep CBM extraction numerical simulation based on hydraulic-mechanical-thermal coupled model," *Journal of China Coal Society*, vol. 41, no. 12, pp. 3076–3085, 2016.
- [28] L. D. Connell, M. Lu, and Z. Pan, "An analytical coal permeability model for tri-axial strain and stress conditions," *International Journal of Coal Geology*, vol. 84, no. 2, pp. 103–114, 2010.
- [29] L. D. Connell, "A new interpretation of the response of coal permeability to changes in pore pressure, stress and matrix shrinkage," *International Journal of Coal Geology*, vol. 162, no. 5, pp. 169–182, 2016.
- [30] J. Chen, J. W. Hopmans, and M. E. Grismer, "Parameter estimation of two-fluid capillary pressure–saturation and permeability functions," *Advances in Water Resources*, vol. 22, no. 5, pp. 479–493, 1999.
- [31] M. Yi, P. Guo, and L. Sun, "An experimental study on relative permeability curve for unsteady-state gas displacement by water," *Natural Gas Industry*, vol. 27, no. 10, pp. 92–94, 2007, http://xueshu.baidu.com/s?wd=paperuri%3A%281d1009acc62bded12bd3d6d1f6ed0ed4%29&filter=sc_long_sign&tn=SE_xueshsource_2kduw22v&sc_vurl=http%3A%2F%2Fkns.cnki.net%2FKCMS%2Fdetail%2Fdetail.aspx%3Ffilename%3Dtrqg200710031%26dbname%3DCJFD%26dbcode%3DCJFQ&ie=utf-8&sc_us=12331676811207054247.
- [32] Y. Gensterblum, A. Busch, and B. M. Krooss, "Molecular concept and experimental evidence of competitive adsorption of H₂O, CO₂ and CH₄ on organic material," *Fuel*, vol. 115, no. 4, pp. 581–588, 2014.
- [33] X.-Q. Liu, X. He, N. X. Qiu et al., "Molecular simulation of CH₄, CO₂, H₂O and N₂ molecules adsorption on heterogeneous surface models of coal," *Applied Surface Science*, vol. 389, no. 12, pp. 894–905, 2016.
- [34] J. Xiang, F. G. Zeng, H. Z. Liang, B. Li, and X. X. Song, "Molecular simulation of the CH₄/CO₂/H₂O adsorption onto the molecular structure of coal," *Science China Earth Sciences*, vol. 57, no. 8, pp. 1749–1759, 2014.
- [35] S. Yu, J. Bo, and L. Wu, "Molecular simulation of CH₄/CO₂/H₂O competitive adsorption on low rank coal vitrinite," *Physical Chemistry Chemical Physics*, vol. 19, no. 27, pp. 17773–17788, 2017.

Research Article

The Visual and Quantitative Study of the Microoccurrence of Irreducible Water at the Pore and Throat System in a Low-Permeability Sandstone Reservoir by Using Microcomputerized Tomography

Xiaoyu Gu,^{1,2} Chunsheng Pu ^{1,2}, Hai Huang,³ Nasir Khan,^{1,2} Jing Liu,^{1,2} Yanlong He,³ Cheng Jing,³ Feifei Huang,^{1,2} and Aojiang Qi³

¹School of Petroleum Engineering, China University of Petroleum (East China), Qingdao, Shandong 266555, China

²China National Key Laboratory for Heavy Oil, Qingdao, Shandong 266555, China

³School of Petroleum Engineering, Xi'an Shiyu University, Xi'an, Shanxi 710065, China

Correspondence should be addressed to Chunsheng Pu; chshpu_tx@126.com

Received 29 March 2018; Accepted 14 June 2018; Published 6 August 2018

Academic Editor: Xiangzhao Kong

Copyright © 2018 Xiaoyu Gu et al. This is an open access article distributed under the Creative Commons Attribution License, which permits unrestricted use, distribution, and reproduction in any medium, provided the original work is properly cited.

The microflow equipment monitored with micro X-ray computerized tomography (CT) is employed to investigate the microoccurrence of the irreducible water in a low-permeability sandstone core. By means of image segmentation and the three-dimensional (3D) image reconstruction technique, the visual microdistribution characteristics of irreducible water in two-dimensional (2D) slices and the 3D pore-throat system are quantitatively evaluated. Some interesting findings are listed as below. Firstly, due to the variant micro geometric structures of the pore-throat systems, specific core slices showed significantly different irreducible water saturation even though these slices had same areal porosity. Secondly, due to the influence of capillary trapping and the existence of oil-wetting clay (main chlorite), the irreducible water saturation in the throat system (64%) is much larger than that in the pore system (36%). Furthermore, the wetting phase (irreducible water) did not spread all over the surface of the pore-throat network which caused a much more complicated oil-water two-phase interface. Thirdly, in micro scale, the main irreducible water occurrence mode in the pore system is much different from that in the throat system. In the pore system, the irreducible water principally existed in the corner of the pores which are linked through a water film. While in the throat system, the irreducible water occurrence is dominated by the water film. However, 25.5% of the throats are blocked by the irreducible water which cut off the crude oil drainage channels.

1. Introduction

With the increasing worldwide demand for crude oil, low-permeability reservoirs are considered to overcome the energy deficit in developing countries [1, 2]. Theory and practice have proved that water flooding is the most economical technology to replenish formation energy and enhance oil recovery (EOR) in low-permeability reservoirs [3]. During the water flooding, many geological factors determine the efficiency of water drives, such as rock permeability, pore-throat structure, irreducible water saturation, and crude oil viscosity [4–6]. Among these factors, the microdistribution

of irreducible water confined in the pore-throat system is one of the critical factors affecting the ultimate recovery [7]. Because of pore geometry structure, the microdistribution of irreducible water in porous media is very complicated. [8]. According to the results of Kewen Li and Roland N. Horne, the irreducible water saturation has a considerable effect on the spontaneous imbibition recovery. Higher irreducible water saturation is always correlated to the lower recovery tendency in low permeable rock [9]. This phenomenon is also verified by Wang et al. [10]. Therefore, how to obtain the quantitative visualized information about the irreducible water microdistribution is necessary to

investigate the mechanisms of irreducible water on micro-flow behaviors in low permeable porous media. For this purpose, specific techniques are currently employed which will be discussed in the below paragraphs.

The two-dimensional (2D) etching glass model and core displacement monitored by nuclear magnetic resonance (NMR) are the main qualitative and quantitative approaches, respectively, to look into the fluid occurrence and its distribution in porous media [11–14]. The principal advantage of the former experimental method is to visualize the water displacement. Specifically, the wettability difference between the natural porous surface and modeled interface poorly reflects the real microdisplacement in natural core samples. Also, the 2D etching glass model cannot be perfectly related to the natural 3D core sample. The above discrepancies have constrained the application of the qualitative approach. As far as core displacement based on NMR is concerned, it is a currently reliable method to determine the distribution of fluids in porous media [15–19]. However, 3D visualization of the natural core sample could not be perfectly developed. As a result, it is essential to look for such a novel experimental method which can perfectly encompass the quantitative microdistribution of irreducible water in 3D porous media along with the acquisition of high-resolution visualizations.

The recent improvement in CT scanning resolution from micron to nanoscale makes it possible for the researchers to investigate pore scale and contained fluid in the low permeable core samples [20–23]. Due to high-precision 3D visualization and quantitative characterization, this technology overcomes the shortcomings of conventional experiment methods [24]. Nevertheless, owing to a limitation in the microflow device, CT scanning technology was frequently applied to analyze the micro pore-throat structure in dry core samples [25–27]. In contrast, this technology was seldom used in research of fluid microdistribution characteristics in low permeable sandstone. The considerable research was conducted to analyze water or gas flooding to investigate the evolution law of residual oil in high-permeability core samples using the CT scanning technique [28–30]. However, to the best of our knowledge, scarce literature is available that has perfectly visualized and quantified the microoccurrence of irreducible water in the pore and throat system [31]. Besides, owing to the huge difference between pore and throat geometries, particularly in low-permeability porous media, the microoccurrence of irreducible water is very complicated. Consequently, it led to lack of in-depth understanding of the microinfluence mechanisms of irreducible water on oil-water two-phase flow behaviors.

The key aim of this study is to investigate the irreducible water microoccurrence which was confined in the pore and throat system in low permeable sandstone, taking the Chang2 low-permeability reservoir sandstone of Ordos Basin in northwest China as a case study. Afterwards, the micro-flow equipment monitored by micro X-ray computerized tomography (CT) is employed to investigate the microoccurrence of the irreducible water in the pore-throat system. Subsequently, the visible information of the pore-throat structure and irreducible water in the pore-throat network is acquired with 1.5 microns per pixel. Besides, the microdistribution

characteristics of irreducible water in two-dimensional (2D) core slices and 3D pore-throat network are also quantitatively evaluated using the image segmentation and three-dimensional (3D) image reconstruction technique. As a consequence, our work would provide reliable experimental evidence for recognizing the micro hydrodynamic mechanisms which play a pivotal role in enhancing water-flooding displacement effectiveness.

2. Experiments

2.1. Rock Sample and Fluids. According to the China National Petroleum Corporation's reservoir quality grading standards (SY/T6285-2011), the Triassic Yanchang Chang2 formation in Ordos Basin is declared as a typical low-porosity and low-permeability reservoir [32]. The oil and core samples were obtained from the Chang2 reservoir in Ordos Basin, northwest China. The parameters of the fluid and rock samples used in this experiment are as follows. Simulated oil had 6.4 mPa·s dynamic viscosity at 25°C temperature. Simulated formation brine was prepared by dissolving potassium iodide (KI). The salinity of formation water is 70,000–90,000 mg/L in the given formation. Therefore, 8 wt. % (KI) brine solution was injected for the reason to exactly simulate the formation water. In this way, the density difference between oil and brine (KI) was enhanced in comparison to distilled water. Furthermore, it could help to differentiate between the oil and water phase in the CT image. Consequently, contained fluids, such as water and oil, could easily be distinguished by image segmentation step. The sandstone core sample that was used in this study has a 5 mm diameter and 10 mm length as shown in Figure 1. The gas permeability and porosity are $4.25 \times 10^{-3} \mu\text{m}^2$ and 15.3%, respectively.

2.2. Experimental Apparatus. A micron CT scanning equipment and microdisplacement device are shown in Figure 2. The experimental parameters of the microdisplacement system and CT scanning are all controlled by a computer. Other instruments used in this research goal are a HAAKE RS600 Rheometer (Thermo Scientific, Germany), a DV-III Brookfield viscometer (Brookfield Company, America), and a 510 model micrometer CT scanner (Zeiss, Germany).

2.3. Experimental Procedure. Before acquiring a high-resolution image, the CT scanning equipment is configured with 50 KeV operational voltage, 1.5 s exposure time span, and 1.5 microns per pixel scanning precision. Besides, the slice thickness is 1.5 μm which contains 1024×1024 pixels. These parameters can meet the requirement of pore size recognition above the micron level. The exact experimental procedure is as follows:

- (1) The system consisting of a CT scanner and flow cell system is assembled as shown in Figure 2. After that, a selected core sample is fixed in the core holder.
- (2) Vacuum (0.1 MPa) the core sample under a confining pressure of 0.1 MPa for 10 hours. Scan the core by CT to obtain the characteristics of pore-throat structures (pore volume as well) of the core.

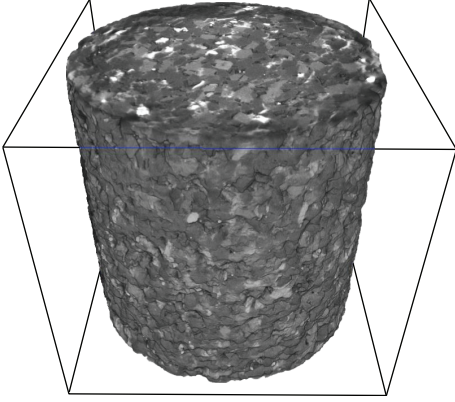


FIGURE 1: The CT scanning image of the core sample.

- (3) Close the vacuum valve. Then, saturate the core with brine (5 PV) at a low speed of 0.002 mL/min. The confining pressure was held at least 0.5 MPa higher than the injection pressure. Then the sample was kept for 72 hours.
- (4) Saturate the core sample with oil (5 PV) by constant flowrate of 0.002 mL/min at room temperature (25°C). In this way, the oil was driven through the core to generate the irreducible water in the core. After keeping the core sample at room temperature (25°C) for 72 hours, CT scanning is conducted to obtain the microdistribution of the irreducible water contained in the pore-throat network.

3. Image Processing and Analysis

3.1. Image Segmentation. Image segmentation is the fundamental part for the distinction of rock particles, the oil phase, and the water phase in the porous media. Median filtration method based on a nonlinear signal processing was used to minimize the noise in the scanning images. More specifically, the filtering mechanism is detailed in Andrew's dissertation [33]. The images before and after median filtration are shown in Figure 3.

By following the abovementioned procedure, the core sample would contain three kinds of substances, such as rock particles, water, and oil. It is visualized on the basis of different X-ray propagations in the abovementioned phases which led to the variant scanning gray peak of each phase. The corresponding peak intensity for rock particles, water, and oil is 18,700, 10,400, and 11,700, respectively. Therefore, it could be distinguished from image segmentation. As a result, the acquired image segmentation outcomes are shown in Figure 4.

3.2. Image 3D Reconstruction. Two-dimensional image segmentation of core sample slices was obtained. Then, the distribution of pore-throat, oil, and water in all 2D slice images was acquired. In the next step, the ORS 3D software was used to add all the 2D images to become a 3D dataset. The 3D reconstruction principle is based on the marching cube algorithm [34]. After that, the visualized 3D distribution of the

pore-throat, oil, and water in the core sample was obtained as shown in Figure 5 and Table 1.

3.3. Quantitative Analysis Method

3.3.1. Calculation of Surface Area and Volume of the Data Cube. Pixels are the basic unit of the building dataset, and these pixel dots of irreducible water and rock particles were obtained after image segmentation. In the next step, the characteristic parameters, for instance, the surface area and the volume of irreducible water and the pore-throat in the core samples, can be calculated using the following equations.

$$V_i = N_v \times V_p, \quad (1)$$

where V_i is the volume of pixel dots (μm^3), N_v is the total number of the pixel dots of the same phase (dimensionless), and V_p is the volume of a single pixel dot which is $3.375 \mu\text{m}^3$ in this experiment.

$$S_i = N_s \times S_p, \quad (2)$$

where S_i is the surface area of a given phase (μm^2), N_s is the number of pixel dots of a given phase (dimensionless), and S_p is the surface area of a single pixel dot which is $9.0 \mu\text{m}^2$ in this experiment.

3.3.2. Microoccurrence of Irreducible Water in the Pore-Throat Network. Due to the micro-occurrence of irreducible water in pore-throat network is very complicated. Hence, different parameters, such as the shape factor and the irreducible water saturation in a given single pore-throat, were used to categorize the complex heterogeneous structures of the given irreducible water block.

$$G_i = \frac{6\sqrt{\pi}V_w}{S_w^{1.5}}, \quad (3)$$

where G_i is the shape factor of the irreducible water block (dimensionless), V_w is the volume (μm^3), and S_w is the surface area of the irreducible water block (μm^2). The shape factor represents the degree of sphericity of an object. In other terms, the lower the G_i value, the more would be the shape irregularity of the given irreducible water blocks and, subsequently, the higher would be the surface roughness. In contrast, the greater the G_i value, the more smooth the surface would be and the more likely the shape would be spherical.

Saturation of irreducible water (S_{Swi}') shows the amount of irreducible water in a given pore or throat. This parameter can be obtained using (4). In general, the higher the irreducible water saturation (S_{Swi}'), the lower would be the flowability in a given channel.

$$S_{\text{Swi}}' = \frac{V_w}{V_{\text{p-t}}} \times 100\%, \quad (4)$$

where S_{Swi}' is the saturation of irreducible water in either the pore or the throat (%), V_w is the irreducible water volume confined in a given pore or throat (μm^3), and $V_{\text{p-t}}$ is the pore or throat volume (μm^3).

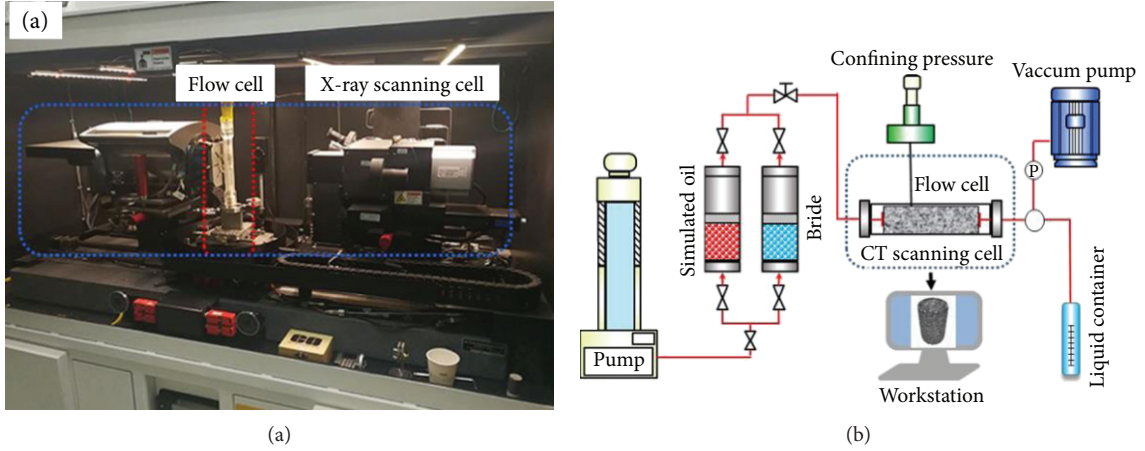


FIGURE 2: (a) The image of a microflow equipment monitored by micro X-ray computerized tomography. (b) The schematic illustration of the microflow equipment. Note: the pumps and valve arrangement is used to control fluid flow to the flow cell within the CT enclosure.

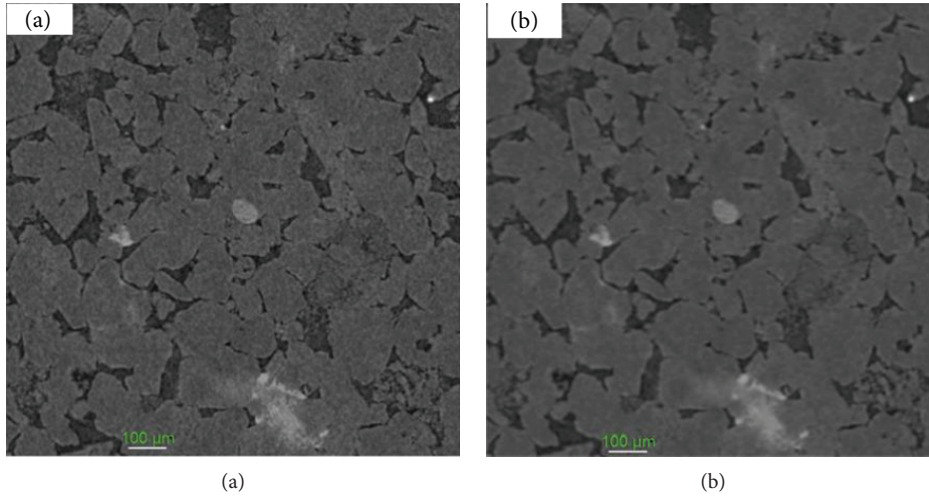


FIGURE 3: Images filtration (a) before and (b) after.

4. Results and Discussion

This section of the current study mainly emphasizes on three aspects: irreducible water distribution characteristics in 500 2D slices, 3D pore-throat network, and microoccurrence modes in the pore and throat system.

4.1. Distribution Characteristics of Irreducible Water in 2D Slices. In this section, irreducible water distribution and its exact content in 500 2D core slices are evaluated by areal porosity and irreducible water that is contained in the pore-throat space (after image segmentation). Meanwhile, the irreducible water saturation of each slice is mathematically calculated using (5), where the areal porosity and irreducible water porosity can be figured out in Figure 6(a).

$$S_{swi} = \frac{\phi_p}{\phi_{swi}} \times 100\%, \quad (5)$$

where S_{swi} is the irreducible water saturation for a given 2D scanning slice (%), ϕ_p is the areal porosity of a 2D slice (%),

and ϕ_{swi} is the areal porosity of irreducible water in a given 2D slice (%).

Irreducible water saturation distribution of all 2D slices is explicitly represented in Figure 6(b) that illustrates the irreducible water saturation alteration in the flow direction. For the evaluated irreducible water saturation in all 2D core slices, the maximum irreducible water saturation is measured to be 50.69% (slice number: 226), while the minimum irreducible water saturation remains at 26.59% (slice number: 343). At the same time, the average value of irreducible water saturation is 36.94%. Additionally, three typical areas along with the alteration of the irreducible water saturation in the flow direction, including the peak, medium, and low regions are identified in Figure 6(b). The average saturation is up to 48.08% in the high-value zone in the continuous region (slice numbers: 213–232). In the peak-value area, average irreducible water saturation is 36.42% in the continuous part (slice numbers: 152–171). As far as the low-value part is concerned, average irreducible water saturation is 29.04% in the continuous part (slice numbers: 333–352).

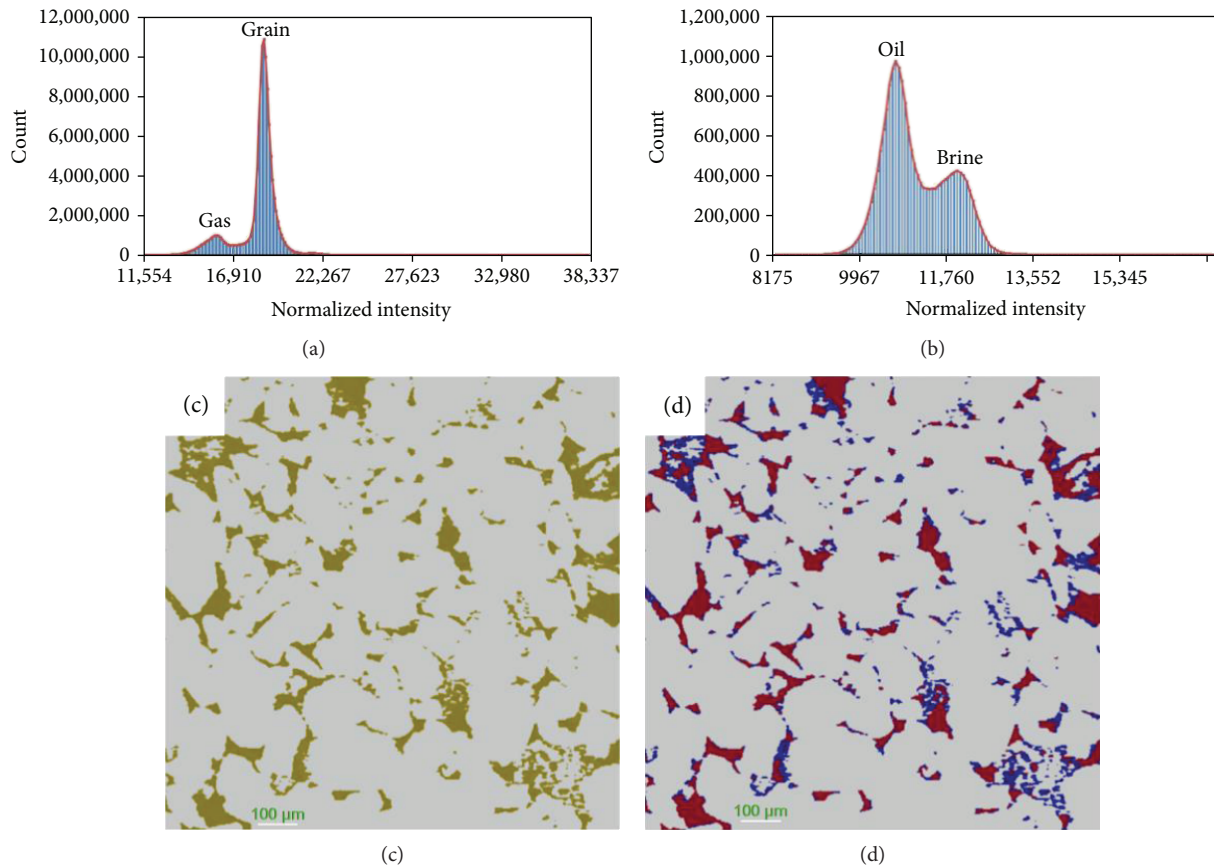


FIGURE 4: Images segmentation results: (a) intensity of gas and grain; (b) intensity of oil and brine; (c) pore-throat network and rock matrix; (d) oil and irreducible water. Note: yellow = pore-throat; gray = rock particles; blue = irreducible water; red = oil.

Figure 6(c) shows the frequency histogram of irreducible water saturation distribution of all slices in the core sample. It indicates that the law of irreducible water saturation (core slices) belongs to a normal distribution, where the peak-value region of irreducible water saturation ranges from 35% to 40%, while the irreducible water saturation value in either the high-value part (over 40%) or the low-value region (below 30%) shares lesser proportions with the corresponding frequency value of 6.8% and 5.6%.

A reasonable relationship between irreducible water saturation and areal porosity can be shown in Figure 6(d). It indicates that (i) an inverse relation is observed between irreducible water saturation and porosity. Moreover, the line became steeper at higher areal porosity. (ii) A significant difference in irreducible water saturation existed among the slices even at the same areal porosity.

To investigate the reason for the phenomenon of the same (similar) areal porosity with a significant difference in 2D slice irreducible water saturation, three typical slices were selected as shown in Figure 7.

Despite the same porosity of the three slices (16.1%~16.4%), the corresponding irreducible water saturation is measured to be 29.57%, 36.37%, and 50.69% as shown in Figure 7. Due to the capillary force, rock surface wettability, and pore geometry, the displacing oil mainly existed in the large-size pore and connected pore-throat. The variant

irreducible water saturation in the case of identical porosity of three slices is due to the difference in pore-throat geometry. In the case of the higher pore radius, fewer pore corners, and lesser narrow throats, lower irreducible water saturation would exist in 2D slices. The distribution characteristics of 2D-slice irreducible water saturation are shown in Figure 8. It can be inferred that the irreducible water is mainly trapped by capillary force. In addition, the in-depth analysis helps to classify irreducible water into three main types:

- (i) Water trapped in pendular rings in complex angular pore geometry beside surface roughness (stationary fluid part).
- (ii) Water trapped in dead ends of the pore-network (pore corner).
- (iii) Water film adherence in wider throats, while narrow throats filled with irreducible water.

4.2. *Distribution Characteristics of Irreducible Water in the 3D Pore-Throat Network.* The pore-throat network governs the liquid flow in low-permeability porous media. However, distinct distribution characteristics of irreducible water exist in the pore-throat network. The pore and throat system recognition was based on the 3D reconstruction technology. The maximal inscribed sphere algorithm was used to identify the

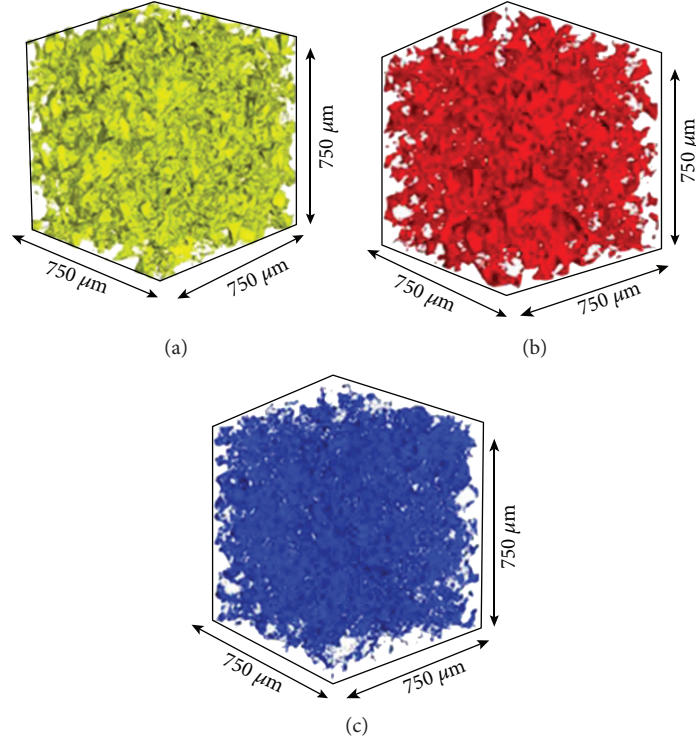


FIGURE 5: 3D reconstruction results. Note: (a) distribution of the pore-throat system in the core sample; (b) distribution of irreducible water; (c) distribution of simulated oil.

TABLE 1: Segmentation result of the core sample containing irreducible water.

Pore and throat (volume/ μm^3)	Irreducible water (volume/ μm^3)	Oil volume (μm^3)	Irreducible water saturation (%)
5.80×10^7	2.14×10^7	3.67×10^7	36.94

certain throat part in varying diameter channels. Along with the connected channel, the shortest distance portion was categorized as the throat. While the connected spherical-shaped body is recognized as the pore. The principle of pore and throat recognition is shown in Figure 9. The details of pore and throat classification methods and principles are reported in Denney and Yang et al. [35, 36]. The information of overall 3D distribution characteristics of irreducible water is extracted by identification of 3D coordinates of the irreducible water pixels existing in the pore and throat system as shown in Figure 10.

According to the 3D reconstruction results based on CT scanning, the volumes of the pore system and throat system are determined to be $5.63 \times 10^7 \mu\text{m}^3$ and $1.69 \times 10^6 \mu\text{m}^3$, respectively. Moreover, the radius distribution, in either case, followed a normal distribution (Figure 10), where the peak-value regions of the pore and throat system are found in the 25–30 μm and 2–2.5 μm ranges, respectively (Figure 11). This fundamental information provides a better platform for less proportion of irreducible water saturation in the pore system than the throat system (Figure 12). The exact irreducible

water saturation proportions are figured out to be (36%) in the pore system which is far less than in the throat system (64%) (Figure 13). This low percentage of irreducible water saturation in the pore system could be attributed to the difference in radius. It is a well-understood fact that permeability of a porous matrix is chiefly relying on the throat radius. However, irreducible water occupied the throat system either in the form of water film or being completely filled with it. Consequently, the effective throat radius would further be decreased in the flooding fluid. This obtained knowledge provided a rationalized answer to the high water-flooding pressure and low hydrocarbon recovery in a low-permeability reservoir. Characteristic parameters of irreducible water, including numbers and volume that exist in the pore and throat system with different sizes, are quantitatively studied in the upcoming part of the current section. In this connection, distribution of frequency number and irreducible water volume in different sizes of the pore and throat system is determined by following the same calculation method which is discussed in Section 3.3. As a consequence, the results are elucidated in Figures 14 and 15.

Figure 14 relates frequency number and volume number to irreducible water saturation in the throat system. It is shown that both characteristic parameters sharply decrease upon an increase in irreducible water saturation in the range of volume less than the average throat volume. Furthermore, this phenomenon can further be interpreted by throat radius determination. As it is widely accepted that the throat volume is proportional to the throat radius which subsequently provides a relatively larger flow area. Consequently, the

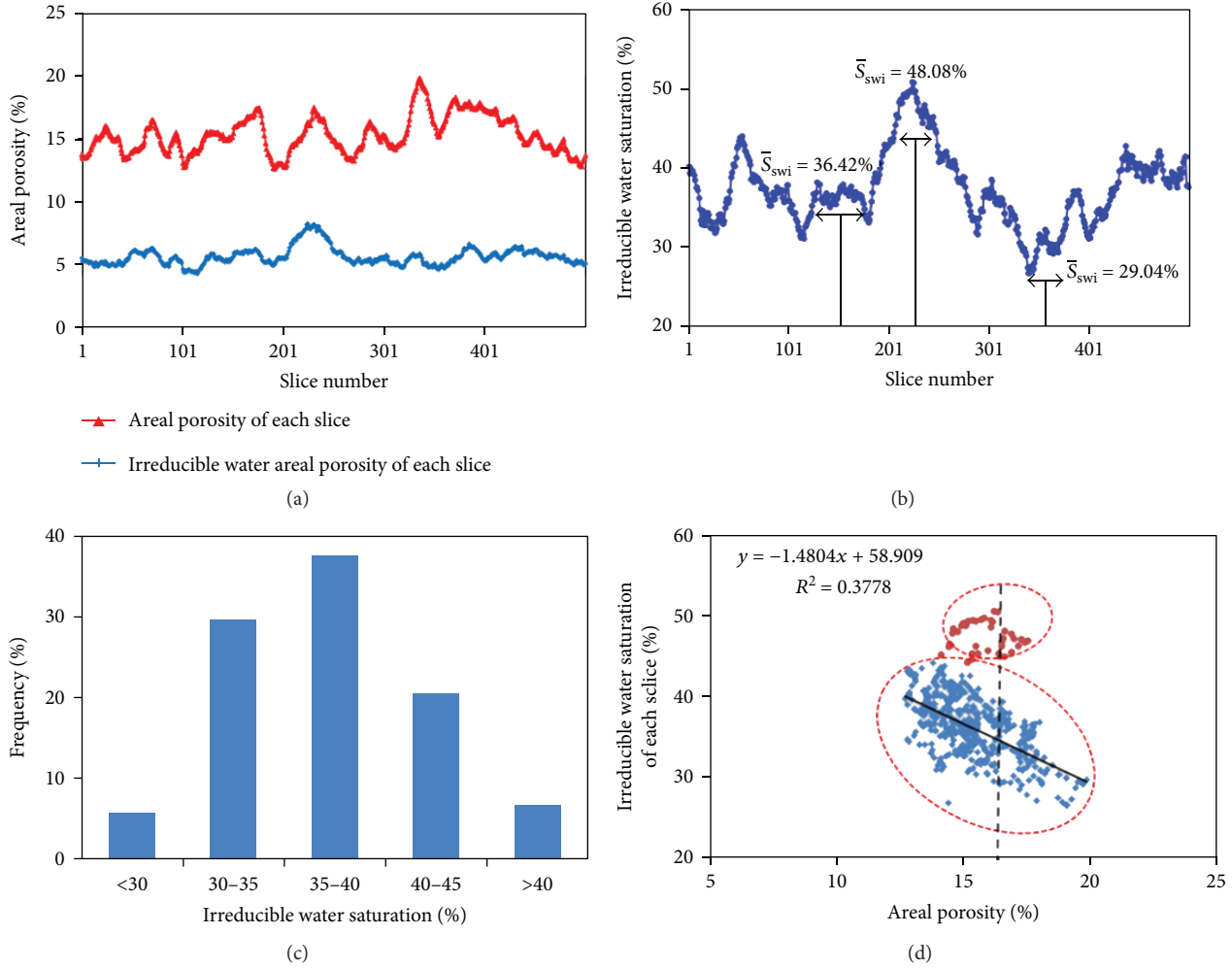


FIGURE 6: 2D distribution characteristics of irreducible water in core slices: (a) distribution of areal porosity and irreducible water porosity in 2D core slices; (b) distribution of irreducible water saturation of a 2D slice; (c) frequency histogram of irreducible water distribution in the core sample; (d) relationship between areal porosity and irreducible water saturation.

exerted capillary force in a comparatively larger flow area would decrease, and it further resulted in the reduction in the throat’s capability to trap irreducible water during the process of oil displacement.

Figure 15 shows that the distribution frequency of the number of irreducible water in the pore system and throat system followed a similar trend, but the volume of irreducible water in the pore system and throat system varies slightly (Figures 14(a) and 15(a)). We can see that with the increase in the number of irreducible water blocks, the trend of the volume frequency distribution of irreducible water with different sizes first descended and then increased. This dramatic turning point (Figure 15(a)) in the trend happened when the volume of irreducible water was over $10^5 \mu\text{m}^3$. This obscure behaviour is explained as; since there are 13 irreducible water blocks in pore system which has volume over $10^5 \mu\text{m}^3$, these 13 irreducible water blocks were extracted. On this basis, the 13 pore spaces were retrieved that contained the corresponding 13 irreducible water blocks. In next step, S_{Swi}^i was calculated. Consequently, results showed that S_{Swi}^i fell in the

80–98% range. It can be inferred that this dramatic turning is due to poor sweeping of irreducible water during oil displacement.

4.3. Microoccurrence of Irreducible Water in the Pore and Throat System. The 3D structure of irreducible water distribution in pore space is complicated due to the combined effect of porous media heterogeneity and the oil-water displacement process. Meanwhile, by 3D visualization, the irreducible water microoccurrence in pore and throat systems is categorized into each mode (Figures 16 and 17), which are further explained below:

(a) Irreducible water in the pore system:

- (i) Conglobation shape: this kind of pores has comparatively small room and has a complicated structure. Moreover, they are produced due to dissolution at different stages and are referred to secondary pores. Referring to irreducible

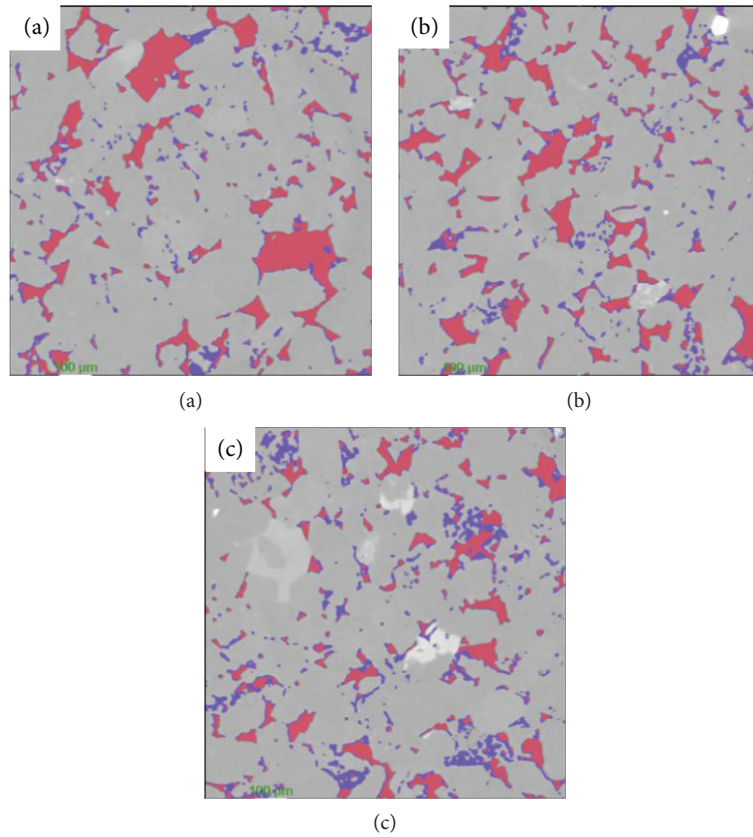


FIGURE 7: Distribution of irreducible water saturation of a given slice with the same areal porosity (void space): (a) $S_{swi} = 29.57\%$ (slice number: 362); (b) $S_{swi} = 36.37\%$ (slice number: 425); (c) $S_{swi} = 50.69\%$ (slice number: 226). Note: gray = rock matrix; white = pyrite; blue = irreducible water; red = oil.

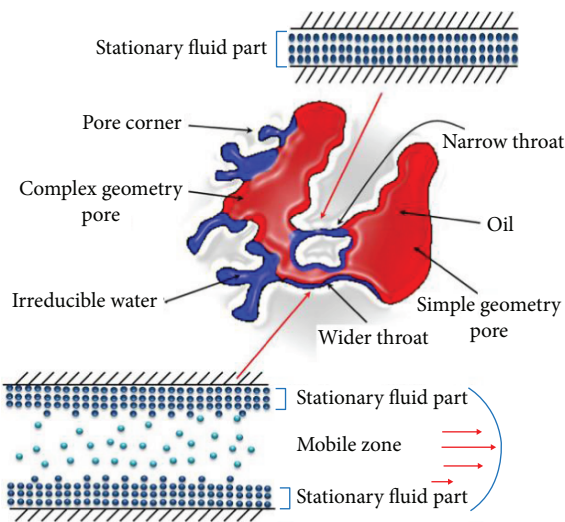


FIGURE 8: Schematic of irreducible water distribution in the pore-throat system.

water presence, it occupied a small volume and its flow is governed by the bottle-necking structure at certain positions as shown in (Figure 16(a)).

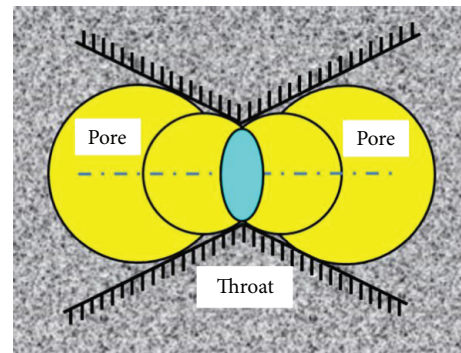


FIGURE 9: Pore and throat recognition principle.

- (ii) Cluster shape: the cluster shape exists in a primary pore with the large compartment. However, due to surface roughness and complex pore geometry, the irreducible water present in the corner is linked to the adhered water film at other parts of the pore space (Figure 16(b)). This shape is more complicated than the water film but simpler than the conglomeration shape.
- (iii) Water film: this type of irreducible water appears as a water film which sticks to the

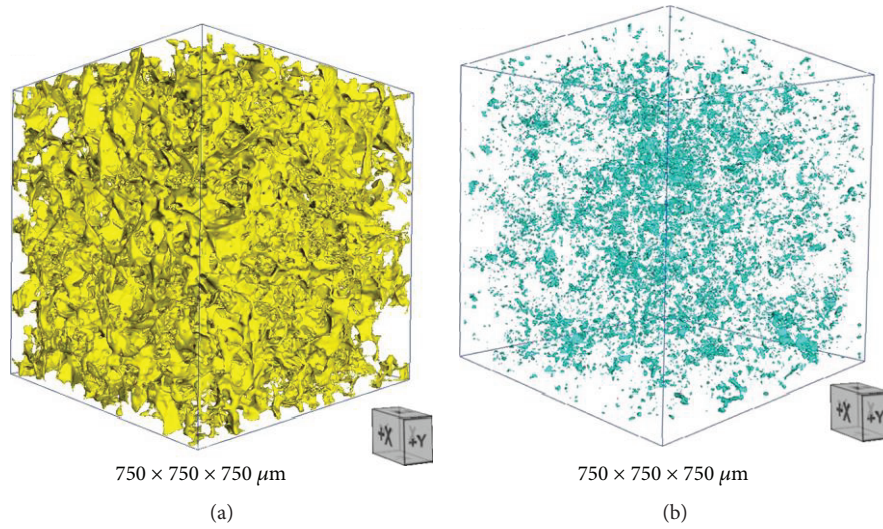


FIGURE 10: 3D structure: (a) pore system; (b) throat system. Note: length × width × height = 750 × 750 × 750 μm .

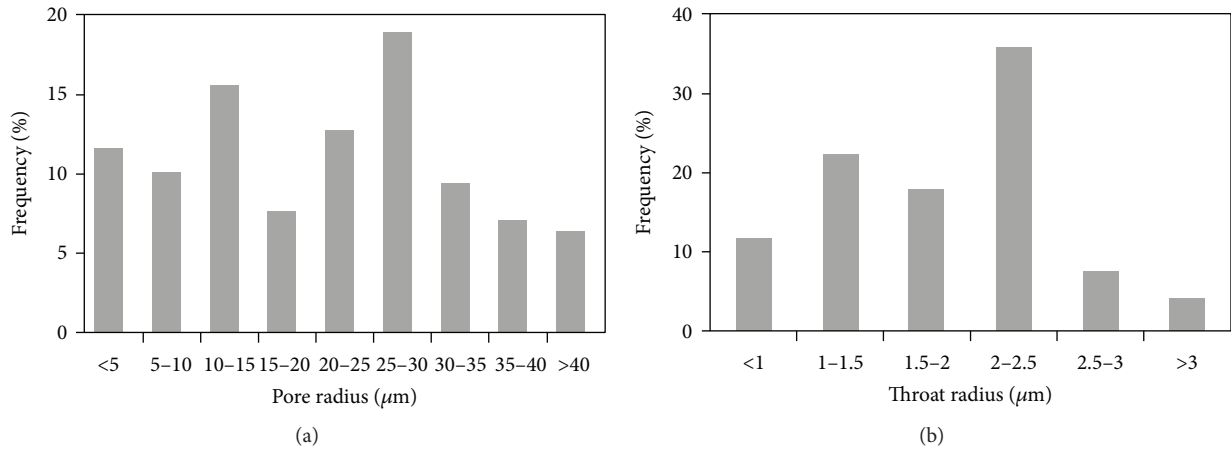


FIGURE 11: (a) Pore; (b) throat radius distribution of the core sample.

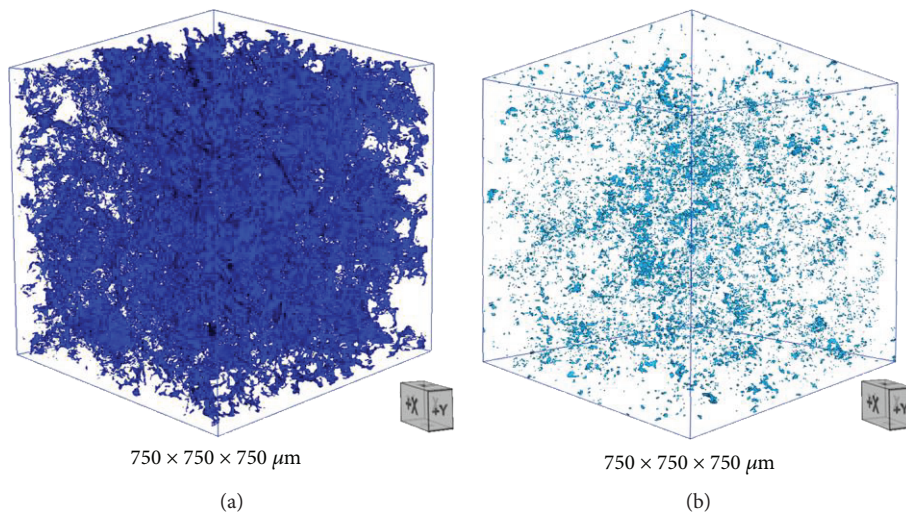


FIGURE 12: 3D distribution of irreducible water: (a) pore system; (b) throat system.

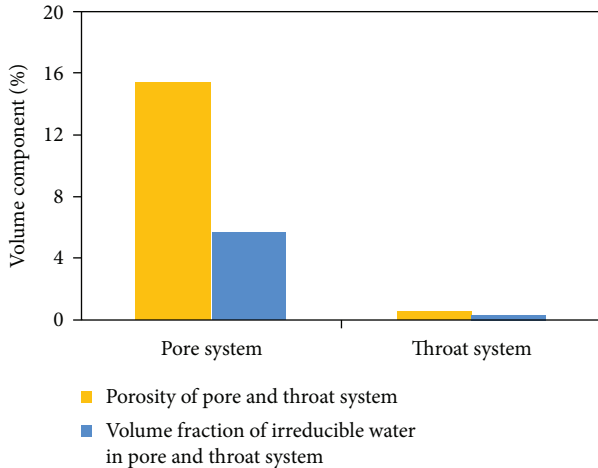


FIGURE 13: Histogram of irreducible water void space in the pore and throat system.

relatively smooth surface of regularly shaped pores (Figure 16(c)). However, it does not occupy all the rock surfaces.

(b) Irreducible water in the throat system:

- (i) Curved piece-necking shape: this kind of throat structure featured with bottle-necking and curved segments besides microeffective seepage radius and large surface area. Consequently, it almost helps to fill the compartment entirely (Figure 17(a)).
- (ii) Slug-filling shape: irreducible water locates precisely at the neck in the slug-filling shape. As a result, it blocks the path for the displacing oil. At the same time, it breaks the continuous oil phase which leads to high water drive pressure. However, upon entering into the wide segment of the same throat, the capillary force suddenly disappeared which tends to cease the spontaneous imbibition phenomenon (Figure 17(b)).
- (iii) Water-film shape: we deal with that kind of irreducible shape, where it sticks to the surface throat in the form of a film, the so-called water film. Meanwhile, it reduced the effective radius for seepage. The channel radius and its complex geometry, the shape of irreducible water along with surface polarity of the pore-throat, are the controlling factors in the 3D distribution of irreducible water. Irreducible water sticks to the surface of the throat as the shape of the water film. Subsequently, the small seepage space is becoming much narrower (Figure 16(c)).

Figures 16(b), 16(c), and 17(c) show that the wetting phase (irreducible water) did not spread all over the surface. It is considered as the “mixed” wetting characteristics of the rock surface. Since the sandstone core sample is water-wetting in nature. But due to the presence of certain clay, for

instance, chlorite, oil may wet certain parts of the entire surface. XRD of the core sample has been conducted which showed that chlorite content contributed around 17.5% of the core sample as shown in Table 2. In a nutshell, the oil-water interface in natural sandstone porous media is complex due to the influence of capillary trapping and the existence of oil-wetting clay. This phenomenon is in agreement with Trantham and Clampitt and Feng et al. [37, 38].

Irreducible water in the pore and throat system can be studied by 3D visualization technique. In this context, irreducible water distribution can be classified according to specific essential parameters, such as shape factors and irreducible water saturation. The standard classification is illustrated in Table 3.

Figure 18(a) shows the irreducible water frequency proportions in three kinds of irreducible water microoccurrence. In detail, the respective proportions in conglomeration shape, cluster shape, and water film shape are 14.2%, 68.4%, and 17.4%, respectively. Figure 18(b) depicts the volume frequency of irreducible water microoccurrence in the throat system which is the curved piece-necking shape (16.9%), slug-filling shape (8.6%), and water-film shape (74.5%). Therefore, the main irreducible water microoccurrence in pores and throats is in cluster and water-film shapes.

At the same time, from the results of the irreducible water microoccurrence, the water-film shape irreducible water is found to be unflowable in the pore-throat network. It is mainly attributed to the attractive force between the water film and the rock surface. As far as the other two kinds of irreducible water patterns, for instance, conglomeration shape and cluster shape, are concerned, irreducible water should be confined by geological structure. It should be noted that these latter types of irreducible water could be fluidized using advanced technology, such as hydraulic fracturing.

Compared with irreducible water contained in the pore system, the microoccurrence of irreducible water in the throat system has severely influenced the oil-water two-phase flow behavior. In the process of spontaneous imbibition, due to the capillary force, water is imbibed along narrow channels and crude oil is driven out from the pores through a comparatively larger size channel. As the saturation of irreducible water in the throat system is much higher than that in the pore system, the amount of imbibed water in the throat system will significantly be reduced. Additionally, some of the channels for crude oil are plugged due to the presence of irreducible slug water (curved piece-necking and slug-filling) in the throat system. Therefore, an inverse correlation between the saturation of irreducible water and spontaneous imbibition recovery could be concluded from this study. Last but not least, the role of lower rock permeability always linked with higher irreducible water saturation could also be explained in the above micromechanism.

5. Conclusions

- (1) The micro geometric structures of the pore-throat systems have a significant influence on the microoccurrence of irreducible water in the low-permeability

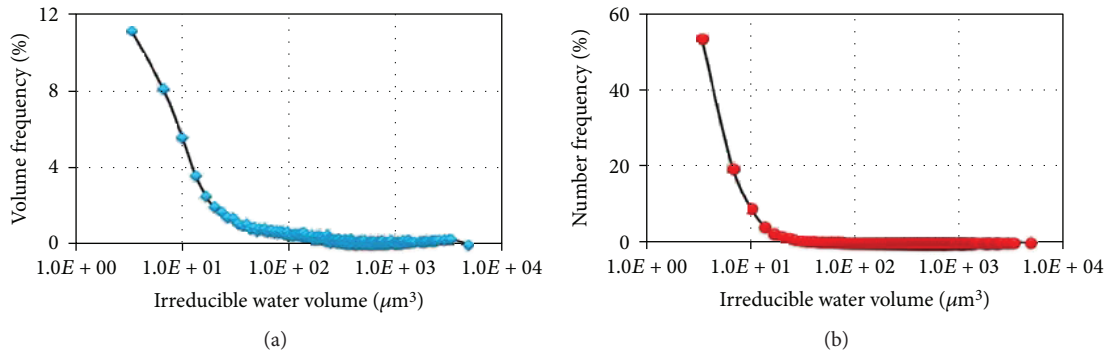


FIGURE 14: (a) Volume; (b) frequency number distribution of irreducible water blocks with different sizes in the throat system.

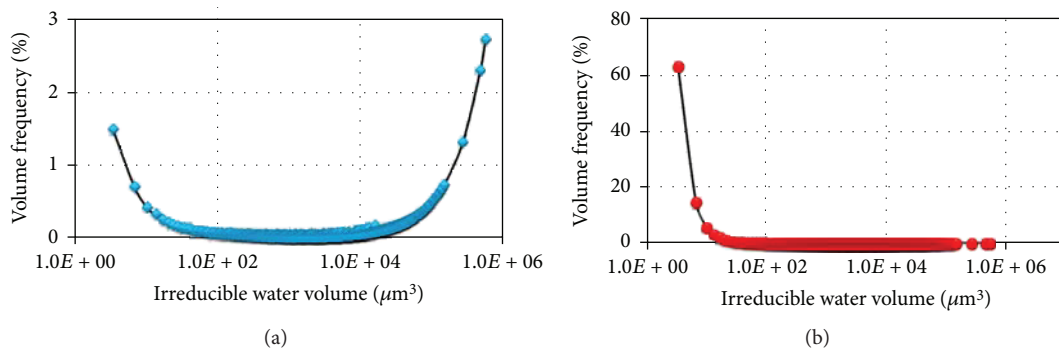


FIGURE 15: (a) Volume; (b) frequency number distribution of irreducible water blocks with different sizes in the pore system.

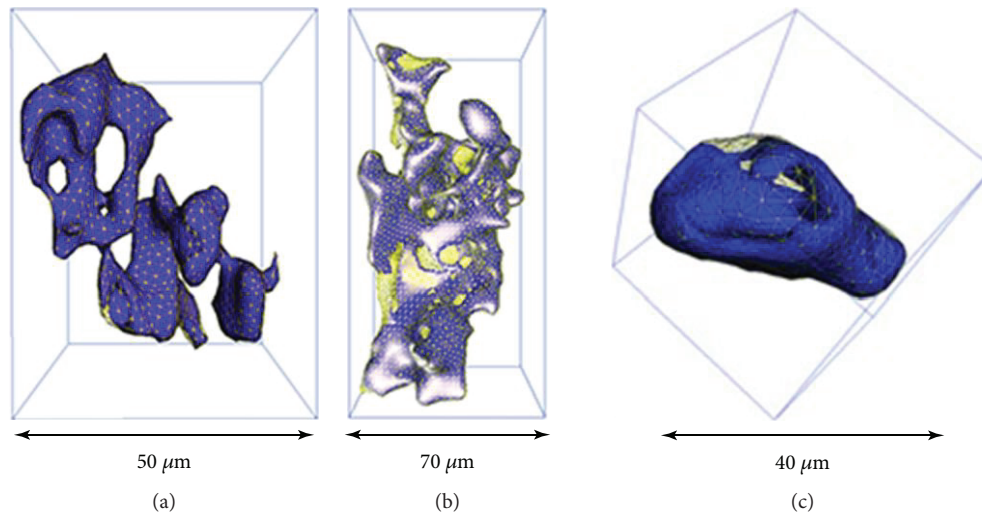


FIGURE 16: Different modes of irreducible water microoccurrence in the pore system: (a) conglobation pattern (ineffective oil reservoir space); (b) cluster pattern (partially effective oil reservoir space); (c) water-film pattern (effective oil reservoir space). Note: the yellow area represents a given pore or throat surface and the blue area represents irreducible water.

sandstone core sample. Certain core slices showed significantly different irreducible water saturation (29.57%–50.69%) even though these slices had the same areal porosity.

- (2) Due to the influence of capillary trapping and the existence of oil-wetting clay, the irreducible water saturation in the throat system (64%) is much larger

than that in the pore system (36%). Furthermore, the wetting phase (irreducible water) did not spread all over the surface of the pore-throat network. Subsequently, oil-water two-phase interface becomes much more complicated.

- (3) In the micro scale, the main irreducible water occurrence in the pore system is much different from that

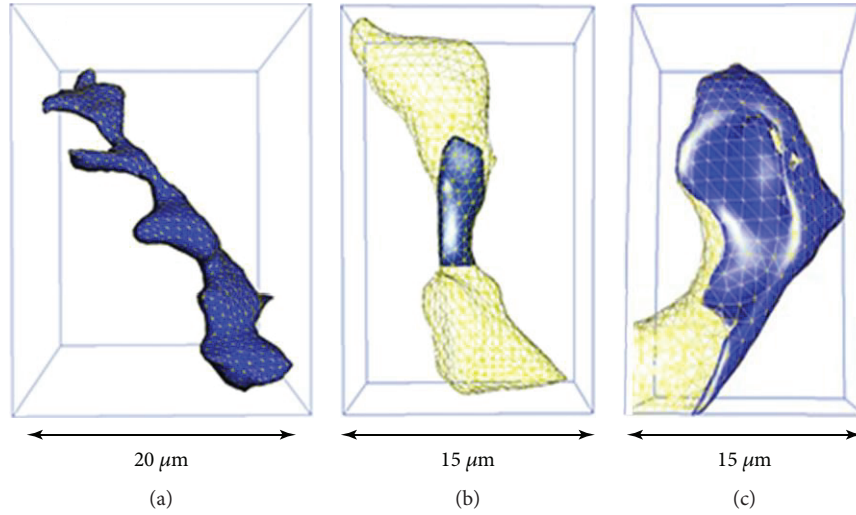


FIGURE 17: Different modes of irreducible water microoccurrence in the throat system: (a) curved piece-necking pattern (complete blockage, ineffective percolation channel); (b) slug-filling (partially blockage, ineffective percolation channel); (c) water-film pattern (partial blockage, effective percolation channel). Note: the yellow area represents a given pore or throat surface and the blue area represents irreducible water.

TABLE 2: XRD results of the core sample.

Clay minerals	Quartz	Plagioclase	Potash feldspar	Calcite	Illite	Chlorite
Wt. %	28.9	34.5	17.3	0.3	1.5	17.5

TABLE 3: Classification of microcharacteristics of irreducible water in the pore and throat system.

Unit	Irreducible water patterns	Shape factor ranges	Range of saturation of irreducible water in a single pore or throat
Pore system	Conglobation	$G < 0.1$	$90 < S'_{Swi} < 100$
	Cluster	$0.1 < G < 0.2$	$30 < S'_{Swi} < 90$
	Water film	$0.2 < G < 0.4$	$10 < S'_{Swi} < 30$
Throat system	Curved piece-necking	$G < 0.2$	$90 < S'_{Swi} < 100$
	Slug-filling	$0.4 < G < 0.7$	$30 < S'_{Swi} < 90$
	Water film	$0.2 < G < 0.4$	$10 < S'_{Swi} < 30$

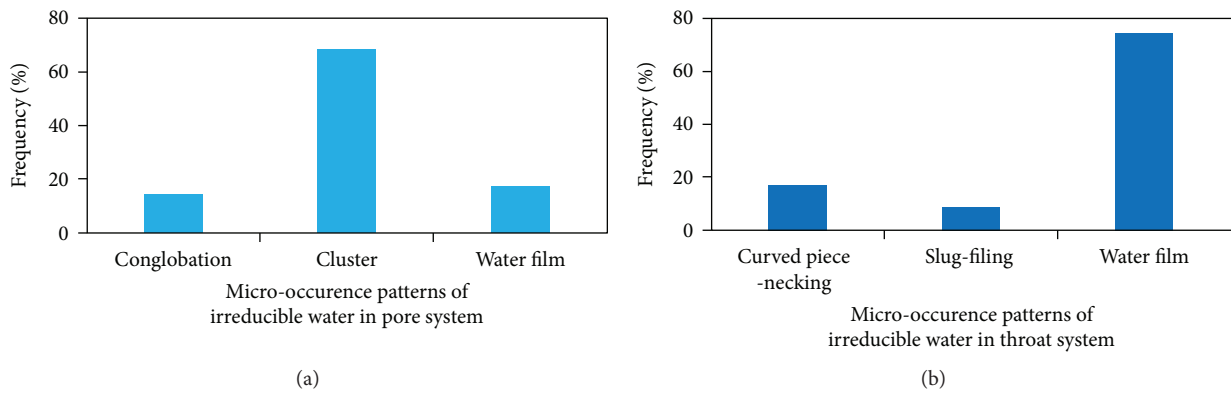


FIGURE 18: Histogram of irreducible water modes distribution: (a) pore system; (b) throat system.

in the throat system. In the pore system, the irreducible water principally existed in the corner of the pores which are linked through the water film. While in the throat system, the irreducible water occurrence is dominated by the water film. However, 25.5% of the throats are blocked by the irreducible water (curved piece-necking and slug-filling) which plug the crude oil drainage channels.

Abbreviations

CT: Computerized tomography
 EOR: Enhance oil recovery
 2D: Two dimensional
 3D: Three dimensional
 KI: Potassium iodide.

Data Availability

The data used to support the findings of this study are available from the corresponding author upon request.

Conflicts of Interest

The authors declare that they have no conflicts of interest.

Acknowledgments

The authors express their appreciation to the National Science and Technology Major Project (no. 2009ZX05009), the project of the China Natural Science Foundation (50774091) for the financial support of this work, and the China Postdoctoral Science Foundation (2018M631765): dynamic research on synergistic action of foam flooding stimulated by low-frequency vibration.

Supplementary Materials

Figure S1. XRD diffraction pattern of the experimental core sample. (*Supplementary Materials*)

References

- [1] R. W. Bentley, "Global oil & gas depletion: an overview," *Energy Policy*, vol. 30, no. 3, pp. 189–205, 2002.
- [2] C. J. Campbell and J. H. Laherrère, "The end of cheap oil," *Scientific American*, vol. 278, no. 3, pp. 78–83, 1998.
- [3] Z. Li, X. Qu, W. Liu, Q. Lei, H. Sun, and Y. He, "Development modes of Triassic Yanchang Formation Chang 7 Member tight oil in Ordos Basin, NW China," *Petroleum Exploration and Development*, vol. 42, no. 2, pp. 241–246, 2015.
- [4] J. M. Dumore and R. S. Schols, "Drainage capillary-pressure functions and the influence of connate water," *Society of Petroleum Engineers Journal*, vol. 14, no. 5, pp. 437–444, 1974.
- [5] J. T. Morgan and D. T. Gordon, "Influence of pore geometry on water-oil relative permeability," *Journal of Petroleum Technology*, vol. 22, no. 10, pp. 1199–1208, 1970.
- [6] S. B. Coskun and N. C. Wardlaw, "Image analysis for estimating ultimate oil recovery efficiency by waterflooding for two sandstone reservoirs," *Journal of Petroleum Science & Engineering*, vol. 15, no. 2-4, pp. 237–250, 1996.
- [7] Y. Sun and D. City, "The influence of reservoir-forming dynamic on irreducible water saturation," *Petroleum Geology & Recovery Efficiency*, vol. 13, no. 2, pp. 64–66, 2007.
- [8] X. Gu, C. Pu, H. Huang et al., "Micro-influencing mechanism of permeability on spontaneous imbibition recovery for tight sandstone reservoirs," *Petroleum Exploration and Development*, vol. 44, no. 6, pp. 1003–1009, 2017.
- [9] K. Li and R. N. Horne, "An analytical scaling method for spontaneous imbibition in gas/water/rock systems," *SPE Journal*, vol. 9, no. 3, pp. 322–329, 2004.
- [10] J. Wang, Y. Liu, M. Chen, L. Liu, and J. Gao, "Experimental study on dynamic imbibition mechanism of low permeability reservoirs," *Petroleum Exploration and Development*, vol. 36, no. 1, pp. 86–90, 2009.
- [11] N. K. Karadimitriou and S. M. Hassanizadeh, "A review of micromodels and their use in two-phase flow studies," *Vadose Zone Journal*, vol. 11, no. 3, pp. 215–228, 2012.
- [12] I. Razmavar, F. M. Alami, M. R. Rasaei, and M. Nadafpour, "Microscopic fractal-dimension study of rate and viscosity changes on displacement pattern by use of 2D glass micromodel," *SPE Reservoir Evaluation & Engineering*, vol. 20, no. 1, pp. 008–018, 2017.
- [13] L. Haibo, G. Hekun, and L. Qiang, "NMR experimental study of water displacing oil of tight oil reservoir," *Journal of Central South University: Science and Technology*, vol. 45, no. 12, pp. 4370–4376, 2014.
- [14] H. Doryani, M. R. Malayeri, and M. Riazi, "Visualization of asphaltene precipitation and deposition in a uniformly patterned glass micromodel," *Fuel*, vol. 182, pp. 613–622, 2016.
- [15] L. Z. Huo, Z. Yang, and X. Liu, "Analysis of NMR moveable fluid parameters in ultra-low permeability glutenite reservoir," *Science & Technology Review*, vol. 28, no. 7, pp. 88–90, 2010.
- [16] H. Gao, Y. Liu, Z. Zhang, B. Niu, and H. Li, "Impact of secondary and tertiary floods on microscopic residual oil distribution in medium-to-high permeability cores with NMR technique," *Energy & Fuels*, vol. 29, no. 8, pp. 4721–4729, 2015.
- [17] P. Yang, H. Guo, and D. Yang, "Determination of residual oil distribution during waterflooding in tight oil formations with NMR relaxometry measurements," *Energy & Fuels*, vol. 27, no. 10, pp. 5750–5756, 2013.
- [18] T. R. Todoruk, C. H. Langford, and A. Kantzas, "Pore-scale redistribution of water during wetting of air-dried soils as studied by low-field NMR relaxometry," *Environmental Science & Technology*, vol. 37, no. 12, pp. 2707–2713, 2003.
- [19] Y. Li, H. Li, S. Chen, E. Mbia, K. Wang, and H. Ren, "Capillarity characters measurement and effects analysis in different permeability formations during waterflooding," *Fuel*, vol. 194, pp. 129–143, 2017.
- [20] A. Polak, D. Elsworth, H. Yasuhara, A. S. Grader, and P. M. Halleck, "Permeability reduction of a natural fracture under net dissolution by hydrothermal fluids," *Geophysical Research Letters*, vol. 30, no. 20, 2003.
- [21] M. Akbarabadi, S. Saraji, M. Piri, D. Georgi, and M. Delshad, "Nano-scale experimental investigation of in-situ wettability and spontaneous imbibition in ultra-tight reservoir rocks," *Advances in Water Resources*, vol. 107, pp. 160–179, 2017.
- [22] L. E. Beckingham, C. A. Peters, W. Um, K. W. Jones, and W. B. Lindquist, "2D and 3D imaging resolution trade-offs in quantifying pore throats for prediction of permeability," *Advances in Water Resources*, vol. 62, no. 4, Part A, pp. 1–12, 2013.

- [23] Q. Luo, C. Zhang, Q. Dai et al., "Characterization of compact carbonate pore-throat network systems in the Xiagou Formation in Qingxi Sag, Jiuquan Basin, China," *Journal of Petroleum Science & Engineering*, vol. 159, pp. 853–868, 2017.
- [24] P. Iassonov, T. Gebrenegus, and M. Tuller, "Segmentation of X-ray computed tomography images of porous materials: a crucial step for characterization and quantitative analysis of pore structures," *Water Resources Research*, vol. 45, no. 9, 2009.
- [25] M. Wang, S.'a. Zhang, F. Zhang et al., "Quantitative research on tight oil microscopic state of Chang 7 Member of Triassic Yanchang Formation in Ordos Basin, NW China," *Petroleum Exploration and Development*, vol. 42, no. 6, pp. 827–832, 2015.
- [26] P. Tiwari, M. Deo, C. L. Lin, and J. D. Miller, "Characterization of oil shale pore structure before and after pyrolysis by using X-ray micro CT," *Fuel*, vol. 107, no. 9, pp. 547–554, 2013.
- [27] R. Song, M. Cui, J. Liu, P. G. Ranjith, and Y. Lei, "A pore-scale simulation on thermal-hydronechanical coupling mechanism of rock," *Geofluids*, vol. 2017, Article ID 7510527, 12 pages, 2017.
- [28] F. F. Hingerl, F. Yang, R. Pini et al., "Characterization of heterogeneity in the Heletz sandstone from core to pore scale and quantification of its impact on multi-phase flow," *International Journal of Greenhouse Gas Control*, vol. 48, pp. 69–83, 2016.
- [29] M. J. Blunt, M. D. Jackson, M. Piri, and P. H. Valvatne, "Detailed physics, predictive capabilities and macroscopic consequences for pore-network models of multiphase flow," *Advances in Water Resources*, vol. 25, no. 8-12, pp. 1069–1089, 2002.
- [30] A. C. Gunde, B. Bera, and S. K. Mitra, "Investigation of water and CO₂ (carbon dioxide) flooding using micro-CT (micro-computed tomography) images of Berea sandstone core using finite element simulations," *Energy*, vol. 35, no. 12, pp. 5209–5216, 2010.
- [31] M. Zhou, D. Lu, J. Dunsmuir, and H. Thomann, "Irreducible water distribution in sandstone rock: two phase flow simulations in CT-based pore network," *Physics and Chemistry of the Earth, Part A: Solid Earth and Geodesy*, vol. 25, no. 2, pp. 169–174, 2000.
- [32] X. Chen, Y. Liu, and Y. Wang, "Research on porosity of Chang 2 reservoir in Zichang oil field," *Ground Water*, vol. 23, no. 2, pp. 156–159, 2013.
- [33] M. Andrew, *Reservoir Condition Pore Scale Imaging of Multiphase Flow Using X-Ray Microtomography*, Imperial Polytechnic University, 2014.
- [34] H. Jian, Q. Maoxin, and L. Nu, "Characterization of residual oil microdistribution at pore scale using computerized tomography," *Acta Petrolei Sinica*, vol. 35, no. 2, pp. 319–325, 2014.
- [35] D. Denney, "Robust determination of the pore-space morphology in sedimentary rocks," *Journal of Petroleum Technology*, vol. 56, no. 5, pp. 69–70, 2004.
- [36] Z. Yang, X. F. Peng, D. J. Lee, and M. Y. Chen, "An image-based method for obtaining pore-size distribution of porous media," *Environmental Science & Technology*, vol. 43, no. 9, pp. 3248–3253, 2009.
- [37] J. C. Trantham and R. L. Clampitt, "Determination of oil saturation after waterflooding in an oil-wet reservoir the North Burbank Unit, Tract 97 Project," *Journal of Petroleum Technology*, vol. 29, no. 5, pp. 491–500, 1977.
- [38] C. Feng, Y. Shi, J. Hao et al., "Nuclear magnetic resonance features of low-permeability reservoirs with complex wettability," *Petroleum Exploration and Development*, vol. 44, no. 2, pp. 274–279, 2017.

Research Article

Effect of Pore-Scale Mineral Spatial Heterogeneity on Chemically Induced Alterations of Fractured Rock: A Lattice Boltzmann Study

Hossein Fazeli ¹, Ravi Patel,² and Helge Hellevang¹

¹Department of Geosciences, University of Oslo, Postboks 1047, Blindern, Oslo, Norway

²Laboratory for Waste Management (LES), Paul Scherrer Institute, 5232 Villigen, Switzerland

Correspondence should be addressed to Hossein Fazeli; hossein.fazeli@geo.uio.no

Received 29 December 2017; Revised 1 May 2018; Accepted 15 May 2018; Published 18 July 2018

Academic Editor: Xiangzhao Kong

Copyright © 2018 Hossein Fazeli et al. This is an open access article distributed under the Creative Commons Attribution License, which permits unrestricted use, distribution, and reproduction in any medium, provided the original work is properly cited.

Fractures are the main flow path in rocks with very low permeability, and their hydrodynamic properties might change due to interaction with the pore fluid or injected fluid. Existence of minerals with different reactivities and along with their spatial distribution can affect the fracture geometry evolution and correspondingly its physical and hydrodynamic properties such as porosity and permeability. In this work, evolution of a fracture with two different initial spatial mineral heterogeneities is studied using a pore-scale reactive transport lattice Boltzmann method- (LBM-) based model. The previously developed LBM transport solver coupled with IPHREEQC in open-source Yantra has been extended for simulating advective-diffusive reactive transport. Results show that in case of initially mixed structures for mineral assemblage, a degraded zone will form after dissolution of fast-dissolving minerals which creates a resistance to flow in this region. This causes the permeability-porosity relationship to deviate from a power-law behavior. Results show that permeability will reach a steady-state condition which also depends on transport and reaction conditions. In case of initially banded structures, a comb-tooth zone will form and the same behavior as above is observed; however, in this case, permeability is usually less than that of mixed structures.

1. Introduction

During reactive transport processes in tight rocks, fractures play an important role as it is the main flow path for species transport. Existence of fractured seals in geological CO₂ sequestration and fractures in the host rock of nuclear waste disposal sites are some practical examples in which hydrodynamic properties of fractures can help to better understand the long-term evolution of the system [1]. These hydrodynamic properties will change due to chemical disequilibrium resulting from interactions between pore fluid and rock minerals. There are experiments which have shown that the presence of reactive and nonreactive (or less reactive) minerals and their spatial distribution with respect to each other can affect the way a fracture evolves as a result of reactions with reactive fluids [2]. For instance, when slow- and fast-reacting minerals are mixed in the rock matrix around a fracture, dissolution of fast-reacting minerals will form a degraded zone around the fracture [2, 3]. In another example, when fractures crossing zones of slow- and fast-

reacting minerals form banded structures, the dissolution of fast-reacting minerals will generate a comb-tooth structure around the fracture [2, 3]. Therefore, fracture permeability evolution might not follow the same behavior when minerals form initially banded and mixed structures, and in addition to the experiments, numerical studies are needed to address the effect of spatial mineral distributions on fracture evolution. There have been different continuum-scale numerical studies that have investigated the fracture evolution [4–7]. In these models, mineral spatial heterogeneities are generally represented in a single discretized cell, but pore-scale models resolving spatial heterogeneities can provide better description of processes and help to understand the role of spatial heterogeneities on fracture evolution [8, 9]. Different pore-scale reactive transport modeling approaches, involving geometry changes due to chemical interactions, have been developed [10–17]. Lattice Boltzmann method- (LBM-) based models have also been developed which are mostly focusing on single mineral dissolution in nonfractured media [5, 18–33]. Recently, Chen et al. [26] investigated the effect of

mineral heterogeneity on evolution of a single fracture surrounded by a rock matrix composed of binary minerals, but the model is limited to a simple mineralogy. In the present work, we utilize a similar setup used in Chen et al.'s work [26], a single fracture surrounded by a rock matrix composed of two different minerals, and focus more on the effect of mineral spatial heterogeneity on fracture geometry evolution by constructing initially mixed and banded mineral structures that are conceptualizations of the structures observed by Ellis et al. [2]. The pore-scale simulations are carried out using a multicomponent reactive transport LBM model proposed by Patel et al. [30] which has been implemented in open-source code Yantra [34]. This model couples the LBM transport solver with a well-known geochemical solver IPHREEQC which allows accounting for complex and realistic reaction networks. In this study, we have further extended the model to include the advective flow component and the kinetic reactions. We use mixed and banded structures in two different parts. In the first part of the paper, we perform single-species simulations to investigate fracture geometry evolutions and also study the effect of different flow and reaction conditions by choosing different dimensionless numbers. The second part of the paper presents results related to a realistic case where a single fracture (representing a leakage pathway) in a caprock, above a formation used for CO₂ storage, is considered where the rock matrix is assumed to be composed of carbonate (calcite) and clay (kaolinite) minerals. This rock is representative of a carbonate-rich caprock such as some intervals in the Draupne shale [35].

2. Numerical Model Description

2.1. Lattice Boltzmann Method for Fluid Flow. The flow of incompressible fluids can be described by continuity and Navier-Stokes (NS) equations [36]

$$\begin{aligned} \nabla \cdot \mathbf{u} &= 0, \\ \rho \frac{\partial \mathbf{u}}{\partial t} + \rho \mathbf{u} \cdot \nabla \mathbf{u} &= -\nabla P + \mu \nabla^2 \mathbf{u} + \mathbf{F}, \end{aligned} \quad (1)$$

where ρ (kg/m³) is density, \mathbf{u} (m/s) is velocity, P (Pa) is pressure, μ (Pa·s) is dynamic viscosity, and \mathbf{F} (N/m³) is body force.

LBM has been used in this study to solve the Navier-Stokes equation. LBM describes the behavior of a collection of particles, and instead of macroscopic equation of fluid dynamics, it is based on the Boltzmann equation which describes dynamics of a gas on a mesoscopic scale [37]:

$$\frac{\partial f}{\partial t} + \xi_\alpha \frac{\partial f}{\partial x_\alpha} + \frac{F_\alpha}{\rho} \frac{\partial f}{\partial \xi_\alpha} = \Omega(f), \quad (2)$$

where f is density of particles with velocity ξ in the α -direction at position x and time t . Also, F is the force term and Ω is a collision operator which represents local distribution of f because of collisions of particles. It can be shown that (2) can recover the NS equation meaning that if one solves (2) and obtains f , then one is able to calculate the macroscopic quantities such as velocity and pressure using f . To solve for f , (2) must be discretized in time, velocity space, and physical space [37]:

$$f_i(\mathbf{x} + \mathbf{c}_i \Delta t, t + \Delta t) = f_i(\mathbf{x}, t) + \Omega_i(f) + \mathbf{F}_i \Delta t, \quad (3)$$

where

$$\begin{aligned} \Omega_i(f) &= \frac{-\Delta t}{\tau} (f_i - f_i^{\text{eq}}), \\ f_i^{\text{eq}} &= w_i \rho \left(1 + \frac{\mathbf{u} \cdot \mathbf{c}_i}{c_s^2} + \frac{(\mathbf{u} \cdot \mathbf{c}_i)^2}{2c_s^4} - \frac{\mathbf{u} \cdot \mathbf{u}}{2c_s^2} \right), \\ \mathbf{F}_i &= w_i \frac{c_{i\alpha}}{c_s^2} F_\alpha, \\ c_s^2 &= \frac{1}{3} \cdot \left(\frac{\Delta x}{\Delta t} \right)^2. \end{aligned} \quad (4)$$

In the above equations, Δx and Δt are space and time resolutions. f_i is the discrete velocity distribution function, f_i^{eq} is the equilibrium distribution function, and τ is the relaxation time. Discrete velocities c_i and their corresponding set of weighing coefficients w_i will form velocity sets. There are different velocity sets used in LBM, and in this study and for fluid flow LBM, we use D2Q9 where 2 is the number of spatial dimensions (x and y) and 9 is the set's number of velocities [37]:

$$\begin{aligned} w_i &= \begin{cases} \frac{4}{9}, & i = 0, \\ \frac{1}{9}, & i = 1, 2, 3, 4, \\ \frac{1}{36}, & i = 5, 6, 7, 8, \end{cases} \\ \mathbf{c}_i &= \begin{cases} (0, 0), & i = 0, \\ \left(\cos\left(\frac{\pi(i-1)}{2}\right), \sin\left(\frac{\pi(i-1)}{2}\right) \right), & i = 1, 2, 3, 4, \\ \sqrt{2} \left(\cos\left(\frac{\pi(i-5)}{2} + \frac{\pi}{4}\right), \sin\left(\frac{\pi(i-5)}{2} + \frac{\pi}{4}\right) \right), & i = 5, 6, 7, 8. \end{cases} \end{aligned} \quad (5)$$

Equation (3) consists of two parts named collision and streaming. Particles move with velocity \mathbf{c}_i to a neighboring node at position $\mathbf{x} + \mathbf{c}_i\Delta t$ during time step $t + \Delta t$, and at the same time, they are affected by the collision operator. So, (3) can be broken into two parts [37]:

$$\begin{aligned} \text{Collision(plus source term): } f_i^*(\mathbf{x}, t) &= f_i(\mathbf{x}, t) + \Omega_i(f) + \mathbf{F}_i\Delta t, \\ \text{Streaming : } f_i(\mathbf{x} + \mathbf{c}_i\Delta t, t + \Delta t) &= f_i^*(\mathbf{x}, t). \end{aligned} \quad (6)$$

Once these two steps are performed, distribution functions f_i in the current timestep can be calculated and then one is able to compute the macroscopic fluid density and velocity [37]:

$$\begin{aligned} \rho &= \sum_{i=0}^8 f_i, \\ \mathbf{u} &= \frac{1}{\rho} \sum_{i=0}^8 f_i \mathbf{c}_i + \frac{\mathbf{F}\Delta t}{2\rho}. \end{aligned} \quad (7)$$

As was mentioned, it can be shown that the LB equation can recover the NS equation using Chapman-Enskog analysis [38], and it can be observed that the kinematic viscosity ν takes the following form in terms of Lattice parameters:

$$\nu = c_s^2 \left(\tau - \frac{\Delta t}{2} \right). \quad (8)$$

2.2. Lattice Boltzmann Method for Advection-Diffusion-Reaction Equation. Reactive transport of chemical species can be described using the advection-diffusion-reaction (ADR) equation [39]:

$$\frac{\partial C_j}{\partial t} + \nabla \cdot (-D_j \nabla C_j + \mathbf{u} C_j) = R_j, \quad (9)$$

where C_j is the concentration of species j , D_j is the diffusion coefficient which is considered constant for all species, and R_j represents the source or sink term due to reactions for species j . R_j is related to the homogeneous reactions while heterogeneous reactions happening at the solid-fluid interface are usually described as boundary conditions.

LBM can also be applied to solve the ADR equation. So, the LB equation for each species j [30]

$$g_i^j(\mathbf{x} + \mathbf{c}_i\Delta t, t + \Delta t) = g_i^j(\mathbf{x}, t) + \Omega_i^j(g) + w_i R_{\text{total}}^j(\mathbf{x}, t)\Delta t, \quad (10)$$

with

$$\Omega_i^j(g) = \frac{-\Delta t}{\tau_g} \left(g_i^j - g_i^{\text{eq},j} \right), \quad (11)$$

$$g_i^{\text{eq},j} = w_i C^j \left(1 + \frac{\mathbf{u} \cdot \mathbf{c}_i}{c_s^2} \right), \quad (12)$$

solves the ADR equation for concentration of species j

$$C^j = \sum_{i=0}^4 g_i^j. \quad (13)$$

In the above equations, g is the distribution function used for species concentration. It should be pointed out that in the LBM model above, the D2Q5 lattice was used for the ADR equation. R_{total}^j is a source-sink term due to both heterogeneous and homogeneous reactions. While in most of previous LBM models [2, 10, 18, 20, 21, 23–27, 29, 40–42], heterogeneous reactions are treated as a boundary flux, in this study, LBM treats heterogeneous reactions as pseudohomogeneous reactions meaning that R_{total}^j at the bulk only includes the homogeneous reactions, but at the fluid nodes adjacent to a solid node, R_{total}^j also includes heterogeneous reactions (now treated as pseudohomogeneous reactions) [30]. Using this approach, both homogeneous and heterogeneous reactions can be treated similarly, and it gives the possibility to couple the LBM transport part with an external geochemical solver such as IPHREEQC which has been used in this work. The validation of the LBM model has been presented in the Appendix.

2.3. Numerical Implementation. Figure 1 shows how the LBM models for fluid flow and mass transport and the reaction solver have been coupled. To initialize the model, first, initial, and boundary concentrations of different species are computed using IPHREEQC. In each time step, first we solve for the velocity profile using the LBM flow solver (as described in Section 2.1). In this study, since the time scale of the fluid flow is much shorter than the other processes, velocity reaches steady-state condition during the chosen time step. Equilibrium distribution functions are calculated using (12), and the collision step is then executed according to the following equation:

$$g_i^{j*}(\mathbf{x}, t) = g_i^j(\mathbf{x}, t) + \Omega_i^j(g). \quad (14)$$

We do not include the reaction source-sink term in this step. In the next step, molar concentrations C_{trnp}^j are transferred to IPHREEQC. IPHREEQC is a class of the PHREEQC geochemical solver that facilitates the usage of PHREEQC along with other software such as transport solvers [43]. After importing concentrations C_{trnp}^j from the transport step into the geochemical solver, new concentrations C_{phrq}^j are calculated by the PHREEQC. Finally, R_{total}^j is calculated using

$$R_{\text{total}}^j(\mathbf{x}, t) = \frac{C_{\text{phrq}}^j - C_{\text{trnp}}^j}{\Delta t}. \quad (15)$$

All these steps are done using a PHREEQC wrapper file which is part of the LBM code used in this study and has been detailed in Patel's work [34] and in open-source code Yantra 1.0.0 which is available online (<https://bitbucket.org/yantralbm/yantra/overview>).

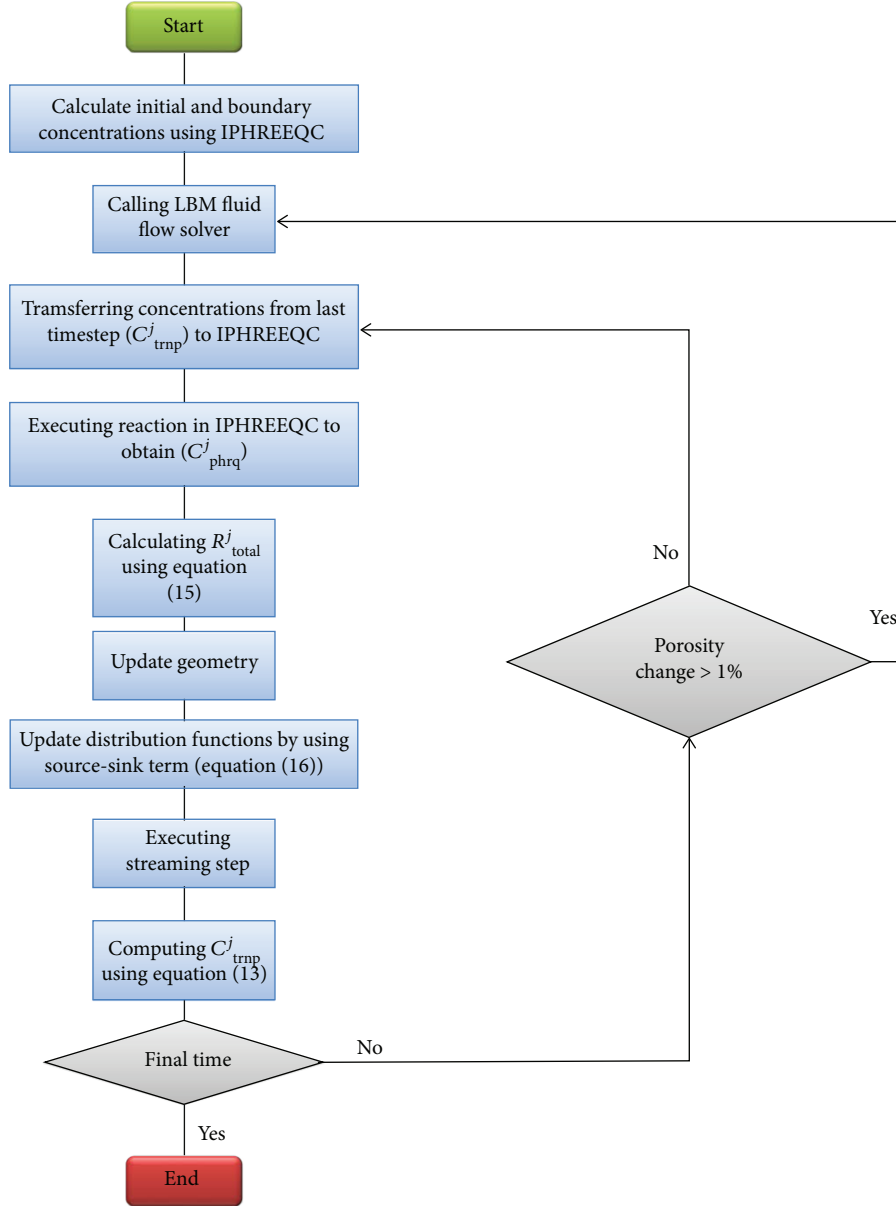


FIGURE 1: Flowchart of the LBM reactive transport model.

The geometry is updated using static update rules detailed in Patel et al. [30]. Before performing the streaming step, to apply the effect of chemical reactions, we update the distribution functions using

$$g_i^{j**}(\mathbf{x}, t) = g_i^{j*}(\mathbf{x}, t) + w_i R_{\text{total}}^j(\mathbf{x}, t) \Delta t, \quad (16)$$

and then the streaming step is executed:

$$g_i^j(\mathbf{x} + \mathbf{c}_i \Delta t, t + \Delta t) = g_i^{j**}(\mathbf{x}, t). \quad (17)$$

Once the streaming step is performed, species concentrations can be obtained using (13), and we go to the next time step. It should be pointed out that in the next time step, we solve for the velocity when there is at least 1% change in the porosity.

3. Results and Discussion

3.1. Generation of Initially Mixed and Banded Mineral Assemblages. To investigate the effect of initial mineral distributions on fracture geometry evolution, the quartet structure generation set (QSGS) algorithm [44] was used to generate mixed and banded mineral distributions around a single fracture (Figures 2 and 3). Both of these two geometries are used for both single- and multispecies simulations. In single-species simulations, a synthetic reactive mineral and an inert mineral are present while in the multispecies simulations, the rock matrix is composed of calcite (fast-reacting) and kaolinite (slow-reacting) minerals. The QSGS algorithm is a reconstruction method which can generate the microstructure of materials composed of different constituents such as rocks with different minerals. There are three tunable parameters

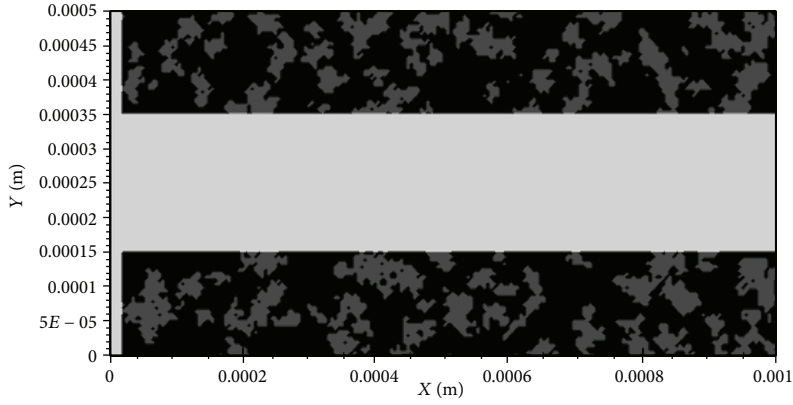


FIGURE 2: The geometry of a single fracture (in light gray) surrounded by reactive (in black) and nonreactive (in dark gray) minerals. In multispecies simulations, dark gray is kaolinite and black is calcite. The QSGS algorithm was used to grow nonreactive minerals inside a reactive mineral (in black) to form a mixed structure.

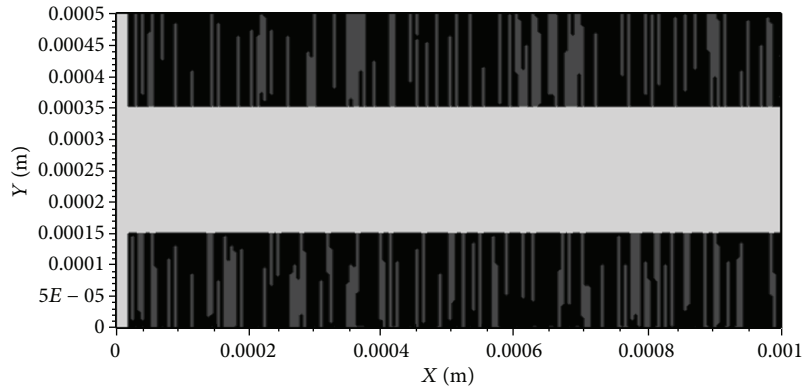


FIGURE 3: The geometry of a single fracture (in light gray) surrounded by reactive (in black) and nonreactive (in dark gray) minerals. In multispecies simulations, dark gray is kaolinite and black is calcite. The QSGS algorithm was used to grow nonreactive minerals inside a reactive mineral (in black) to form a banded structure.

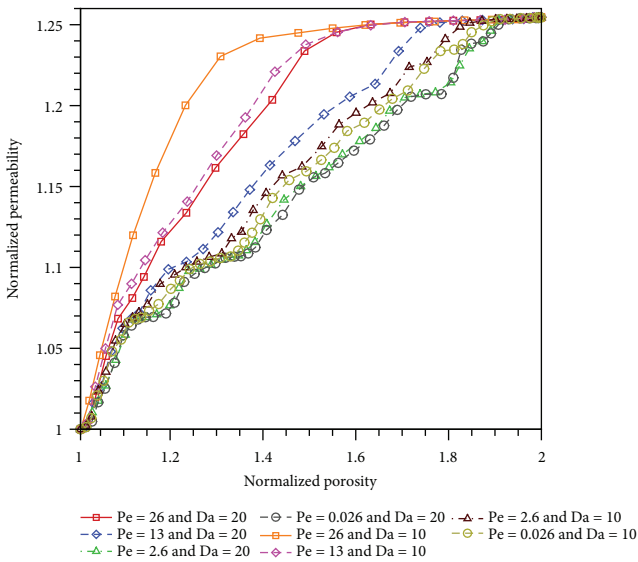


FIGURE 4: Normalized permeability versus normalized porosity at different Pe and Da numbers for initially mixed mineral assemblage.

(c_d , D_i , and Φ) in the QSGS algorithm to control how different phases (minerals) are growing inside a nongrowing phase. c_d represents the probability of a location in the nongrowing phase to become a nucleus for the first growing mineral. In this study, the nonreactive (in a single-species case) and kaolinite minerals (in a multispecies case) were considered as the growing phases which grow inside the reactive (in the single-species case) and calcite minerals (in the multispecies case), respectively. D_i is the probability for a nongrowing phase cell in direction i , to merge into a neighboring growing cell. In this study, eight different growth directions are considered for the growing phases. Also, Φ indicates the volume fraction of the growing phase in the nongrowing phase and is considered to be equal to 0.3 in this study. In both mixed and banded structure cases, c_d is equal to 0.015. To generate mixed mineral structures (Figure 2), we used $D_{i=1,2,3,4} = 0.04$ and $D_{i=5,6,7,8} = 0.01$. To generate banded structures, values of $D_{i=2,4} = 0.04$ and $D_{i=1,3,5,6,7,8} = 0$ were chosen to allow the vertical growth of growing minerals so that it can generate initial banded structures for the mineral spatial distribution (Figure 3).

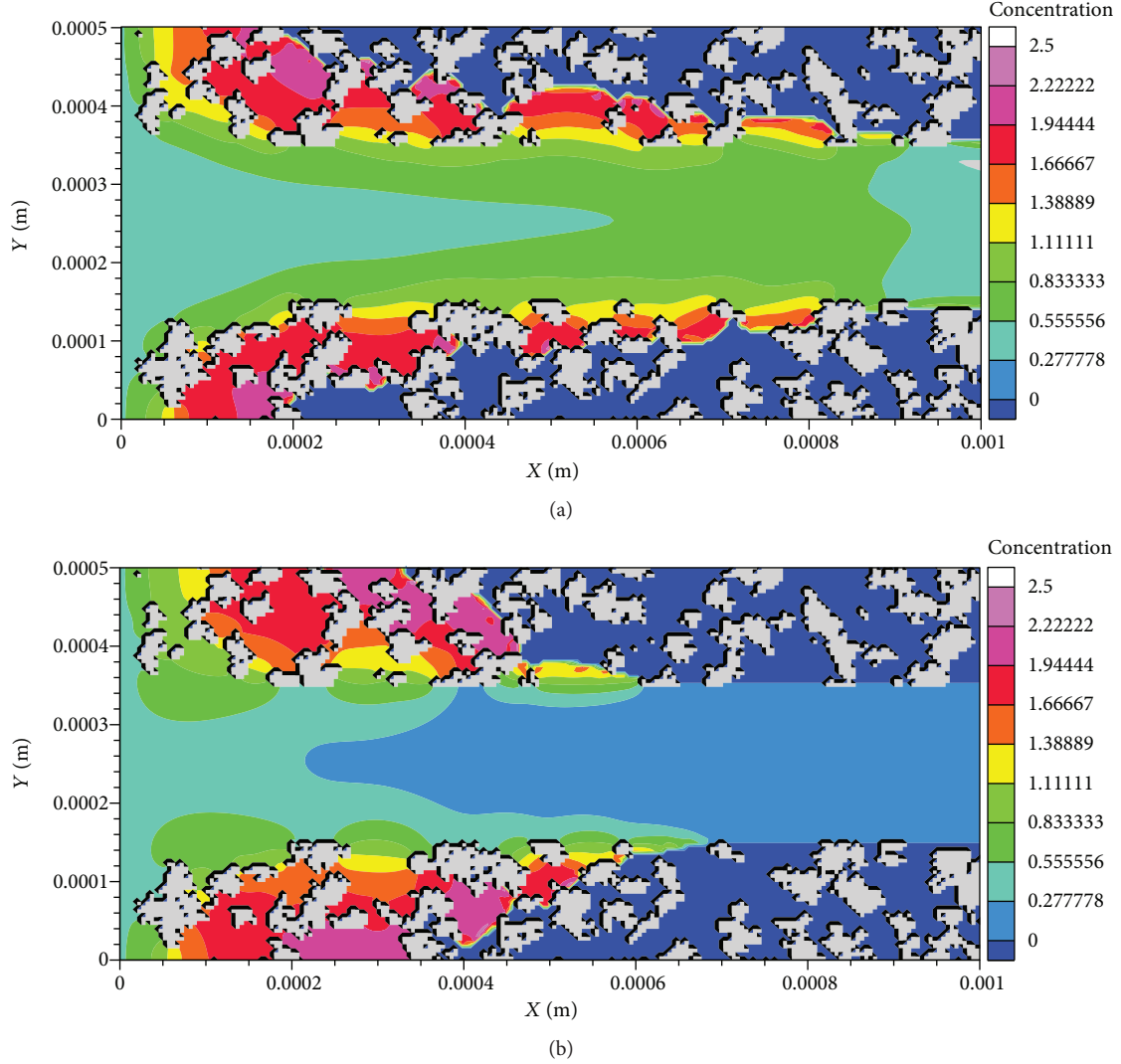


FIGURE 5: Concentration (mol/L) of species $A_{(aq)}$ when (a) $Pe = 26$ and $Da = 20$ and (b) $Pe = 0.026$ and $Da = 20$. In both (a) and (b), porosity (after dissolution) is near 0.59 but permeability (after dissolution) is $1.60 \times 10^{-9} \text{ m}^2$ for (a) and $1.48 \times 10^{-9} \text{ m}^2$ for (b). The nonreactive minerals are illustrated in light gray. The areas showing a zero concentration of species $A_{(aq)}$ are representing reactive minerals.

3.2. Single-Species Fracture Dissolution. In this section, it is assumed that the rock matrix around the fracture consists of two different minerals. For the single-species case, it is considered that one mineral is reactive (with molar volume of $2 \times 10^{-3} \text{ m}^3/\text{mol}$) and the other is inert. A single synthetic species $A_{(aq)}$ is injected into the fracture and reacts with the reactive mineral $A_{(s)}$ according to a first-order kinetic reaction with dissolution rate given by the following equation [45]:

$$R_A = k_r s c_A, \quad (18)$$

where c_A is the concentration of $A_{(aq)}$ and s is the reactive surface area.

3.2.1. Initial Mineral Distribution: Mixed Structures. Figure 2 is used as the geometry for the mixed-structure case. The dimension of the domain is $1 \text{ mm} \times 0.5 \text{ mm}$ with a resolution of $5 \mu\text{m}$. Initially, concentration of species $A_{(aq)}$ is zero in the

fracture. The flow with kinematic viscosity of $10^{-6} \text{ m}^2/\text{s}$ (representing water) is driven using a constant pressure gradient in the x-direction and with no flow top and bottom boundaries. Species $A_{(aq)}$ is injected into the fracture from the inlet where it is a constant concentration boundary with a concentration equal to 0.5 mol/L and all other boundaries are zero-gradient concentration boundaries. To see how hydrodynamic properties (permeability and porosity) of the fracture change during dissolution under different transport and reaction conditions, we run simulations at different Peclet (Pe) and Damkohler (Da) numbers defined as follows:

$$\begin{aligned} Pe &= \frac{UL}{D}, \\ Da &= \frac{k_r L}{D}, \end{aligned} \quad (19)$$

where L is the initial aperture of the fracture equal to $200 \mu\text{m}$, D is the diffusion coefficient with a value of

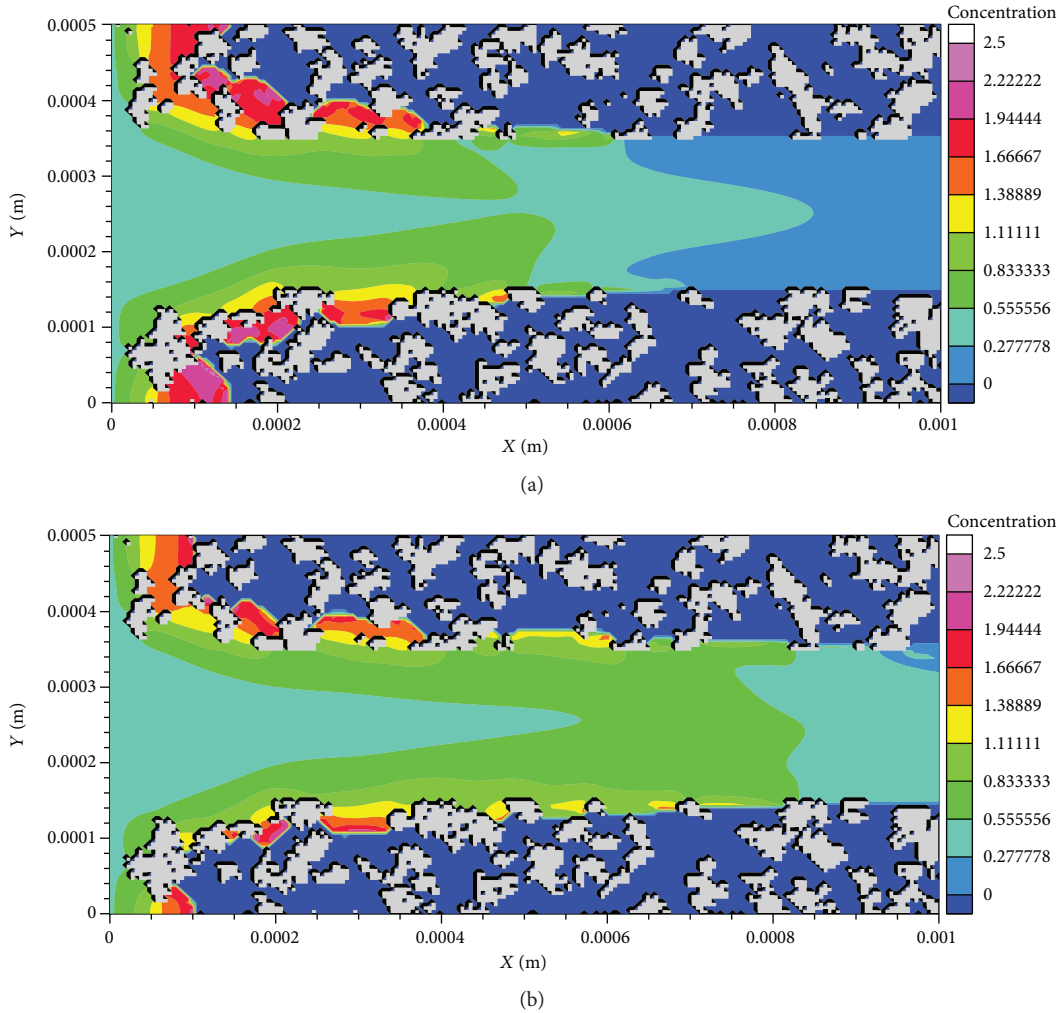


FIGURE 6: Concentration (mol/L) of species $A_{(aq)}$ when (a) $Pe = 26$ and $Da = 20$ and (b) $Pe = 26$ and $Da = 10$. In both (a) and (b), porosity (after dissolution) is near 0.50 but permeability (after dissolution) is $1.47 \times 10^{-9} \text{ m}^2$ for (a) and $1.56 \times 10^{-9} \text{ m}^2$ for (b). The nonreactive minerals are illustrated in light gray. The areas showing a zero concentration of species $A_{(aq)}$ are representing reactive minerals.

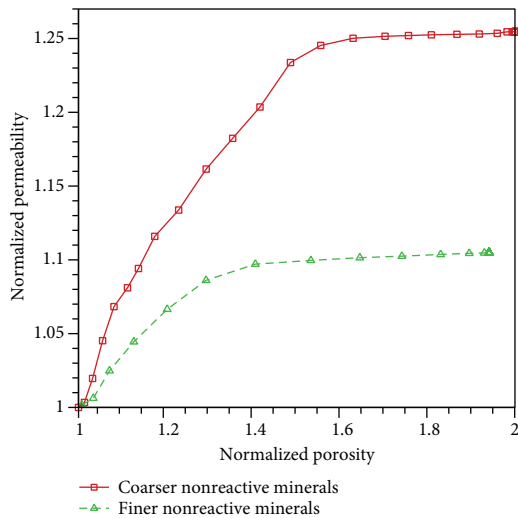


FIGURE 7: Normalized permeability versus normalized porosity at $Pe = 26$ and $Da = 20$ for initially mixed mineral assemblage where two different mineral sizes are used for nonreactive minerals.

$10^{-11} \text{ m}^2/\text{s}$, k_r is the reaction rate constant obtained from $k_r = (5 \times 10^{-8} \cdot Da) \text{ m/s}$, and U is the average velocity calculated by $U = (5 \times 10^{-8} \cdot Pe) \text{ m/s}$. Normalized permeability (permeability divided by initial permeability) and their corresponding normalized porosity (porosity divided by initial porosity) values have been obtained for different Pe and Da numbers. As shown in Figure 4, for a constant Da , higher Pe will lead to a higher permeability increase for a given porosity. As the flow regime will change from a diffusive to advective regime, it results in faster flow of the reactant through the fracture consequently leading to more dissolution of minerals along the fracture walls and quicker increase in fracture aperture. Figure 5 compares the fracture evolution for two Pe numbers of 26 and 0.026 while Da is 20 for both cases. These two cases have the same porosity (after dissolution) of 0.59, but permeability values (after dissolution) in Figures 5(a) and 5(b) are 1.60×10^{-9} and $1.48 \times 10^{-9} \text{ m}^2$, respectively. In Figure 5(a), the dissolution front quickly moves along

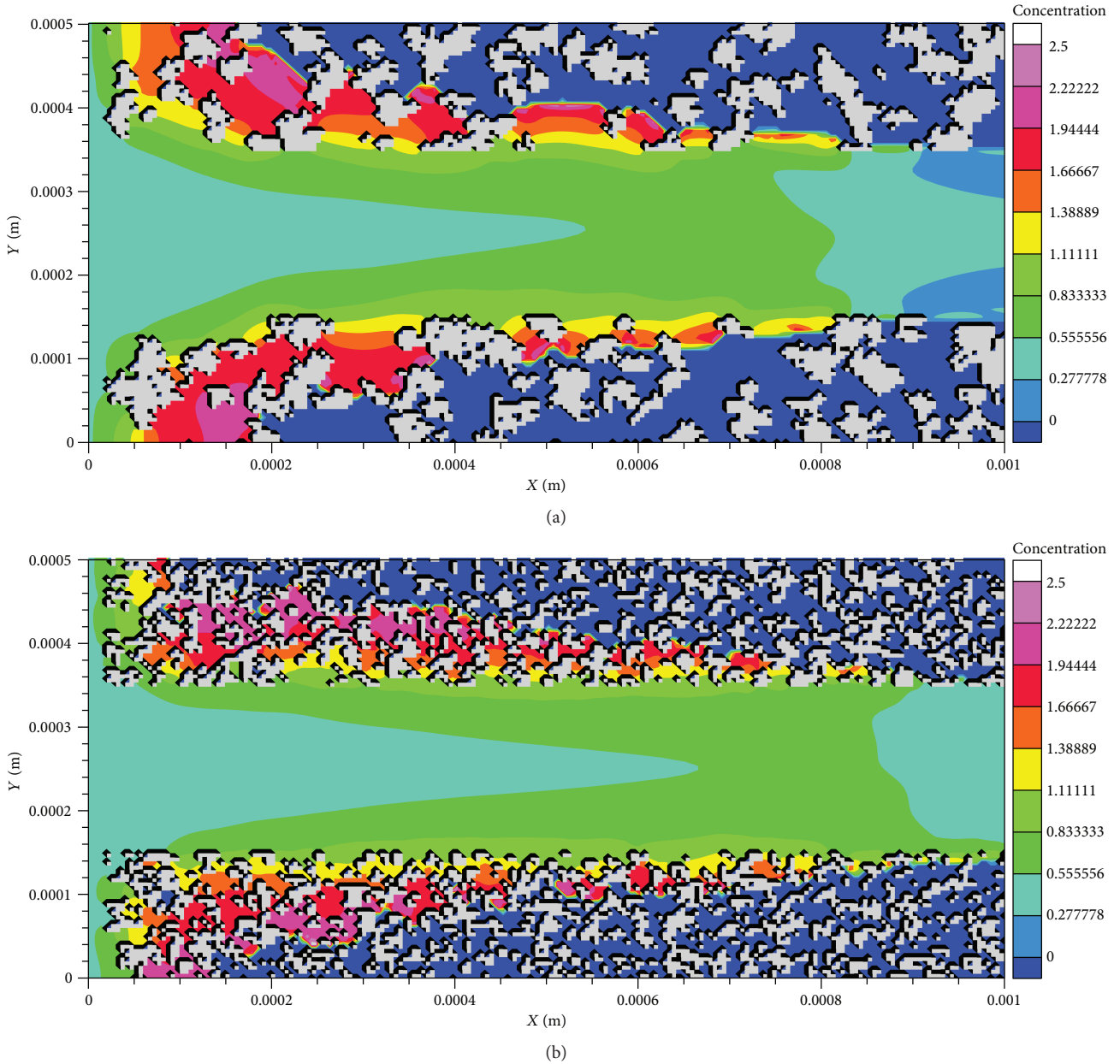


FIGURE 8: Concentration (mol/L) of species $A_{(aq)}$ when $Pe = 26$ and $Da = 20$, for (a) coarser and (b) finer nonreactive minerals. In both (a) and (b), porosity (after dissolution) is near 0.56 but permeability (after dissolution) is $1.56 \times 10^{-9} \text{ m}^2$ for (a) and $1.41 \times 10^{-9} \text{ m}^2$ for (b). The nonreactive minerals are illustrated in light gray. The areas showing a zero concentration of species $A_{(aq)}$ are representing reactive minerals.

the fracture increasing the aperture along the fracture wall which translates into higher fracture permeability. However, in Figure 5(b), most of the dissolution happens near to the inlet, and it does not increase fracture aperture as much as Figure 5(a) along the flow direction.

Figure 4 also shows how increasing the reaction rate (Da number) results in lower permeability values. Figures 6(a) and 6(b) are related to the cases with $Da = 20$ and $Da = 10$, respectively, while both have the same porosity of 0.50 (after dissolution) and Pe equal to 26. As it can be observed, in Figure 6(b), the fracture walls have been dissolved more than Figure 6(a) along

the flow direction; hence, dissolution in Figure 6(b) has more effect on increasing the fracture permeability, and permeability values confirm this difference where permeability in Figure 6(a) is $1.47 \times 10^{-9} \text{ m}^2$ and in Figure 6(b) is $1.56 \times 10^{-9} \text{ m}^2$. In all previous cases, either when Pe is constant and Da differs or when Da is constant and Pe changes, dissolution of reactive minerals in regions far away from the main channel has less impact on increasing permeability since the generated porous zone does not play an important role in increasing permeability and flow regime is more diffusive in this porous layer.

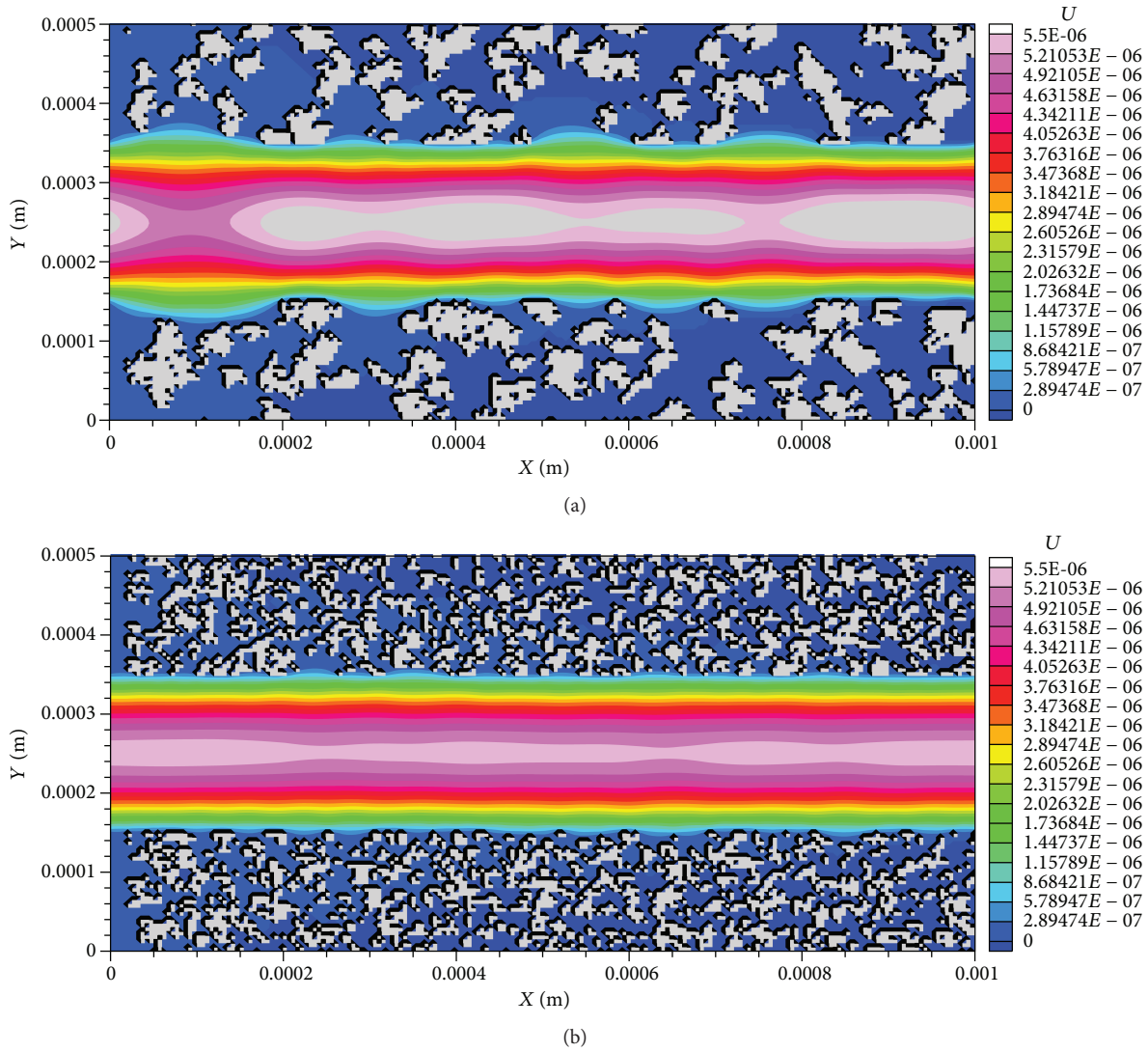


FIGURE 9: Velocity profile (m/s) for cases with (a) coarser and (b) finer nonreactive minerals when $Pe = 26$ and $Da = 20$. In both (a) and (b), porosity (after dissolution) is near 0.56 but permeability (after dissolution) is $1.56 \times 10^{-9} \text{ m}^2$ for (a) and $1.41 \times 10^{-9} \text{ m}^2$ for (b).

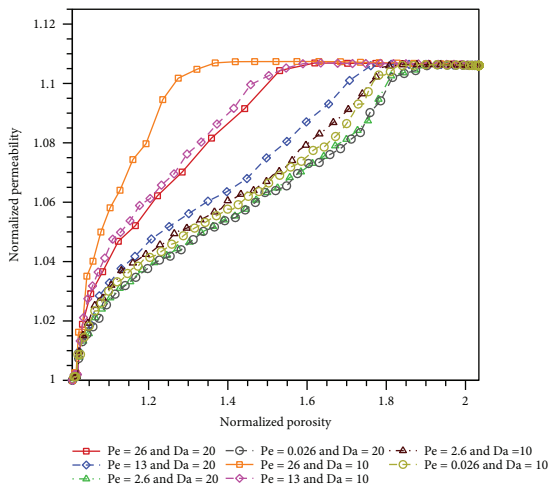


FIGURE 10: Normalized permeability versus normalized porosity at different Pe and Da numbers for initially banded mineral assemblage.

We also ran a case in which distribution of inert minerals inside the reactive minerals form finer mixed structures. Figure 7 shows that if the initial mixed distribution of nonreactive minerals inside the reactive minerals contains finer nonreactive minerals, the porous region formed after dissolution has more negative effect on permeability enhancement. Figures 8(a) and 8(b) are snapshots of species concentration having a porosity of 0.56 (after dissolution) and permeabilities (after dissolution) equal to 1.56×10^{-9} and $1.41 \times 10^{-9} \text{ m}^2$, respectively. Although the extent of dissolution (along the fracture wall and in the flow direction) in Figure 8(b) is even a bit more than Figure 8(a), the generated porous zone in Figure 8(b) creates more resistance to flow, and this region would be more tortuous than a porous region containing coarser inert minerals and that is why we observe lower permeability for the case with finer nonreactive minerals. This effect can be observed in Figures 9(a) and 9(b) where the velocity magnitude (in the degraded zone) for the case

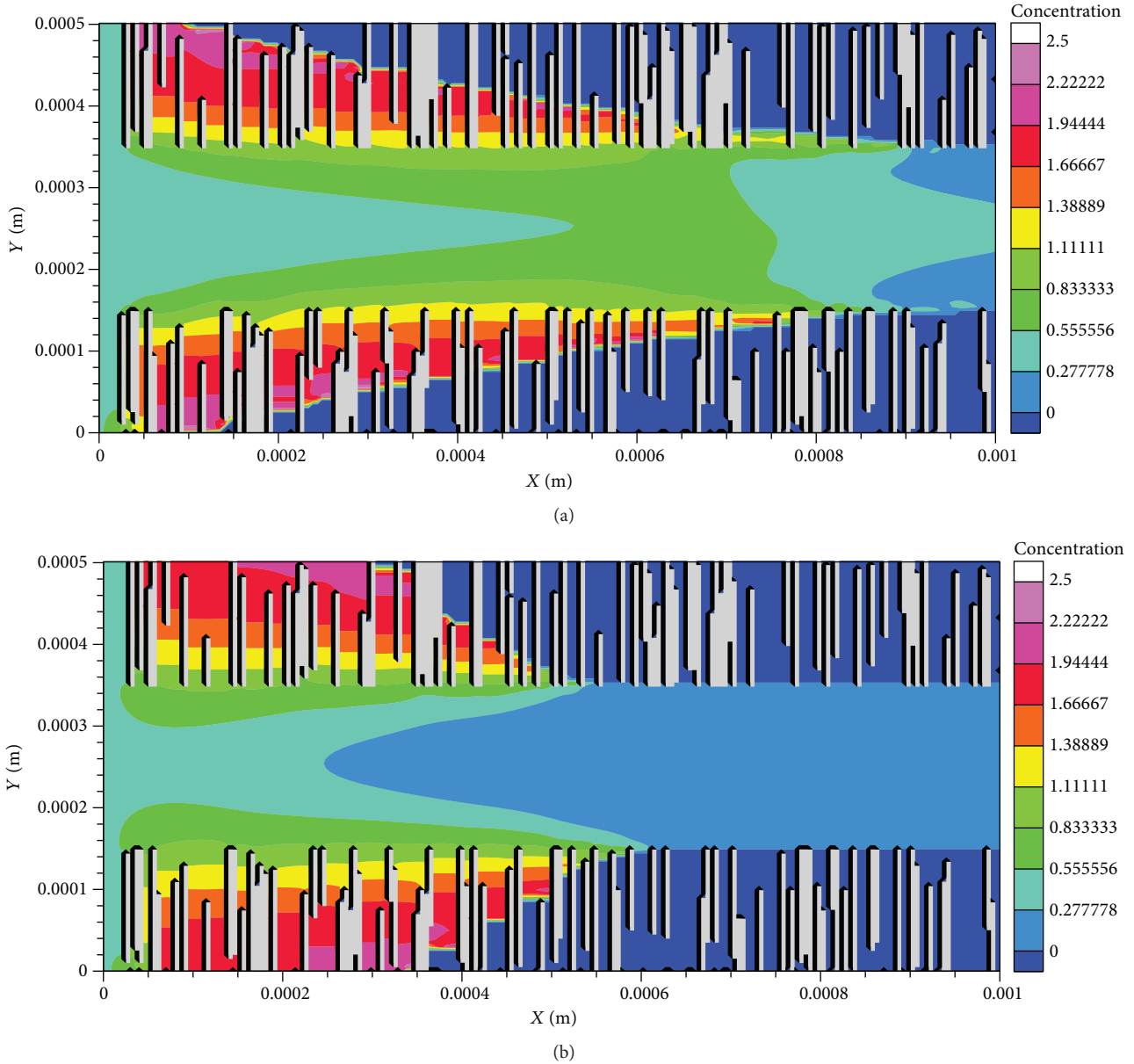


FIGURE 11: Concentration (mol/L) of species $A_{(aq)}$ when (a) $Pe = 26$ and $Da = 20$ and (b) $Pe = 0.026$ and $Da = 20$. In both (a) and (b), porosity (after dissolution) is near 0.58 but permeability (after dissolution) is $1.42 \times 10^{-9} \text{ m}^2$ for (a) and $1.37 \times 10^{-9} \text{ m}^2$ for (b). The nonreactive minerals are illustrated in light gray. The areas showing a zero concentration of species $A_{(aq)}$ are representing reactive minerals.

with finer minerals is less than that of the case with coarser minerals.

3.2.2. Initial Mineral Distribution: Banded Structures. For the banded structures, the geometry illustrated in Figure 3 is used. All the initial and boundary conditions for flow and mass transfer and also the type of reaction are the same as the ones used in the mixed-structure case. Simulations were performed at different Pe and Da numbers. As with Figure 4 (for the mixed structures), Figure 10 also displays that at a constant Da , higher permeability values can be reached when an advective flow regime is more dominant (higher Pe).

The contour maps in Figures 11(a) and 11(b) compare the fracture aperture along fracture walls (when Da number is 20 and porosity (after dissolution) is 0.58) showing that in Figure 11(a), which corresponds to $Pe = 26$, the aperture increase is more uniform compared to that in Figure 11(b), with Pe of 0.026, in which the aperture is increasing more locally and near the inlet. Therefore, permeability is higher in Figure 11(a). Also, in the case of constant Pe and different Da numbers, it can be observed in Figure 10 that there is a negative correlation between the Da number and permeability increase. Figure 12(a) which corresponds to a larger Da number indicates a face-dissolution behavior and less

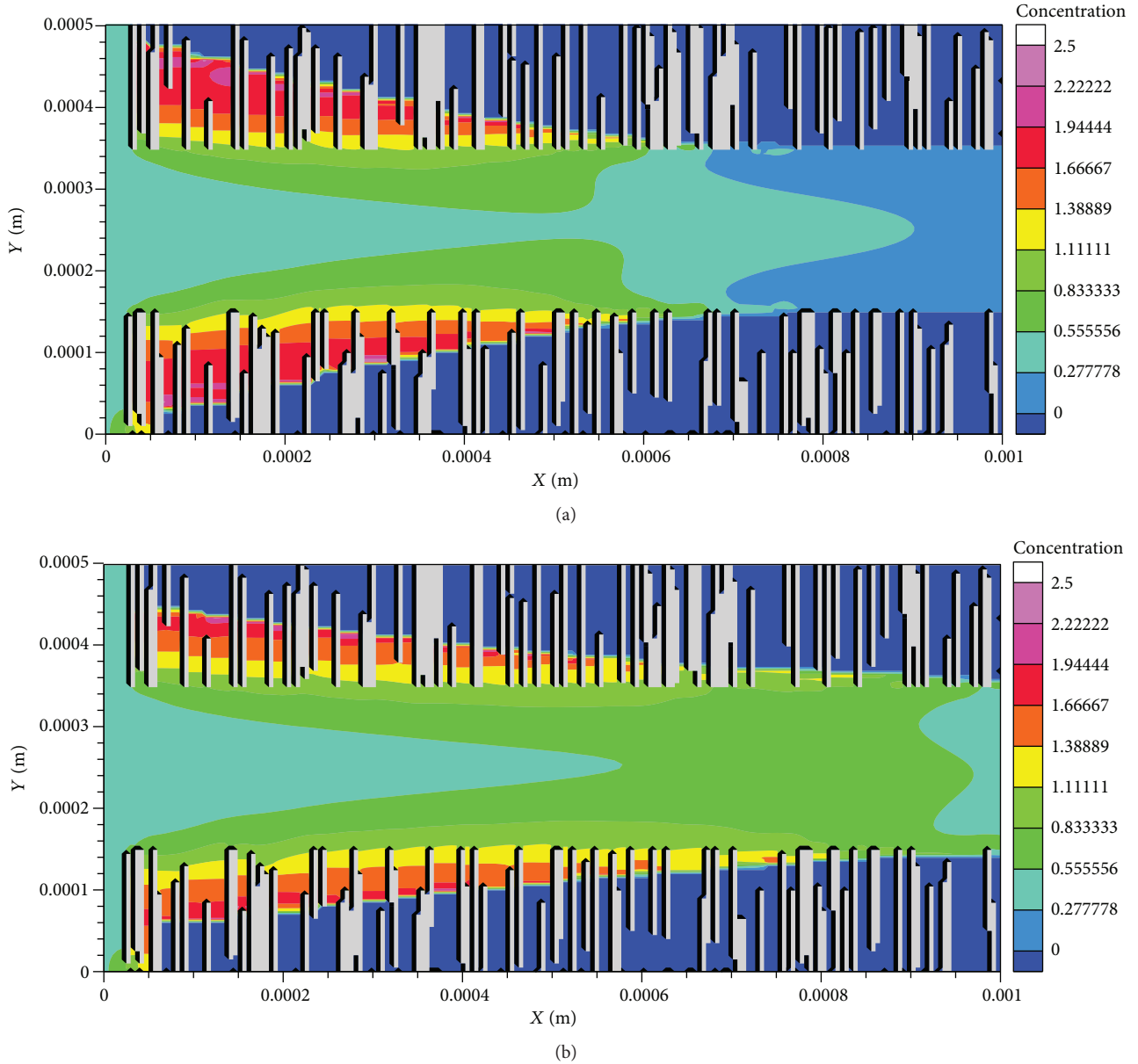


FIGURE 12: Concentration (mol/L) of species $A_{(aq)}$ when (a) $Pe = 26$ and $Da = 20$ and (b) $Pe = 26$ and $Da = 10$. In both (a) and (b), porosity (after dissolution) is near 0.52 but permeability (after dissolution) is $1.39 \times 10^{-9} \text{ m}^2$ for (a) and $1.43 \times 10^{-9} \text{ m}^2$ for (b). The nonreactive minerals are illustrated in light gray. The areas showing a zero concentration of species $A_{(aq)}$ are representing reactive minerals.

permeability while the dissolution in Figure 12(b) is happening uniformly along the fracture wall leading to a higher permeability.

In the banded structure case as well as the mixed structures, it can be observed that the permeability increases until it reaches a constant value. Pe and Da numbers can affect the time it takes for the permeability to reach this steady-state condition, but it is the existence of nonreactive minerals that causes this plateau in permeability-porosity curve. This behavior in normalized permeability-porosity relationship indicates that the relation $k = k_0(\phi/\phi_0)^3$ (which is normally used in many continuum modeling approaches to relate fracture permeability changes to porosity [39]) is not always valid when minerals with different reactivities exist in the fractured

media. This cubic relation is valid for single mineral cases where fracture planes are parallel and smooth. Figure 13 displays normalized permeability versus normalized porosity for a fracture geometry such as Figure 2 with only reactive minerals present in the rock matrix (no nonreactive mineral was considered). Figure 13 shows that in absence of nonreactive minerals, there will be no steady-state behavior in permeability values and normalized permeability-porosity relationship takes a power-law form, and the exponent of this power-law equation can be equal to 3 for a specific Da and Pe number.

3.3. *Multispecies Fracture Dissolution.* In the previous section, effects of mineral spatial heterogeneity and different

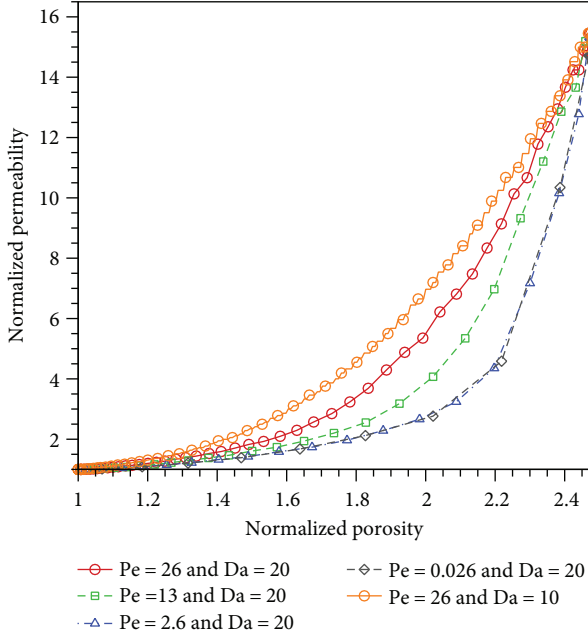


FIGURE 13: Normalized permeability versus normalized porosity at different Pe and Da numbers when a single fracture is surrounded only by a single reactive mineral and no nonreactive mineral exists in the rock matrix.

TABLE 1: Concentrations used for the initial and inlet solutions.

Parameter	Initial value in the fracture	Value at the inlet
pH	7.4	3.9
Ca	3.401×10^{-3} mol/kg _w	5.510×10^{-3} mol/kg _w
C	6.975×10^{-3} mol/kg _w	1.334 mol/kg _w
Na	1 mol/kg _w	1 mol/kg _w
Cl	1 mol/kg _w	1 mol/kg _w
Al	1.777×10^{-6} mol/kg _w	—
Si	1.777×10^{-6} mol/kg _w	—

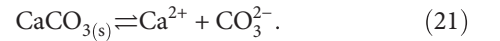
reactive transport conditions on fracture evolution were investigated when synthetic single-species reactive and nonreactive minerals were present in the model. In reality, however, the minerals are composed of different species and have more complicated kinetic rate equations which might affect the fracture textural evolution in ways that are not the same as evolutions related to the synthetic minerals. Therefore, in this section, simulations

are performed to show the ability of the developed pore-scale reactive transport model to handle more complicated cases where different minerals with more sophisticated kinetic rate equations exist in the model. As discussed before, in this section, we simulate preferential dissolution of calcite minerals while kaolinite minerals are also present in a fractured caprock, under two different initial mineral distributions.

3.3.1. Initial Mineral Distribution: Mixed Structures. In this section, the geometry illustrated in Figure 2 was used with the black and dark gray areas representing calcite and kaolinite minerals, respectively. The domain dimensions, grid resolution, type of flow, and mass transfer boundary conditions are similar to the synthetic mineral case. A constant pressure gradient is applied on the domain such that the average velocity in the entire domain equals to $U = (5 \times 10^{-7} \cdot Pe)$ m/s. The diffusion coefficient for all species is considered to be 10^{-10} m²/s. The initial and inlet species concentrations are listed in Table 1. The inlet solution is assumed to be a CO₂-saturated brine which has a pH around 4 and is undersaturated with respect to calcite with saturation index Ω ($\Omega = \log(Q/K)$, where Q is the ion activity product and K is the equilibrium constant) of -3 . When solving our chemical reaction system in IPHREEQC, there are different speciation and kinetic reactions. Among those reactions, calcite and kaolinite reactions are considered as kinetic reactions. For the calcite reaction, the following reaction rate equation based on the transition state theory (TST) is used [46]:

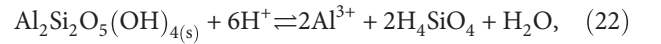
$$R_{\text{CaCO}_3} = \left(k_1 a_{\text{H}^+} + k_2 a_{\text{H}_2\text{CO}_3^*} + k_3 \right) \left(1 - \frac{a_{\text{Ca}^{2+}} a_{\text{CO}_3^{2-}}}{K_{\text{eq,CaCO}_3}} \right), \quad (20)$$

which corresponds to the following reaction:



In (20), a_i is the activity of species i ; R_{CaCO_3} is the reaction rate; k_1 , k_2 , and k_3 are reaction rate constants which are equal to 0.89, 5.01×10^{-4} , and 6.6×10^{-7} mol/(m²·s), respectively. The equilibrium constant of the reaction ($K_{\text{eq,CaCO}_3}$) is $10^{-8.49}$.

The kaolinite reaction is described as



and its overall reaction rate equation is given by [47]:

$$R_{\text{Al}_2\text{Si}_2\text{O}_5(\text{OH})_4} = \left(k_{\text{H}} a_{\text{H}^+}^{0.4} + k_{\text{OH}} a_{\text{OH}^-}^{0.3} \right) \left(1 - \left(\frac{(a_{\text{Al}^{3+}})^2 (a_{\text{H}_4\text{SiO}_4})^2}{(a_{\text{H}^+})^6 K_{\text{eq,Al}_2\text{Si}_2\text{O}_5(\text{OH})_4}} \right)^{0.9} \right), \quad (23)$$

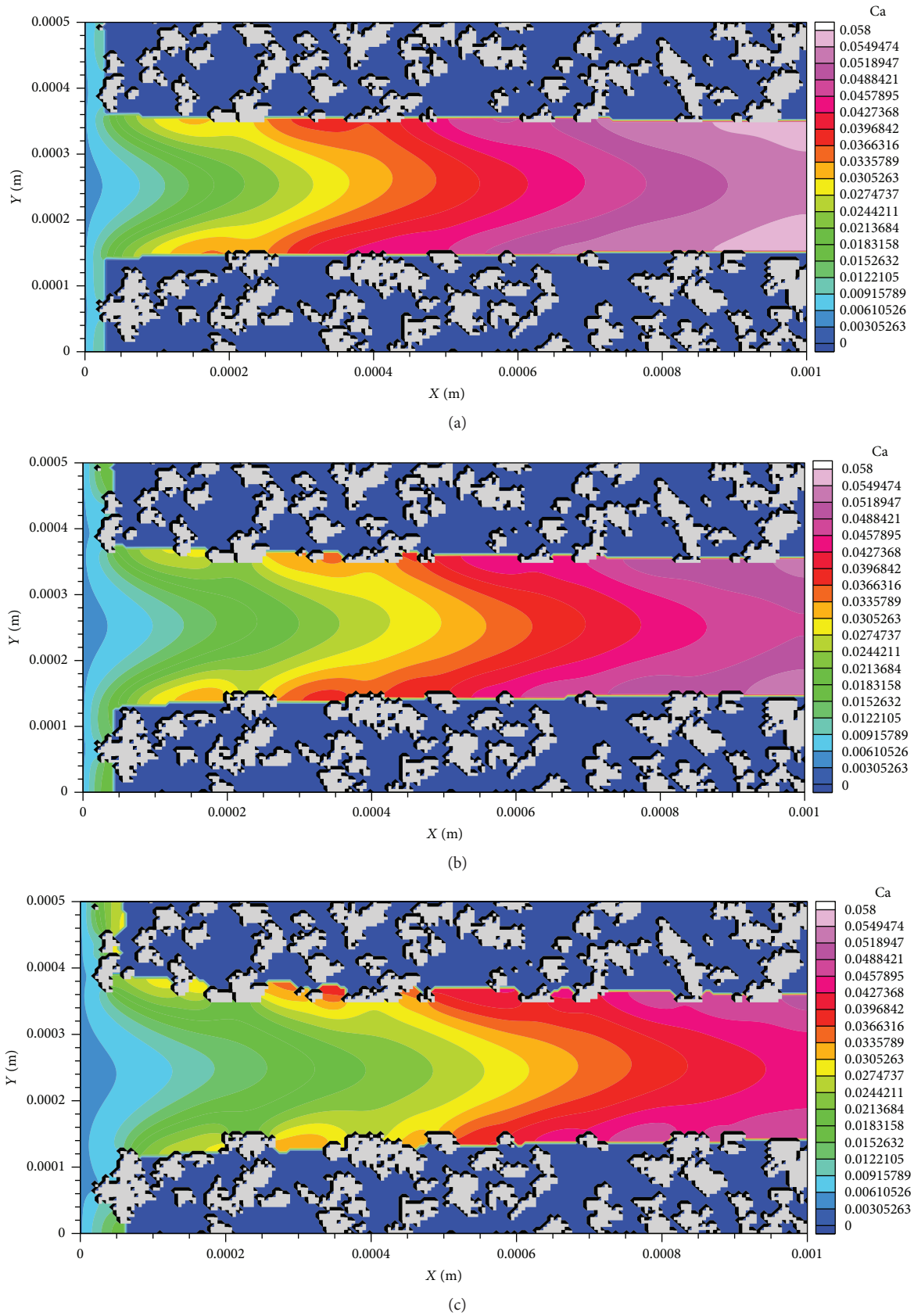


FIGURE 14: Ca concentrations (mol/L) at (a) $t = 1.5$ hr, (b) $t = 4.9$ hr, and (c) $t = 8.7$ hr. In all three cases, $Pe = 2.6$ and kaolinite is illustrated in light gray.

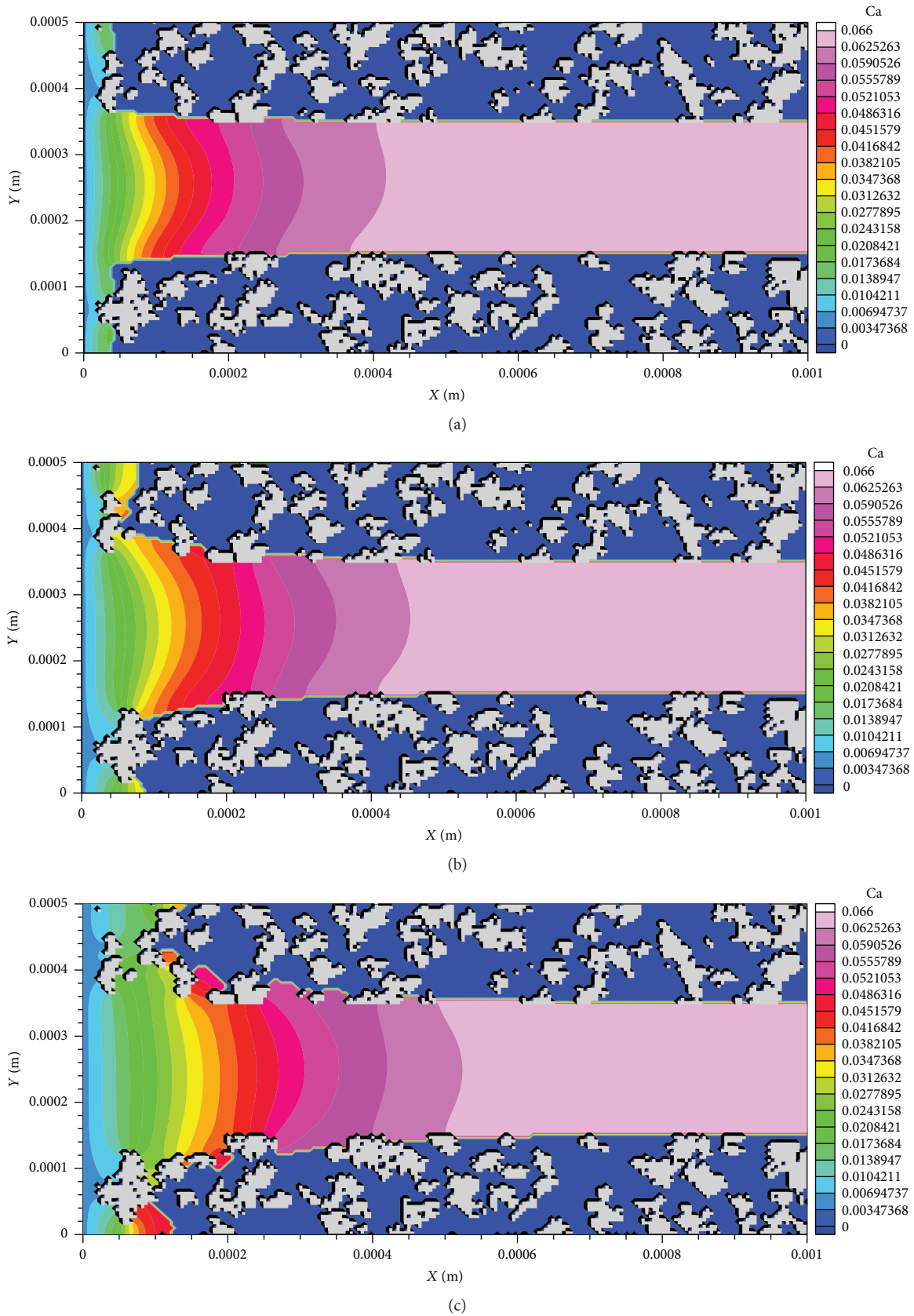


FIGURE 15: Ca concentrations (mol/L) at (a) $t = 6.2$ hr, (b) $t = 20.5$ hr, and (c) $t = 42$ hr. In all three cases, $Pe = 0.026$ and kaolinite is illustrated in light gray.

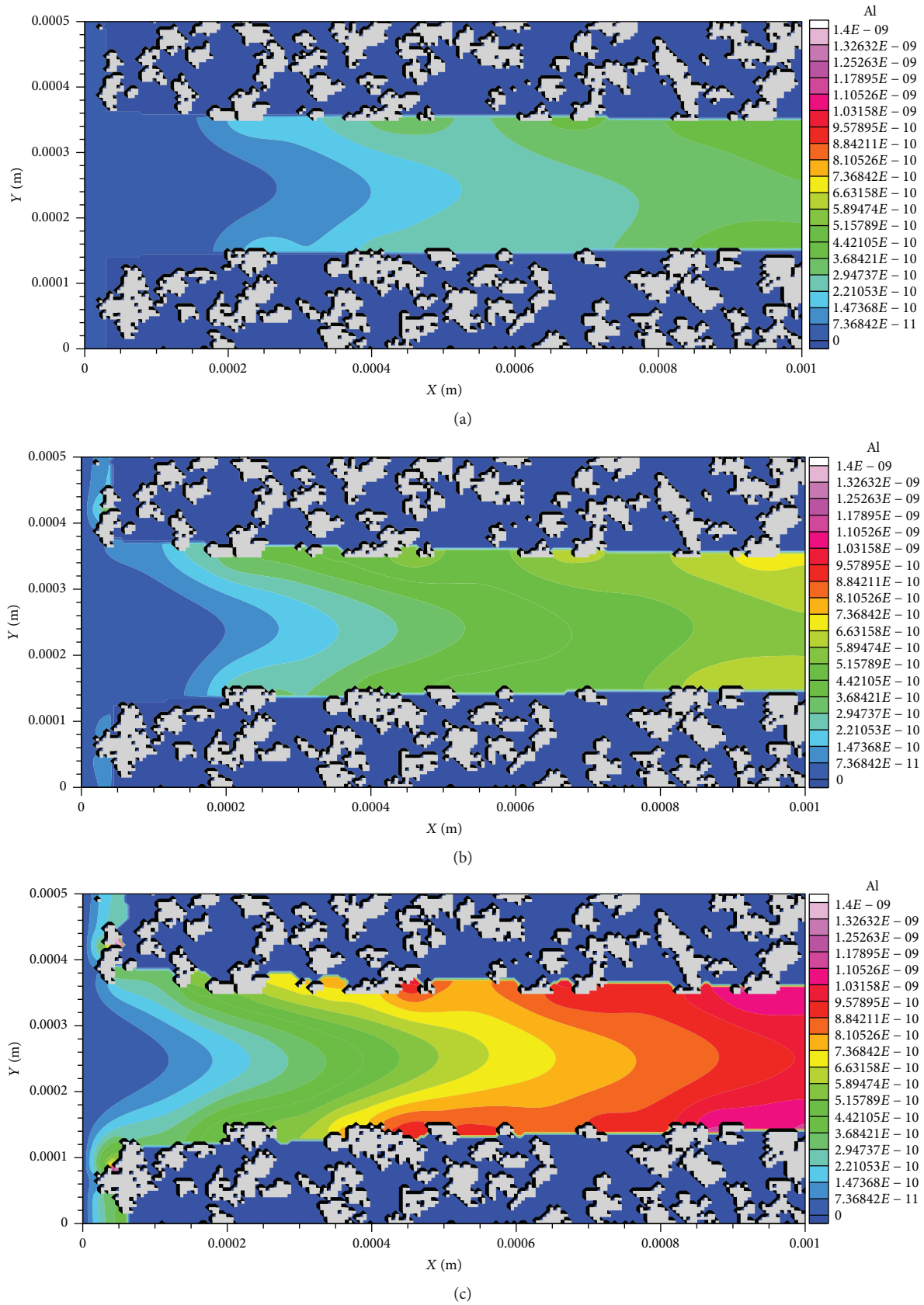


FIGURE 16: Al concentrations (mol/L) at (a) $t = 1.5$ hr, (b) $t = 4.9$ hr, and (c) $t = 8.7$ hr. In all three cases, $Pe = 2.6$ and kaolinite is illustrated in light gray.

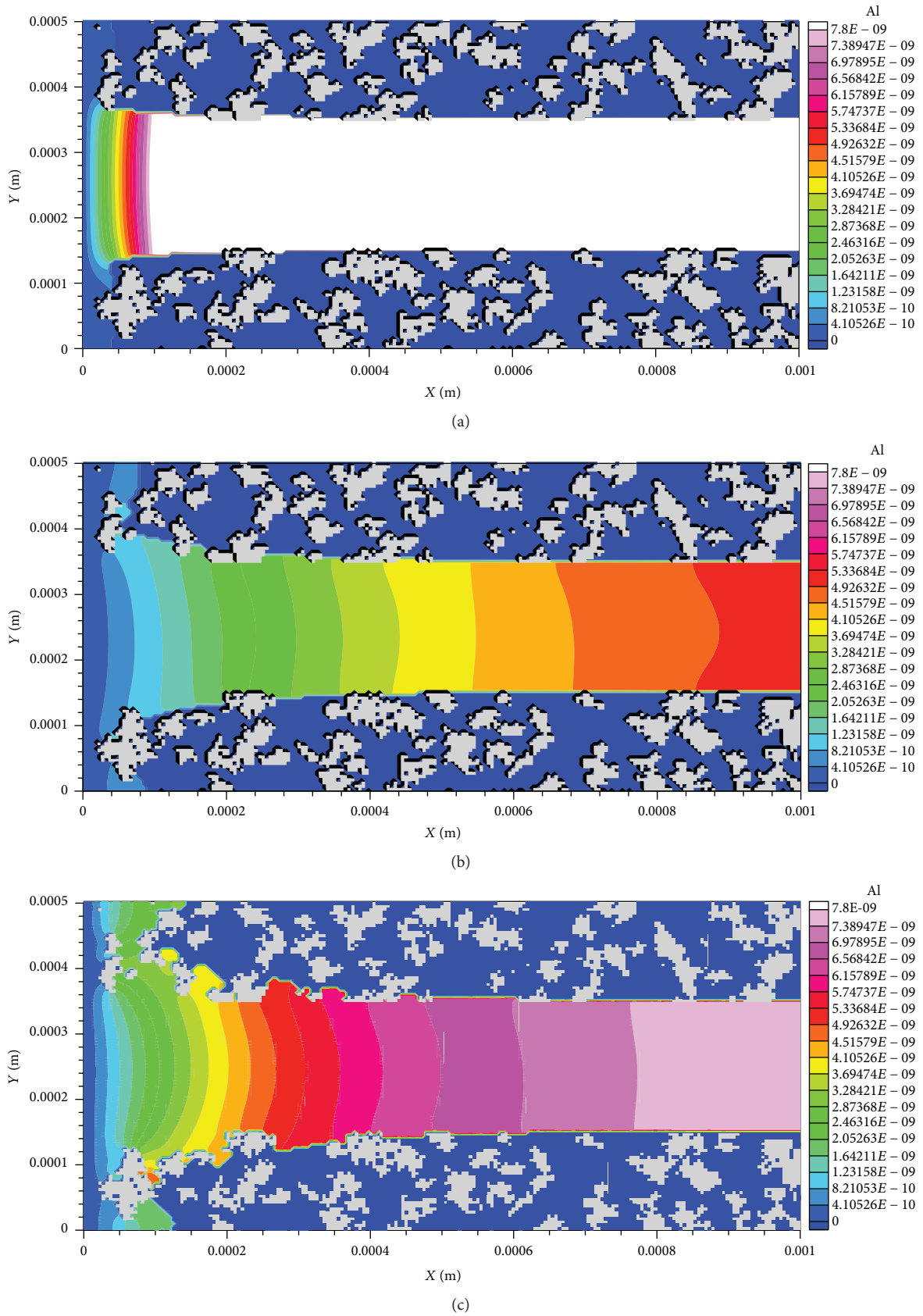


FIGURE 17: Al concentrations (mol/L) at (a) $t = 6.2$ hr, (b) $t = 20.5$ hr, and (c) $t = 42$ hr. In all three cases, $Pe = 0.026$ and kaolinite is illustrated in light gray.

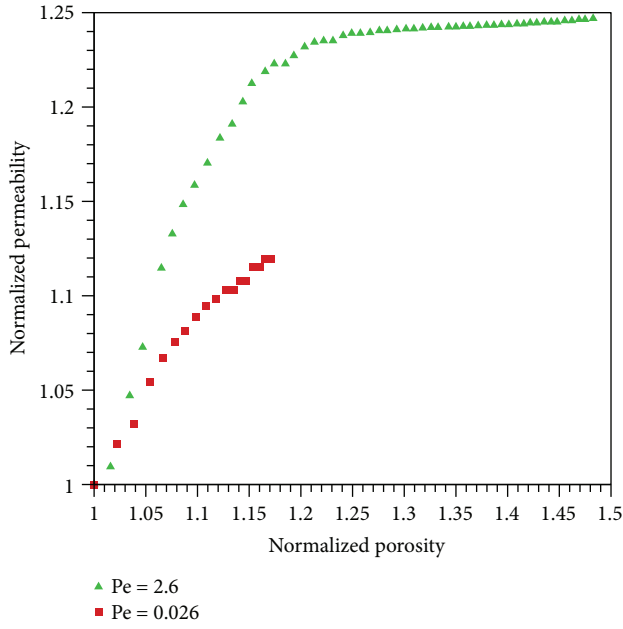


FIGURE 18: Normalized permeability versus normalized porosity at two different Pe numbers for initially mixed mineral assemblage (multispecies case).

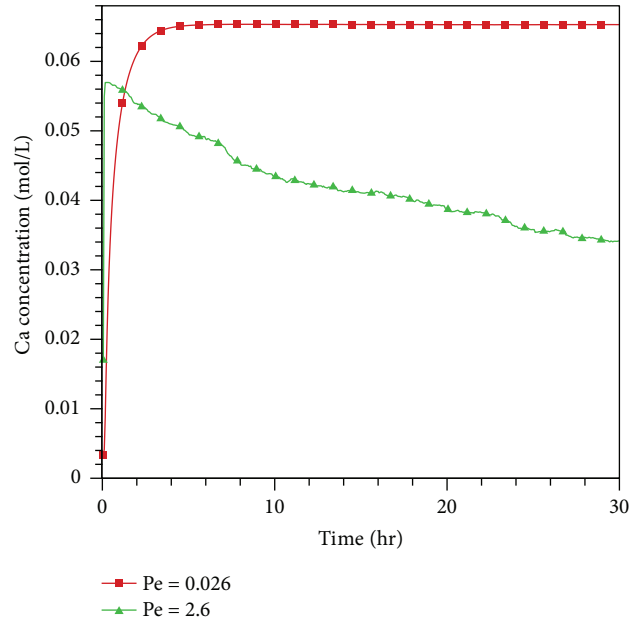


FIGURE 19: Effluent Ca concentrations versus time at two different Pe numbers.

where reaction rate constants k_H and k_{OH} are $10^{-10.8}$ and $10^{-15.7}$ mol/(m²·s), respectively, and reaction equilibrium constant $K_{eq,Al_2Si_2O_5(OH)_4}$ is $10^{7.435}$. It should be pointed out that all the reaction rate and equilibrium constants correspond to 25°C.

We performed simulations at two different Pe numbers of 2.6 and 0.026. Ca and Al concentrations at three different times are shown in Figures 14–17 for these two Pe numbers. As it can be observed in these figures, for the lower Pe number, the dissolution is limited to the inlet (face dissolution) while for the higher Pe number, since the carbonated water can react with more reactive minerals along the fracture length, the dissolution is uniform along the fracture. These two different dissolution patterns (face dissolution and uniform dissolution) cause different permeability values for the fracture. For the face-dissolution case, the aperture increase happens closer to the inlet and a degraded zone forms in this region where it does not contribute to the permeability increase due to the high flow resistance in this layer. However, in the case of uniform dissolution, the aperture increases uniformly throughout the fracture and it has more positive effect on the permeability enhancement. Due to this behavior, it can be seen in Figure 18 that when the flow regime is more diffusive, the permeability is lower than that of a more advective flow regime.

Also, Ca and Al concentrations at the outlet are plotted in Figures 19 and 20, respectively. For the lower Pe number, Ca concentration increases and then it becomes constant whereas for the higher Pe number, it increases to a maximum and then starts decreasing. This behavior

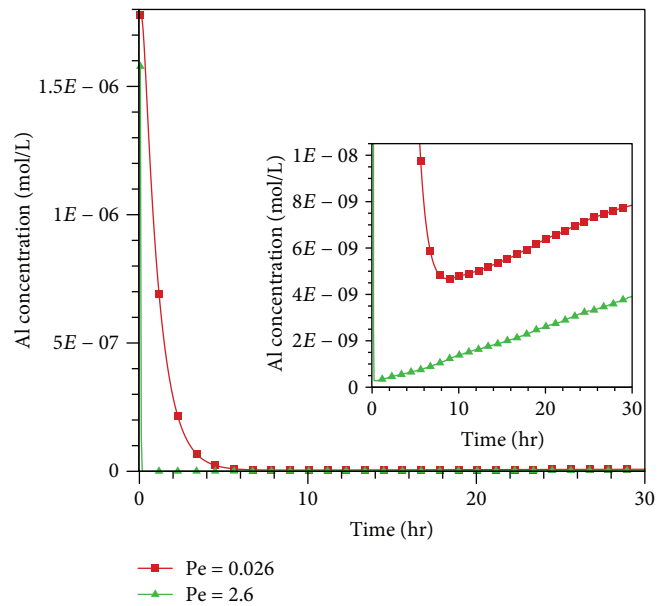


FIGURE 20: Effluent Al concentrations versus time at two different Pe numbers.

can be attributed to a decrease in calcite dissolution rate. When calcite surfaces are near to the main flow channel, the fluid velocity is higher and the fluid reactivity can be maintained along the fracture channel. Hence, the dissolution rate is higher which leads to the increase in Ca concentration. However, when calcite surfaces dissolve and become further away from the main flow channel, the reactive fluid (here, the low-pH solution) cannot

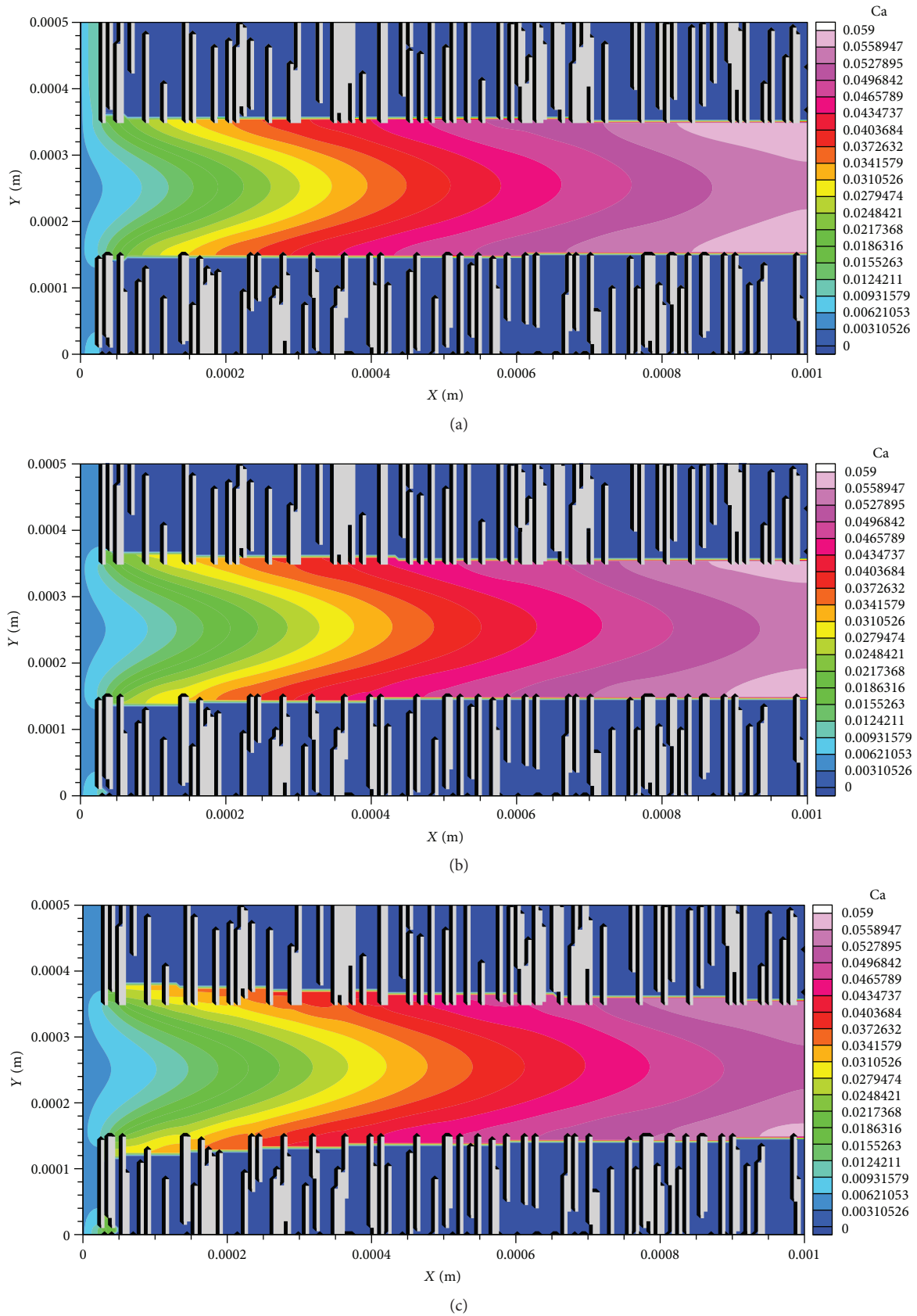


FIGURE 21: Ca concentrations (mol/L) at (a) $t = 1.3$ hr, (b) $t = 2.8$ hr, and (c) $t = 6.4$ hr. In all three cases, $Pe = 2.6$ and kaolinite is illustrated in light gray.

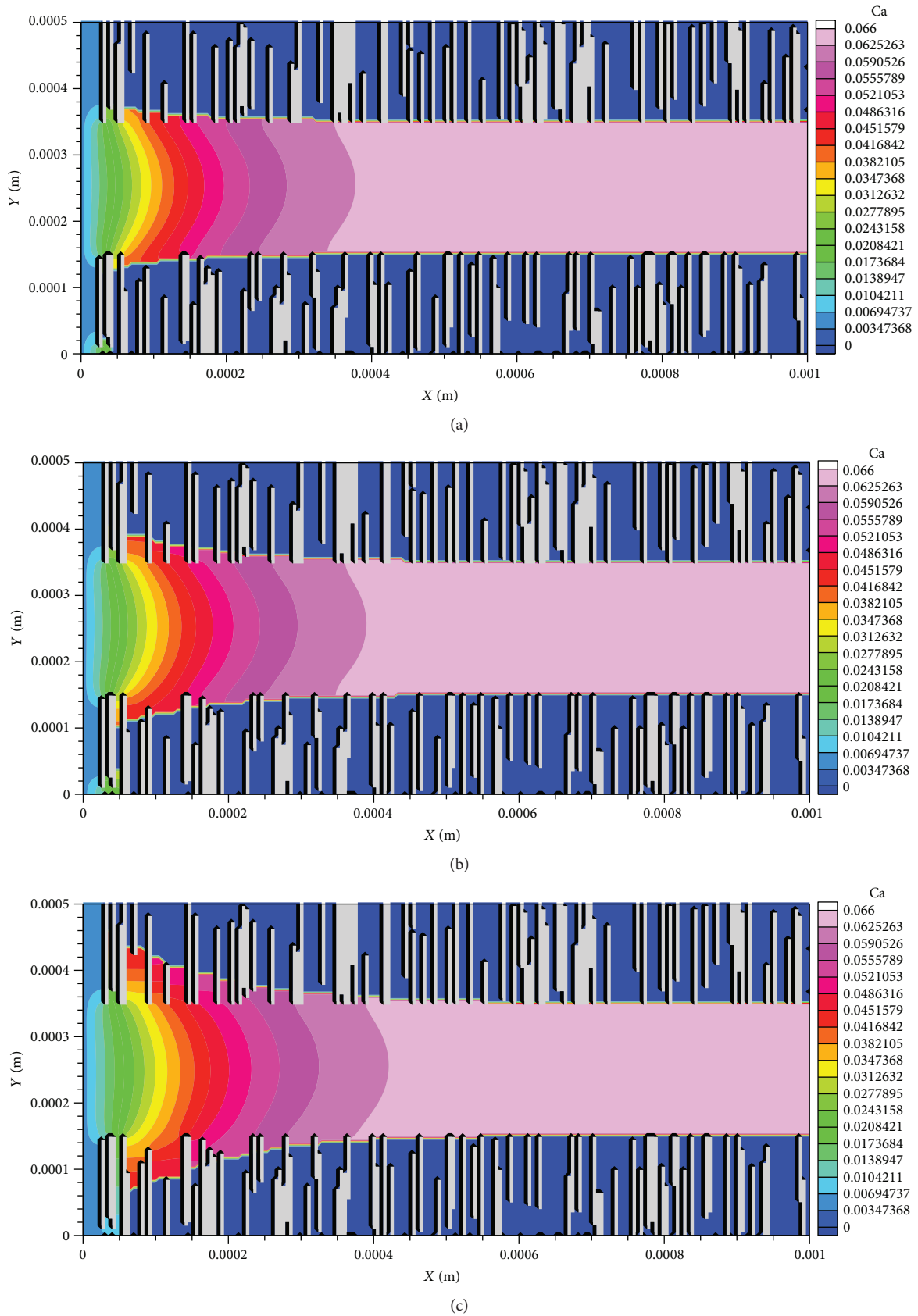


FIGURE 22: Ca concentrations (mol/L) at (a) $t = 5.1$ hr, (b) $t = 12.6$ hr, and (c) $t = 29.3$ hr. In all three cases, $Pe = 0.026$ and kaolinite is illustrated in light gray.

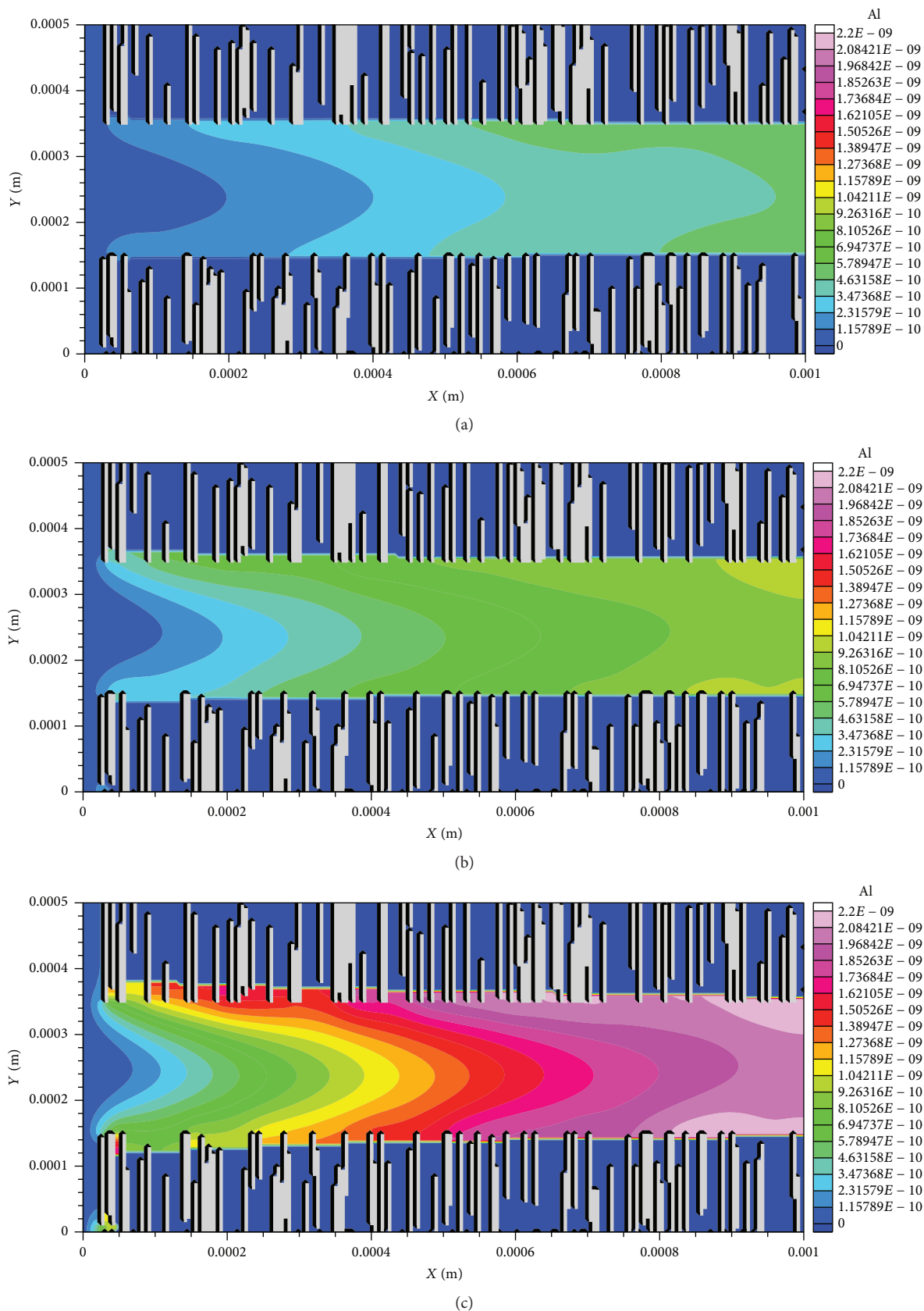


FIGURE 23: Al concentrations (mol/L) at (a) $t = 1.3$ hr, (b) $t = 2.8$ hr, and (c) $t = 6.4$ hr. In all three cases, $Pe = 2.6$ and kaolinite is illustrated in light gray.

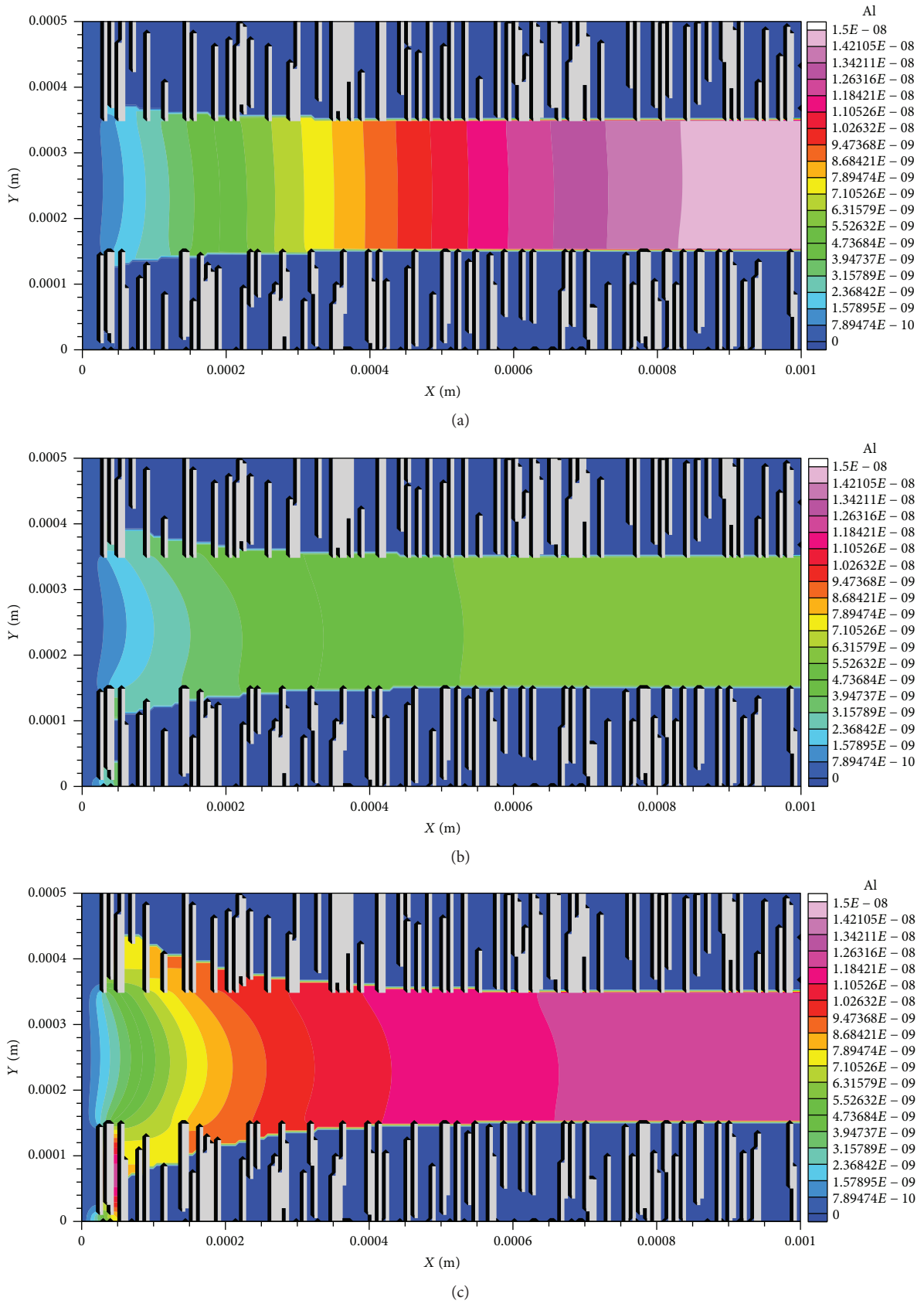


FIGURE 24: Al concentrations (mol/L) at (a) $t = 5.1$ hr, (b) $t = 12.6$ hr, and (c) $t = 29.3$ hr. In all three cases, $Pe = 0.026$ and kaolinite is illustrated in light gray.

easily flow into the degraded zone because the flow barrier is high in this region. Therefore, the solution in those regions becomes buffered, and the saturation index is closer to zero meaning that the rate of calcite dissolution would be lower and limited by diffusion. So, we observe a decreasing trend in the Ca concentration at the outlet. Also, Figure 20 shows that Al concentration decreases quickly when the inlet solution is introduced to the domain. This is because the inlet solution does not contain Al and also kaolinite dissolution rate is very slow, so the Al concentration will decrease in the domain. But a closer look at Figure 20 indicates that after a sharp decrease at the beginning, Al concentration starts to increase very slowly in which this increase confirms the kaolinite dissolution reaction which is of course very slow at the time scale considered here.

3.3.2. Initial Mineral Distribution: Banded Structures. As in Section 3.3.1, we simulate two different cases where $Pe=2.6$ and $Pe=0.026$. Similar dissolution patterns as in the mixed structures can be seen (Figures 21–24); a smaller Pe number results in face dissolution and higher Pe number leads to uniform dissolution. Also, a smaller Pe number translates into lower permeability values compared to the higher permeability values obtained for the higher Pe number (Figure 25). As in the mixed structures, in the banded structure case, when fluid velocity is higher and uniform aperture increase is visible along the fracture walls, dissolution has a more positive role in increasing fracture permeability than the case with lower velocity leading to more localized dissolution near the inlet.

It should be pointed out that in the banded structure, compared to the mixed-structure case, the permeability values are smaller indicating that when nonreactive minerals are distributed as banded structures, they act as a flow barrier and, as can be observed in Figures 26(a) and 26(b), generate more resistance to flow compared to the porous zone formed after dissolution in the case of mixed structures.

Also, similar to the mixed-structure case, while calcite dissolves and recedes from the main flow channel, the rate of calcite dissolution decreases due to buffering effect and lower velocity in the areas between two vertical kaolinite bands (comb-tooth zones). This will cause a decrease in Ca concentration after it reaches a maximum at the beginning (Figure 27). However, Figure 28 displays that effluent Ca concentrations for the case of banded structures are higher than those of mixed structures. Although in both cases of mixed and banded structures, after calcite dissolution, the calcite surfaces will be further away from the main flow channel, but as Figure 26 showed, in the case of a banded structure, it would be more difficult for the carbonated water to enter the comb-tooth zone compared to the degraded zone. Therefore, in the case of mixed structures, the extent of buffering would be more than the banded structure case, and that is why lower Ca concentrations are observed at the outlet for mixed-structure cases.

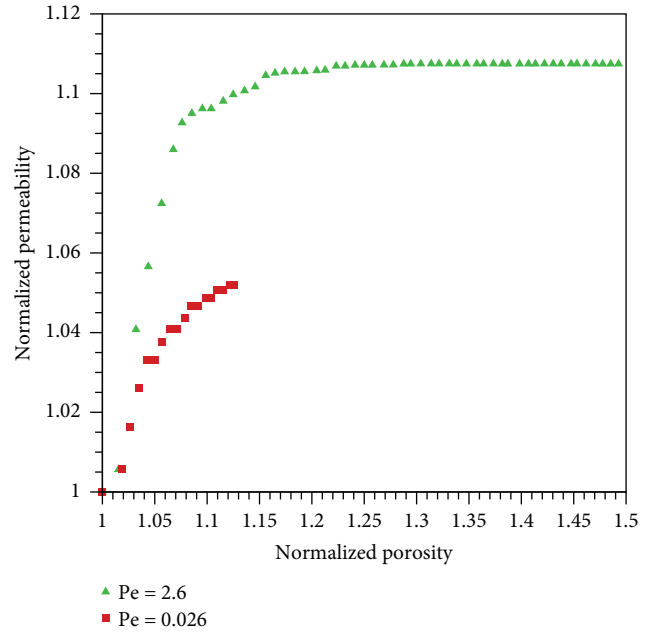


FIGURE 25: Normalized permeability versus normalized porosity at two different Pe numbers for an initially banded mineral assemblage (multispecies case).

Also, higher concentrations of Al between thinner kaolinite bands near to the inlet (Figures 23(c) and 24(c)), also confirm the increasing trend in Al concentration indicated in Figure 29.

4. Conclusions

In this study, a previously developed LBM transport solver coupled with IPHREEQC has been extended for simulating advective-diffusive reactive transport. The LBM was used to investigate the effects of initial mineral spatial heterogeneity on textural alteration of a fracture and consequently on its hydrodynamic properties. The LBM coupled with IPHREEQC geochemical solver enables us to model a broad range of different geochemical reactions. To simulate the effects of different mineral spatial distributions, synthetic models were constructed. Results showed that the generated degraded and comb-tooth zones [3] as observed in experiments done by Ellis et al. [2] will cause the permeability of the fracture to increase until a steady-state condition while in most of continuum-scale models, a power-law relation is used for permeability-porosity relationship which can overestimate the permeability values when multiminerals exist in the system. In addition to the existence of different minerals, this permeability-porosity relation is a function of transport and reaction conditions. At a constant Da number, increasing Pe causes higher permeability values, and at constant Pe , increasing the Da number will lead to a permeability decrease.

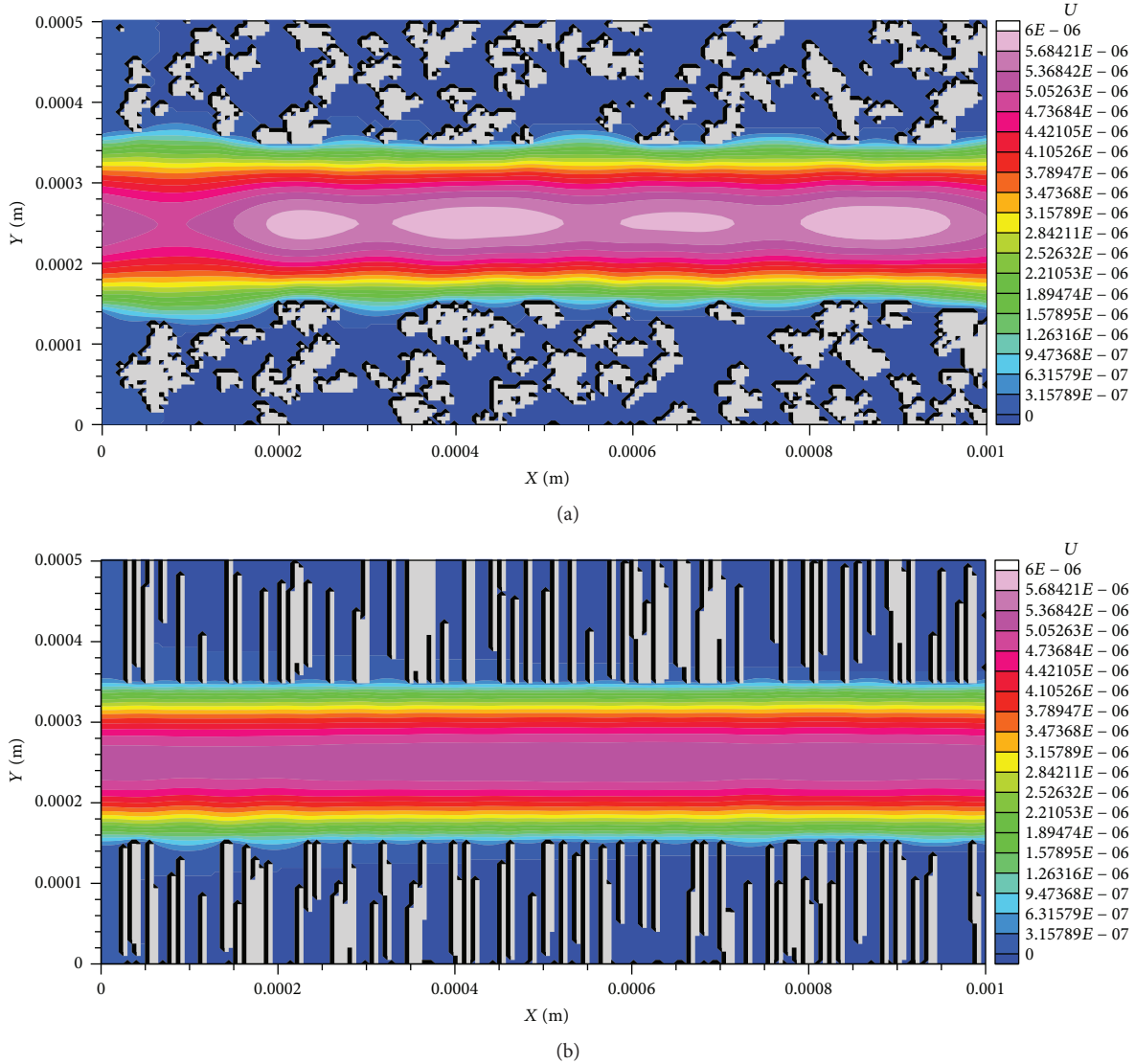


FIGURE 26: Velocity profile (m/s) for cases with (a) mixed and (b) banded structures when $Pe = 2.6$ for a multispecies case. In both (a) and (b), porosity (after dissolution) is near 0.47 but permeability (after dissolution) is $1.58 \times 10^{-9} \text{ m}^2$ for (a) and $1.43 \times 10^{-9} \text{ m}^2$ for (b).

Moreover, to show the ability of the LBM model for realistic cases, we simulated a case with calcite and kaolinite minerals which were assumed to represent two main minerals in a rock matrix around a single fracture inside a caprock. It was observed that the tortuosity in the degraded zone (in the case of initially mixed distributions) and distance from the main flow channel (in the case of initially banded structures) lowers the permeability of the fracture. Also, a decreasing trend in the effluent Ca concentration confirmed the effect of degraded and comb-tooth zones on decreasing the dissolution rate of calcite in those regions.

3D simulations need to be done in order to better understand the effects of initial mineral distributions on fracture hydrodynamic properties. The developed LBM can also be used to simulate the 3D geometries as well, and this will be published in a future work.

Appendix

A. Validation of LBM Model

The applicability of the current LBM approach (without flow solver) used in this work has been previously demonstrated for ion exchange problems [48] or cases in which reactions were at local equilibrium [30]. In this study, we will perform two different benchmark tests to show the performance of our LBM model where kinetic reactions exist in the problem.

A.1 Reaction-Diffusion of a Single Species in a Square Domain. This benchmark shows how a single species A (with constant concentration) diffuses from left boundary into a square domain with size $a \times b$ (Figure 30) and reacts with a solid A_s (according to the reaction $A \rightleftharpoons A_s$)

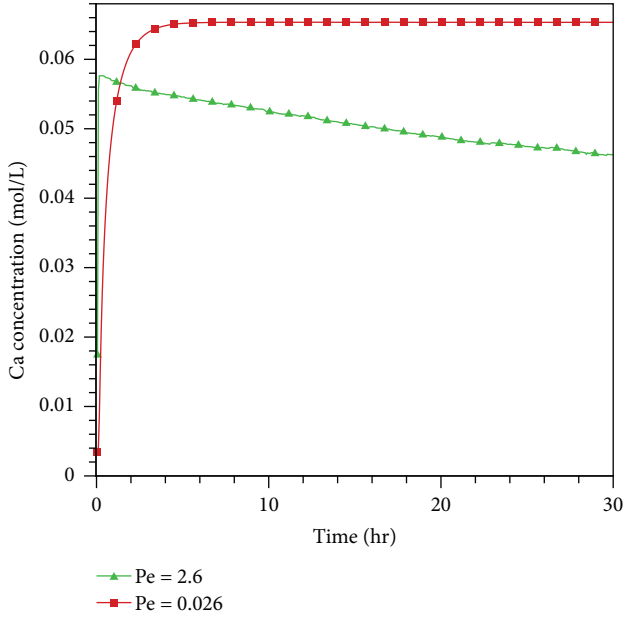


FIGURE 27: Effluent Ca concentrations versus time at two different Pe numbers.

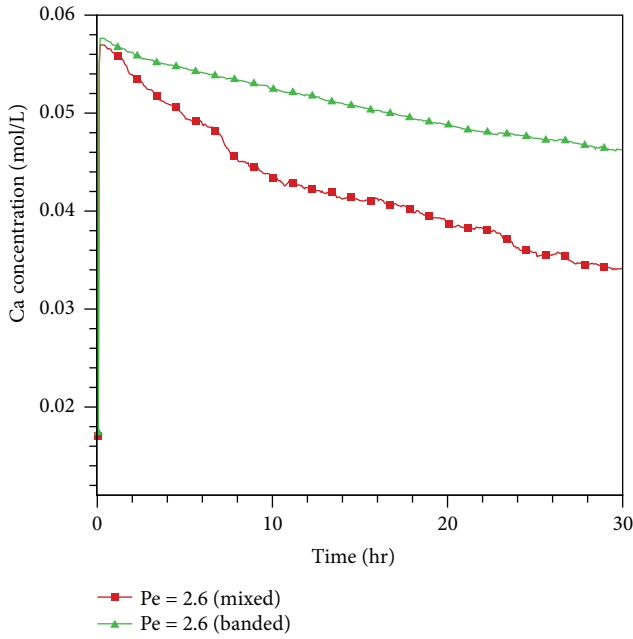


FIGURE 28: Effluent Ca concentrations versus time for mixed and banded structures when Pe = 2.6.

at the top boundary. The governing equation for the stationary condition is [19]

$$\frac{\partial^2 c}{\partial x^2} + \frac{\partial^2 c}{\partial y^2} = 0, \quad (\text{A.1})$$

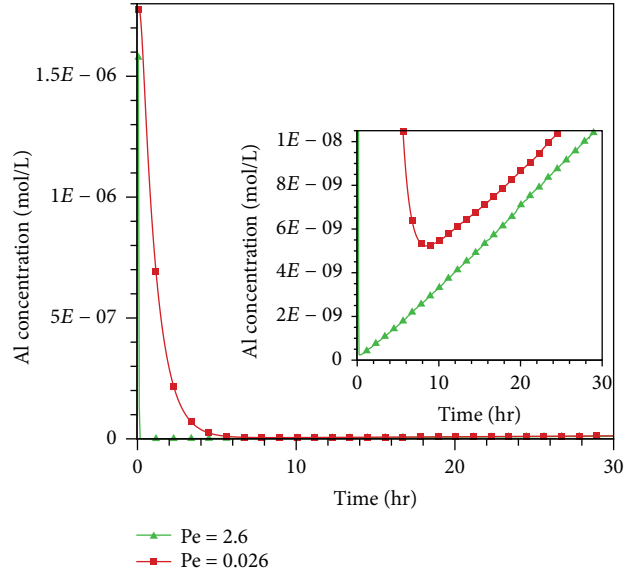


FIGURE 29: Effluent Al concentrations versus time at two different Pe numbers.

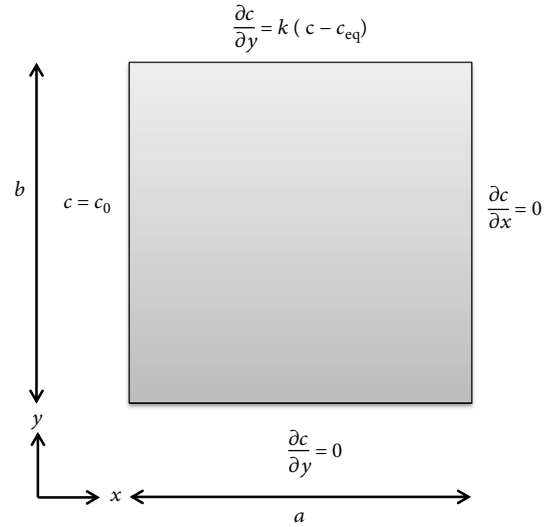


FIGURE 30: Schematic of the domain used for single-species reaction-diffusion benchmark.

with the boundary conditions

$$\begin{aligned} c(0, y) &= c_0, \\ \frac{\partial c}{\partial y}(x, y=b) &= k(c - c_{eq}), \\ \frac{\partial c}{\partial y}(x, 0) &= 0, \\ \frac{\partial c}{\partial x}(a, y) &= 0. \end{aligned} \quad (\text{A.2})$$

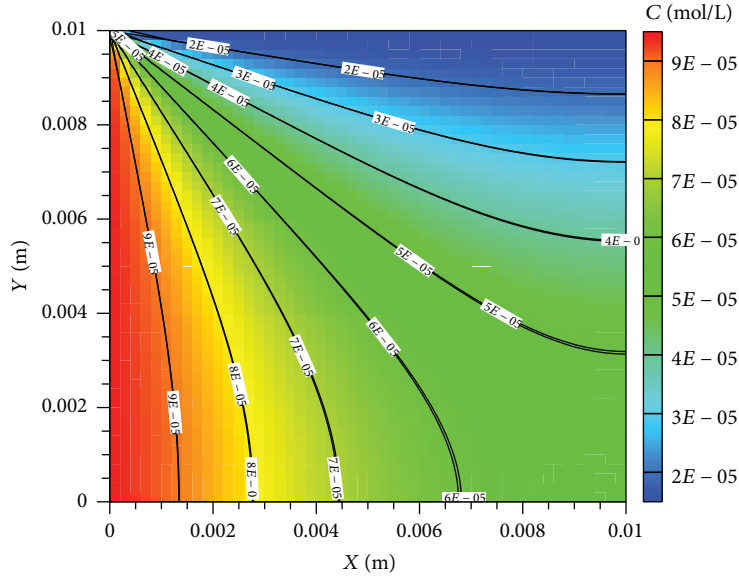


FIGURE 31: Steady-state concentrations, obtained by analytical (contour and solid lines) and LB (dashed lines) methods, for a single species diffusing through the left boundary of a square domain and reacting at the top boundary according to a first-order reaction while other boundaries are zero concentration gradients.

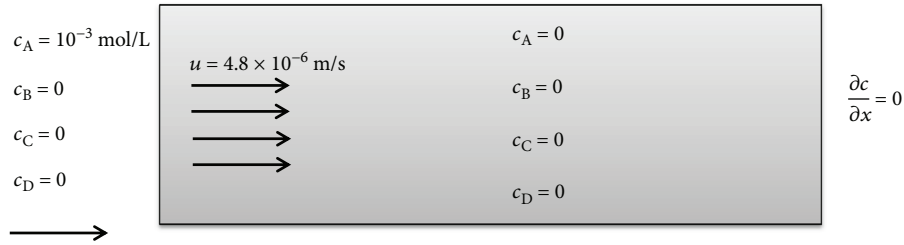


FIGURE 32: Sketch of domain used for 1D simulation of advection-diffusion-reaction of four species involved in a chain of decay reactions. The left boundary is maintained at constant concentration for different species, and the right boundary is a zero concentration gradient.

The analytical solution of (A.1) is [49]

$$c(x, y) = (c_0 - c_{eq}) \sum_{n=0}^{\infty} \frac{\sin(\beta_n b)}{N_n^2 \beta_n} \cdot \frac{\cosh(\beta(x-a))}{\cosh(\beta_n a)} \cos(\beta_n y) + c_{eq}, \quad (\text{A.3})$$

where

$$N_n^2 = \frac{b}{2} \left(1 + \frac{\sin(2\beta_n b)}{2\beta_n b} \right), \quad (\text{A.4})$$

and β_n can be calculated by solving the following equation:

$$(\beta_n b) \tan(\beta_n b) = \frac{kb}{D}. \quad (\text{A.5})$$

In the above equations, c is species concentration, c_0 is concentration at the inlet, c_{eq} is initial concentration at the

domain, k is reaction rate constant, and D is diffusion coefficient. To compute the analytical and numerical solutions of the problem, a domain size of $1 \text{ cm} \times 1 \text{ cm}$ was considered which was discretized into 50×50 grids for the LBM. Inlet and equilibrium (initial) concentrations are $10 \times 10^{-5} \text{ mol/L}$ and $1 \times 10^{-5} \text{ mol/L}$, respectively. Also, the values used for reaction rate and diffusion constants are $4.8 \times 10^{-3} \text{ m/s}$ and $10^{-9} \text{ m}^2/\text{s}$, respectively. As it was mentioned earlier, the reaction part is done using IPHREEQC. Figure 31 shows the steady-state solution obtained using analytical (the contour map and solid lines) and numerical (dashed lines) LBM. As it can be observed, analytical and numerical methods agree very well indicating the ability of the proposed LBM coupled with IPHREEQC.

A.2 Advection-Diffusion-Reaction of Multispecies Involved in a Kinetic Decay-Chain. To further verify the implementation of a coupled LBM-IPHREEQC reactive transport model, a 1D simulation of advection-diffusion-reaction (ADR) was considered in which four different species A,

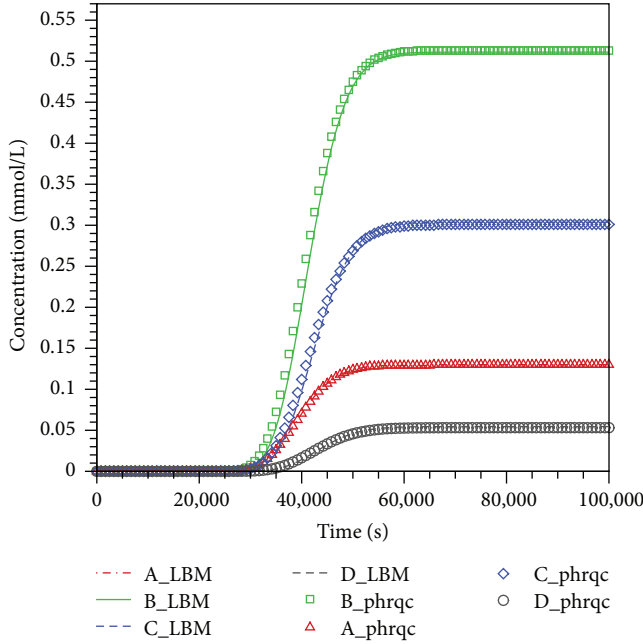


FIGURE 33: Breakthrough curves for four different species at the outlet of a domain where species A is injected into the domain and a chain of decay reactions occurs between four species. Different lines show the results obtained with the LBM approach, and symbols indicate the results simulated using PHREEQC.

B, C, and D are reacting according to the following decay reactions [50, 51].

$$R_A = \frac{dc_A}{dt} = -k_A c_A, \quad (\text{A.6})$$

$$R_B = \frac{dc_B}{dt} = k_A c_A - k_B c_B, \quad (\text{A.7})$$

$$R_C = \frac{dc_C}{dt} = k_B c_B - k_C c_C, \quad (\text{A.8})$$

$$R_D = \frac{dc_D}{dt} = k_C c_C - k_D c_D, \quad (\text{A.9})$$

where R_i ($i = A, B, C,$ and D) refers to the reaction rate, c_i is species concentration, and k_i is the reaction rate constant. As illustrated in Figure 32, species A with constant concentration of 10^{-3} mol/L is introduced to the domain (with a length of 0.2 m) from inlet while other species concentrations are kept zero at this boundary. All other boundaries have a zero-gradient boundary condition for concentration. The initial concentration for all species is zero. Velocity is constant and equal to 4.8×10^{-6} m/s and diffusion coefficient is 10^{-8} m²/s. Once A enters the domain, a chain of decay reactions occurs according to (A.6)–(A.9). In these equations k_A , k_B , k_C , and k_D are 5×10^{-4} , 2×10^{-4} , 1×10^{-4} , and 5×10^{-5} 1/s, respectively. The simulation was run until 10^5 s, and comparisons of the results were made between the reactive transport modules of PHREEQC and LBM-IPHREEQC. The breakthrough curves for different species concentrations have been plotted in Figure 33. Results show a very good agreement

between both solvers confirming the correctness of coupling of LBM with IPHREEQC.

Conflicts of Interest

The authors declare that there is no conflict of interest regarding the publication of this paper.

Acknowledgments

Funding for this study was provided by the PROTECT project (no. 233736) financed by the Research Council of Norway, Total E&P, and DEA which is gratefully acknowledged.

References

- [1] C.-F. Tsang, J. Birkholzer, and J. Rutqvist, “A comparative review of hydrologic issues involved in geologic storage of CO₂ and injection disposal of liquid waste,” *Environmental Geology*, vol. 54, no. 8, pp. 1723–1737, 2008.
- [2] B. Ellis, C. Peters, J. Fitts et al., “Deterioration of a fractured carbonate caprock exposed to CO₂-acidified brine flow,” *Greenhouse Gases: Science and Technology*, vol. 1, no. 3, pp. 248–260, 2011.
- [3] J. P. Fitts and C. A. Peters, “Caprock fracture dissolution and CO₂ leakage,” *Reviews in Mineralogy and Geochemistry*, vol. 77, no. 1, pp. 459–479, 2013.
- [4] H. Deng, S. Molins, C. Steefel et al., “A 2.5D reactive transport model for fracture alteration simulation,” *Environmental Science & Technology*, vol. 50, no. 14, pp. 7564–7571, 2016.
- [5] H. Deng, M. Voltolini, S. Molins et al., “Alteration and erosion of rock matrix bordering a carbonate-rich shale fracture,” *Environmental Science & Technology*, vol. 51, no. 15, pp. 8861–8868, 2017.
- [6] F. Gherardi, T. Xu, and K. Pruess, “Numerical modeling of self-limiting and self-enhancing caprock alteration induced by CO₂ storage in a depleted gas reservoir,” *Chemical Geology*, vol. 244, no. 1-2, pp. 103–129, 2007.
- [7] F. Liu, P. Lu, C. Zhu, and Y. Xiao, “Coupled reactive flow and transport modeling of CO₂ sequestration in the Mt. Simon sandstone formation, Midwest U.S.A.,” *International Journal of Greenhouse Gas Control*, vol. 5, no. 2, pp. 294–307, 2011.
- [8] J. P. Nogue, J. P. Fitts, M. A. Celia, and C. A. Peters, “Permeability evolution due to dissolution and precipitation of carbonates using reactive transport modeling in pore networks,” *Water Resources Research*, vol. 49, no. 9, pp. 6006–6021, 2013.
- [9] C. I. Steefel, S. Molins, and D. Trebotich, “Pore scale processes associated with subsurface CO₂ injection and sequestration,” *Reviews in Mineralogy and Geochemistry*, vol. 77, no. 1, pp. 259–303, 2013.
- [10] M. Liu and P. Mostaghimi, “Characterisation of reactive transport in pore-scale correlated porous media,” *Chemical Engineering Science*, vol. 173, pp. 121–130, 2017.
- [11] S. Molins, D. Trebotich, G. H. Miller, and C. I. Steefel, “Mineralogical and transport controls on the evolution of porous media texture using direct numerical simulation,” *Water Resources Research*, vol. 53, no. 5, pp. 3645–3661, 2017.
- [12] L. Algive, S. Bekri, and O. Vizika, “Pore-network modeling dedicated to the determination of the petrophysical-property

- changes in the presence of reactive fluid,” *SPE Journal*, vol. 15, no. 3, pp. 618–633, 2010.
- [13] C. Z. Qin, S. M. Hassanizadeh, and A. Ebigbo, “Pore-scale network modeling of microbially induced calcium carbonate precipitation: insight into scale dependence of biogeochemical reaction rates,” *Water Resources Research*, vol. 52, no. 11, pp. 8794–8810, 2016.
- [14] J. Pereira Nunes, M. Blunt, and B. Bijeljic, “Pore-scale simulation of carbonate dissolution in micro-CT images,” *Journal of Geophysical Research: Solid Earth*, vol. 121, no. 2, pp. 558–576, 2016.
- [15] S. Oveysi and M. Piri, “Pore-space alteration induced by brine acidification in subsurface geologic formations,” *Water Resources Research*, vol. 50, no. 1, pp. 440–452, 2014.
- [16] S. Kim and J. C. Santamarina, “Reactive fluid flow in CO₂ storage reservoirs: a 2-D pore network model study,” *Greenhouse Gases: Science and Technology*, vol. 5, no. 4, pp. 462–473, 2015.
- [17] C. Varloteaux, M. T. Vu, S. Békri, and P. M. Adler, “Reactive transport in porous media: pore-network model approach compared to pore-scale model,” *Physical Review E*, vol. 87, no. 2, article 023010, 2013.
- [18] M. Liu, M. Shabaninejad, and P. Mostaghimi, “Impact of mineralogical heterogeneity on reactive transport modelling,” *Computers & Geosciences*, vol. 104, pp. 12–19, 2017.
- [19] Q. Kang, P. C. Lichtner, and D. Zhang, “An improved lattice Boltzmann model for multicomponent reactive transport in porous media at the pore scale,” *Water Resources Research*, vol. 43, no. 12, 2007.
- [20] Q. Kang, P. C. Lichtner, and D. Zhang, “Lattice Boltzmann pore-scale model for multicomponent reactive transport in porous media,” *Journal of Geophysical Research: Solid Earth*, vol. 111, no. B5, 2006.
- [21] Q. Kang, D. Zhang, S. Chen, and X. He, “Lattice Boltzmann simulation of chemical dissolution in porous media,” *Physical Review E*, vol. 65, no. 3, article 036318, 2002.
- [22] E. S. Boek, I. Zacharoudiou, F. Gray, S. M. Shah, J. P. Crawshaw, and J. Yang, “Multiphase-flow and reactive-transport validation studies at the pore scale by use of lattice Boltzmann computer simulations,” *SPE Journal*, vol. 22, no. 3, 2017.
- [23] Q. Kang, P. C. Lichtner, H. S. Viswanathan, and A. I. Abdel-Fattah, “Pore scale modeling of reactive transport involved in geologic CO₂ sequestration,” *Transport in Porous Media*, vol. 82, no. 1, pp. 197–213, 2010.
- [24] M. Liu and P. Mostaghimi, “Pore-scale modelling of CO₂ storage in fractured coal,” *International Journal of Greenhouse Gas Control*, vol. 66, pp. 246–253, 2017.
- [25] M. Liu and P. Mostaghimi, “Pore-scale simulation of dissolution-induced variations in rock mechanical properties,” *International Journal of Heat and Mass Transfer*, vol. 111, pp. 842–851, 2017.
- [26] L. Chen, Q. Kang, H. S. Viswanathan, and W. Q. Tao, “Pore-scale study of dissolution-induced changes in hydrologic properties of rocks with binary minerals,” *Water Resources Research*, vol. 50, no. 12, pp. 9343–9365, 2014.
- [27] A. Hiorth, E. Jettestuen, L. M. Cathles, and M. V. Madland, “Precipitation, dissolution, and ion exchange processes coupled with a lattice Boltzmann advection diffusion solver,” *Geochimica et Cosmochimica Acta*, vol. 104, pp. 99–110, 2013.
- [28] J. Gao, H. Xing, Z. Tian et al., “Reactive transport in porous media for CO₂ sequestration: pore scale modeling using the lattice Boltzmann method,” *Computers & Geosciences*, vol. 98, pp. 9–20, 2017.
- [29] Q. Kang, D. Zhang, and S. Chen, “Simulation of dissolution and precipitation in porous media,” *Journal of Geophysical Research: Solid Earth*, vol. 108, no. B10, 2003.
- [30] R. A. Patel, J. Perko, D. Jacques, G. De Schutter, K. Van Breugel, and G. Ye, “A versatile pore-scale multicomponent reactive transport approach based on lattice Boltzmann method: application to portlandite dissolution,” *Physics and Chemistry of the Earth, Parts A/B/C*, vol. 70–71, pp. 127–137, 2014.
- [31] Z. Tian and J. Wang, “Lattice Boltzmann simulation of CO₂ reactive transport in network fractured media,” *Water Resources Research*, vol. 53, no. 8, pp. 7366–7381, 2017.
- [32] Z. Tian and J. Wang, “Lattice Boltzmann simulation of dissolution-induced changes in permeability and porosity in 3D CO₂ reactive transport,” *Journal of Hydrology*, vol. 557, pp. 276–290, 2018.
- [33] A. Fakhari, Y. Li, D. Bolster, and K. T. Christensen, “A phase-field lattice Boltzmann model for simulating multiphase flows in porous media: application and comparison to experiments of CO₂ sequestration at pore scale,” *Advances in Water Resources*, vol. 114, pp. 119–134, 2018.
- [34] R. Patel, *Lattice Boltzmann Method Based Framework for Simulating Physico-Chemical Processes in Heterogeneous Porous Media and Its Application to Cement Paste*, Ghent University, Ghent, Belgium, 2016.
- [35] E. Skurtveit, E. Skurtveit, L. Grande et al., “Mechanical testing and sealing capacity of the Upper Jurassic Draupne Formation, North Sea,” in *49th U.S. Rock Mechanics/Geomechanics Symposium*, San Francisco, CA, USA, June–July 2015.
- [36] W. Graebel, *Advanced Fluid Mechanics*, Academic Press, Cambridge, MA, USA, 2007.
- [37] T. Krüger, H. Kusumaatmaja, A. Kuzmin, O. Shardt, G. Silva, and E. M. Viggen, *The Lattice Boltzmann Method*, Springer, 2017.
- [38] S. Chapman and T. G. Cowling, “The mathematical theory of non-uniform gases: an account of the kinetic theory of viscosity, thermal conduction and diffusion in gases,” Cambridge University Press, Cambridge, UK, 1970.
- [39] C. Steefel, C. A. J. Appelo, B. Arora et al., “Reactive transport codes for subsurface environmental simulation,” *Computational Geosciences*, vol. 19, no. 3, pp. 445–478, 2015.
- [40] F. Verhaeghe, J. Liu, M. Guo, S. Arnout, B. Blanpain, and P. Wollants, “Dissolution and diffusion behavior of Al₂O₃ in a Ca O–Al₂ O₃–SiO₂ liquid: an experimental-numerical approach,” *Applied Physics Letters*, vol. 91, no. 12, article 124104, 2007.
- [41] X. He, N. Li, and B. Goldstein, “Lattice Boltzmann simulation of diffusion-convection systems with surface chemical reaction,” *Molecular Simulation*, vol. 25, no. 3–4, pp. 145–156, 2000.
- [42] F. Verhaeghe, S. Arnout, B. Blanpain, and P. Wollants, “Lattice-Boltzmann modeling of dissolution phenomena,” *Physical Review E*, vol. 73, no. 3, article 036316, 2006.
- [43] S. R. Charlton and D. L. Parkhurst, “Modules based on the geochemical model PHREEQC for use in scripting and programming languages,” *Computers & Geosciences*, vol. 37, no. 10, pp. 1653–1663, 2011.
- [44] M. Wang, J. Wang, N. Pan, and S. Chen, “Mesoscopic predictions of the effective thermal conductivity for microscale

- random porous media,” *Physical Review E*, vol. 75, no. 3, article 036702, 2007.
- [45] P. Szymczak and A. J. Ladd, “Instabilities in the dissolution of a porous matrix,” *Geophysical Research Letters*, vol. 38, no. 7, 2011.
- [46] L. Chou, R. M. Garrels, and R. Wollast, “Comparative study of the kinetics and mechanisms of dissolution of carbonate minerals,” *Chemical Geology*, vol. 78, no. 3-4, pp. 269–282, 1989.
- [47] L. Li, C. A. Peters, and M. A. Celia, “Upscaling geochemical reaction rates using pore-scale network modeling,” *Advances in Water Resources*, vol. 29, no. 9, pp. 1351–1370, 2006.
- [48] R. A. Patel, J. Perko, D. Jaques, G. De Schutter, G. Ye, and K. Van Breugel, “Lattice Boltzmann based multicomponent reactive transport model coupled with geochemical solver for scale simulations,” in *Coupled Problems 2013: Proceedings of the 5th International Conference on Computational Methods for Coupled Problems in Science and Engineering, Ibiza*, pp. 806–817, Ibiza, Spain, June 2013.
- [49] H. Carslaw and J. Jaeger, *Conduction of Heat in Solids*, Oxford Univ. Press, Oxford, 1959.
- [50] D. L. Parkhurst, K. L. Kipp, and S. R. Charlton, *PHAST Version 2—A program for simulating groundwater flow, solute transport, and multicomponent geochemical reactions*, US Geological Survey Techniques and Methods, 2010, 6, A35.
- [51] D. L. Parkhurst and L. Wissmeier, “PhreeqcRM: a reaction module for transport simulators based on the geochemical model PHREEQC,” *Advances in Water Resources*, vol. 83, pp. 176–189, 2015.

Research Article

Quantify the Pore Water Velocity Distribution by a Celerity Function

Wei Shao,^{1,2} Ye Su ,³ Zongji Yang ,⁴ Xieyao Ma,¹ and Jakub Langhammer³

¹Key Laboratory of Meteorological Disaster, Ministry of Education / Joint International Research Laboratory of Climate and Environment Change / Collaborative Innovation Centre on Forecast and Evaluation of Meteorological Disasters / School of Hydrology and Water Resources, Nanjing University of Information Science and Technology, Nanjing, Jiangsu 210044, China

²Water Resources Section, Faculty of Civil Engineering and Geosciences, Delft University of Technology, Stevinweg 1, PO Box 5048, 2600 GA Delft, Netherlands

³Department of Physical Geography and Geoecology, Faculty of Science, Charles University, Albertov 6, 128 43 Prague 2, Czech Republic

⁴Key Laboratory of Mountain Hazards and Surface Process, Institute of Mountain Hazards and Environment, Chinese Academy of Sciences, Chengdu 610041, China

Correspondence should be addressed to Ye Su; ye.su@natur.cuni.cz

Received 2 February 2018; Revised 4 April 2018; Accepted 7 May 2018; Published 3 July 2018

Academic Editor: Joaquín Jiménez-Martínez

Copyright © 2018 Wei Shao et al. This is an open access article distributed under the Creative Commons Attribution License, which permits unrestricted use, distribution, and reproduction in any medium, provided the original work is properly cited.

Celerity and velocity of subsurface flow in soil porous medium are intimately linked with tracer transport, while only few current studies focused on their relations. This study conducted theoretical analyses based on a pore bundle model, under which celerity in unsaturated flow is equivalent to maximum velocity. Furthermore, under 3 models Brooks-Corey model and unmodified and modified Mualem-van Genuchten models, we used a celerity function to derive breakthrough curves aiming to quantify the advective tracer transport for 5 typical soil textures. The results showed that the celerity under near-saturated conditions can be 5 up to 100 times larger than the saturated hydraulic conductivity, and a small volumetric fraction (<15%) of pores contributed more than half of the specific discharge. First arrival time and extensive tailing of the breakthrough curves were controlled by maximum velocity and velocity distribution, accordingly. As the kinematic ratio in the Brooks-Corey model remained constantly for each specific soil, we used it to quantify the ratio of maximum tracer velocity over average tracer velocity. We also found that a bimodal soil hydraulic function (for a dual-permeability model) may result in similar soil hydraulic conductivity functions for different parameter sets, but their celerities are different. The results showed that the proposed celerity function can assist in investigating subsurface flow and tracer transport, and the kinematic ratio could be used to predict the first arrival time of a conservative tracer.

1. Introduction

Subsurface flow is conducted in the soil porous medium, in which the pore structure (i.e., pore connectivity, tortuosity, and pore size distribution) controls the permeabilities and pore water velocities in numerous flow paths [1–3]. In hydrological studies, it is impractical to deterministically represent the pore-scale fluid dynamics and transport processes in soil, for the variability of pore water velocity is difficult to observe or predict [4–6]. For describing the subsurface flow processes, the continuum approach was often used

to conceptualize the discrete materials and water particles as one single continuous mass. The soil hydraulic properties (e.g., the lumped hydraulic conductivity and moisture capacity) and state variables (e.g., volumetric water content and capillary pressure) are often quantified in a representative elementary volume (REV) [7, 8]. The continuum subsurface flow equation (i.e., the well-known Darcy-Richards equation) calculates specific discharge and average pore water velocity for transport phenomenon. Specifically, the specific discharge quantifies the volumetric flow [9, 10], and the average pore water velocity can be coupled with an advection-

diffusion equation to simulate solute/thermal transport [10–12]. Applications of the Darcy-Richards equation rely on the indicators of velocities and specific discharge.

For describing the water fluid dynamics, the terminologies of velocity (i.e., pore water velocity) and celerity have been commonly used in various hydrological systems, such as river channels [13–15], estuaries [16, 17], and soil porous medium [8, 18, 19]. Theoretically, velocity expresses mass flux, while celerity represents the speed of pressure propagation through a flow domain [20]. In surface water, for instance, the pressure wave is a flood wave propagating through river channels. Similarly, the celerity in subsurface flow describes a perturbation-induced pressure wave that is affected by precipitation, evaporation, or fluid injection and extraction [21, 22]. In saturate soil, the difference between velocity and celerity can be illustrated by a virtual experimental [20], and the authors pointed out: “*in a cylinder full of sand and saturated with water, changing the flow rate or head at the input boundary will immediately cause a change in flow at the output boundary. While the water flow velocity through the sand is slow, the celerity in this case is (theoretically) instant, hence the immediate response. At larger scales, this case is analogous to a confined aquifer with incompressible water and rock. Allowing for the compressibility will slow the celerity a little, but the velocities of flow will still be much less than the celerities.*”

In confined saturated flow, the nearly-instant celerity is caused by the low compressibility of water and soil porous medium. While in unsaturated soil, the pressure propagation was achieved by the variation of capillary pressure that is driven by different mechanisms. For example, a response of the pore water pressure in unsaturated soil can be caused by either preferential flow [23] or pressure wave through the entrapped air [24]. However, how to distinguish the initial cause-effect mechanism of pressure response is still a challenge [22, 25]. Many studies used the kinematic wave equation to simulate unsaturated flow [8, 18, 26, 27], in which the celerity was defined as a first-order derivative of hydraulic conductivity (i.e., equal to specific discharge) with respect to the water content [22, 28, 29]. These studies illustrated the celerity as “mobility of water in soil” [29, 30], and the mechanisms of pressure propagation in unsaturated zone was, however, not discussed.

On the other hand, the pore water velocity in numerous flow paths is dictated by the pore structure such as pore connectivity, tortuosity, and pore size distribution [1–3]. Especially, the soil hydraulic functions can be derived as an integration of pore water velocities in all flow paths if considers a unit gradient condition [10, 12, 31]. Based on a pore bundle model, the hydraulic properties of each flow path can be equivalent to that of a cylinder tube with a small circular cross section and a sufficient length [32–34], then the experimentally measured water retention curve is used to infer pore size distribution and pore water velocity distribution [35–38]. Under such condition, each tube conducts the viscous flow; therefore, the relations of the equivalent tube radius to capillarity pressure and pore hydraulic conductivity can be, respectively, described by a capillary rise equation (i.e., Young-Laplace equation) and a pipe/cylinder liquid

flow equation (i.e., the Hagen-Poiseuille law). The hydraulic conductivity functions integrated from pore velocity distribution can indirectly reflect the pore-scale hydraulic properties [39, 40]. As the first-order derivative of hydraulic conductivity can be defined as a celerity function for unsaturated soil [22, 24], the celerity can be related to the pore water velocity distribution.

The complex solute transport behaviours are caused by the pore water velocity distribution in a subsurface flow system [28, 41–43], which have been captured either by an experimentally obtained breakthrough curve [5, 44–46] or by natural and artificial tracers in a hydrological system [28, 47, 48]. The breakthrough curve expresses the time series of the tracer concentration of drainage flow, which was often characterized by a coexisting early initial breakthrough and extensive tailing [44]. The tracer experiment in a hillslope or a catchment assists in inferring the travel time distribution [49, 50]. However, many tracer studies found a paradox behaviour; that is, during a high-intensity rainstorm a large amount of “old” water resident in soil or groundwater is expelled into the stream, while the labelled “new” water of the rainfall on the hillslope immediately starts to appear in the stream after a fast infiltration through a fast flow path [51–54]. Those complex tracer transport behaviours address the importance of quantifying the pore water velocity distribution for achieving the more detailed physical interpretations of unsaturated flow and transport [28, 55].

The celerity and velocity are intimately linked with tracer transport, while most of the current studies focused on one or two aspects. For example, mathematical derivations for the celerity and kinematic ratio have been provided by Rasmussen et al. [22], while they did not find the relation between tracer transport and pressure propagation. Wang et al. [24] and Mohammadi et al. [56] found the derivation of the tracer breakthrough curve through the soil hydraulic conductivity functions, and their method have been validated through their experiments. However, the studies from Wang et al. [24] and Mohammadi et al. [56] were based on the soil hydraulic functions of either the Brooks-Corey model or the van Genuchten model for a single-permeability model, and more soil hydraulic functions still need further studies. There is no report existing that explored the relations among celerity (pressure propagation), velocity (water transport), and tracer transport (pore velocity distribution) yet.

The objective of this paper was to (i) illustrate the concept of celerity in unsaturated flow, (ii) propose a new soil hydraulic function (i.e., celerity function) to express the pore water velocity distribution, and (iii) quantify the advective breakthrough curves using the proposed celerity function. Specifically, in Section 2.1, the definitions of velocity and celerity were given to illustrate the mechanisms of pressure propagation in unsaturated soils. Based on a pore bundle model, Section 2.2 mathematically proved the equivalence between celerity in unsaturated soil and maximum pore water velocity among all flow paths that conduct water. Furthermore, a theoretical analysis was conducted to illustrate the difference between celerity and velocity of wetting front under a unit-hydraulic-gradient condition, showing that the celerity

function derived from a perturbation analysis can reveal the pore water velocity distribution (see Section 2.3). The celerity functions of the Brooks-Corey model and both unmodified and modified Mualem-van Genuchten models are provided in Section 2.4. The impact of velocity distribution on tracer transport can be illustrated by mathematically deriving a breakthrough curve through a celerity function (Section 2.5). Functions for the celerity in dual-permeability models are derived in Section 2.6. Section 3 analysed the hydraulic characteristic and breakthrough curves of typical soil textures by using the proposed celerity function. Hereto, the pore water velocity distribution and breakthrough curve of typical soils were analysed using the existing parameter sets of the Mualem-van Genuchten model and the Brooks-Corey model. Additionally, the equifinal parameter sets of a bimodal soil hydraulic function were distinguished by the celerity function. The follow-up discussion focused on the mechanism of pressure propagation and tracer transport in a natural subsurface flow system.

2. Theory

2.1. Definitions. In subsurface, the vertical component q (LT^{-1}) of a specific discharge vector (i.e., the volume flux of water per unit cross-sectional area) is formulated using Darcy's law as

$$q = -K \frac{\partial}{\partial z} (h - z), \quad (1)$$

where K (LT^{-1}) is the hydraulic conductivity, h (L) is the pressure head, and z (L) is the vertical coordinate (positive downward).

The average pore water velocity \bar{v} (LT^{-1}) is

$$\bar{v} = \frac{q}{\theta - \theta_r}, \quad (2)$$

where θ (–) is the volumetric water content and θ_r (–) is the residual water content.

The continuity equation for one-dimensional vertical flow is

$$\frac{\partial \theta}{\partial t} + \frac{\partial q}{\partial z} = 0. \quad (3)$$

The derivative of specific discharge q with respect to z is written as

$$\frac{\partial q}{\partial z} = \frac{\partial q}{\partial \theta} \frac{\partial \theta}{\partial z}. \quad (4)$$

Substitution of (4) for $\partial q / \partial z$ in (3) results in an advection equation

$$\frac{\partial \theta}{\partial t} + c \frac{\partial \theta}{\partial z} = 0, \quad (5)$$

where c (LT^{-1}) is the celerity [22]

$$c = \frac{\partial q}{\partial \theta}. \quad (6)$$

Theoretically, the advection equation represents the advection of the soil-water content θ with speed c . When c is a constant value, it would mean that an arbitrarily shaped pulse of θ moves with constant speed c without changing its shape. The celerity is, however, not a constant but a function of water content. Hence, the celerity is an approximate advection speed of a small pulse of θ .

A ratio between celerity and average velocity is called the kinematic ratio α_K (–), as defined by Rasmussen et al. [22]:

$$\alpha_K = \frac{c}{\bar{v}}. \quad (7)$$

2.2. Celerity and Maximum Pore Velocity. The pore sizes and their intrinsic permeabilities vary throughout the unsaturated zone. Based on a pore bundle model, many previous studies considered soil as a bundle of nonintersecting, parallel, and cylindrical tubes with varying radii to quantify the water and solute transport [32–34, 57]. When water enters soil flowing through a pore of certain size, each pore is either entirely filled with water or entirely empty. Considering variably saturated conditions, pores are filled from the smallest tube group ($i = 1$) to the largest ($i = N$). Under unsaturated conditions, M of the N tube groups are filled with water. The pore water velocity v_i (LT^{-1}) in one specific equivalent (saturated) cylinder tube i can be determined by its specific discharge

$$v_i = -k_i \frac{\partial}{\partial z} (h - z), \quad (8)$$

where k_i (LT^{-1}) is a coefficient relating the head gradient and the average velocity in pore i .

The pores with the same size and the same pore water velocity can be classified as one group, based on which the water content θ (i.e., all the volumetric fractions of the pore space filled with water) is discretised in N fragments of equal water content $\Delta\theta$ and ordered from small pores to larger pores. Assuming a unique, nonhysteretic relationship between water content and capillary pressure, water can flow through the water-filled saturated smaller pores with higher capillary pressure, while the larger pores will remain empty and inactivated for conducting unsaturated flow [58].

By discretizing the flow domain into numerous flow tubes that are vertically homogeneous, the hydraulic characteristics of each tube can be formulated as functions of the volumetric water content θ . Considering the pore size distribution, the pore water flow velocity v_i follows a distribution ordering from smallest pore group (with velocity v_1) to largest pore group (with velocity v_M). At a certain water content value, $v(\theta)$ (LT^{-1}) may denote the maximum pore water flow velocity taking place in the water-filled pore with the largest equivalent radius—then the specific discharge q (LT^{-1}) and the hydraulic conductivity K (LT^{-1}) can be obtained through a summation:

$$q = \sum_{i=1}^M v_i \Delta\theta, \quad (9)$$

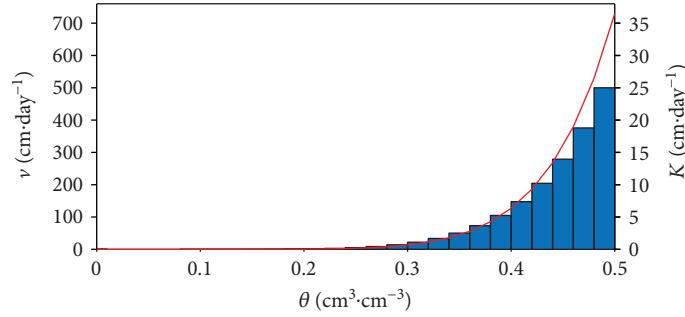


FIGURE 1: A numerical integration of pore water velocities from pore groups.

where M is the largest tube group filled with water. Substitution of (8) for v_i in (9) gives

$$q = \sum_{i=1}^M v_i \Delta\theta = \sum_{i=1}^M -k_i \frac{\partial}{\partial z} (h-z) \Delta\theta = -K \frac{\partial}{\partial z} (h-z), \quad (10)$$

where the hydraulic conductivity K is defined as

$$K = \sum_{i=1}^M k_i \Delta\theta. \quad (11)$$

The unit hydraulic gradient condition considers a gravity-driven vertical infiltrating flow (i.e., when $\nabla h = 0$ and $K = q$), and the hydraulic conductivity function $K(\theta)$ therefore can be obtained by summing up the pore water velocity v_i from a limited number of pore groups as shown in Figure 1.

The integral equation of (9) is

$$q = \int_{\theta_i}^{\theta} v d\theta, \quad (12)$$

and the integral equation of (11) is

$$K = \int_{\theta_i}^{\theta} k d\theta. \quad (13)$$

The celerity is now obtained as

$$c(\theta) = \frac{\partial q}{\partial \theta} = v|_{\theta_i}^{\theta} = v(\theta), \quad (14)$$

where $v(\theta)$ is the maximum velocity corresponding to the water content θ . Hence, the celerity is equal to the maximum velocity corresponding to a certain water content θ .

Many previous studies using the pore bundle model to derive the hydraulic conductivity function by upscaling pore water velocities to REV scale were similar to (12)–(13) [32–34], while an inverse derivation in (14) demonstrates that the celerity in unsaturated flow is equal to the maximum pore water flow velocity. Moreover, Figure 1 implies that the piecewise linear approximation of the soil hydraulic conductivity function can infer the flow paths (or tubes groups) in which the water flow has distinct velocities.

2.3. Expressing Pore Water Velocity Distribution by a Celerity Function. The effects of pore water velocity distribution on soil hydrology can be visualized by a perturbation analysis with a hypothetical infiltration experiment. Considering soil under unit hydraulic gradient condition as $\partial(h-z)/\partial z = -1$ (when h is constant), the specific discharge is equal to the hydraulic conductivity ($q = K$) [58]. Under this condition, an increment of water flow on the surface boundary will cause downward pressure propagation. The pressure propagation may be linked to the celerity as maximum pore water velocity, while it can also be described by a similar terminology of the velocity of wetting front. A hypothetical analysis is provided hereafter to exemplify their different roles in quantifying the pressure wave propagation under unit hydraulic gradient condition.

Considering a steady flow condition driven by an infiltration flow q , the increments of Δq to the upper boundary correspondingly induce an increment of soil water content $\Delta\theta$ that generates a piston-shaped advancing wetting front with velocity $v_{\text{WF}} (\text{LT}^{-1})$ expressed as [59]

$$v_{\text{WF}} = \frac{\Delta q}{\Delta\theta} = \frac{q(\theta + \Delta\theta) - q(\theta)}{\Delta\theta} = \frac{K(\theta + \Delta\theta) - K(\theta)}{\Delta\theta}. \quad (15)$$

The velocity of wetting front v_{WF} expresses the average pore water velocity of the newly activated pore system with the volumetric fraction of $\Delta\theta$, which is induced by a change of the specific discharge Δq .

On the other hand, the celerity in unsaturated flow can be illustrated by a perturbation analysis; namely, a small increment of δq at the surface boundary will activate water flow in a larger-size pore with water content of $\delta\theta$:

$$c = \frac{\delta q}{\delta\theta} = v(\theta). \quad (16)$$

Furthermore, under unit hydraulic gradient condition, the celerity can be mathematically linked to the maximum pore hydraulic conductivity

$$c = \frac{\partial K}{\partial \theta} = k(\theta). \quad (17)$$

A perturbation (i.e., an small increment) of water flow at the surface boundary will activate water flow in the “new” tube group with larger size and higher pore hydraulic conductivity $k(\theta)$, and the flow velocity $v(\theta)$ in the newly

TABLE 1: Constitutive relationships under the unit hydraulic gradient condition formulated by the Brooks-Corey model and the modified Mualem-van Genuchten model.

Property	Definition	Brooks-Corey	Modified Mualem-van Genuchten
Water retention	$\Theta = f(h)$	$\Theta = \begin{cases} \alpha_{BC}h ^{-n_{BC}}, & \alpha_{BC}h < -1, \\ 1, & \alpha_{BC}h > -1 \end{cases}$	$\varepsilon\Theta = \begin{cases} [1 + \alpha_{VG}h ^{n_{VG}}]^{-m_{VG}}, & h < h_s, \\ 1, & h \geq h_s \end{cases}$
Specific capacity	$\frac{d\theta}{dh}$	$\alpha_{BC}n_{BC}(\theta_s - \theta_r)\Theta^{1+1/n_{BC}}$	$m_{VG}n_{VG}\alpha_{VG}(\theta_s - \theta_r)\Theta^{1/m_{VG}}(1 - \Theta^{1/m_{VG}})^{m_{VG}}$
Specific discharge	$q = K$	$K_s\Theta^{(2/n_{BC})+3}$	$K_s\Theta^{l_{VG}} \left[\frac{1 - (1 - (\varepsilon\Theta)^{1/m_{VG}})^{m_{VG}}}{1 - (\varepsilon\Theta)^{1/m_{VG}}} \right]^2$
Average pore velocity	$\bar{v} = \frac{q}{\theta - \theta_r}$	$\frac{K_s}{\theta_s - \theta_r} \Theta^{(2/n_{BC})+2}$	$\frac{K_s}{\theta_s - \theta_r} \Theta^{l_{VG}-1} \left[\frac{1 - (1 - (\varepsilon\Theta)^{1/m_{VG}})^{m_{VG}}}{1 - (\varepsilon\Theta)^{1/m_{VG}}} \right]^2$
Celerity	$c = v = \frac{dK}{d\theta}$	$\frac{a_K K_s}{\theta_s - \theta_r} \Theta^{(2/n_{BC})+2}$	$\frac{a_K K_s}{\theta_s - \theta_r} \Theta^{l_{VG}-1} \left[\frac{1 - (1 - (\varepsilon\Theta)^{1/m_{VG}})^{m_{VG}}}{1 - (\varepsilon\Theta)^{1/m_{VG}}} \right]^2$
Kinematic ratio	$\alpha_K = \frac{c}{\bar{v}}$	$\frac{2}{n_{BC}} + 3$	$l_{VG} + \frac{2[1 - (\varepsilon\Theta)^{1/m_{VG}}]^{m_{VG}-1} (\varepsilon\Theta)^{1/m_{VG}}}{1 - [1 - (\varepsilon\Theta)^{1/m_{VG}}]^{m_{VG}}}$

Notation of table: α (L^{-1}), n (-), and m (-) are the fitting parameters for the Brooks-Corey model (denoted with subscription of ‘‘BC’’) and the Mualem-van Genuchten model (denoted with subscription of ‘‘VG’’); Θ is the effective saturation (-) that is defined as $\Theta = (\theta - \theta_r)/(\theta_s - \theta_r)$; ε is the correction factor to modify the van-Genuchten model $\varepsilon = (\theta_s - \theta_r)/(\theta_m - \theta_r)$, with $\theta_m = \theta_r + (\theta_s - \theta_r)[1 + |\alpha_{VG}h_s|^{n_{VG}}]^{m_{VG}}$; h_s is the minimum capillary height, which becomes zero when $\theta_m = \theta_s$; and l_{VG} is the pore connectivity parameter and is usually assumed to be 0.5.

activated water flow path will be larger than other water-filled tubes. Assuming that the fluid dynamics are independent among tubes, the celerity under variably saturated condition express the one-to-one correspondence between the maximum pore water velocities with the water content [58]. When exerting the perturbation analysis in saturated/unsaturated soil, the celerity as a first-order derivative of the hydraulic conductivity function can quantify the pore hydraulic conductivity distribution (equivalent to the pore water velocity distribution) under unit hydraulic gradient condition.

2.4. Different Soil Hydraulic Models. The pore water velocity distribution can be obtained by a celerity function that was derived as the first-order derivative of the hydraulic conductivity function. The two most widely used soil hydraulic conductivity functions of the Brooks-Corey model and the Mualem-van Genuchten model [35, 37, 60] have been chosen by Rasmussen et al. [22] to formulate celerity functions. However, the kinematic ratio and celerity under the Mualem-van Genuchten model in near-saturated soil is approaching an infinite value, which is caused by a mathematical artefact [38]. To overcome this problem, the modified Mualem-van Genuchten model was used to prevent the unrealistic variations in unsaturated hydraulic conductivity for the near-saturation range [38, 61–63].

The mathematical formulations of water retention curve, hydraulic conductivity, average pore velocity, celerity, and kinematic ratio based on the Brooks-Corey and Modified Mualem-van Genuchten parameterization are shown in Table 1 [35, 38]. The modified Mualem-van Genuchten model here includes a nonzero minimum capillary height of air entry pressure to overcome the mathematical artefact, and the results will be given in Section 3.1. The unmodified Mualem-van Genuchten model sets the air entry pressure

h_s to zero, so that the parameter ε equals one. The formulation of the kinematic ratio derived from the Brooks-Corey model is a constant value of $2/n_{BC} + 3$ that equals to the power index in the hydraulic conductivity function.

The kinematic ratio is a constant value if deriving it from a power function that describes unsaturated hydraulic conductivity [64, 65], and its value usually falls in a range between 2.5 and 24.5 [65]. Similarly, the celerity in surface water has been extensively investigated for describing fluid dynamics [13–15, 17]. The kinematic ratio for surface flow is approximately equal to 1.67 derived from the Manning resistance coefficient in a kinematic wave equation for open-channel flow [15]. Since the celerity in unsaturated subsurface flow is analogous to the wave celerity in surface flow [8], the kinematic ratio of unsaturated flow can be 1.5–14.7 times larger than that of surface flow, which implies that the velocity distribution in unsaturated subsurface flow is highly nonlinear.

2.5. Derivation of a Breakthrough Curve through the Celerity Function. Transport of a conservative tracer in a porous medium is governed by physical mechanisms of advection, dispersion, and molecular diffusion, among which advection and dispersion are a function of the velocity distribution. The tracer advection is governed by the average pore water velocity, and the tracer dispersion is caused by the velocity distribution [66, 67].

Considering a one-dimensional and uniform flow under the unit hydraulic gradient condition, the transport of conservative tracer in a subsurface flow system can be described with the pore bundle model, and the breakthrough curve can be derived from velocity distribution [58]. If the water content is constant and equal to θ_w , M of the N tube groups are filled with water, so that the water content θ_w may be written as

$$\theta_w = \frac{M}{N} \theta_s, \quad (18)$$

Considering a soil column with length L (L) with a uniform distributed water content θ_w , the specific discharge is equal to the specified constant water flow at the upper boundary under unit hydraulic gradient condition. Considering the varying pore water velocities in numerous vertical flow paths in a soil column, the time t_i needed for tracer breakthrough from a pore group with a velocity v_i can be expressed as

$$t_i = \frac{L}{v_i}. \quad (19)$$

Tracer breakthrough sequentially occurs from the largest water-filled pores to the smallest one. Especially, the first arrival time of the tracer transport is associated with the maximum pore water velocity $L/v(\theta_w)$ and thus can be calculated with $L/c(\theta_w)$.

When the tracer concentration in the surface flow is changing from C_0 to $C_0 + \Delta C$, the tracer breakthrough will be achieved at the time of $L/c(\theta_w)$, and then the concentration of the drainage flow will be increased gradually. At time t_i (after the first arrival time), water in all tube groups $j > i$ has travelled from the top of the column to the bottom of the column; the concentration of drainage flow can be formulated through a summation [57]:

$$C(t_i) = C_0 + \frac{\sum_{j=i}^M v_j \Delta \theta}{\sum_{j=1}^M v_j \Delta \theta} \Delta C. \quad (20)$$

The integral equivalent of (21) is

$$\begin{aligned} C(t_c) &= C_0 + \frac{\int_{\theta_r}^{\theta_w} v d\theta}{\int_{\theta_r}^{\theta_w} v d\theta} \Delta C \\ &= C_0 + \frac{\int_{\theta_r}^{\theta_w} v d\theta - \int_{\theta_r}^{\theta_r} v d\theta}{\int_{\theta_r}^{\theta_w} v d\theta} \Delta C, \end{aligned} \quad (21)$$

where

$$t_c = \frac{L}{v_c}, \quad (22)$$

where v_c is pore water flow velocity in a certain flow path at the arrival time of t_c for tracer breakthrough

$$v_c = c(\theta_c). \quad (23)$$

θ_c is the water content corresponding to a flow velocity v_c that is equal to the celerity and thus

$$t_c = \frac{L}{c(\theta_c)}. \quad (24)$$

Under unit hydraulic gradient condition, the integrals in (21) are equal to the specific discharge (see (12)), which are equal to the hydraulic conductivity, so that it becomes

$$C(t_c) = C_0 + \left[1 - \frac{K(\theta_c)}{K(\theta_w)} \right] \Delta C. \quad (25)$$

The mathematical expression for the breakthrough curve $C(t)$ based on the Mualem-van Genuchten parameterization requires an analytical approach [56]. In this study, the numerical approach was used to derive the breakthrough curve of the unmodified and modified Mualem-van Genuchten models. We hereafter demonstrate an example of deriving the breakthrough curve $C(t_c)$ of a nonreactive tracer from the celerity function based on the Brooks-Corey model, to be more explicitly linking the tracer transport with the pore water velocity distribution [58].

Substitution of the celerity equation for the Brooks-Corey model in Table 1 into (25) and rearrangement of terms giving the pore water velocity $v(\theta_c)$ can be calculated as

$$v(\theta_c) = c(\theta_c) = \alpha_K \frac{K_s}{\theta_s - \theta_r} \left[\frac{\theta_c - \theta_r}{\theta_s - \theta_r} \right]^{(2/n_{BC})+2}. \quad (26)$$

If the initial tracer concentration is zero, the breakthrough curve for the Brooks-Corey model can be written explicitly as

$$\frac{C(t_c)}{\Delta C} = \begin{cases} 0; & t \leq \frac{L}{c(\theta_w)} \\ 1 - \frac{K_s}{K_w} \left[\frac{\theta_s - \theta_r L}{\alpha_K K_s t} \right]^{(3n_{BC}+2)/(2n_{BC}+2)}; & t > \frac{L}{c(\theta_w)}, \end{cases} \quad (27)$$

where $L/c(\theta_w)$ approximates the first arrival time of the tracer. Eq. (27) indicates that the first arrival time of a tracer is determined by the maximum pore water velocity, and the tailing is determined by the pore water velocity distribution. The above-given mathematical derivations are similar with the previous work that also formulated the breakthrough curve by soil hydraulic conductivity functions under the saturated condition [57]. In this study, we extended the formulation to unsaturated soils and further formulated the tracer transport as a function of kinematic ratio α_K that simplified (28) by replacing n_{BC} :

$$\frac{C(t^*)}{\Delta C} = \begin{cases} 0; & t^* \leq \frac{1}{\alpha_K} \\ 1 - \left[\frac{1}{\alpha_K t^*} \right]^{(a_K/a_K-1)}; & t^* > \frac{1}{\alpha_K}, \end{cases} \quad (28)$$

with t^* as a dimensionless time defined as

$$t^* = \frac{\bar{v}}{L} t_c = \frac{K_w}{L(\theta_w - \theta_r)} t_c. \quad (29)$$

When t^* is equal to 1, the flow through a soil column is equal to one pore volume.

The breakthrough curve expressed with (28) shows that the kinematic ratio can directly determine the first arrival time and tailing of a conservative tracer in drainage flow. For an extreme case, when the kinematic ratio is equal to 1, the pore water velocity in all the flow paths is equal to the

average pore water velocity. Such a uniform pore water velocity distribution leads to a piston-shaped breakthrough curve:

$$\frac{C(t^*)}{C_1} = \begin{cases} 0; & t^* \leq 1, \\ 1; & t^* > 1. \end{cases} \quad (30)$$

Eq. (30) expresses only the tracer advection that is controlled by the average pore water velocity, while excluding the dispersion effect caused by the pore water velocity distribution.

For the Brooks-Corey model, substituting the hydraulic conductivity function (from Table 1) into (29), the dimensionless time can be formulated as a function of either soil water content or specific discharge:

$$t^* = \frac{K_s \Theta^{\alpha_k - 1}}{L(\theta_s - \theta_r)} t_c = \frac{K_s}{L(\theta_s - \theta_r)} \left(\frac{K_w}{K_s} \right)^{1 - (1/\alpha_k)} t_c. \quad (31)$$

The kinematic ratio is a constant in the Brooks-Corey model (see Table 1), which means that the breakthrough curve as a function of dimensionless time t^* in variably saturated soil is independent of the specific discharge or effective saturation for the Brooks-Corey model.

2.6. Celerity of the Bimodal Soil Hydraulic Functions. This section derives a celerity function through the bimodal soil hydraulic conductivity functions for quantifying the pore water velocity distribution in structured soil. Conceptualizing a soil porous medium as two overlapping continua of the matrix domain and the preferential flow domain as a dual-continuum pore system [41, 68], the composite bimodal soil hydraulic functions use two water retention curves and hydraulic conductivity functions to, respectively, describe the soil hydraulic properties [69–74]. The preferential flow domain consists of the pores with relatively large size (often taken as larger than 0.3 mm in equivalent tube diameter) and low tortuosity, such as worm burrows, root channels, tension cracks, and interaggregate pores [41, 75, 76]. The remaining micropore volume is classified as the matrix domain. The bimodal soil hydraulic function has been widely used to parameterize the dual-permeability models that simulate two groups of state variables (i.e., different pressure heads, water contents, and tracer concentrations between two domains) for describing the nonequilibrium phenomena [77]. The hydraulic characteristics of the preferential flow domain and the matrix domain can be distinguished by their parameterization in bimodal soil hydraulic functions [70, 78]. Below, we derive the soil hydraulic functions of average pore water velocity and celerity for a dual-continuum system under unit hydraulic gradient condition.

First, the volumetric ratio of the preferential flow domain and the matrix flow domain sums up to 1:

$$w_f + w_m = 1, \quad (32)$$

where the subscripts f and m denote the preferential flow and matrix flow domains, respectively. The total water content and total specific discharge of a soil with a dual-continuum pore system are calculated as the weighted average of the two domains water content and specific discharge:

$$\theta = w_f \theta_f + w_m \theta_m, \quad (33)$$

$$q = w_f q_f + w_m q_m. \quad (34)$$

The average pore velocity of each a domain is defined as

$$v_f = \frac{q_f}{\theta_f - \theta_{rf}}, \quad (35)$$

$$v_m = \frac{q_m}{\theta_m - \theta_{rm}}.$$

Then, the average pore velocity of the dual-continuum pore system is

$$v = \frac{q}{\theta - \theta_r} = \frac{w_f q_f + w_m q_m}{\theta - \theta_r}. \quad (36)$$

Under the steady flow condition, the celerity of each a domain can be defined as follows:

$$c_f = \frac{\partial q_f}{\partial \theta_f}, \quad (37)$$

$$c_m = \frac{\partial q_m}{\partial \theta_m}.$$

Finally, the celerity of the dual-continuum pore system can be expressed as

$$c = \max(c_f, c_m). \quad (38)$$

When the matrix domain is unsaturated, the matrix conducts water, and the preferential flow domain remains inactive. Therefore, pressure propagation will take place in the matrix domain as well. When the matrix domain approaches near-saturation condition, the preferential flow domain becomes activated. At this stage, the water flow in the preferential domain quickly takes over the majority of water flow and consequently the pressure propagation of celerity.

3. Analysis

3.1. Soil Hydraulic Functions under a Single-Domain Conceptualization. This section combines the theoretical formulation (given in Section 2) with the existing parameterization of 5 typical soils to analyse the soil hydraulic behaviours. Table 2 shows the standard parameter sets of 5 typical soils obtained from the UNSODA database [79, 80]. The detailed values of each soil type have slightly different values of saturated hydraulic conductivity and residual/saturated water content, which might be related to the different fitting algorithms and sampling data. Considering that the values of these parameters are drastically varied for different soil textures, we then decided to use dimensionless indicators, for example, the effective saturation. Furthermore, the values of specific discharge, average velocity, and celerity were all divided by the saturated hydraulic conductivity to convert those variables to dimensionless values. Consequently, all the values of each individual indicator for the different soil types fall in a similar range (Figure 2). The air entry pressure

TABLE 2: Parameter sets of 5 typical soils in the Brooks-Corey model and the van-Genuchten model.

Soil	Brooks-Corey model					Van-Genuchten model					
	K_s (m day ⁻¹)	θ_r (-)	θ_s (-)	α_{BC} (m ⁻¹)	n_{BC} (-)	K_s (m day ⁻¹)	θ_r (-)	θ_s (-)	α_{VG} (m ⁻¹)	n_{VG} (-)	h_s (m)
Sand	5.0400	0.020	0.417	13.8	0.592	7.1280	0.045	0.430	14.5	2.680	0.072
Sandy loam	0.6216	0.041	0.412	6.8	0.322	1.0610	0.065	0.410	7.5	1.890	0.147
Loam	0.1632	0.027	0.434	9.0	0.220	0.2496	0.078	0.430	3.6	1.560	0.111
Clay loam	0.0522	0.075	0.390	3.9	0.194	0.0624	0.095	0.410	1.9	1.310	0.256
Silty clay loam	0.0360	0.040	0.432	3.1	0.151	0.0168	0.089	0.430	1.0	1.230	0.322

Note. h_s is the air entry pressure value of the Brooks-Corey model and the modified Mualem-van Genuchten model.

values in the modified Mualem-van Genuchten model were adopted from those of the Brooks-Corey model for all 5 typical soils and listed in the last column of Table 2. Solely using either specific discharge or average pore water velocity to quantify the transport processes is theoretically insufficient [20, 22, 81]; we included the celerity and kinematic ratio in Table 2 to provide a more complete illustration of the dependence of pore water flow velocity and pressure propagation on soil effective saturation.

The water retention curves (first row in Figure 2) for 5 typical soils have distinct curvatures attributed to the different pore size distributions [38, 76]. Specifically, in coarse texture soil (e.g., sandy soil), a flatter curve might manifest a relatively uniform pore size distribution and homogeneous soil hydraulic characteristic of the coarse texture. When approaching the fully saturated state, the slopes of the water retention curve from the Mualem-van Genuchten model reaches an infinite value; instead, the slopes from the Brooks-Corey model and the modified Mualem-van Genuchten model (Figures 2(a) and 2(c)) are close to 0, which are attributed to the inclusion of an air entry pressure head stemmed from the observation of various types of soils [80].

Celerity, average pore water velocity, and specific discharge all increase as the effective saturation increases, but the ranges of their values differ. Specifically, q/K_s ranges from 0 to 1 as expected. \bar{v}/K_s is between 0 and 3 (because $\theta_s - \theta_r$ is around 0.35; see Table 2). c/K_s ranges from 0 to 70. α_K also ranges from 0 to 30, except for the unmodified Mualem-van Genuchten model under near-saturated condition. All four dimensionless variables reach their maximum value when soils are saturated. The celerity curves can manifest the maximum pore water velocity at a certain saturation state, and Figure 2 shows that the celerity is over 20 times larger than the average pore water velocity and 10 up to 100 times larger than the specific discharge.

The celerity curves show different patterns for different soil types. Near saturation, c/K_s can reach above 50 for fine textured soils, while it reaches around 20 for coarse-textured soils. On the contrary, when the effective saturation drops below 0.8–0.9, c/K_s is much smaller. The value of K/K_s is below 0.5 for $\theta = 0.85$ for all soil types. The value of K/K_s is highest for sand (= 0.5) and lowest for clay (= 0.2), which means that more than 50% of the specific discharge flows through only 15% of the pore space when flow is saturated.

The K/K_s curves are near-exponentially increased with the effective saturation increasing till the soils reach the fully

saturated state. However, the celerity curves show different patterns under the parameters set for different soil types. Under near-saturated condition, in fine-textured soil (i.e., sandy clay and clay), the celerity responds to the effective saturation more significantly than that in coarse soil textures. c/K_s in coarse-textured soil (e.g., sandy soil) only changes from 0 to around 15 (Figures 2(i) and 2(j)), while the celerity curve of fine texture soil has a much larger range (e.g., c/K_s of silty soil ranges from 0 to 70). Under the low saturation state (e.g., $\Theta < 0.7$), specific discharge and average pore water velocity behave similarly with the relative low values between different soil textures. Till the effective saturation Θ reaches 0.9, K/K_s is below 0.5 in all soil types (sand $K/K_s = 0.5$ and clay $K/K_s = 0.2$), which implicitly manifests that more than 50% of specific discharge is conducted in pores with a volumetric fraction less than 10%.

The slope of the α_K curve is used as an indicator, shown in Figure 3. The kinematic ratios derived from the unmodified Mualem-van Genuchten model approach the infinite values, which were induced by a mathematical artefact. However, the kinematic ratios under the modified Mualem-van Genuchten model and the Brooks-Corey model consistently have (nearly) constant values for all the saturation ranges (specific values are given in Table 3). α_K indicates that the celerity is proportionally increasing with the average pore water velocity (see Figure 3(a)).

3.2. Breakthrough Curves. The pore water velocity distribution can further dictate the tracer transport, which can be formulated and illustrated with a breakthrough curve (Figure 4). The functions of the breakthrough curve in typical soils used the same parameter set given in Table 2. Breakthrough curves were plotted for three soil hydraulic models, using an analytic approach for the Brooks-Corey model and a numerical approach for the unmodified and modified van-Genuchten models. We adopted a dimensionless time (see (29)) to exclude the impact of K_s , θ_s , and θ_r on breakthrough curve. It is recalled that only advective transport is considered based on the pore bundle model, where water particles remain in the same pore group (and hence travel with the same velocity) for the entire length of the column. Here, we used dimensionless time t^* to eliminate the influence of different specific discharges in various soil textures, and the kinematic ratio is directly correlated with the shape of breakthrough curves (following (28)).

The generated breakthrough curves are presented in Figure 4 for saturated conditions and Figures 5 and 6 for

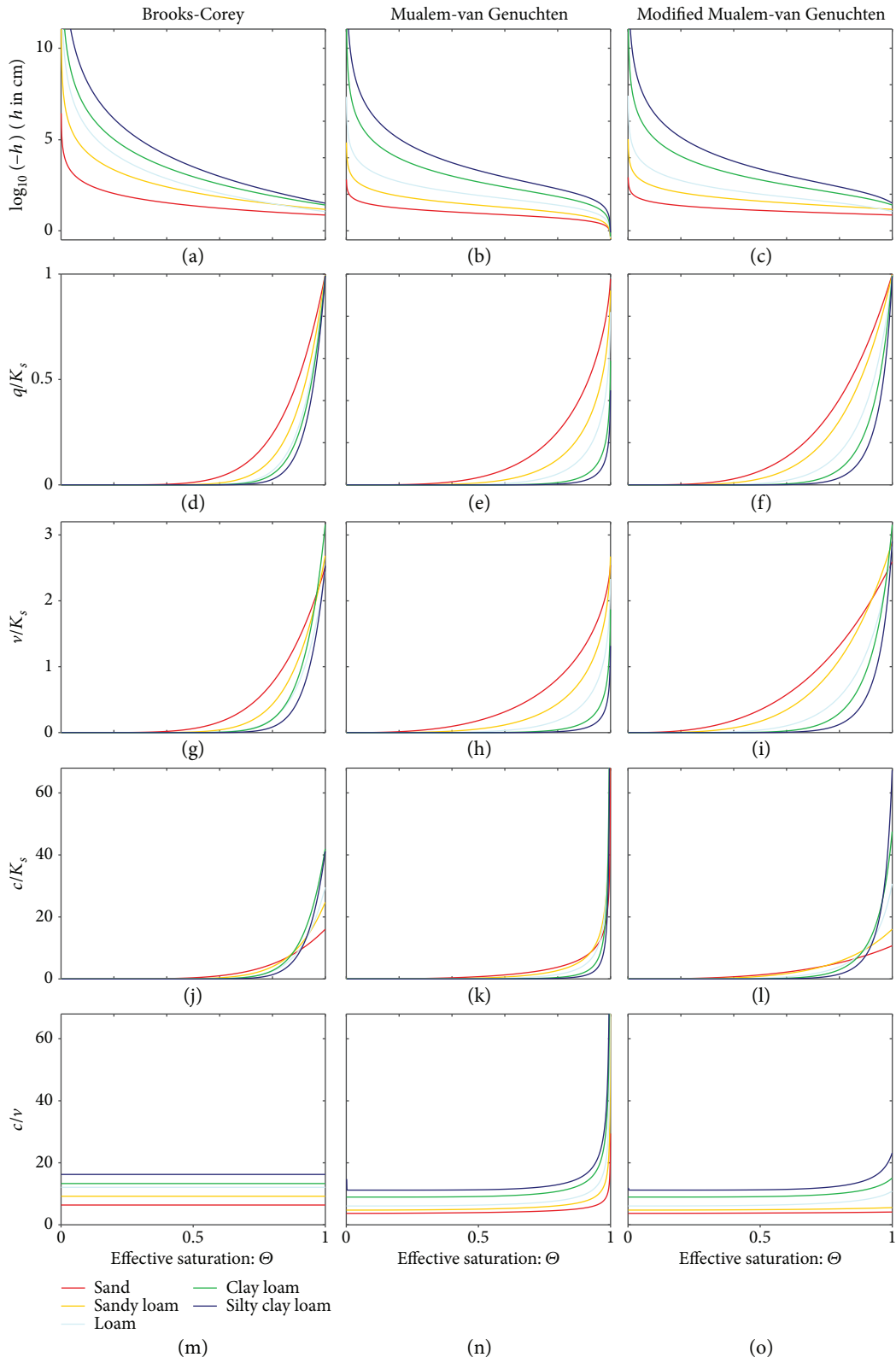


FIGURE 2: Constitutive relations of the effective saturation to logarithmic pressure head (a-c), dimensionless specific discharge (d-f), dimensionless average pore water velocity (g-i), dimensionless celerity (j-l), and kinematic ratio (m-o) in 5 typical soils under models of Brook-Corey, unmodified Mualem-van Genuchten, and modified Mualem-van Genuchten (illustrated in each column).

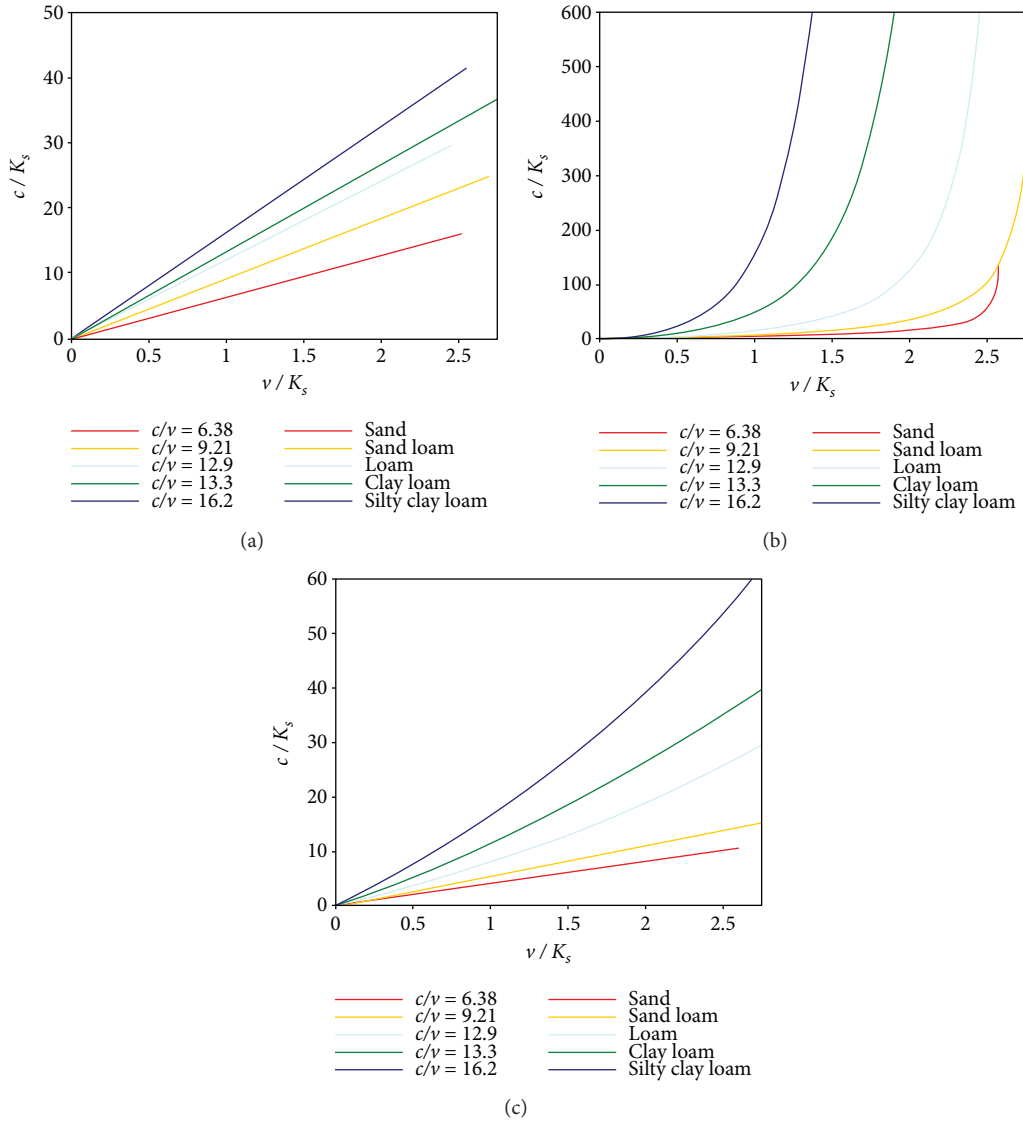


FIGURE 3: Relations between dimensionless celerity and dimensionless average pore water velocity for 5 typical soils under (a) the Brooks-Corey model, (b) unmodified Mualem-van Genuchten model, and (c) modified Mualem-van Genuchten model.

TABLE 3: Kinematic ratio under low saturation condition (effective saturation $\Theta < 0.5$).

Soil types	Sand	Sandy loam	Loam clay	Loam	Silty clay loam
Brooks-Corey model	6.378	9.211	12.091	13.309	16.245
Modified Van-Genuchten model	3.691	4.747	6.071	8.952	11.196

unsaturated conditions. The piston-shaped breakthrough curves (black lines in Figure 4, based on (31)) were computed for tracer advection driven by flow with uniform velocity distribution. The dimensionless first arrival time can be determined as a reciprocal of the kinematic ratio (see (28)). Specifically, the kinematic ratio is lower in coarse-textured soil than in fine-textured soil; therefore, the dimensionless first arrival time of fine-textured soil is earlier. The first arrival time described by the Brooks-Corey model and the modified Mualem-van Genuchten model is significantly larger than that calculated by the unmodified Mualem-van

Genuchten model for saturated condition. The kinematic ratio under the unmodified Mualem-van Genuchten model is expressed as an infinite value under saturated condition, which is caused by the overestimated celerity leading to a nearly instant breakthrough of the tracer.

After the first arrival time, the increment of relative concentration over the dimensionless time in each soil is caused by pore water velocity distribution. When $t^* = 1$, the relative concentration is above 0.7 for all soil types and all soil hydraulic models. All breakthrough curves show very long tailing, caused by the low velocity in the smaller pore

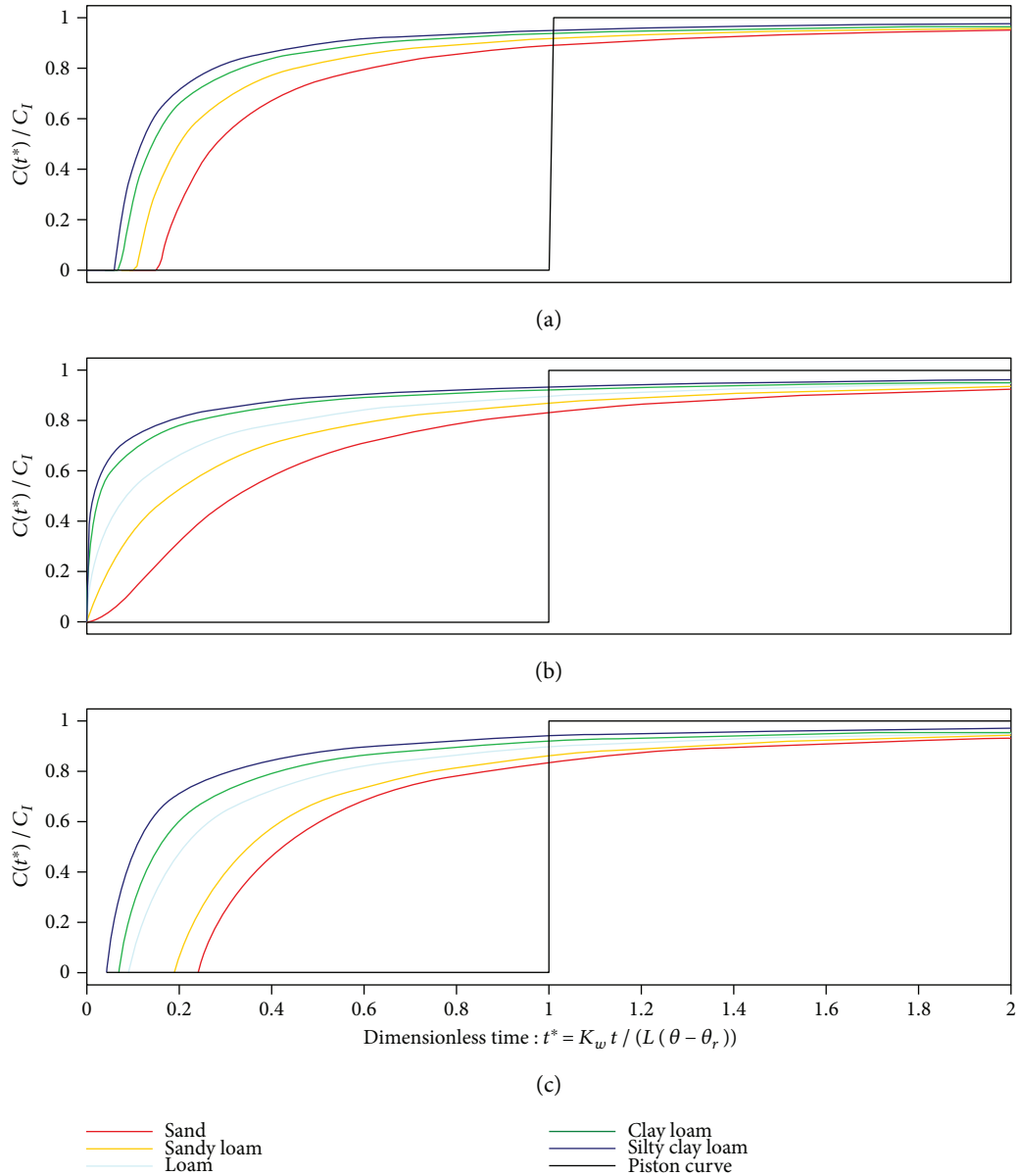


FIGURE 4: Breakthrough curves and the piston-shaped breakthrough curves under the unit hydraulic gradient condition for 5 typical saturated soils in (a) the Brook-Corey model, (b) the unmodified Mualem-van Genuchten model, and (c) the modified Mualem-van Genuchten model.

bundles. When $t^* < 1$, the relative concentration $C(t^*)/\Delta C$ approximately ranges between 0 and 0.7; the water particle transport process is dominated by the pore water velocity that is larger than the average pore water velocity. When $t^* > 1$, the relative concentration $C(t^*)/\Delta C$ generally approaches 1.0, and the slopes of the breakthrough curves turn to be flatter. The long tailing is determined by the pore water velocity distribution, because a significant fraction of pores with the low pore water velocity needs much longer time for tracer breakthrough.

In the Brooks-Corey model, the kinematic ratio is constant, and the breakthrough curves are independent of the effective saturation. In the modified Mualem-van Genuchten model, the shapes of the breakthrough curves for

saturated soil are affected by the value of the air entry pressure, while the shapes of the breakthrough curves for unsaturated soil are not affected by the effective saturation.

The effect of the air entry pressure on the breakthrough curves for sandy loam soil under saturated and unsaturated ($\theta = 0.8$) conditions is shown in Figure 5. Under saturated conditions (Figure 5(a)), the dimensionless first arrival time is zero for the unmodified Mualem-van Genuchten model ($h_s = 0$), and it approaches 0.2 when the air entry pressure is increased from 3 cm to 30 cm. In contrast, breakthrough curves do not depend significantly on the air entry pressure in unsaturated sandy loam (Figure 5(b)).

Breakthrough curves are shown for different effective saturation values for sandy loam under the unmodified

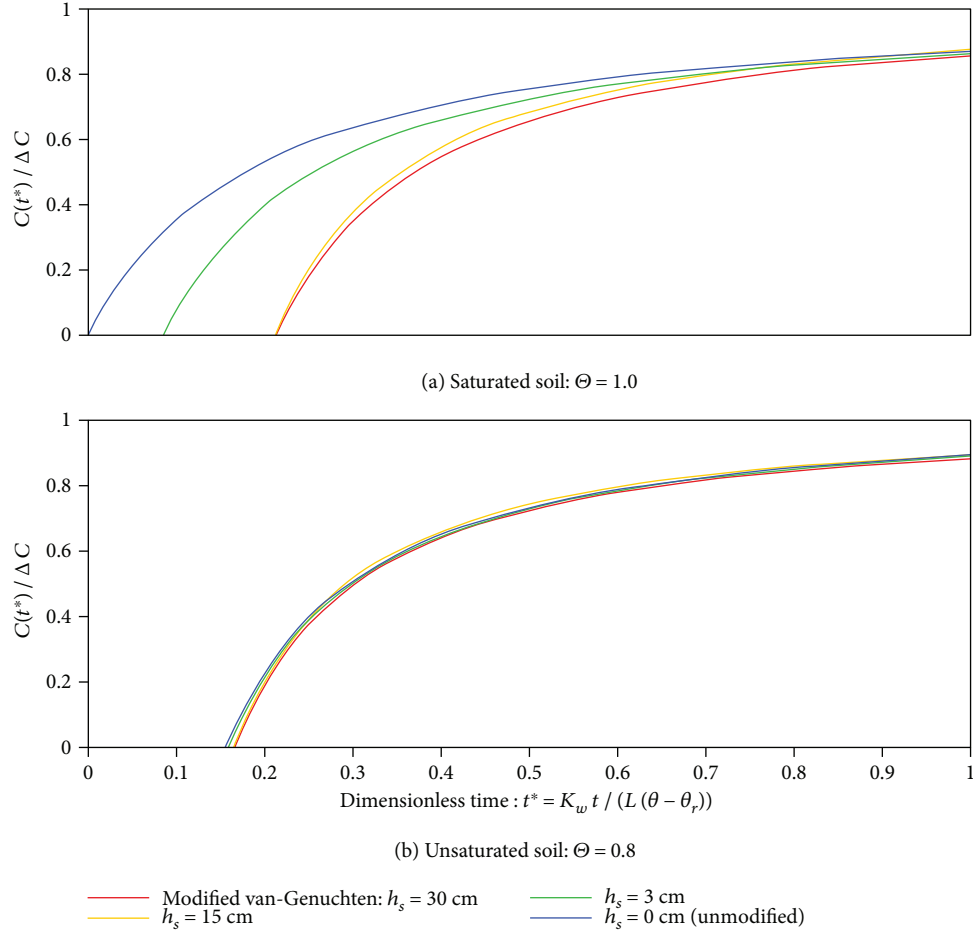


FIGURE 5: Effect of air entry pressure and effective saturation on breakthrough curves for sandy loam soil in the (a) unmodified Mualem-van Genuchten model and (b) the modified Mualem-van Genuchten model.

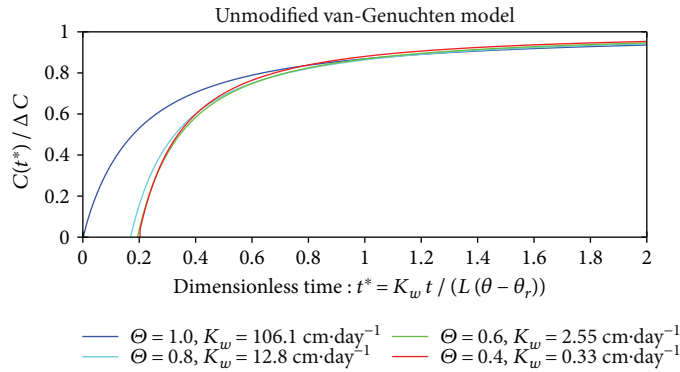


FIGURE 6: Effect of effective saturation on breakthrough curves for sandy loam soil for the unmodified Mualem-van Genuchten model.

Mualem-van Genuchten model in Figure 6. Except for the saturated case ($\Theta = 1.0$), the other three breakthrough curves are very similar.

3.3. Analysis of the Dual-Permeability Model. The bimodal soil hydraulic function describes the hydraulic properties of a conceptualized dual-continuum pore system as a composite function. However, parameterization of a bimodal soil

hydraulic function is difficult as two conceptualized domains cannot be experimentally separated. Fitting the parameter set of the bimodal soil hydraulic function according to the measurable single-continuum soil hydraulic function of the water retention curve and soil hydraulic conductivity might result in the “equifinal” parameter sets. For example, based on the Mualem-van Genuchten model, Köhne et al. [70] obtained 5 sets of the equifinal parameters of bimodal soil

TABLE 4: Equifinal parameter sets of the bimodal soil hydraulic function for a hypothetical single-continuum soil.

w (-)	Matrix flow domain					Preferential flow domain				
	K_s (cm day ⁻¹)	θ_r (-)	θ_s (-)	α_{VG} (cm ⁻¹)	n_{VG} (-)	K_s (cm day ⁻¹)	θ_r (-)	θ_s (-)	α_{VG} (cm ⁻¹)	n_{VG} (-)
0.1	2.01	0.05	0.350	0.01	1.2	1000	0	0.6	0.1	2.5
0.025	1.9	0.0	0.345	0.01	1.2	3990	0	1.0	0.1	2.508

hydraulic functions, all of which can perfectly fit a single-continuum water retention curve and hydraulic conductivity function. Different soil hydraulic behaviours described by those 5 parameter sets are difficult to distinguish. Therefore, this section demonstrates a way to distinguish the soil hydraulic characteristics of the equifinal parameter sets in the bimodal soil hydraulic function, by quantifying the celerity as a function of pressure head.

Table 4 shows the hydraulic properties of each pore domain specified by the Mualem-van Genuchten model under two “equifinal” parameter settings [70]. Under unit hydraulic gradient condition, it is often assumed that the pressure heads in the matrix flow domain and in the preferential flow domain are the same when facilitating the illustration of the hydraulic behaviour of structured soil [70]. For a dual-continuum conceptualization, the hydraulic characteristics in the matrix domain, preferential flow domain, and total domain were obtained according to (32)–(38).

Figure 7(a) shows the water retention curve for the bulk soil; the fitted bimodal water retention curve using two groups of parameters ($w = 0.1$ and $w = 0.025$) for a dual-continuum porous medium (shown as “Total” in Figure 7) agrees well with that of the single-continuum soil hydraulic model (shown as “Single” in Figure 7). Figures 7(b) and 7(c) further show that the specific discharge and average pore water velocity in a bimodal hydraulic conductivity function under two groups of “equifinality” parameter sets are different from that in single-continuum soil hydraulic function. However, the parameter sets of a bimodal soil hydraulic function generate an equifinal phenomenon in the formulated total hydraulic conductivity and total average pore water velocity. Thus, under the equifinal parameter sets of the bimodal soil hydraulic model, the higher hydraulic conductivity of the preferential flow domain can be compensated by a smaller volumetric fraction of w for conducting the equivalent amount of total specific discharge.

The proposed constitutive relation between celerity and pressure head $c(h)$ (in Figure 7(d)) is able to distinguish the implicitly formulated pore water velocity distribution of equifinal parameter sets. The celerity in the matrix domain is nearly the same for the two parameter sets. When the pressure head is smaller than -35 cm, the celerity is controlled by the matrix flow, and the preferential flow domain can be regarded as an insignificant component contributing to the pressure propagation, while when the pressure head is larger than -35 cm, the celerity is in turn controlled by the preferential flow with a much higher pore water velocity than the matrix flow, and the pressure propagation is induced by the preferential flow with much higher pore water velocity than that of the matrix flow.

The relative difference of the hydraulic conductivity and the celerity for the total domain is shown in Figure 8. For the two parameter sets, the relative difference of the hydraulic conductivity is less than 5% (Figure 8(a)). However, the celerity for the second parameter set ($w = 0.025$) in $c(h)$ is approximately twice as large as with the first parameter set ($w = 0.1$) (Figure 8(b)). This is an important result, as it can be decided which of the two parameter sets is the better one, if the celerity can be measured. The celerity can be measured with a tracer experiment by using a conservative tracer and measuring the first arrival time of the tracer. In summary, the proposed constitutive relation between celerity and pressure head (i.e., $c(h)$) is able to distinguish the implicitly formulated pore water velocity distribution of equifinal parameter sets.

4. Discussion

4.1. Relations of Soil Hydraulic Properties to the Breakthrough Curve. The pore water velocity distribution is feasible by measuring the variation of both specific discharge and water content under a perturbation analysis (i.e., by generally increasing the water fluxes on the soil surface) [33]. The pore bundle model is linking the measurable REV-scale variable with the pore-scale hydraulic characteristics. On such a basis, the proposed celerity function enables the derivation of the breakthrough curve to express the influence of pore water velocity distribution on tracer transport. Consequently, the mathematical derivation (in Section 2) implies that the same parameter set for the water retention curve or hydraulic conductivity function can also be used to parameterize pore water velocity distribution and the breakthrough curve. Inversely, the measured breakthrough curve might also be used to infer the parameter for soil hydraulic function. Recent studies show that the breakthrough curve derived from a tracer experiment could assist in obtaining a reasonably accurate parameter estimation for describing the water retention curve and the hydraulic conductivity function [56, 57]. Thus, mutually fitting the breakthrough curve, water retention curve, and hydraulic conductivity function by an inverse parameter estimation through experiments can provide a more accurately mathematical formulation to express the soil hydraulic properties.

The obtained pore water velocity distribution in typical soil textures is highly nonlinear [31, 38], which manifests that the nonuniform pore size distribution influences both water and tracer transport. In the breakthrough curve, the first arrival time is dictated by the maximum pore water velocity, and the long tailing is dictated by the relatively low pore water velocity. This phenomenon implies that the transport processes are significantly different in the preferential flow

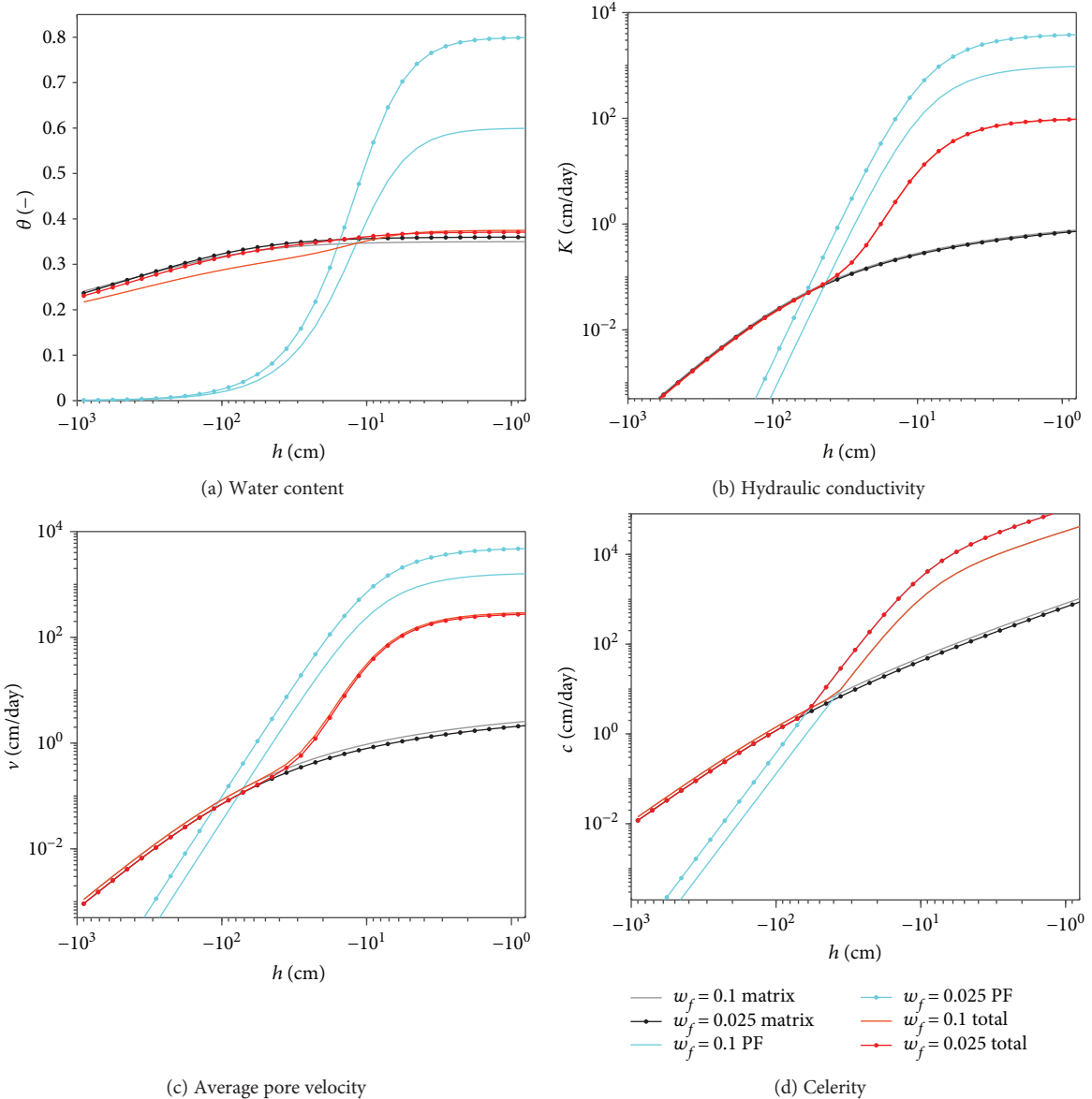


FIGURE 7: Under parameter settings of a single-continuum soil hydraulic model in Table 4, bimodal soil hydraulic functions of (a) water retention $\theta(h)$, (b) hydraulic conductivity $K(h)$, (c) average pore velocity $\bar{v}(h)$, and (d) celerity $c(h)$ for matrix flow (matrix), preferential flow (PF), single-continuum model, and dual-continuum model (dual) are given, respectively.

path within the matrix. A large volumetric fraction of water stored in micropores is nearly stagnant or with extremely low velocity [50], being classified as the matrix domain, which causes an extensive tailing of tracer concentration in the breakthrough curve. The matrix flow has a relatively insignificant contribution in delivering specific discharge and propagating pressure wave under near-saturated condition, while flow occurs in a small volumetric fraction of pores (e.g., macropores) that can be categorized as the preferential flow path dominating the transport processes and pressure propagation.

4.2. Implementing the Kinematic Ratio to Predict the Maximum Tracer Velocity. The fast tracer transport in heterogeneous soil will be dominated by the preferential flow

with the high flow velocity; thus, the effect of absorption, reaction, or diffusion might be negligible. Nimmo [23] analysed 64 field experiments and determined that the maximum tracer velocities varied within a small range, which could be predicted with by a simple model. These tracer experiments were conducted in various types of soil or bedrock with a transport distance ranging from 0.3 to 1300 m, and the maximum tracer velocities (with a 90% probability) spread between 0.8 and 200 m/day. Nimmo [23] proposed a predictive model using a ratio to link the fastest tracer velocity v_0 with an effective precipitation rate i_0 (a spatially and temporarily averaged precipitation applied to the surface boundary) and suggested that the ratio of v_0/i_0 is an essentially constant value which equaled to 18 based on an empirical estimation from their geometric mean. The obtained

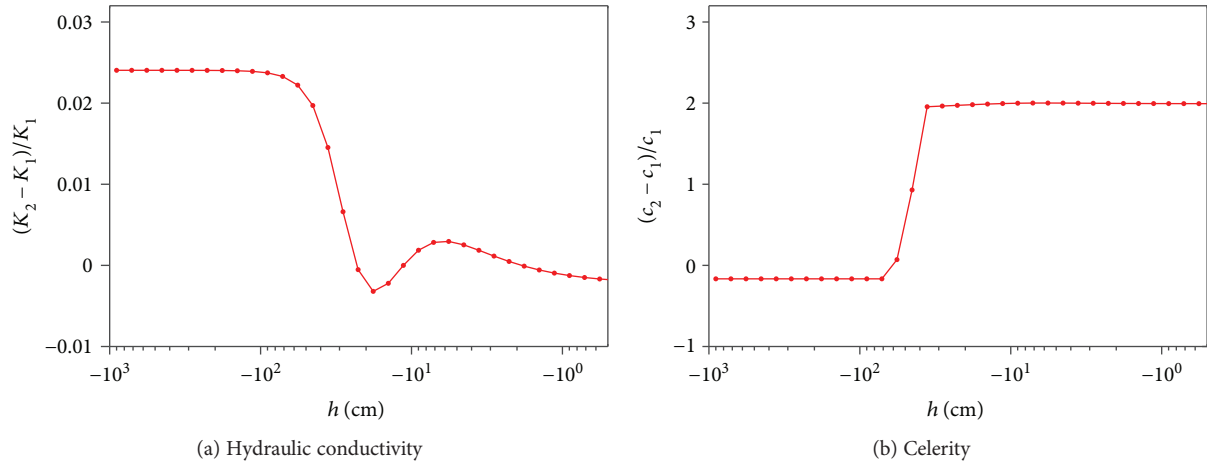


FIGURE 8: Relative difference of (a) unsaturated hydraulic conductivity and (b) celerity of total soils under the two parameter sets of Table 3.

ratio with an order-of-magnitude accuracy facilitates a fast prediction of worst-case contaminate travel times. Nimmo illustrated that the low variability of the ratio v_0/i_0 could be caused by a natural speed limit of the preferential flow in terms of frictional force and water exchange (e.g., via absorption) from the macropore to the matrix. However, the predicting ability of Nimmo's model might be hampered due to lack of the parameter constrains.

Based on our analyses of celerity, a theoretical proof and parameter constrain for Nimmo's model can be achieved by using a kinematic ratio to predict the maximum tracer velocity. Considering a hillslope, the process of water particle and tracer transport can be summarized as follows. For vertical infiltration flow in an unsaturated zone, celerity represents the maximum pore water velocity as well as the maximum tracer velocity, and the kinematic ratio approximately represents the ratio between maximum tracer velocity and average tracer velocity. For lateral flow in a saturated zone, celerity represents a nearly instant pressure propagation, yet the actual flow velocity in each pore is related with the intrinsic permeability depending on the size and tortuosity of the pore [31, 38]. Therefore, the celerity function derived for unsaturated flow can express the pore water velocity distribution even in saturated soil. In Section 3.1, we found that the kinematic ratio of unsaturated flow is likely to be a constant value for all ranges of saturation. Therefore, it can be used as an indicator to quantify the ratio between maximum tracer velocity and average tracer velocity for both the saturated soil and unsaturated soil.

The presented analysis of celerity in unsaturated soils can be compared to Nimmo's model. The ratio v_0/i_0 in Nimmo's paper has the same physical meaning as the ratio of c/q that can be defined in this study. The value of c/q is related to both kinematic ratio and soil water content as $c/q = c/(\bar{v}\theta) = \alpha_K/\theta$. The kinematic ratio of unsaturated flow based on the Brooks-Corey model is constant and ranges from 3 to 16 for the soils of Table 2, and q is equal to K under unit gradient condition.

The ratio c/K is plotted versus the effective saturation Θ in Figures 9(a)–9(c). The value of c/K decreases with Θ for the Brooks-Corey and the modified van Genuchten model.

The value of c/K approaches infinity when the effective saturation decreases from 0.3 to 0, which is not shown here because the corresponding specific discharge is very small. Except for the unmodified van Genuchten model, c/K is fairly constant and only weakly depends on the specific discharge (q/K_s) as shown in Figures 9(d)–9(f). Assuming that the soil-water content in the natural system is within a range of 0.2–0.5 (effective saturation is within a range of 0.4–1.0), we can also derive c/K which approximately ranges between 6 and 80. The geometric mean of c/K is 23 based on this rough estimation, which is close to the value of 18 from Nimmo's experimental finding. Moreover, the value of the kinematic ratio can be approximately inferred by the soil textures, water retention curve, soil hydraulic function, or maximum tracer velocity, and using the estimated kinematic ratio can provide an additional parameter constrain.

5. Conclusion

We conducted a theoretical study attempting to investigate the mechanism of pressure propagation and tracer transport in a subsurface flow system by analyzing the celerity in unsaturated flow. The celerity was firstly defined according to the continuum equations. Furthermore, based on the conceptualization of a pore bundle model, a mathematical derivation showed that the celerity in unsaturated flow can be illustrated as the maximum pore water velocity among all the water-filled flow paths, and the kinematic ratio can be illustrated as the ratio of the maximum pore water velocity to the average pore water velocity. Under unit hydraulic gradient condition, the celerity function is formulated as a first-order derivative of the soil hydraulic conductivity function to manifest the pore water velocity distribution, which can further be used to derive a breakthrough curve for tracking the tracer and water particle transport under steady flow condition.

The soil hydraulic characteristic of typical soil textures is reanalysed by using the (un/modified) Mualem-van Genuchten and Brooks-Corey models with standard parameter sets. The results of all soil textures present nonlinear relations of effective saturation with hydraulic conductivity and celerity.

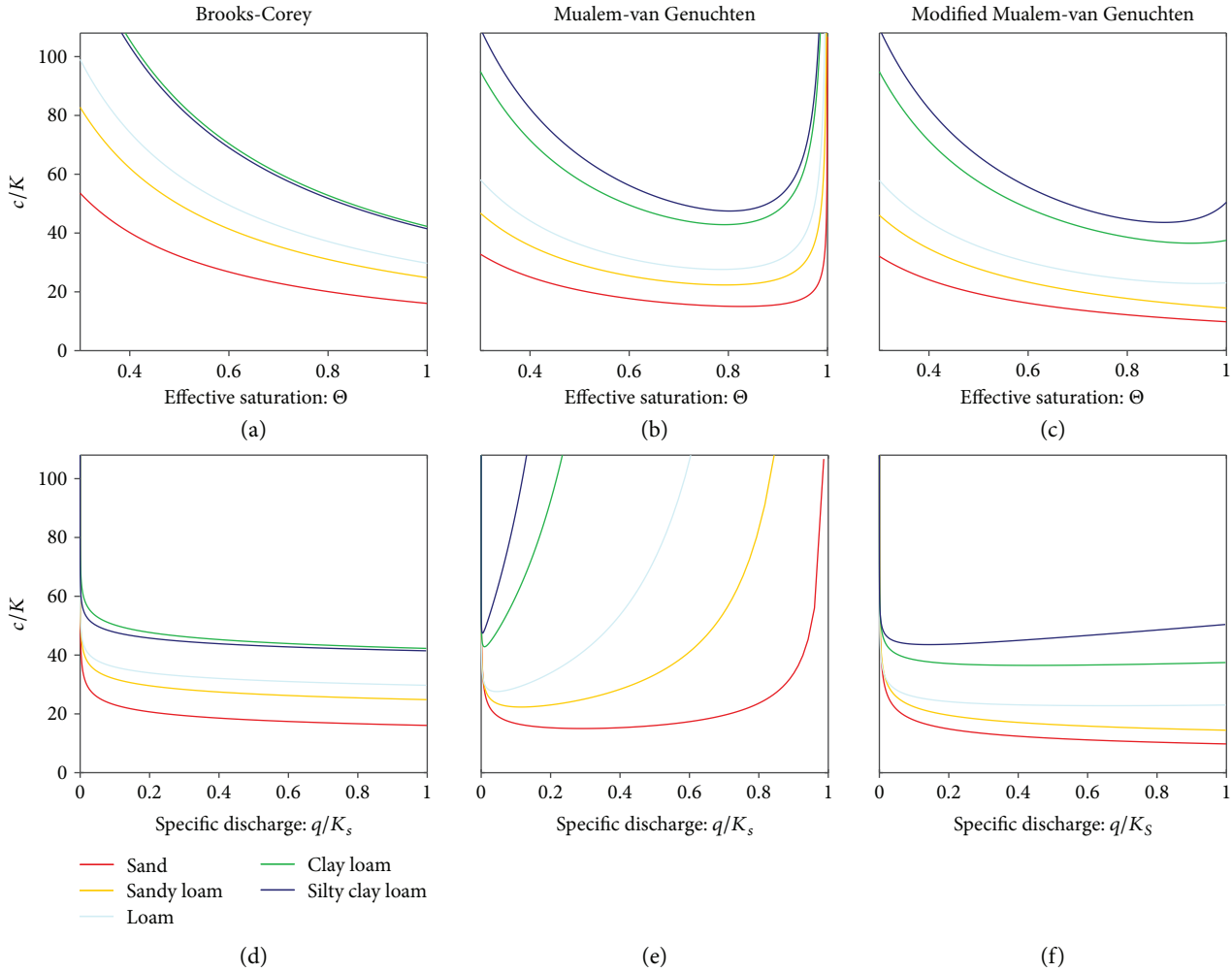


FIGURE 9: Under 3 models (illustrating in each column), (a–c) the relation between the ratio of c/K with effective saturation Θ and (d–f) the relation between the ratio of c/K with relative specific discharge q/K_s are illustrated.

The results show that water in a small volumetric fraction (around 15%) of pores has a much higher velocity than the remaining pore volume. The derived breakthrough curve can manifest the influence of pore water velocity distribution on the advective tracer transport. The first arrival time of the tracer is determined by the maximum pore water velocity, and the long tailing is caused by the nearly stagnate matrix flow in micropores with a large volumetric fraction. Furthermore, the pore water velocity distribution formulated in a composite bimodal soil hydraulic function can also be described by the proposed celerity function. Different parameter sets may result in similar water retention curves and soil hydraulic functions, but their celerities differ significantly which shows that the equifinal parameter sets of a bimodal soil hydraulic function can be distinguished by using the celerity function.

Analyzing the celerity in unsaturated flow facilitates the understanding and quantification of the pore-scale hydraulic characteristics and the complex subsurface transport processes. The celerity-effective saturation curve may be applicable to the bimodal soil hydraulic functions to demonstrate the distributions of pore water velocities for natural

soils. Furthermore, the following possible approaches for implementation are suggested and discussed in Section 4. Under unit hydraulic gradient, the three constitutive relations (i.e., water retention curve $\theta(h)$, hydraulic conductivity function $K(\theta)$, and celerity function $c(\theta)$) and the derived breakthrough curve share the same parameter set, which could facilitate the formulation and parameterization of soil hydraulic models. Finally, we found that the ratio of celerity and specific discharge c/q is fairly constant for specific soil texture, in accordance with published experiment findings.

Data Availability

The data used to support the findings of this study are available from the corresponding author upon request.

Conflicts of Interest

The authors declare that they have no conflicts of interest.

Acknowledgments

This work was financially supported by the National Natural Science Foundation of China (Grant nos. 41771021 and 41471012), the China Postdoctoral Science Foundation (nos. 2017M621783 and 2018T110527), the International Postdoctoral Exchange Fellowship Program by the China Postdoctoral Council (year 2017), and the Startup Foundation for Introducing Talent of Nanjing University of Information Science and Technology (no. 2017r045). The authors would also like to thank Professor Huub Savenije, Professor Mark Bakker, and Dr. Thom Bogaard for their comments and suggestions for this manuscript.

References

- [1] J. Bear, *Dynamics of Fluids in Porous Media*, Dover, 1988.
- [2] K. Beven, "Changing ideas in hydrology — the case of physically-based models," *Journal of Hydrology*, vol. 105, no. 1-2, pp. 157–172, 1989.
- [3] D. R. Nielsen, M. Th. Van Genuchten, and J. W. Biggar, "Water flow and solute transport processes in the unsaturated zone," *Water Resources Research*, vol. 22, no. 9S, pp. 89S–108S, 1986.
- [4] X. Bai, B. He, X. Li et al., "First assessment of sentinel-1A data for surface soil moisture estimations using a coupled water cloud model and advanced integral equation model over the Tibetan plateau," *Remote Sensing*, vol. 9, no. 7, p. 714, 2017.
- [5] W. Durner and H. Flüßler, "Multi-domain model for pore-size dependent transport of solutes in soils," *Geoderma*, vol. 70, no. 2–4, pp. 281–297, 1996.
- [6] L. Wei, J. Dong, M. Gao, and X. Chen, "Factors controlling temporal stability of surface soil moisture: a watershed-scale modeling study," *Vadose Zone Journal*, vol. 16, no. 10, 2017.
- [7] H. Flüßler, W. Durner, and M. Flury, "Lateral solute mixing processes — a key for understanding field-scale transport of water and solutes," *Geoderma*, vol. 70, no. 2–4, pp. 165–183, 1996.
- [8] V. P. Singh, *Kinematic Wave Modeling in Water Resources, Environmental Hydrology*, John Wiley & Sons, 1997.
- [9] P. D'Odorico, S. Fagherazzi, and R. Rigon, "Potential for landsliding: dependence on hyetograph characteristics," *Journal of Geophysical Research: Earth Surface*, vol. 110, 2005.
- [10] S. K. Kampf and S. J. Burges, "A framework for classifying and comparing distributed hillslope and catchment hydrologic models," *Water Resources Research*, vol. 43, no. 5, 2007.
- [11] O. Cainelli, A. Bellin, and M. Putti, "On the accuracy of classic numerical schemes for modeling flow in saturated heterogeneous formations," *Advances in Water Resources*, vol. 47, pp. 43–55, 2012.
- [12] M. van Genuchten, C. Naveira-Cotta, T. Skaggs, A. Raoof, and E. Pontedeiro, "The Use of Numerical Flow and Transport Models in Environmental Analyses," in *Application of Soil Physics in Environmental Analyses*, W. G. Teixeira, M. B. Ceddia, M. V. Ottoni, and G. K. Donnagema, Eds., pp. 349–376, Springer International Publishing, 2014.
- [13] M. J. Lighthill and G. B. Whitham, "On kinematic waves. I. Flood movement in long rivers," *Proceedings of the Royal Society A: Mathematical, Physical and Engineering Sciences*, vol. 229, no. 1178, pp. 281–316, 1955.
- [14] V. P. Singh, *Kinematic Wave Modeling in Water Resources, Surface-Water Hydrology*, John Wiley & Sons, 1996.
- [15] T. S. W. Wong, "Influence of upstream inflow on wave celerity and time to equilibrium on an overland plane," *Hydrological Sciences Journal*, vol. 41, no. 2, pp. 195–205, 1996.
- [16] H. H. G. Savenije, "3 - Tidal Dynamics," in *Salinity and Tides in Alluvial Estuaries*, H. H. G. Savenije, Ed., pp. 69–107, Elsevier Science Ltd, Amsterdam, 2005.
- [17] H. H. G. Savenije and E. J. M. Veling, "Relation between tidal damping and wave celerity in estuaries," *Journal of Geophysical Research: Oceans*, vol. 110, no. C4, 2005.
- [18] P. F. Germann and K. Beven, "Kinematic wave approximation to infiltration into soils with sorbing macropores," *Water Resources Research*, vol. 21, no. 7, pp. 990–996, 1985.
- [19] V. P. Singh and E. S. Joseph, "Kinematic-wave model for soil-moisture movement with plant-root extraction," *Irrigation Science*, vol. 14, no. 4, pp. 189–198, 1994.
- [20] J. J. McDonnell and K. Beven, "Debates—the future of hydrological sciences: a (common) path forward? A call to action aimed at understanding velocities, celerities and residence time distributions of the headwater hydrograph," *Water Resources Research*, vol. 50, no. 6, pp. 5342–5350, 2014.
- [21] J. Davies and K. Beven, "Comparison of a multiple interacting pathways model with a classical kinematic wave subsurface flow solution," *Hydrological Sciences Journal*, vol. 57, no. 2, pp. 203–216, 2012.
- [22] T. C. Rasmussen, R. H. Baldwin, J. F. Dowd, and A. G. Williams, "Tracer vs. pressure wave velocities through unsaturated saprolite," *Soil Science Society of America Journal*, vol. 64, no. 1, pp. 75–85, 2000.
- [23] J. R. Nimmo, "Simple predictions of maximum transport rate in unsaturated soil and rock," *Water Resources Research*, vol. 43, no. 5, 2007.
- [24] Z. Wang, J. Feyen, D. R. Nielsen, and M. T. van Genuchten, "Two-phase flow infiltration equations accounting for air entrapment effects," *Water Resources Research*, vol. 33, no. 12, pp. 2759–2767, 1997.
- [25] Y. Su, J. Langhammer, and J. Jarsjö, "Geochemical responses of forested catchments to bark beetle infestation: evidence from high frequency in-stream electrical conductivity monitoring," *Journal of Hydrology*, vol. 550, pp. 635–649, 2017.
- [26] A. Alaoui, P. Germann, N. Jarvis, and M. Acutis, "Dual-porosity and kinematic wave approaches to assess the degree of preferential flow in an unsaturated soil," *Hydrological Sciences Journal*, vol. 48, no. 3, pp. 455–472, 2003.
- [27] R. E. Smith, "Approximate soil water movement by kinematic characteristics," *Soil Science Society of America Journal*, vol. 47, no. 1, pp. 3–8, 1983.
- [28] K. Beven and P. Germann, "Macropores and water flow in soils revisited," *Water Resources Research*, vol. 49, no. 6, pp. 3071–3092, 2013.
- [29] R. J. Charbeneau, "Kinematic models for soil moisture and solute transport," *Water Resources Research*, vol. 20, no. 6, pp. 699–706, 1984.
- [30] V. P. Singh, "Is hydrology kinematic?," *Hydrological Processes*, vol. 16, no. 3, pp. 667–716, 2002.
- [31] A. Peters, W. Durner, and G. Wessolek, "Consistent parameter constraints for soil hydraulic functions," *Advances in Water Resources*, vol. 34, no. 10, pp. 1352–1365, 2011.

- [32] N. T. Burdine, "Relative permeability calculations from pore size distribution data," *Journal of Petroleum Technology*, vol. 5, no. 3, pp. 71–78, 1953.
- [33] E. C. Childs and N. Collis-George, "The permeability of porous materials," *Proceedings of the Royal Society A Mathematical, Physical and Engineering Sciences*, vol. 201, no. 1066, pp. 392–405, 1950.
- [34] Y. Mualem, "A new model for predicting the hydraulic conductivity of unsaturated porous media," *Water Resources Research*, vol. 12, no. 3, pp. 513–522, 1976.
- [35] R. H. Brooks and A. T. Corey, *Hydraulic Properties of Porous Media*, Colorado State University, 1964.
- [36] M. Tuller and D. Or, "Hydraulic conductivity of variably saturated porous media: film and corner flow in angular pore space," *Water Resources Research*, vol. 37, no. 5, pp. 1257–1276, 2001.
- [37] M. T. van Genuchten, "A closed-form equation for predicting the hydraulic conductivity of unsaturated soils," *Soil Science Society of America Journal*, vol. 44, no. 5, pp. 892–898, 1980.
- [38] H. J. Vogel, "A numerical experiment on pore size, pore connectivity, water retention, permeability, and solute transport using network models," *European Journal of Soil Science*, vol. 51, no. 1, pp. 99–105, 2000.
- [39] M. A. Celia, P. C. Reeves, and L. A. Ferrand, "Recent advances in pore scale models for multiphase flow in porous media," *Reviews of Geophysics*, vol. 33, no. S2, pp. 1049–1057, 1995.
- [40] H. Dahle, M. Celia, and S. M. Hassanizadeh, "Bundle-of-Tubes Model for Calculating Dynamic Effects in the Capillary-Pressure-Saturation Relationship," in *Upscaling Multiphase Flow in Porous Media*, D. B. Das and S. M. Hassanizadeh, Eds., pp. 5–22, Springer Netherlands, 2005.
- [41] K. Beven and P. Germann, "Macropores and water flow in soils," *Water Resources Research*, vol. 18, no. 5, pp. 1311–1325, 1982.
- [42] J. Freer, J. J. McDonnell, K. J. Beven et al., "The role of bedrock topography on subsurface storm flow," *Water Resources Research*, vol. 38, no. 12, pp. 5-1–5-16, 2002.
- [43] T. Uchida, Y. Asano, T. Mizuyama, and J. J. McDonnell, "Role of upslope soil pore pressure on lateral subsurface storm flow dynamics," *Water Resources Research*, vol. 40, no. 12, 2004.
- [44] M. L. Brusseau and P. S. C. Rao, "Modeling solute transport in structured soils: a review," *Geoderma*, vol. 46, no. 1–3, pp. 169–192, 1990.
- [45] F. A. Dullien, *Porous Media: Fluid Transport and Pore Structure*, Academic press, 1991.
- [46] A. G. Williams, J. F. Dowd, D. Scholefield, N. M. Holden, and L. K. Deeks, "Preferential flow variability in a well-structured soil," *Soil Science Society of America Journal*, vol. 67, no. 4, pp. 1272–1281, 2003.
- [47] C. Kendall and J. J. McDonnell, "Preface," in *Isotope Tracers in Catchment Hydrology*, C. K. J. McDonnell, Ed., pp. vii–vix, Elsevier, Amsterdam, 1998.
- [48] J. M. Köhne, S. Köhne, and J. Šimůnek, "A review of model applications for structured soils: (a) water flow and tracer transport," *Journal of Contaminant Hydrology*, vol. 104, no. 1–4, pp. 4–35, 2009.
- [49] J. Beckers and Y. Alila, "A model of rapid preferential hillslope runoff contributions to peak flow generation in a temperate rain forest watershed," *Water Resources Research*, vol. 40, no. 3, 2004.
- [50] J. Renée Brooks, H. R. Barnard, R. Coulombe, and J. J. McDonnell, "Ecohydrologic separation of water between trees and streams in a Mediterranean climate," *Nature Geoscience*, vol. 3, no. 2, pp. 100–104, 2010.
- [51] M. Hrachowitz, H. H. G. Savenije, G. Blöschl et al., "A decade of predictions in ungauged basins (PUB)—a review," *Hydrological Sciences Journal*, vol. 58, no. 6, pp. 1198–1255, 2013.
- [52] J. W. Kirchner, "A double paradox in catchment hydrology and geochemistry," *Hydrological Processes*, vol. 17, no. 4, pp. 871–874, 2003.
- [53] F. M. Phillips, "Hydrology: soil-water bypass," *Nature Geoscience*, vol. 3, no. 2, pp. 77–78, 2010.
- [54] M. Weiler, B. L. McGlynn, K. J. McGuire, and J. J. McDonnell, "How does rainfall become runoff? A combined tracer and runoff transfer function approach," *Water Resources Research*, vol. 39, no. 11, 2003.
- [55] J. Seibert, T. Grabs, S. Köhler, H. Laudon, M. Winterdahl, and K. Bishop, "Linking soil- and stream-water chemistry based on a riparian flow-concentration integration model," *Hydrology and Earth System Sciences*, vol. 13, no. 12, pp. 2287–2297, 2009.
- [56] M. H. Mohammadi, M. R. Neishabouri, and H. Rafahi, "Predicting the solute breakthrough curve from soil hydraulic properties," *Soil Science*, vol. 174, no. 3, pp. 165–173, 2009.
- [57] Q. Wang, R. Horton, and J. Lee, "A simple model relating soil water characteristic curve and soil solute breakthrough curve 1," *Soil Science*, vol. 167, no. 7, pp. 436–443, 2002.
- [58] W. Shao, *Numerical Modeling of the Effect of Preferential Flow on Hillslope Hydrology and Slope Stability*, Doctoral thesis, TU Delft Water Resources, 2017.
- [59] J. L. Nieber, R. Z. Dautov, A. G. Egorov, and A. Y. Sheshukov, "Dynamic capillary pressure mechanism for instability in gravity-driven flows; review and extension to very dry conditions," *Transport in Porous Media*, vol. 58, no. 1-2, pp. 147–172, 2005.
- [60] S. C. Iden and W. Durner, "Free-form estimation of the unsaturated soil hydraulic properties by inverse modeling using global optimization," *Water Resources Research*, vol. 43, no. 7, 2007.
- [61] P. Nasta, J. A. Vrugt, and N. Romano, "Prediction of the saturated hydraulic conductivity from Brooks and Corey's water retention parameters," *Water Resources Research*, vol. 49, no. 5, pp. 2918–2925, 2013.
- [62] A. Peters and W. Durner, "A simple model for describing hydraulic conductivity in unsaturated porous media accounting for film and capillary flow," *Water Resources Research*, vol. 44, no. 11, 2008.
- [63] M. G. Schaap and M. T. van Genuchten, "A modified Mualem–van Genuchten formulation for improved description of the hydraulic conductivity near saturation," *Vadose Zone Journal*, vol. 5, no. 1, pp. 27–34, 2006.
- [64] G. S. Campbell, "A simple method for determining unsaturated conductivity from moisture retention data," *Soil Science*, vol. 117, no. 6, pp. 311–314, 1974.
- [65] Y. Mualem and G. Dagan, "Hydraulic conductivity of soils: unified approach to the statistical models," *Soil Science Society of America Journal*, vol. 42, no. 3, pp. 392–395, 1978.
- [66] D. Jacques, J. Šimůnek, A. Timmerman, and J. Feyen, "Calibration of Richards' and convection–dispersion equations to field-scale water flow and solute transport under rainfall

- conditions,” *Journal of Hydrology*, vol. 259, no. 1–4, pp. 15–31, 2002.
- [67] J. Vanderborght, M. Vanclooster, A. Timmerman et al., “Overview of inert tracer experiments in key Belgian soil types: relation between transport and soil morphological and hydraulic properties,” *Water Resources Research*, vol. 37, no. 12, pp. 2873–2888, 2001.
- [68] W. Shao, T. Bogaard, M. Bakker, and M. Berti, “The influence of preferential flow on pressure propagation and landslide triggering of the Rocca Pitigliana landslide,” *Journal of Hydrology*, vol. 543, pp. 360–372, 2016.
- [69] W. Durner, “Hydraulic conductivity estimation for soils with heterogeneous pore structure,” *Water Resources Research*, vol. 30, no. 2, pp. 211–223, 1994.
- [70] J. M. Köhne, S. Köhne, and H. H. Gerke, “Estimating the hydraulic functions of dual-permeability models from bulk soil data,” *Water Resources Research*, vol. 38, no. 7, pp. 261–2611, 2002.
- [71] D. Mallants, P.-H. Tseng, N. Toride, A. Tinunerman, and J. Feyen, “Evaluation of multimodal hydraulic functions in characterizing a heterogeneous field soil,” *Journal of Hydrology*, vol. 195, no. 1–4, pp. 172–199, 1997.
- [72] B. P. Mohanty, R. S. Bowman, J. M. H. Hendrickx, and M. T. van Genuchten, “New piecewise-continuous hydraulic functions for modeling preferential flow in an intermittent-flood-irrigated field,” *Water Resources Research*, vol. 33, no. 9, pp. 2049–2063, 1997.
- [73] N. Romano, P. Nasta, G. Severino, and J. W. Hopmans, “Using bimodal lognormal functions to describe soil hydraulic properties,” *Soil Science Society of America Journal*, vol. 75, no. 2, pp. 468–480, 2011.
- [74] T. Zurmühl and W. Durner, “Determination of parameters for bimodal hydraulic functions by inverse modeling,” *Soil Science Society of America Journal*, vol. 62, no. 4, pp. 874–880, 1998.
- [75] J. M. Hendrickx and M. Flury, “Uniform and Preferential Flow Mechanisms in the Vadose Zone,” in *Conceptual Models of Flow and Transport in the Fractured Vadose Zone*, pp. 149–188, National Academies Press, Washington, DC, USA, 2001.
- [76] N. J. Jarvis, “A review of non-equilibrium water flow and solute transport in soil macropores: principles, controlling factors and consequences for water quality,” *European Journal of Soil Science*, vol. 58, no. 3, pp. 523–546, 2007.
- [77] W. Shao, J. Ni, A. K. Leung, Y. Su, and C. W. W. Ng, “Analysis of plant root-induced preferential flow and pore-water pressure variation by a dual-permeability model,” *Canadian Geotechnical Journal*, vol. 54, no. 11, pp. 1537–1552, 2017.
- [78] W. Shao, T. A. Bogaard, M. Bakker, and R. Greco, “Quantification of the influence of preferential flow on slope stability using a numerical modelling approach,” *Hydrology and Earth System Sciences*, vol. 19, no. 5, pp. 2197–2212, 2015.
- [79] F. J. Leij, *The UNSODA Unsaturated Soil Hydraulic Database: User’s Manual*, National Risk Management Research Laboratory, Office of Research and Development, US Environmental Protection Agency, 96, 1996.
- [80] M. T. Van Genuchten, F. Leij, and S. Yates, *The RETC Code for Quantifying the Hydraulic Functions of Unsaturated Soils*, Robert S. Kerr Environmental Research Laboratory, 1991.
- [81] G. W. Waswa, A. D. Clulow, C. Freese, P. A. L. Le Roux, and S. A. Lorentz, “Transient pressure waves in the vadose zone and the rapid water table response,” *Vadose Zone Journal*, vol. 12, no. 1, 2013.

Research Article

Upscaling Strategies of Porosity-Permeability Correlations in Reacting Environments from Pore-Scale Simulations

Nikolaos I. Prasianakis ¹, Michael Gatschet,^{1,2} Aida Abbasi,¹ and Sergey V. Churakov^{1,2}

¹Laboratory for Waste Management LES, Nuclear Energy and Safety Department, Paul Scherrer Institute, 5232 Villigen, Switzerland

²Institute of Geological Sciences, University of Bern, 3012 Bern, Switzerland

Correspondence should be addressed to Nikolaos I. Prasianakis; nikolaos.prasianakis@psi.ch

Received 2 February 2018; Accepted 29 April 2018; Published 19 June 2018

Academic Editor: Ilenia Battiato

Copyright © 2018 Nikolaos I. Prasianakis et al. This is an open access article distributed under the Creative Commons Attribution License, which permits unrestricted use, distribution, and reproduction in any medium, provided the original work is properly cited.

In geochemically reacting environments, the mineral dissolution and precipitation alters the structural and transport properties of the media of interest. The chemical and structural heterogeneities of the porous media affect the temporal evolution of the permeability with respect to porosity. Such correlations follow a nonlinear trend, which is difficult to estimate a priori and without knowledge of the microstructure itself, especially under the presence of strong chemical gradients. Macroscopic field-scale codes require such an input, and in the absence of exact descriptions, simplified correlations are used. After highlighting the diversity of microstructural evolution paths, due to dissolution, we discuss possible upscaling strategies.

1. Introduction

Precipitation and dissolution reactions in porous media dominate and control a large number of geochemical processes and industrial applications. The precipitation and dissolution of minerals from aqueous solutions alters the pore space and its connectivity. This has a strong effect on the mass convection and diffusion through the porous medium. When a mineral precipitates/dissolves at the reactive porous surface, the overall porosity decreases/increases, leading to a subsequent decrease/increase in permeability and effective diffusivity. At the same time, the connectivity of the pores can also change in a way to block or to facilitate the mass diffusion processes.

Reactive transport modelling at the field scale is usually based on a macroscopic finite element or a finite volume discretization scheme [1]. In such descriptions, the computational domain is divided into small elements/volumes, the so-called voxels. The voxels are typically several orders of magnitude larger than the typical pore diameter, and as a consequence, all chemical and transport properties within such volumes are homogenized and smoothed out. The pore space and its transport properties are therefore represented

using macroscopic parameters, such as the porosity, the tortuosity, the diffusivity, and the permeability. In such a description, the small scale geometrical characteristics and the heterogeneities of the porous materials are neglected. Such an assumption allows making accurate numerical predictions in the case of relatively mild chemical gradients, as well as in the case where chemical reactions can be approximated by equilibrium values. However, when strong chemical gradients are present with simultaneous dissolution and precipitation reactions, the pure macroscopic reactive transport codes fail to make accurate predictions of the evolution of the system.

Dissolution and precipitation reactions change the pore space and the resulting material properties, in a nonlinear way, and therefore have a strong feedback in the transport properties of the porous medium. The lack of explicit pore structure description and of appropriate material-specific correlations is responsible, for example, for the numerical artefact, relevant to the dependency of the resulting clogging times on the spatial grid discretization [1–5]. An improvement to the numerical predictions can be achieved (a) by coupling pore-level solvers to the macroscopic ones in a multiscale simulator [6–8] or (b) by providing the necessary

microscopic feedback in terms of appropriate correlations or tabulated values, which can be defined from pore-level simulations (upscaling of results). Pore-level methods allow the simulation of the advection-diffusion-reaction processes at the pore space, where surface charges and reactive surface areas can be explicitly considered. Representative structures can be generated via computer models or can be obtained via X-ray or other microtomography techniques. When combined with appropriate kinetic and thermodynamic solvers that act at the submicrometer level, it is possible to reproduce accurately the experimental observations.

Depending on the level of abstraction, different pore-level methodologies exist. The more detailed ones solve the relevant flow equations or some approximation depending on the flow regime and the flow physics that are involved, in realistic geometries. Such methods are the lattice Boltzmann method [9–13], the methods based on particle hydrodynamics [14, 15], as well as the standard finite volume methods when applied in complex geometries with moving boundaries [16–18]. Lattice Boltzmann models can resolve transport processes in realistic complex geometries, involving complex interactions between species and phases, but are more computational intensive compared to pore network models. A significant advantage of the lattice Boltzmann methodology is the minimum effort to discretize the realistic computational domain, as well as the efficient continuous solid structure update per time step. Such an example is the evolution of a system when simultaneous dissolution and precipitation processes are competing and drive the evolution of the system [11, 19]. Efficient parallelization though allows running simulations with many billion degrees of freedom in relatively small computer clusters, especially when GPGPUs are used [20, 21]. We note that the numerical extraction of microscopic properties using realistic geometries has the potential to provide useful input to the effective medium theories, which are used to upscale porous medium flows [22]

In this paper, we construct pore geometries with target porosity and initial permeability following a methodology similar to [23, 24]. The target permeability is selected in a way to represent limestone rock samples commonly found in hydrocarbon reservoirs or in geothermal fields. The implemented chemical reaction is representing the calcite dissolution under the presence of acid, a common process used in the field stimulation, in order to enhance the permeability of the formation. The evolution of selected geometries is examined using the lattice Boltzmann framework, and permeability-porosity correlations are numerically extracted. Upscaling strategies that allow passing information to the macroscopic solvers and therefore bridge pore level and macroscopic scales, are discussed based on the output of the simulations.

2. Reactive Transport Modelling

2.1. Pore-Level Modelling. For the simulation presented in the next sections, the lattice Boltzmann methodology is implemented. This method is a special discretization of the Boltzmann equation. The elementary variables are the so-

called populations or velocity probability distribution functions f_i . At every distribution function corresponds to a discrete velocity vector [25–27]. Different discretization schemes lead to different numbers of discrete velocities, which results in several lattice models [28, 29]. For two-dimensional simulations, the standard D2Q9 square lattice with 9 discrete velocities is usually implemented due to its simplicity and robustness in complex geometry domains (see Figure 1).

For the modelling of the advection-diffusion and precipitation processes, a multicomponent LB model is used as described in [19]. For the sake of completeness, we briefly present it also here. The model is composed of a basis fluid medium that recovers the Navier-Stokes equations at the macroscopic limit, plus a passive scalar-coupled population set that simulates the diffusion of ions. The isothermal-guided equilibrium nine-velocity model (D2Q9 lattice) of Prasianakis et al. [30] is selected as the basis model. The discrete velocities of populations f_i for $i = 0-8$ are $c_i = (0, 0)$ for $i = 0$, $c_i = (\pm 1, 0)$ and $(0, \pm 1)$ for $i = 1-4$, and $c_i = (\pm 1, \pm 1)$ for $i = 5-8$ [29].

The following population moments correspond to the density of the solution ρ and the momentum j_a in the direction $a = x, y$:

$$\begin{aligned} \sum_{i=0}^8 f_i &= \rho, \\ \sum_{i=0}^8 c_{ia} f_i &= j_a. \end{aligned} \quad (1)$$

The guided equilibrium populations f_i^{eq} are given in a closed form, where $T_0 = 1/3$:

$$f_i^{\text{eq}} = \rho \prod_{a=x,y} \left(\frac{2c_{ia}^2 - 1}{2c_{ia}^2} \right) (c_{ia}^2 - 1 + c_{ia}u_a + u_a^2 + T_0). \quad (2)$$

The Boltzmann BGK equation is solved: $\partial_t f_i + c_{ia} \partial_a f_i = -1/\tau (f_i - f_i^{\text{eq}})$, where τ is the relaxation parameter, and $\mu = \tau \rho T_0$ is the resulting macroscopic dynamic viscosity. BGK stands for the Bhatnagar-Gross-Krook collision model as depicted in the right hand side of the aforementioned equation and describes the relaxation of populations f_i to their equilibrium state f_i^{eq} with a single relaxation time τ . Implementation of the BGK model for porous medium flows needs specific care, since under specific circumstances, high slip velocities might arise at the solid-fluid interface. This could affect the numerical measurements of permeability and the evolution of the geometries due to reactions. A detailed study on this issue has been presented in [31]. Here, we operate the model in conditions as described in the aforementioned reference. For the advection-diffusion-reaction equations of the reactive species, a D2Q9 model is also implemented.

The equilibrium populations ξ_i^{eq} for the reactive species ξ_i are given:

$$\xi_i^{\text{eq}} = C_i \prod_{\alpha=x,y} \left(\frac{1 - 2c_{i\alpha}^2}{2c_{i\alpha}^2} \right) (c_{i\alpha}^2 - 1 + c_{i\alpha}u_\alpha + T_0), \quad (3)$$

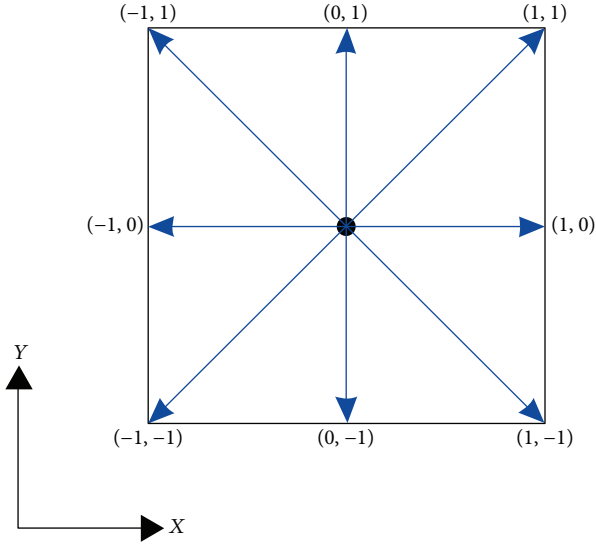


FIGURE 1: The two-dimensional 9-velocity lattice (D2Q9).

where C_i is the concentration of the considered ions, and u_α is obtained from the basis model. The relevant population moment that corresponds to the concentration is

$$\sum_{i=0}^8 \xi_i = C_i. \quad (4)$$

2.2. Computer-Generated Stochastic Porous Media. Characteristic material microstructures can be resolved and digitalized, using a variety of experimental techniques that span from X-ray tomographic techniques to the combination of FIB-SEM microscopy. At the same time, there is a lot of effort in the algorithmic stochastic reconstruction of porous geometries (clays, membranes, etc.) that respect certain structural and statistical properties. In Figure 2, two such examples are shown. Figure 2(a) is obtained using the methodology of Tyagi et al. [32]. This pore map is constructed such that it matches the targeted rock's mineralogical components and its macroscopic properties such as porosity, grain, and pore size distributions. This methodology allows generating anisotropic structures, which are composed of different grain types. The map in Figure 2(a) represents a clay material, where grains and interlayers within the grains are present.

The pore map in Figure 2(b) was created by following the methodology of [23, 24]. A Voronoi tessellation of randomly distributed points on a plane is used as a template. Subsequently, the edges of the tessellation are used as guides to open the pore space, resulting in fully connected porosity. Here, we increase the degree of heterogeneity by varying the channel size and by distributing variable size spherical pores at the junctions of the pore channels. We construct our pore maps based on the latter methodology due to its simplicity and in order to work with a generic porous medium.

2.3. Description of the Reactive System and Boundary Conditions. The evolution of a porous geometry, due to

mineral reactions, depends strongly on the aqueous mixture species concentrations and the flow regime. The quantification of these conditions is aided from dimensional analysis. The nondimensional numbers that are used to characterize geochemical reactive flows at low Reynolds number (Darcy regime) are the Péclet number: $Pe = UL/D_0$ and the Damköhler number: $Da = kL/D_0C_0$, where D_0 is the mass diffusivity, U is the convective flow velocity, C_0 in this work is the acid concentration at inlet, and L is the characteristic linear dimension of the system of interest. Whenever mentioned in this text, the Pe and Da values correspond to the initial conditions of the flow setup.

The solid domain of the generated microstructures represents pure calcite. In the connected void space, a water solution is allowed to advect, diffuse, and react at the solid interface.

The reactant enters the domain from the left boundary with a uniform flow rate. The top and bottom boundary conditions are treated as periodic, while the right boundary as a zero gradient boundary.

For simplification, we here consider a single-step heterogeneous reaction of the dissolution of calcite applicable for low pH conditions: $H^+ + CaCO_3 \rightarrow Ca^{2+} + HCO_3^-$.

The reaction constant is $k_1 = 8.9 \times 10^{-1} \text{ mol/m}^2 \text{ s}$ [33, 34], and the reaction rate is a first-order reaction $R = k_1 \alpha_{H^+}$, where α_{H^+} is the activity of H^+ in the solution. The diffusion coefficient is $D_0 = 10^{-9} \text{ m}^2/\text{s}$, and the kinematic viscosity of the fluid $\nu = 10^{-6} \text{ m}^2/\text{s}$.

3. Results and Discussion

3.1. Permeability of Computer-Generated Structures. Several pore map realizations have been generated using the same set of rules (distribution of channel width and distribution of spherical pore sizes), differing only in the number of original random seed points. The two-dimensional domain size was selected to be square and is discretized by a 1500×1500 computational grid, whose total size corresponds to a $100 \mu\text{m} \times 100 \mu\text{m}$ domain. This allows constructing random pore maps with variable target porosities that range from $\varepsilon = 0.1$ to 0.9 . The permeability ($K \text{ (m}^2\text{)}$) of the generated structures was numerically measured by flow simulations similar to [31]. The results are plotted in the log-linear plot of Figure 3. The permeability correlates positively with the porosity. In the framework of macroscopic reactive transport codes, the microstructural information is implicitly considered using permeability-porosity correlations. In reactive environments, for example, when dissolution or precipitation processes take place, the porosity increases or decreases at a pace dictated by the flow and the chemical kinetics. In the case where the generated geometries are representing a real material, a first approximation, due to the lack of mechanistic understanding, would be to update the porosity according to the thermodynamics or kinetics. Subsequently, the permeability of the respective voxel would be updated following the permeability-porosity trend of the pristine structures (black circles in Figure 3). As it will be shown in the next section, such an approximation would

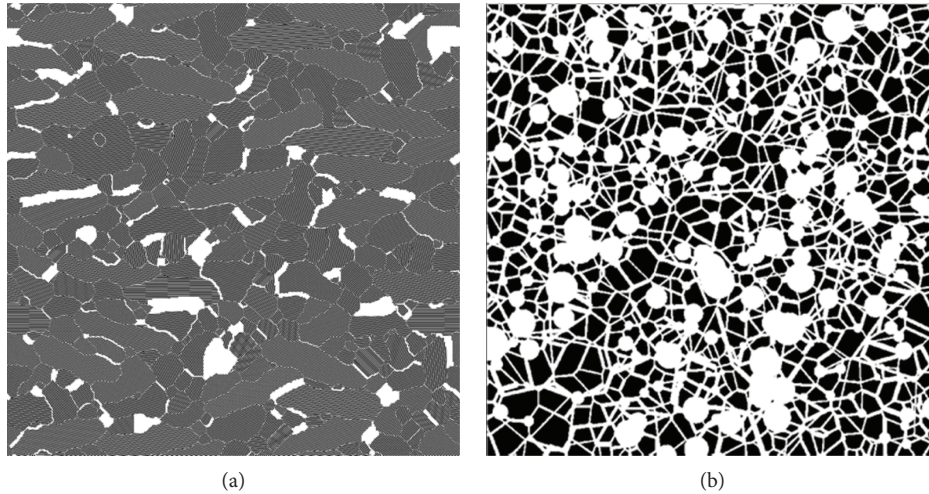


FIGURE 2: Digitally reconstructed pore maps. (a) Clay-type structure using lattice Monte Carlo methodology. (b) Generic porous medium based on Voronoi tessellation.

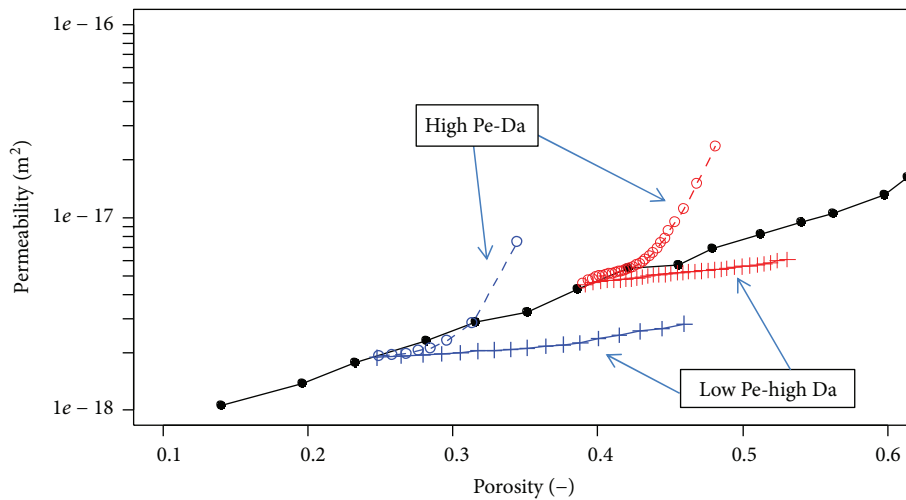


FIGURE 3: Permeability-porosity trends for several scenarios. Black-filled circles connected with a black line correspond to the permeability versus the porosity of the computer-generated unreacted samples. Blue ($\varepsilon = 0.25$) and red ($\varepsilon = 0.39$) curves correspond to the distinct permeability-porosity temporal evolution paths under different reactive transport conditions (circles: high Pe-high Da, crosses: moderate Pe-high Da).

not be accurate for reactive transport calculations in the presence of strong chemical gradients.

3.2. Evolution of Permeability in Reactive Environments. The use of the lattice Boltzmann framework to study the evolution of pore structures in reactive environments provides process understanding of the underlying mechanisms ([10, 12, and references within, 9, 19, 35]). The effect of different transport and chemical conditions has been studied by several authors [10, 36]. Depending on the chemical conditions and the flow properties, the evolving geometries due to dissolution follow distinct paths. The change in pore topology and connectivity will have an effect on permeability. Different regimes have been identified and have been categorized in phase diagrams based on the characteristic

nondimensional numbers that describe the reactive environment. For high Pe and Da numbers, the cross sections of the preferential flow paths increase fast, due to the strong supply of reactants (Pe) and the fast reaction rates (Da). Soon, the so-called wormholes start to appear resulting in the fast increase of the permeability versus the porosity of the reacting structure. At the other end, permeability increases at the slowest pace, when Pe is moderate and Da is high. The reason for that is the fast depletion of reactants at the incoming boundaries leading to face dissolution [12]. This categorization is verified also here.

We selected two different geometries stemming from the analysis of the previous section, with initial pristine porosity of $\varepsilon = 0.25$ (see Figure 4, top row) and $\varepsilon = 0.39$ (see Figure 4, bottom row). The evolution of each of the two pore

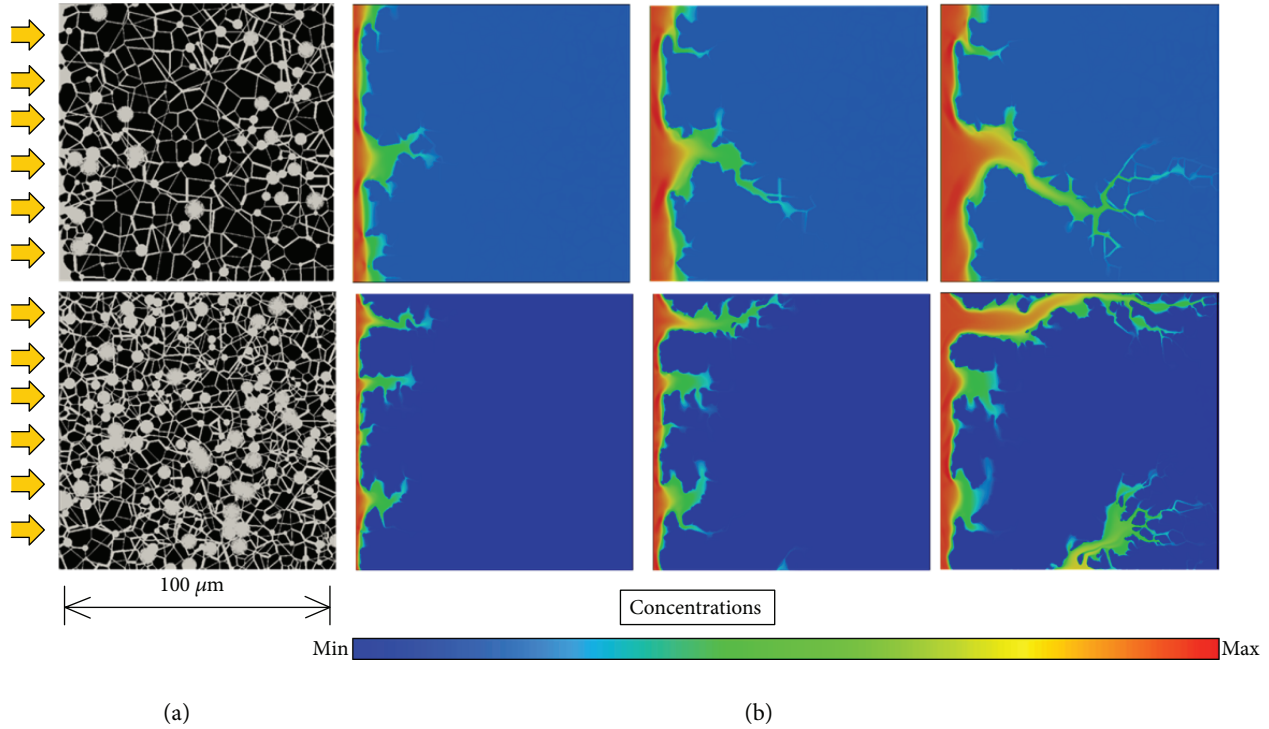


FIGURE 4: (a) Initial pristine pore structures with porosity 0.25 (top) and 0.39 (bottom), black is solid, gray is void. From (a) to (b), temporal evolution for the high $Pe = 400$ -high $Da = 87 \times 10^5$ boundary condition leading to the creation of wormholes. Contour gradient of the reactant concentration is plotted.

realizations was examined under two different flow conditions. In the first case, HCl acid 0.001 M ($pH=3$) was injected from the left boundary resulting in $Pe = 4$ and $Da = 87 \times 10^6$. This case evolved as face dissolution. In the second case, HCL acid 0.01 M ($pH=2$) was injected at higher rates resulting in higher $Pe = 400$ and $Da = 87 \times 10^5$. These conditions lead to the formation of wormholes. The evolution of the latter cases is shown in Figure 4. After specific time intervals, the evolved structures were extracted, and their permeability was measured in a similar manner as done in the previous section. The resulting permeabilities that represent the evolved pore structures are plotted in Figure 3. Blue lines and symbols represent the evolution of the $\epsilon = 0.25$ structure, and red lines and symbols represent the evolution of the $\epsilon = 0.39$ one.

3.3. Extracting Correlations from Pore-Level Simulations and Upscaling Strategies. The pore-level simulations provide the basic understanding of the underlying mechanisms, which dictate the structural evolution of porous media in reactive conditions. At the same time, it is possible to provide the necessary input to the macroscopic algorithms via upscaling of the results. This can be simply done by replacing, for example, the permeability-porosity correlations that are modelled in a macroscopic code, with more precise and case-specific correlations. To that end, there are mainly three different approaches. First, the result can be transmitted in the form of power law or Kozeny-Carman type of function as $K = f(\epsilon)$. Second, tabulated values can be provided instead

of a power law, such that during the macroscopic simulations, specific values can be calculated, after interpolating between successive points. Third, the macroscopic code could call on demand the pore-level solver, to deliver the prediction of evolution in a fully coupled multiscale manner.

The permeability porosity correlations that describe the evolution of the structures in the presence of velocity and chemical gradients have been extracted after fitting known type of relationships. As a first remark, it should be mentioned that it was not possible to fit the results using as a model of Kozeny-Carman-type function. This was especially true for the case of high Pe - Da (wormholes). The most appropriate and simple type of model was found to be the $K = a \times \epsilon^b$, where a and b are the fitting parameters. The results are shown in Figure 5 for the pore map $\epsilon = 0.39$ (see Videos S1 and S2 in the Supplementary Materials, which depicts the temporal evolution of the porous medium and the respective mass transport).

The scaling with respect to the porosity was found to be of the order $b = 0.9$ for the moderate Pe case. The high Pe - Da results could not be fitted using only one function of that type due to the existence of two distinct evolution regimes. Evolution starts with a relatively weak scaling, where $b = 2.4$ (for $0.39 < \epsilon < 0.45$) and corresponds to the wormhole formation, and continues with a strong scaling regime where $b = 13.7$ (for $0.45 < \epsilon < 0.5$) and corresponds to the point where the flow is accelerated due to the growing of the major wormholes. For the upscaling of these results, specific care has to be taken that the simulation

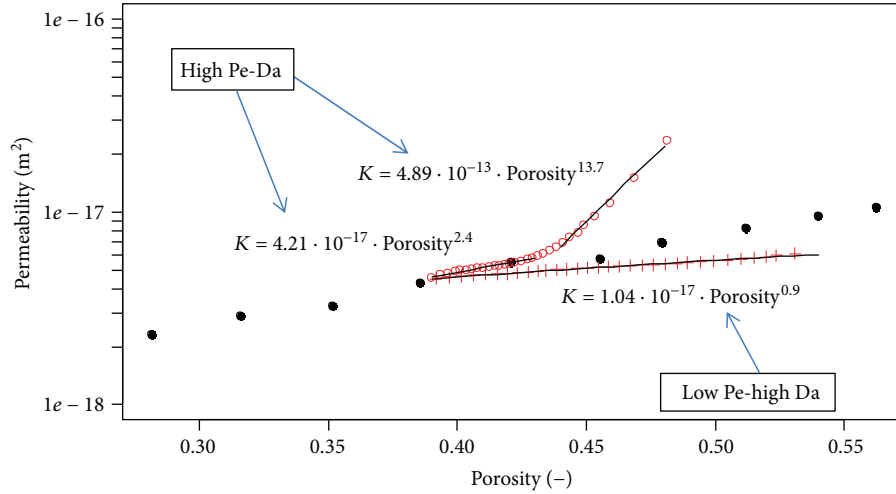


FIGURE 5: Fitted permeability porosity correlations, describing the evolution of permeability of the pore structure $\varepsilon = 0.39$, for two different reactive and flow conditions. Open red circles correspond to the evolution under high Pe-high Da conditions and have been fitted using two correlation functions (black lines). Red solid line and crosses depict the low Pe-high Da case. Black circles represent the permeability of the pristine structures.

domains are indeed representative element volumes (REV). This is especially important in the case where wormholes are formed. Running several simulations in larger and smaller geometries can clarify the interaction between different wormholes.

At the moment, it seems that such a fitting cannot be fully automated in the classical sense. The existence of (a) very small numbers among the fitted parameters and (b) different scaling regimes, will always be a source of error when transferring such functionals to macroscopic codes. Nevertheless, if done with care, this kind of microscopic feedback has the potential to substantially improve the modelling perspectives, provided that digitalized characteristic microstructures are available. By passing, we note that the two geometries ($\varepsilon = 0.25$ and $\varepsilon = 0.39$) seem to evolve in a similar way under similar conditions (see Figure 3). The comparison between the blue and the red set of curves in Figure 3 goes beyond the scope of this paper. For the extraction of safe conclusions, it would be needed to test several geometries in reactive environments, and proceed with statistical analysis of the results.

The second approach would be to tabulate the a priori executed pore-level simulation results and provide these tables as input to a macroscopic code. Exact values for specific cases can be determined via interpolation schemes. This would not require a fitting process and shall be efficient as soon as a minimum number of information (size and accuracy of tables) has to be passed to the next level of description. We note that for complex chemically reactive systems, this option would require the precalculation of a large number of different scenarios. The subsequent storage of the resulting information with very high accuracy could become impractical.

The third option would be to fully couple the pore-level codes with macroscopic codes in a multiscale manner. Executing several pore-level simulations for every voxel, in order to extract the microscopic physics, would defeat the purpose

of pore-level simulations. At the same time, it would result in an extremely slow simulation. Nevertheless, novel much promising machine learning techniques started recently to appear as, for example, in [37]. In that paper, the authors demonstrate a technique to accelerate the solution of chemical equilibrium equations, by using previous equilibrium calculations of similar input conditions. Such algorithms, when applied to the problem described in this paper, can identify voxels with similar input and save the most representative cases, for use in future calculations. This would accelerate a fully coupled multiscale code.

4. Conclusions

The evolution of permeability with respect to porosity in reactive environments is of great importance in geochemical reactive transport modelling and subsequent predictions. Within the porous structure, the mineral dissolution and precipitation processes alter the pore topology in a strongly nonlinear way. In this paper, we have constructed calcite microstructures in a stochastic way and have traced their temporal evolution in the presence of an acid. Permeability-porosity correlations have been extracted for each of the different evolution paths. Using this paradigm, we discussed possible upscale strategies and the numerical bridging between pore level understanding and macroscopic modelling. We conclude that such approaches are viable under the condition of fully automating the communication between the solvers.

Data Availability

Data can be requested from the authors, and all information necessary to reproduce results are mentioned within the article.

Conflicts of Interest

The authors declare that there is no conflict of interest regarding the publication of this paper.

Acknowledgments

Useful discussions with T. Gimmi, G. Kosakowski, D. Kulik, and W. Pfingsten on upscaling procedures are kindly acknowledged. This work was partially supported from the Swiss National Cooperative for the Disposal of Radioactive Waste (Nagra) and the Swiss National Science Foundation (SNSF) Project no. 200021_172618. Simulations were run at Swiss National Supercomputing Center, CSCS under the projects “psi12” and “psi13”.

Supplementary Materials

Video S1: temporal evolution of the pore map $\varepsilon = 0.39$ in the case of moderate Pe-high Da flow (face dissolution).
Video S2: temporal evolution of the pore map $\varepsilon = 0.39$ in the case of high Pe-high Da flow (wormhole formation).
(*Supplementary Materials*)

References

- [1] M. Xie, K. U. Mayer, F. Claret et al., “Implementation and evaluation of permeability-porosity and tortuosity-porosity relationships linked to mineral dissolution-precipitation,” *Computational Geosciences*, vol. 19, no. 3, pp. 655–671, 2015.
- [2] M. Hayek, G. Kosakowski, and S. Churakov, “Exact analytical solutions for a diffusion problem coupled with a precipitation-dissolution reaction and feedback of porosity change,” *Water Resources Research*, vol. 47, no. 7, 2011.
- [3] M. Hayek, G. Kosakowski, A. Jakob, and S. V. Churakov, “A class of analytical solutions for multidimensional multispecies diffusive transport coupled with precipitation-dissolution reactions and porosity changes,” *Water Resources Research*, vol. 48, no. 3, 2012.
- [4] V. Lagneau and J. van Der Lee, “Operator-splitting-based reactive transport models in strong feedback of porosity change: the contribution of analytical solutions for accuracy validation and estimator improvement,” *Journal of Contaminant Hydrology*, vol. 112, no. 1–4, pp. 118–129, 2010.
- [5] N. C. M. Marty, C. Tournassat, A. Burnol, E. Giffaut, and E. C. Gaucher, “Influence of reaction kinetics and mesh refinement on the numerical modelling of concrete/clay interactions,” *Journal of Hydrology*, vol. 364, no. 1–2, pp. 58–72, 2009.
- [6] D. A. Barajas-Solano and A. M. Tartakovsky, “Hybrid multiscale finite volume method for advection-diffusion equations subject to heterogeneous reactive boundary conditions,” *Multiscale Modeling & Simulation*, vol. 14, no. 4, pp. 1341–1376, 2016.
- [7] I. Battiato, D. M. Tartakovsky, A. M. Tartakovsky, and T. D. Scheibe, “Hybrid models of reactive transport in porous and fractured media,” *Advances in Water Resources*, vol. 34, no. 9, pp. 1140–1150, 2011.
- [8] M. Yousefzadeh and I. Battiato, “Physics-based hybrid method for multiscale transport in porous media,” *Journal of Computational Physics*, vol. 344, pp. 320–338, 2017.
- [9] C. Huber, B. Shafei, and A. Parmigiani, “A new pore-scale model for linear and non-linear heterogeneous dissolution and precipitation,” *Geochimica et Cosmochimica Acta*, vol. 124, pp. 109–130, 2014.
- [10] Q. Kang, L. Chen, A. J. Valocchi, and H. S. Viswanathan, “Pore-scale study of dissolution-induced changes in permeability and porosity of porous media,” *Journal of Hydrology*, vol. 517, pp. 1049–1055, 2014.
- [11] Q. Kang, P. C. Lichtner, and D. Zhang, “Lattice Boltzmann pore-scale model for multicomponent reactive transport in porous media,” *Journal of Geophysical Research: Solid Earth*, vol. 111, no. B5, 2006.
- [12] Q. Kang, D. Zhang, S. Chen, and X. He, “Lattice Boltzmann simulation of chemical dissolution in porous media,” *Physical Review E*, vol. 65, no. 3, 2002.
- [13] A. Parmigiani, C. Huber, O. Bachmann, and B. Chopard, “Pore-scale mass and reactant transport in multiphase porous media flows,” *Journal of Fluid Mechanics*, vol. 686, pp. 40–76, 2011.
- [14] R. Chatelin and P. Poncet, “A hybrid grid-particle method for moving bodies in 3D stokes flow with variable viscosity,” *SIAM Journal on Scientific Computing*, vol. 35, no. 4, pp. B925–B949, 2013.
- [15] A. M. Tartakovsky, P. Meakin, T. D. Scheibe, and B. D. Wood, “A smoothed particle hydrodynamics model for reactive transport and mineral precipitation in porous and fractured porous media,” *Water Resources Research*, vol. 43, no. 5, 2007.
- [16] S. Molins, D. Trebotich, C. I. Steefel, and C. Shen, “An investigation of the effect of pore scale flow on average geochemical reaction rates using direct numerical simulation,” *Water Resources Research*, vol. 48, no. 3, 2012.
- [17] C. Soulaire and H. A. Tchelepi, “Micro-continuum approach for pore-scale simulation of subsurface processes,” *Transport in Porous Media*, vol. 113, no. 3, pp. 431–456, 2016.
- [18] D. Trebotich, M. F. Adams, S. Molins, C. I. Steefel, and C. Shen, “High-resolution simulation of pore-scale reactive transport processes associated with carbon sequestration,” *Computing in Science & Engineering*, vol. 16, no. 6, pp. 22–31, 2014.
- [19] N. I. Prasianakis, E. Curti, G. Kosakowski, J. Poonoosamy, and S. V. Churakov, “Deciphering pore-level precipitation mechanisms,” *Scientific Reports*, vol. 7, no. 1, article 13765, 2017.
- [20] M. Januszewski and M. Kostur, “Sailfish: a flexible multi-GPU implementation of the lattice Boltzmann method,” *Computer Physics Communications*, vol. 185, no. 9, pp. 2350–2368, 2014.
- [21] M. A. Safi, N. I. Prasianakis, J. Mantzaras, A. Lamibrac, and F. N. Büchi, “Experimental and pore-level numerical investigation of water evaporation in gas diffusion layers of polymer electrolyte fuel cells,” *International Journal of Heat and Mass Transfer*, vol. 115, pp. 238–249, 2017.
- [22] C. Bringedal, I. Berre, I. S. Pop, and F. A. Radu, “Upscaling of non-isothermal reactive porous media flow with changing porosity,” *Transport in Porous Media*, vol. 114, no. 2, pp. 371–393, 2016.
- [23] M. S. Newman and X. Yin, “Lattice Boltzmann simulation of non-Darcy flow in stochastically generated 2D porous media geometries,” *SPE Journal*, vol. 18, no. 1, pp. 12–26, 2013.
- [24] F. Xiao and X. Yin, “Geometry models of porous media based on Voronoi tessellations and their porosity-permeability relations,” *Computers & Mathematics with Applications*, vol. 72, no. 2, pp. 328–348, 2016.

- [25] U. Frisch, D. d'Humieres, B. Hasslacher, P. Lallemand, Y. Pomeau, and J. P. Rivet, "Lattice gas hydrodynamics in two and three dimensions," LA-UR-87-2524; CONF-8610281-2, Los Alamos National Lab.; Observatoire de Nice; Ecole Normale Supérieure, Los Alamos, NM, USA; Paris, France, 1986.
- [26] S. Succi, *The Lattice Boltzmann Equation: For Fluid Dynamics and beyond*, Oxford University Press, 2001.
- [27] S. Succi, E. Foti, and F. Higuera, "Three-dimensional flows in complex geometries with the lattice Boltzmann method," *Europhysics Letters (EPL)*, vol. 10, no. 5, pp. 433–438, 1989.
- [28] F. J. Higuera, S. Succi, and R. Benzi, "Lattice gas dynamics with enhanced collisions," *Europhysics Letters (EPL)*, vol. 9, no. 4, pp. 345–349, 1989.
- [29] Y. H. Qian, D. d'Humières, and P. Lallemand, "Lattice BGK models for Navier-Stokes equation," *Europhysics Letters (EPL)*, vol. 17, no. 6, pp. 479–484, 1992.
- [30] N. I. Prasianakis, I. V. Karlin, J. Mantzaras, and K. B. Boulouchos, "Lattice Boltzmann method with restored Galilean invariance," *Physical Review E*, vol. 79, no. 6, 2009.
- [31] N. I. Prasianakis, T. Rosén, J. Kang, J. Eller, J. Mantzaras, and F. N. Büichi, "Simulation of 3D porous media flows with application to polymer electrolyte fuel cells," *Communications in Computational Physics*, vol. 13, no. 3, pp. 851–866, 2013.
- [32] M. Tyagi, T. Gimmi, and S. V. Churakov, "Multi-scale microstructure generation strategy for up-scaling transport in clays," *Advances in Water Resources*, vol. 59, pp. 181–195, 2013.
- [33] L. Chou, R. M. Garrels, and R. Wollast, "Comparative study of the kinetics and mechanisms of dissolution of carbonate minerals," *Chemical Geology*, vol. 78, no. 3-4, pp. 269–282, 1989.
- [34] L. N. Plummer, T. M. L. Wigley, and D. L. Parkhurst, "The kinetics of calcite dissolution in CO₂-water systems at 5 degrees to 60 degrees C and 0.0 to 1.0 atm CO₂," *American Journal of Science*, vol. 278, no. 2, pp. 179–216, 1978.
- [35] A. Parmigiani, S. Faroughi, C. Huber, O. Bachmann, and Y. Su, "Bubble accumulation and its role in the evolution of magma reservoirs in the upper crust," *Nature*, vol. 532, no. 7600, pp. 492–495, 2016.
- [36] I. Battiato and D. M. Tartakovsky, "Applicability regimes for macroscopic models of reactive transport in porous media," *Journal of Contaminant Hydrology*, vol. 120-121, pp. 18–26, 2011.
- [37] A. M. M. Leal, D. A. Kulik, and M. O. Saar, "Ultra-fast reactive transport simulations when chemical reactions meet machine learning: chemical equilibrium," 2017, <https://arxiv.org/abs/1708.04825>.

Research Article

Fluid Interfaces during Viscous-Dominated Primary Drainage in 2D Micromodels Using Pore-Scale SPH Simulations

Rakulan Sivanesapillai and Holger Steeb 

Institute of Applied Mechanics, University of Stuttgart, Pfaffenwaldring 7, 70 569 Stuttgart, Germany

Correspondence should be addressed to Holger Steeb; holger.steeb@mechbau.uni-stuttgart.de

Received 27 December 2017; Accepted 8 April 2018; Published 14 June 2018

Academic Editor: Emanuele Romano

Copyright © 2018 Rakulan Sivanesapillai and Holger Steeb. This is an open access article distributed under the Creative Commons Attribution License, which permits unrestricted use, distribution, and reproduction in any medium, provided the original work is properly cited.

We perform pore-scale resolved direct numerical simulations of immiscible two-phase flow in porous media to study the evolution of fluid interfaces. Using a Smoothed-Particle Hydrodynamics approach, we simulate saturation-controlled primary drainage in heterogeneous, partially wetttable 2D porous microstructures. While imaging the evolution of fluid interfaces near capillary equilibrium becomes more feasible as fast X-ray tomography techniques mature, imaging methods with suitable temporal resolution for viscous-dominated flow have only recently emerged. In this work, we study viscous fingering and stable displacement processes. During viscous fingering, pore-scale flow fields are reminiscent of Bretherton annular flow, that is, the less viscous phase percolates through the core of a pore-throat forming a hydrodynamic wetting film. Even in simple microstructures wetting films have major impact on the evolution of fluid interfacial area and are observed to give rise to nonnegligible interfacial viscous coupling. Although macroscopically appearing flat, saturation fronts during stable displacement extend over the length of the capillary dispersion zone. While far from the dispersion zone fluid permeation obeys Darcy's law, the interplay of viscous and capillary forces is found to render fluid flow within complex. Here we show that the characteristic length scale of the capillary dispersion zone increases with the heterogeneity of the microstructure.

1. Introduction

Assessing the stability and evolution of saturation fronts, or, from a pore-scale point of view, interfaces between immiscible bulk fluid phases, is key with respect to understanding a multitude of subsurface processes. Examples include sequestration of carbon dioxide in geological media, groundwater contamination remediation, or enhanced oil recovery. Depending on the governing capillary number (Ca), viscosity ratio (M), properties of the porous microstructure, and boundary conditions, primary drainage results in flow regimes as diverse as viscous fingering, stable displacement, or capillary finger branching [1]. In traditional macroscopic continuum models, a phenomenological extension of Darcy's law is assumed to be applicable with relative permeability and capillary pressure functions representing constitutive model inputs [2]. Calibration of these constitutive relations in light of a particular flow regime typically renders them nonlinear

and hysteretic [3–5]. In an attempt to face the latter, contemporary models acknowledge the role of interfacial areas in hysteresis [6–10] or explicitly account for mass-exchange between hydraulically reservoir-connected and reservoir-disconnected subphases [11, 12].

Considerable effort has been devoted to studying two-phase flow patterns at the length scale of pore-networks, both experimentally [13–18] and numerically [19–25], providing a reliable set of data for the Ca - M phase diagram of drainage displacement patterns as introduced by [1]. However, the pore-scale dynamics of fluid interfaces and the mechanisms by means of which they evolve remain poorly understood.

To this end, recent advances in pore-scale imaging-based characterization methods (see review [26]) that enable the fast visualization of two-phase flow at pore-scale resolution, most notably microscopy imaging of thin micromodels [18, 27–29], X-ray computed tomography [30–34], and confocal microscopy [35, 36], have provided valuable insights into

the interplay of viscous, capillary, gravitational, and inertial forces constituting the complexity of interface dynamics at the pore-scale. For instance, free-energy driven Haines jumps have been confirmed as dominant displacement mechanism for flow at small capillary numbers [29, 32]. Clearly, these observations deviate from the assumptions underlying generalized Darcy flow. Besides experimental approaches, we consider direct numerical simulations (DNS) to be an important complementary tool for quantitative characterization of multiphase flow in porous media [26, 37].

Our method of choice is a quasi-incompressible Smoothed-Particle Hydrodynamics (SPH) model [38–41] which incorporates the Navier-Stokes equations together with the Continuum Surface Stress method [42, 43] to account for the interfacial balance equations. Advantages of SPH in the context of two-phase flow in porous media include its mesh-free nature. The reproducing kernel interpolation of SPH does not require nodal integration points (particles) to be distributed on grids or meshes. The latter renders spatial discretization of complex pore spaces less computationally expensive as compared to traditional grid or mesh-based methods. Typical SPH methods use an updated Lagrangian approach; that is, particles are advected in space according to their local advection velocity. Hence, nonlinear convection terms are not required to be modeled. The latter further implies that phase indicator fields are advected through particle motion. As a result, implementation of the Continuum Surface Stress method does not require interface-tracking such that SPH constitutes an attractive approach to model formation, coalescence, and fragmentation of fluid interfaces in complex pore spaces. Moreover, the updated Lagrangian formulation simplifies modeling of locally large Reynolds numbers [44, 45]. Disadvantages of SPH include its high computational costs associated with repetitive use of neighbor searching algorithms. In the context of using explicit time integration schemes, time stepping stability criteria such as the CFL-condition may be rather restrictive. Moreover, since uncorrected SPH interpolation stencils lack the Kronecker delta property, the application of essential boundary conditions remains nontrivial [46, 47].

In this work, we present pore-scale resolved DNS of two-phase flow in 2D partially wettable porous media of particulate microstructure. We perform numerical experiments of saturation-controlled primary drainage for various magnitudes of Ca and M . While much effort has been devoted to studying the pore-scale distribution of fluid interfaces near capillary equilibrium, pore-scale numerical studies for viscous-dominated flow remain comparatively sparse. Rather than studying the emerging macroscopic displacement patterns we discuss pore-scale flow fields. For viscous fingering we discuss the formation of hydrodynamic wetting films and their impact on the evolution of specific interfacial area and interfacial viscous coupling effects. For stable displacement we discuss the microscopic dispersion of stable saturation fronts (capillary dispersion zone) and the role of microstructure heterogeneity. In an attempt to elucidate the trade-off between modeling assumptions, topological constraints of

2D simulations, and physical meaningfulness, we critically discuss our numerical approach.

2. Methods

2.1. Direct Numerical Simulation Approach. We model isothermal flow of a Newtonian, quasi-incompressible wetting (Ω_w) and nonwetting (Ω_n) fluid phase through the pore-space (Ω_f) of a rigid solid matrix (Ω_s). Bulk fluid balance equations for mass density and linear momentum in phase domains $\Omega_\alpha \in \{\Omega_n, \Omega_w\}$ read

$$\dot{\rho}^\alpha = -\rho^\alpha \text{div } \mathbf{u}_\alpha, \quad (1)$$

$$\rho^\alpha \dot{\mathbf{u}}_\alpha = \text{div } \mathbf{T}_E^\alpha - \text{grad } p^\alpha, \quad (2)$$

respectively. The Newtonian viscous extra stress tensor reads $\mathbf{T}_E^\alpha = \mu^\alpha (\text{grad } \mathbf{u}_\alpha + \text{grad}^T \mathbf{u}_\alpha)$ and \mathbf{u}_α denotes local velocity. Dynamic viscosity μ^α is considered constant. A superimposed dot denotes the material time derivative. Fluid pressure p^α is related to bulk mass density ρ^α by a stiff barotropic equation of state $p^\alpha = f(\rho^\alpha) + p_0$ such that density fluctuations are small implying quasi-incompressibility. A constant, positive backpressure p_0 is included to avoid negative pressures that otherwise lead to a numerical tensile instability which SPH methods are prone to [48].

Immiscibility and solid wettability are accounted for using interfacial balance equations for all Gibbs material interfaces $\Gamma_{\alpha\beta} \in \{\Gamma_{wn}, \Gamma_{ns}, \Gamma_{ws}\}$. Interfacial balance equations are expressed in terms of jump conditions using the Rankine-Hugoniot jump operator $[[\cdot]]_{\alpha\beta}$. The interfacial mass balances

$$[[\rho(\mathbf{u} - \mathbf{u}^{\alpha\beta}) \cdot \mathbf{n}^{\alpha\beta}]]_{\alpha\beta} = 0, \quad (3)$$

where $\mathbf{u}^{\alpha\beta}$ denotes interfacial velocity, imply kinematic coupling along the interfacial normal vector $\mathbf{n}^{\alpha\beta}$. Interfacial balances of linear momentum read

$$[[[(\mathbf{T}_E - p\mathbf{I}) \cdot \mathbf{n}^{\alpha\beta}]]_{\alpha\beta} = -\text{div}^{\alpha\beta} \mathbf{\Pi}^{\alpha\beta}, \quad (4)$$

where $\text{div}^{\alpha\beta}$ denotes the surface divergence operator and the interfacial Cauchy stress tensor $\mathbf{\Pi}^{\alpha\beta} = \sigma^{\alpha\beta}(\mathbf{I} - \mathbf{n}^{\alpha\beta} \otimes \mathbf{n}^{\alpha\beta})$. Interfacial tensions $\sigma^{\alpha\beta}$ are considered constant which is considered reasonable in the absence of surface-active agents. Solid wettability properties are prescribed by setting parameters σ^{wn} , σ^{ns} , and σ^{ws} appropriately.

An alternative expression of the interfacial balance of linear momentum (4) for the fluid-fluid interface Γ_{wn} reads

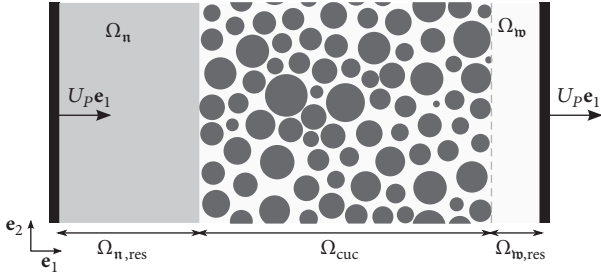
$$(\mathbf{T}_E^n - \mathbf{T}_E^w) \cdot \mathbf{n}^{\alpha\beta} + (p^w - p^n + \sigma^{wn} \kappa^{wn}) \mathbf{n}^{wn} = \mathbf{0}, \quad (5)$$

where $\kappa^{\alpha\beta} = -\text{div}^{\alpha\beta} \mathbf{n}^{\alpha\beta}$ is twice the mean curvature. The first term in (5) implies interfacial viscous coupling whereas the second term introduces a pressure jump condition according to the Young-Laplace equation [49].

Our DNS approach [41, 45, 50] is based on the Continuum Surface Stress method [42, 43] whereby bulk balance equations are formulated for the whole-fluid domain

TABLE 1: Overview of microstructure parameters. Intrinsic permeabilities k were calculated using single-phase flow simulations.

Microstructure	A	B	C
<i>Pore-throat size distribution</i>			
Mean value m_T [mm]	0.42	0.41	0.41
Standard deviation v_T [mm]	0.14	0.15	0.21
<i>Grain diameter distribution</i>			
Mean value m_G [mm]	1.63	1.61	1.60
Standard deviation v_G [mm]	0.20	0.34	0.44
<i>Miscellaneous</i>			
Porosity ϕ_{cuc} [%]	45.5	46.0	44.3
Intrinsic permeability k_{cuc} [10^{-9} m ²]	4.41	4.55	4.55
Dimensions [mm ²]		20 × 15	
Grain count	88	85	86

FIGURE 1: Schematic diagram of simulation setup at initial time $t = 0$. Black bars represent displacing pistons.

$\Omega_f = \Omega_n \cup \Omega_{nb}$. The latter is achieved by immersing jump conditions (4) using interface Dirac delta distributions $\delta^{\alpha\beta}$ which are compactly supported on points of $\Gamma_{\alpha\beta}$ only. The resulting whole-fluid balance of linear momentum is expressed as

$$\rho_f \dot{\mathbf{u}}_f = \text{div} \mathbf{T}_E^f - \text{grad} p^f + \sum_{\alpha\beta} \text{div} (\Pi^{\alpha\beta} \delta^{\alpha\beta}) \cdot \mathbf{I}^{fs}, \quad (6)$$

where the solid surface identity tensor $\mathbf{I}^{fs} := \mathbf{I} - \mathbf{n}^{fs} \otimes \mathbf{n}^{fs}$ is introduced to remove the otherwise unbalanced contact line stress $\sigma^{\text{wn}} \sin \Theta$ normal to the solid surface [45, 50], that is, to reduce contact line forces to planes tangent to the solid surface. Discretization of (6) using SPH leads to the intuitive motion equation

$$m_i \dot{\mathbf{u}}_i = \sum_j \mathbf{F}_{ij}^V - \sum_j \mathbf{F}_{ij}^P + \sum_{\alpha\beta} \mathbf{F}_i^{\alpha\beta} \quad (7)$$

for a fluid particle $\mathcal{P}_i \in \Omega_f$ with lumped mass m_i . Upon discretization, internal bulk forces due to viscous diffusion and pressure gradient result in discrete interaction forces (\mathbf{F}_{ij}^V and \mathbf{F}_{ij}^P) that act between \mathcal{P}_i and its neighboring particles \mathcal{P}_j .

2.2. Simulation Setup and Microstructures. The total computation domain (Figure 1) is comprised of wetting phase (WP) and nonwetting phase (NWP) reservoirs denoted by $\Omega_{n,\text{res}}$

and $\Omega_{n,\text{res}}$, respectively, as well as the porous computational unit cell Ω_{cuc} . The unit cell has side lengths $L_W = 20$ mm and $L_H = 15$ mm in direction of the unit vectors \mathbf{e}_1 and \mathbf{e}_2 , respectively. The microstructure exhibits L_H -periodicity in direction of \mathbf{e}_2 such that periodic boundary conditions are applied with respect to \mathbf{e}_2 . The latter avoids boundary artifacts that otherwise arise due to wall confinement. Initially, the sample is completely saturated by the WP. Saturation levels inside the porous sample are controlled by imposing the velocity $\mathbf{U}_P = U_P \mathbf{e}_1$ of pistons that displace the reservoir fluids relative to Ω_{cuc} . As a result of choosing U_P constant, saturation rates remain constant during drainage. Simulations are halted as soon as the NWP penetrates into the WP reservoir, that is, at breakthrough.

Three different microstructures (Appendix) comprised of disordered, nonoverlapping circles (hereinafter referred to as grains) have been generated using an event-driven particle dynamics algorithm [51, 52]. Pore-throat sizes and grain diameters are normally distributed. Mean values and standard deviations are denoted by m_T and v_T for pore-throat size distribution and m_G and v_G for grain diameter distribution, respectively. Microstructures are constructed such that they only differ by the degree of heterogeneity as measured by v_T and v_G , while mean values m_T and m_G , intrinsic permeabilities, and porosities are in close agreement (Table 1). Mean pore-throat size m_T serves as characteristic length scale for the reference capillary pressure $P_C^{\text{ref}} := 2 \cos \Theta \sigma^{\text{wn}} m_T^{-1}$. Given its small size, the computational unit cell Ω_{cuc} does not constitute a representative unit cell. However, clipping the sample width L_W by 50% was observed to yield changes in v_T and v_G of less than 10%. In other words, we consider the domain size large enough to study pore-scale effects related to the length scale of microstructure heterogeneity. Nonetheless, a suitable representative size of the computation domain needs to be studied using an in-depth converge analysis.

Varying the piston velocity U_P , which also represents the prescribed specific discharge, we control the capillary number

$$\text{Ca} := \frac{\mu^n U_P}{\sigma^{\text{wn}}}. \quad (8)$$

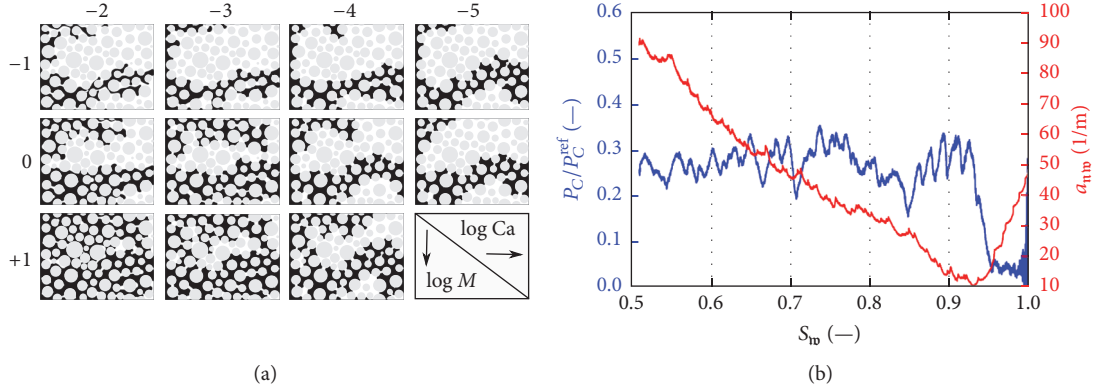


FIGURE 2: (a) NWP distributions (black) at breakthrough for microstructure C in (Ca, M) feature plane. Solid phase and WP are colored gray and white, respectively. (b) Normalized macroscopic capillary pressure $P_C(S_{wp})/P_C^{\text{ref}}$ and specific fluid interfacial area $a_{wp}(S_{wp})$ for capillary-dominated primary drainage in microstructure C at $\log_{10}(Ca, M) = (-5, 0)$. During the preentry regime, P_C increases to the entry capillary pressure level while $a_{wp}(S_{wp})$ decreases as the meniscus comes in contact with the solid phase. During the postentry regime, P_C exhibits a constant mean value with fluctuations related to spontaneous Haines jumps.

Primary drainage processes are studied for $Ca \in \{10^{-2}, 10^{-3}, 10^{-4}, 10^{-5}\}$. Fluid viscosities are varied to prescribe the viscosity ratio:

$$M := \frac{\mu^n}{\mu^w}. \quad (9)$$

The simulated set of viscosity ratios is $M \in \{10^{-1}, 10^0, 10^1\}$ by considering the viscosity 2-tuples $\log_{10}(\mu^n, \mu^w) = (-4, -3), (-3, -3), (-3, -4)$ Pa s, respectively. The fluid-fluid interfacial tension is chosen $\sigma^{\text{nn}} = 5$ N/mm whereas Young's equilibrium contact angle $\Theta = 30^\circ$. The latter is achieved by setting fluid-solid interfacial tensions $\sigma^{\text{ns}} = 0$ and $\sigma^{\text{nw}} = \sigma^{\text{nn}} \cos \Theta$ following Young's equation. Since the contact angle is fixed for all simulations, effects related to variations in solid surface wettability are not studied herein. Volumetric forces such as gravity are absent and macroscopic inertial effects are considered negligible, that is, small macroscopic Reynolds numbers. The parameterization of fluid densities is thus expected to play a minor role such that we set $\rho^f = \rho^n = \rho^w$. Neither the mean pore-throat size $m_T \approx 0.41$ mm nor the interfacial tension σ^{nw} is chosen with regard to a particular reservoir system but rather in an attempt to optimize computational costs. Both, for larger values of σ^{nn} and smaller values of m_T , time stepping constraints become increasingly restrictive.

SPH particles are initially placed on the vertices of a Cartesian grid with grid spacing dx . Our choice of numerical resolution dx depends on mean pore-throat size m_T as well as Ca and M . For viscous fingering, the pore-scale flow field is found to resemble an annular flow with wetting films which require a fine spatial resolution to ensure numerical accuracy. Hence, for viscous fingering we choose $dx = \bar{m}_T/19 = 21.7 \mu\text{m}$ which leads to wetting films being represented by approximately 4 particles in direction of film thickness. For all remaining cases, we choose $dx = \bar{m}_T/14 = 29.5 \mu\text{m}$. It was previously shown in [45, 50] that the incorporated choices of dx can reproduce local pressure, menisci, and velocity profiles with reasonable accuracy. The total number of SPH

particles is approximately $6 \cdot 10^5$. Average computation time for a single time step was 0.6 s using a moderately optimized code running 6 threads in parallel on an Intel® Xeon® CPU E5-1650. The total number of time steps varied between $1.1 \cdot 10^6$ for small and $1.6 \cdot 10^5$ for large capillary numbers.

Animated simulation results showing phase, pressure, and velocity magnitude distributions during primary drainage are available as supplementary information (Movies S01–S09). While these animations demonstrate that the numerical model is capable of representing Haines jumps during capillary-dominated flow, in the following we focus on viscous-dominated flow. Phase distributions at breakthrough (Figure 2(a)) are consistent with the expected displacement patterns (capillary finger branching for sufficiently low Ca and stable displacement at sufficiently large Ca and $M > 1$, and viscous fingering at sufficiently large Ca and $M < 1$); however, their statistical characterization is not insightful herein due to the limited size of the unit cells. A prevailing feature of the present microstructures is that capillary-dominated primary drainage is found to occur at near-constant macroscopic capillary pressure P_C and linear growth of specific fluid interfacial area a_{wp} (Figure 2(b)) until breakthrough occurs. Macroscopic capillary pressure is computed as the difference in reservoir-averaged fluid pressures $P_C \equiv \langle p^n \rangle_{\text{res}} - \langle p^w \rangle_{\text{res}}$ whereas a_{wp} is the ratio of total fluid-fluid interfacial area to total unit cell volume. While constant P_C relates to a narrow entry pressure distribution along the percolating capillary finger, linear growth of interfacial area is due to morphological simplicity of the microstructures as previously observed in both modeling and experimental studies of primary drainage in particulate microstructures [18, 53–55].

In an attempt to highlight methodological limitations, we discuss the most crucial restrictions of the present simulations. (a) The present model is only applicable to ideal solid surfaces with absent chemical imperfections, surface roughness, or dust particles. In the presence of inhomogeneous solid surfaces a phenomenon referred to as

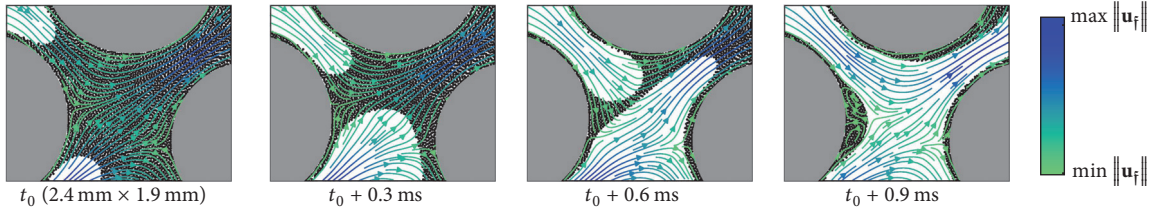


FIGURE 3: Hydrodynamic wetting film entrainment in subdomain of microstructure A for $\log_{10}(\text{Ca}, M) = (-2, -1)$. Solid phase domain is colored gray whereas WP SPH particles are represented by black markers. NWP SPH particles are omitted for improved visibility. Streamlines are colored according to the magnitude of local fluid velocity.

contact line hysteresis has to be taken into account. (b) Given the computational costs associated with pore-scale resolved SPH simulations, we restrict ourselves to two-dimensional problems. The latter implies topological constraints related to connectivity in 2D microstructures as well as a lack of representing depth-related effects, for example, due to curvature of menisci in the out-of-plane direction. (c) When a gas bubble invades a capillary tube that is initially saturated with a WP of nonnegligible viscosity, a residual wetting film is hydrodynamically entrained between gas bubble and channel wall regardless of solid wettability characteristics [56]. The latter constitutes a special case of the Landau-Levich-Derjaguin problem [57]. When the thickness of the wetting film $\delta \sim \mathcal{O}(0.1\text{m})$ [58], mutual interaction of meniscus and solid surface separated by the molecularly thin wetting film gives rise to an additional contribution to pressure inside the film referred to as disjoining pressure [57, 59] which has a crucial effect on the stability of molecularly thin wetting films. While the present model reproduces hydrodynamic entrainment of wetting films well within the viscous fingering regime, it does not take into account the effect of disjoining pressure.

3. Results and Discussion

3.1. Viscous Fingering Regime: Hydrodynamic Wetting Films. Viscous fingering, i.e., the Saffman-Taylor instability [60], occurs when a less viscous fluid displaces a more viscous fluid ($M < 1$) at sufficiently large capillary numbers. While invasion percolation is considered a suitable stochastic model for capillary fingering, viscous fingering is stochastically reminiscent of diffusion-limited aggregation (DLA) [61–63]. In this section, we empirically study the annular pore-scale flow profiles during viscous fingering and the impact of wetting films on the evolution of specific interfacial area and related dynamic effects. Hydrodynamic entrainment of wetting films at large Ca was previously shown in micromodel experiments of [18].

As the present model does not take into account disjoining pressure, wetting film effects are discussed well within the viscous fingering regime ($\text{Ca} \sim 10^{-2}$) where films are sufficiently thick. For core-annular gas-liquid flow in straight capillary tubes, i.e., Bretherton flow [56], lubrication theory [57] predicts the thickness of liquid films $\delta \sim m_T \text{Ca}_m^{2/3}$, where the microscopic capillary number Ca_m incorporates a characteristic microscopic velocity rather than U_p . While

lubrication theory has provided closed-form expressions for wetting film thicknesses in curved capillary tubes as well [64], the complexity of pore-networks is expected to necessitate either laboratory experiments or DNS to study hydrodynamic film entrainment in porous media.

If sufficiently fine spatial resolutions are used the present simulations reveal the underlying annular flow fields. Menisci are of spherical shape near fingertip regions whereas the curvature of wetting films is determined by the solid surface (Figure 3). Transition from spherical tip to wetting film is observed less obvious when the finger percolates through a pore-body (Figure 3, $t_0 + 0.6\text{ms}$). The mean curvature flow assumption clearly does not apply for viscous fingering. In 2D microstructures, dynamic wetting films become hydraulically reservoir-disconnected (trapped) when viscous fingers coalesce (Figure 3, $t_0 + 0.9\text{ms}$). The latter does not hold for 3D microstructures where flow through wetting films that extend over the surface of the entire pore-network might constitute a relevant transport mechanism [65]. The interface of an entrapped wetting film exhibits a ridge in the wake region of the wetted grain as previously observed in micromodel experiments [18]. Due to viscous coupling, recirculating fluid flow takes place within the ridge (Figure 3, $t_0 + 0.9\text{ms}$).

Following [66], we consider our choice of viscosity parameters for $M = 10^{-1}$ a rough representation of a carbon dioxide- (CO_2 -) water system in deep sedimentary formations. In particular, the modeled NWP has small but nonnegligible viscosity ($\mu^n = 0.1\text{mPa}\cdot\text{s}$). Annular flow may thus constitute a relevant transport mechanism during supercritical CO_2 sequestration if local flow rates are sufficiently high. The presence of wetting films implies not only a decrease in the effective channel width, but also a change in apparent boundary conditions. Before drainage the kinematic no-slip boundary condition applies with respect to the percolating WP whereas after drainage the dynamic interfacial viscous coupling condition applies with respect to the percolating NWP. Despite the fact that streamline patterns before and after drainage are rather comparable to each other due to laminar flow, the dynamic boundary condition is expected to affect energy dissipation.

It is intuitively understood that wetting films have considerable effect on the evolution of specific interfacial areas. For viscous fingering at $\text{Ca} = 10^{-2}$ and $M = 10^{-1}$, the rate of change of a_{bnn} is observed to be significantly larger as compared to stable displacement and capillary fingering (Figure 4(a)). The magnitude of a_{bnn} at breakthrough is

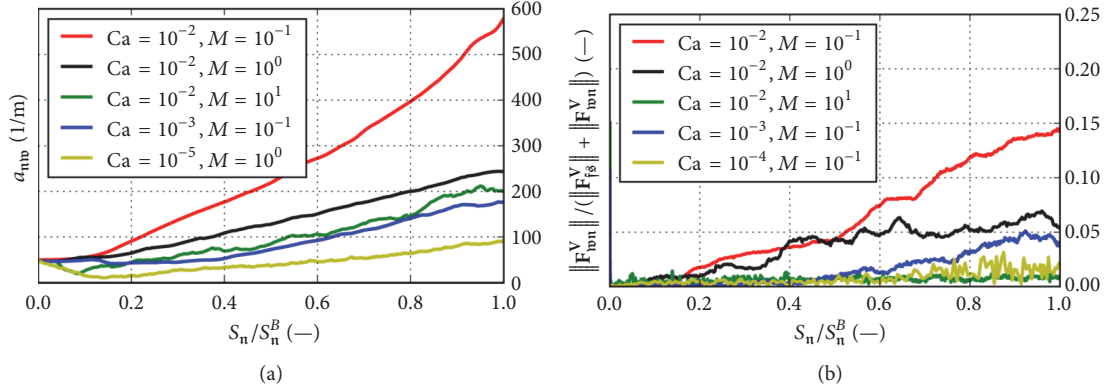


FIGURE 4: (a) Evolution of specific fluid-fluid interfacial area a_{wpn} in microstructure C. (b) Ratio of total interfacial viscous force to total resistance force in microstructure C. Data are presented as a function of normalized NWP saturation where S_n^B denotes NWP saturation at breakthrough.

found nearly six times the corresponding value for capillary fingering. The latter difference is expected to be even more pronounced for domain sizes large enough such that fractal branching can be statistically reproduced.

In an attempt to quantify the dynamic role of wetting films, we measure the total forces the reservoir pistons have to do work against to displace the NWP into the pore-space. For viscous-dominated flow we expect the total resistance force against drainage to be additively composed of the total skin friction force due to viscous shear between fluid and solid phase, that is, Darcian drag, and the total viscous coupling force acting between WP and NWP, that is, the Yuster effect [67, 68]. Total skin friction and viscous coupling force are evaluated as

$$\begin{aligned} \mathbf{F}_{\text{fs}}^V &:= \oint_{\partial\Omega_s} \mathbf{T}_E^f \cdot \mathbf{t}^{\text{fs}} da, \\ \mathbf{F}_{\text{wn}}^V &:= \oint_{\Gamma_{\text{wn}}} \mathbf{T}_E^n \cdot \mathbf{t}^{\text{wn}} da, \end{aligned} \quad (10)$$

respectively, where $\mathbf{t}^{\alpha\beta}$ denotes a vector tangent to the interface $\Gamma_{\alpha\beta}$. The ratio $\|\mathbf{F}_{\text{wn}}^V\|/(\|\mathbf{F}_{\text{fs}}^V\| + \|\mathbf{F}_{\text{wn}}^V\|)$ is a measure for the relative dominance of viscous coupling forces in total resistance. Both for capillary fingering ($\text{Ca} \leq 10^{-4}$) and for stable displacement ($\text{Ca} \geq 10^{-2}, M > 10^0$) viscous coupling forces are negligible (Figure 4(b)). The latter does not apply for viscous fingering where the relative dominance of \mathbf{F}_{wn}^V increases monotonically with S_n and in a manner qualitatively similar to $a_{\text{wpn}}(S_n)$. At breakthrough, nearly one-sixth of total resistance is due to viscous coupling and this trend is expected to be even more pronounced for finer microstructures, larger domain sizes, and higher saturations. These results suggest that viscous coupling terms should be accounted for in macroscopic models for viscous fingering in porous media since otherwise lubrication effects are lumped into relative permeability functions, which, by definition, are related to momentum exchange between solid and fluid phases only.

3.2. Stable Displacement Regime: Capillary Dispersion Zone. Viscosity stabilizes interfacial perturbations when a more viscous fluid displaces a less viscous fluid ($M > 1$) at sufficiently large capillary numbers. The latter gives rise to compact displacement patterns, stochastically referred to as anti-DLA patterns [62, 63], and interfaces that macroscopically appear as being flat. Stable displacement is hence desirable during enhanced oil recovery (EOS) due to optimal sweeping efficiency. In our simulations, compact patterns are observed for $M > 1$ and $\text{Ca} > 10^{-3}$ (Figure 2(a)). While large Ca implied that capillarity effects are macroscopically negligible, the latter does not apply at smaller length scales. On the contrary, capillarity greatly affects pore-scale interfacial dynamics within the capillary dispersion zone (CDZ) [69–71].

Disregarding boundary effects, saturation profiles $S_{\text{w}}(X_1)$ that arise during stable displacement are sigmoidal in shape and, in a rough approximation, upper and lower asymptotes to $S_{\text{w}}(X_1)$ can be considered the saturation limits $S_{\text{w}}^u = 1$ and $S_{\text{w}}^l \approx 0$, respectively (Figure 5). Considerable saturation gradients are observed only in the localized CDZ. Since we associate macroscopic saturation gradients with the presence of microscopic interfaces, sigmoidal profiles evidence compact patterns. However, rather than being sharp as one would anticipate on the basis of the Buckley-Leverett equation [72] and its admissible shock wave solutions, capillarity is observed to regularize the shock wave within the CDZ.

We define the width $L_C(t)$ of the CDZ as spatial difference between both points where saturation profiles $S_{\text{w}}(X_1, t)$ approach the asymptotes. While these asymptotes are observed to be barely sensitive to properties of the microstructures, the width $L_C(t)$, on the other hand, appears to increase with the degree of microstructure heterogeneity. In an attempt to quantify the latter, we compute the temporal average of $L_C(t)$ during drainage, hereafter denoted by \bar{L}_C . In order to avoid boundary artifacts, we consider the averaging window for \bar{L}_C equal to the time frame during which the CDZ is entirely contained within the porous unit cell. The average width of the CDZ is found to increase linearly with standard

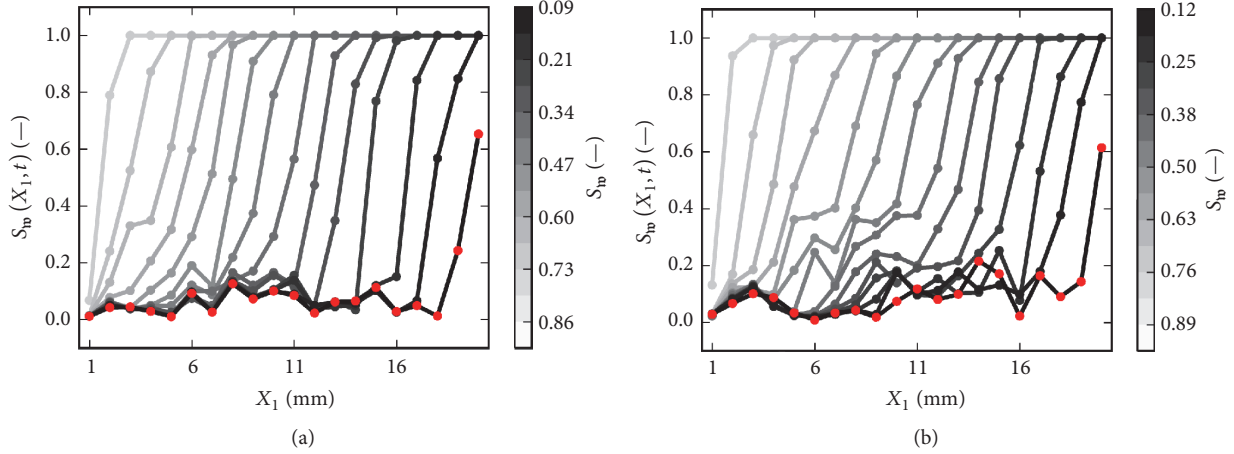


FIGURE 5: Evolving saturation profiles in flow direction for stable displacement in microstructures A (a) and C (b) at $\log_{10}(Ca, M) = (-2, 1)$. Among the tested microstructures, microstructure A exhibits the narrowest grain diameter distribution and microstructure C exhibits the widest one. Width of vertical slices for computing saturation profiles was chosen $\Delta X_1 = L_W/20$. Red markers indicate residual saturation profile $S_w^B(X_1)$ at breakthrough.

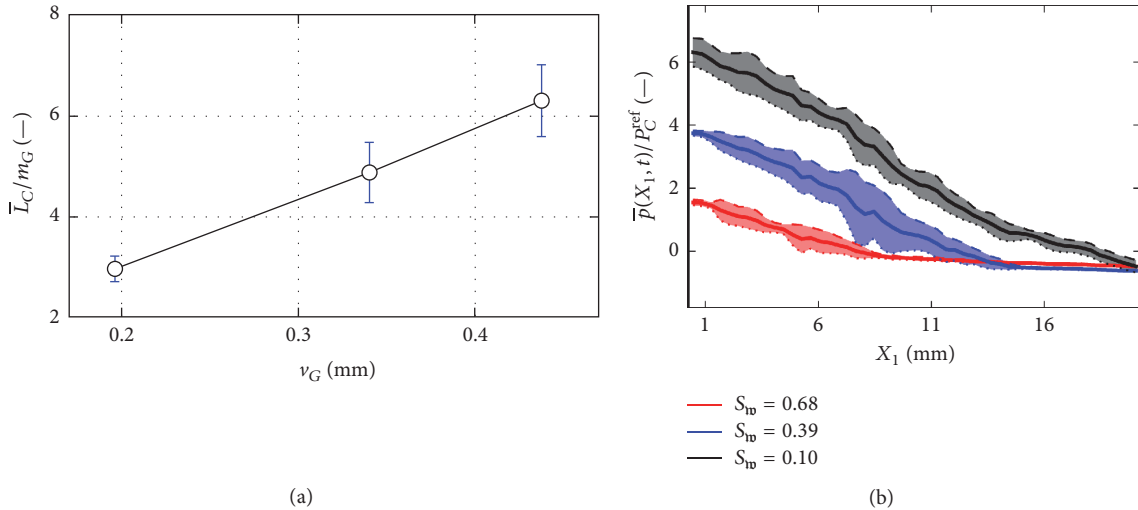


FIGURE 6: (a) Normalized average width \bar{L}_C of CDZ during stable displacement as a function of standard deviation v_G of grain diameter distribution. Blue error bars correspond to standard deviations of $L_C(t)$. (b) Normalized pressure profiles in flow direction for microstructure C at $\log_{10}(Ca, M) = (-2, 1)$. Solid lines represent average fluid pressure profiles $\bar{p}(X_1, t)$ within vertical averaging slices of width $\Delta X_1 = L_W/50$. Dotted and dashed lines correspond to lower and upper bounds to fluid pressure distribution and envelop 87% of pressure data (shaded area).

deviation v_G of grain diameter distribution (Figure 6(a)). In particular, $\bar{L}_C \approx 14v_G m_G$ yields a reasonable fit to the present data. We emphasize that drainage rates, interfacial tensions, and viscosities, which are all expected to affect $L_C(t)$, are kept constant meanwhile. Moreover, microstructures A–C only differ by the degree of heterogeneity expressed in terms of v_G while porosities, intrinsic permeabilities, and mean values m_G and m_T are comparable (Table 1). This suggests that, in addition to permeability, flow velocity, viscosity, and characteristic capillary pressure [73], the capillary dispersion length scale also depends on the second central moment of the grain size distribution ($\sim v_G$).

Within the CDZ, fluid interfaces and hydraulically reservoir-disconnected WP clusters are subject to the interplay of viscous and capillary forces. This is discussed in terms of the temporal evolution of mean pressure profiles $\bar{p}(X_1, t)$ (Figure 6(b)). Mean pressure profiles are found to be continuous, piecewise linear functions composed of two line segments. Each line segment can be intuitively attributed to Darcy flow of WP and NWP, respectively. As the kink point moves downstream with increasing NWP saturation, pressure gradients appear invariant to the degree of saturation. The latter is due to the fact that intrinsic permeability, bulk viscosities, and specific discharge remain constant during drainage. While all of the above is consistent

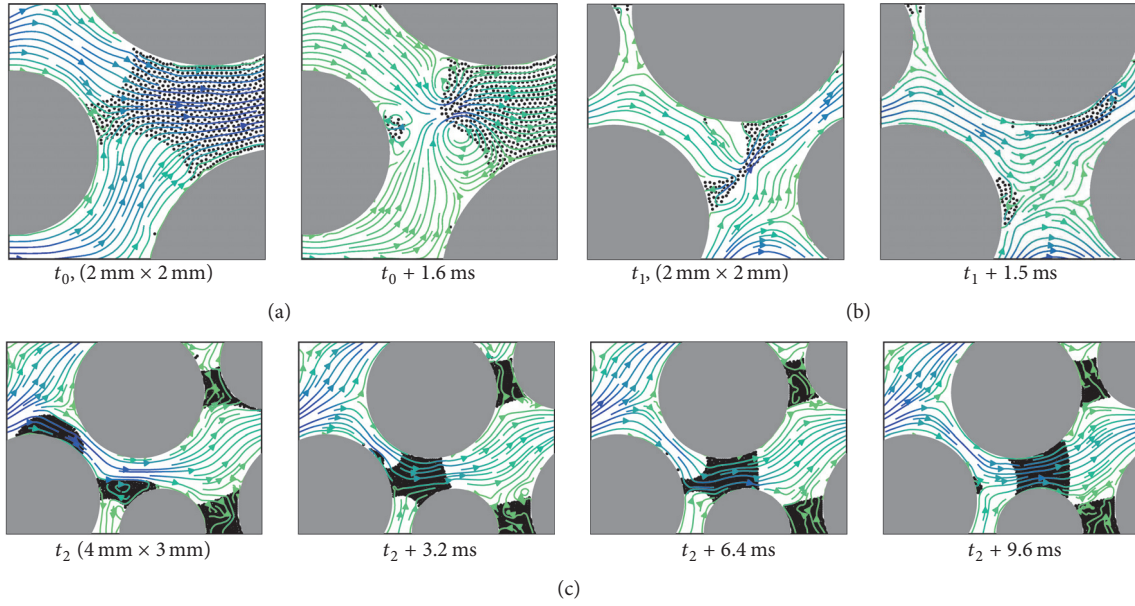


FIGURE 7: Pore-scale interfacial dynamics during stable displacement at $\log_{10}(\text{Ca}, M) = (-2, 1)$. Visual representation is equivalent to Figure 3. Spherical wetting cap formation due to menisci overlap near the saturation front ((a), t_0). Fragmentation of a pendular bridge into multiple wetting caps within the CDZ ((b), t_1). Wetting phase cluster mobilization by sequence of fragmentation and coalescence events within CDZ ((c), t_2).

with the macroscopic assumption that fluid permeation obeys Darcy's law a broad fluid pressure distribution is found within the CDZ which we attribute to transient pore-scale events related to disconnected WP cluster dynamics. The latter is most pronounced when the entire CDZ is contained within the porous unit cell (Figure 6(b), blue area).

We empirically discuss the types of pore-scale events that occur near the saturation front and within the CDZ (Figure 7). At the saturation front, adjacent menisci are observed to overlap, a mechanism referred to as Melrose event [74, 75]. The point of overlap is generally located at some distance downstream of the solid surface whereby the enclosed WP becomes hydraulically disconnected and forms a spherical cap (Figure 7, t_0). In close vicinity to the saturation front, the local viscous pressure drop is negligible (Figure 6(b)) as the local saturation of the less viscous WP is comparatively high. Due to the resulting local dominance of capillary forces, entry pressure thresholds govern flow near the saturation front; that is, invasion percolation takes place at the saturation front. Besides wetting cap formation, capillary trapping mechanisms, for example, pendular bridge formation, thus contribute to disconnection of the WP near the saturation front. As the saturation front further advances, the local viscous pressure drop across a wetting cluster increases due to higher viscosity of the surrounding NWP. The latter leads to fragmentation of large wetting clusters such as the transition of pendular bridges into multiple wetting caps (Figure 7, t_1). Wetting caps that are of spatial extent large enough for the pressure distribution to be nonuniform are found to be mobilized due to viscous entrainment and eventual coalescence with other disconnected clusters (Figure 7, t_2). If the size of a wetting cap falls below a critical

threshold size, mobilization due to viscous entrainment does not occur. While these results are consistent with previous reports [36], we emphasize that meaningful predictions for the critical threshold size necessitate that contact line pinning and dynamic contact angle effects are accounted for.

3.3. Critical Discussion on Connectivity in 2D Simulations. Recent studies emphasize the importance of integral geometry [76] and, in particular, use of the Euler characteristic χ to relate topological properties of microstructures [30, 77] or displacement patterns [34] to macroscopic hydraulic properties. For instance, [34] recently demonstrated the fundamental role of fluid topology in permanent hysteresis effects during drainage and imbibition. The lack of representing topological properties of 3D processes is the main drawback of 2D simulations. Indeed, while the solid matrix of a 3D consolidated porous material is generally composed of a single connected component, the solid matrix in 2D simulations has to be composed of disjoint sets for the fluid phase to percolate. We concisely study the evolution of the Euler characteristic χ_{w} of the total WP to emphasize topological implications of 2D simulations. In 2D, the Euler characteristic can be expressed as $\chi_{\text{w}} = \mathcal{N}_{\text{w}} - \mathcal{L}_{\text{w}}$, where \mathcal{N}_{w} denotes the number of isolated components and \mathcal{L}_{w} denotes the number of circular holes (Betti Numbers). For further introduction to integral geometry, the reader is referred to the above references. The notation $\chi(\Omega_{\square}) = \chi_{\square}$ applies in the following.

During stable displacement, reservoir-connected WP as well as NWP remain compact clusters and changes in connectivity only occur within the narrow CDZ. On the one hand, the number of isolated components \mathcal{N}_{w} increases

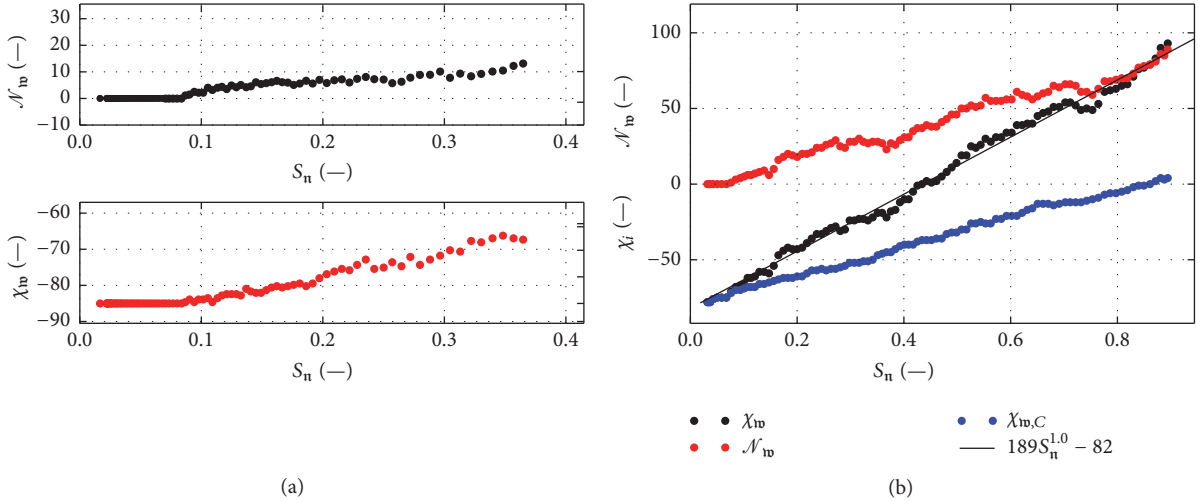


FIGURE 8: (a) Number of isolated components (\mathcal{N}_w) and Euler characteristic (χ_w) of WP for viscous fingering at $\log_{10}(\text{Ca}, M) = (-2, -1)$ in microstructure B. (b) Euler characteristics of WP and reservoir-connected WP ($\chi_{w,C}$) as well as number of isolated components for stable displacement at $\log_{10}(\text{Ca}, M) = (-2, 1)$ in microstructure B.

due to wetting cap or pendular cluster formation. On the other hand, the number of circular holes within the WP decreases as fewer grains are enclosed by the WP. The distinct characteristic of stable displacement is that the rate of change of $\chi_w(S_n)$, $\mathcal{N}_w(S_n)$ and $\mathcal{L}_w(S_n)$ with saturation is constant, that is, invariant with respect to the position of the compact saturation front. At initial time t_0 , WP saturates the entire pore-space such that $\mathcal{L}_w(t_0)$ is equal to the genus of the pore-space and $\mathcal{N}_w(t_0)$ is one. As saturation levels increase both \mathcal{N}_w and χ_w are observed to increase linearly with saturation (Figure 8(b)). These results are consistent with experiments reported in [34], where the Euler characteristics of compact displacement patterns that emerge during main imbibition were shown to change linearly with saturation. We therefore argue that 2D simulations of compact displacement patterns exhibit topological properties applicable to 3D compact patterns as well.

For viscous fingering, on the other hand, 2D simulations are not topologically representative of 3D processes. In 3D, dynamic wetting films are considered to extend over the surface of the entire pore-network and remain connected to the WP reservoir such that χ_w should remain constant during viscous fingering in 3D unless discrete WP clusters snap off. On the contrary, dynamic wetting films that emerge during viscous fingering in 2D become reservoir-disconnected as interfaces coalesce and thus form isolated objects of topological genus one (homeomorphic to a circle). As \mathcal{N}_w increases with the number of isolated films, the total number of holes $\mathcal{L}_w(S_n) = \mathcal{L}_w(t_0)$, however, is expected to remain unchanged since grains remain wetted by WP. As a result, we expect χ_w to change with the same rate as that of \mathcal{N}_w as NWP saturation increases. While our results qualitatively reproduce the expected trends (Figure 8(a)), χ_w is found to increase with a slightly higher rate as that of \mathcal{N}_w . This implies that \mathcal{L}_w slightly decreases which can be attributed to the unstable breakup of dynamic wetting films, that is,

isolated wetting films of genus one breakup into multiple clusters of genus zero. For an isolated wetting film to be stable in equilibrium, the pressure inside the film must equal the capillary pressure difference across the curved film meniscus when disjoining pressure effects are neglected. As this is generally not the case since film isolation occurred during viscous entrainment, films tend to breakup at later stages of the simulation. Both the isolation and subsequent breakup of dynamic wetting films are 2D phenomena. Nonetheless, the impacts of films on specific interfacial area a_{wn} and viscous coupling \mathbf{F}_{wn}^V as discussed in Section 3.1 are expected to apply regardless of above topological issues.

4. Summary and Open Questions

While pore-scale imaging methods, for example, fast X-ray tomography methods, to study the distribution and evolution of fluid interfaces for capillary-dominated flow become increasingly mature, their applicability to viscous-dominated flow is limited by temporal resolution. We consider hydrodynamic direct numerical simulations a suitable complementary approach for pore-scale modeling of viscous-dominated two-phase flow. Using a Smoothed-Particle Hydrodynamics model, we performed pore-scale simulations of primary drainage in partially wettable 2D porous media of particulate microstructure at large Ca. We have demonstrated the use of the mesh-free model to study hydrodynamic entrainment of thick wetting films during viscous fingering as well as the dispersion of stable saturation fronts.

While the impact of wetting films on the dynamics of viscous fingering was outlined, the identification of capillary numbers where the onset of wetting film formation takes place requires further efforts. As the modeling of thin wetting films requires disjoining pressure forces to be accounted for, the present model was only applied to thick hydrodynamic wetting films well within the viscous fingering regime. While

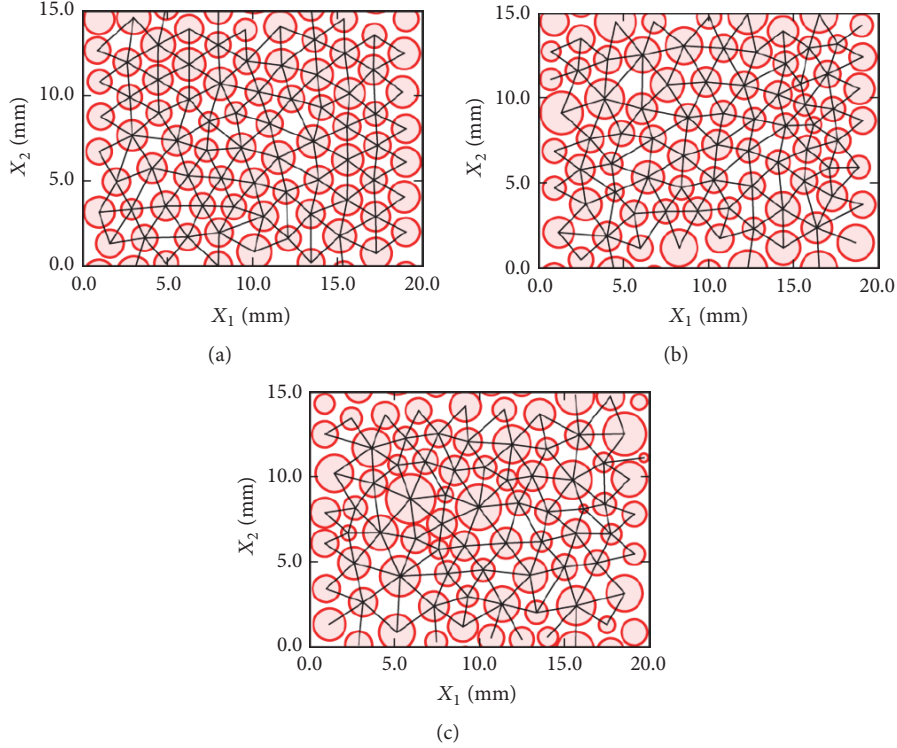


FIGURE 9: Computational unit cells A, B, and C (from (a) to (c)). Black lines in microstructure plots correspond to Delaunay edges that have been used to generate pore-throat size histograms (Table 1).

the relative dominance of interfacial viscous coupling forces is observed to monotonically increase during viscous fingering, their impact on relative permeability functions remains open. While mesh-free methods were shown to be a viable approach to study viscous fingering phenomena, significant computational resources and algorithmic optimizations are currently required to render 3D mesh-free simulations feasible.

In contrast to viscous fingering, the 2D topological properties of the compact wetting phase during stable displacement were found qualitatively equivalent to those in 3D. The observation that the width of capillary dispersion zones increases with microstructure heterogeneity is thus considered to apply to 3D processes as well. The latter may thus motivate the regularization of Buckley-Leverett models to account for capillary dispersion. Mobilization, fragmentation and coalescence of disconnected wetting phase clusters were found as processes entirely local to the capillary dispersion zone. Hence, the dispersion zone decisively impacts residual wetting phase distribution in form of disconnected wetting caps and pendular bridges. This implies that the region of interest to study wetting phase entrapment during stable displacement using pore-scale imaging methods can be restricted to the capillary dispersion zone. For an accurate numerical prediction of threshold sizes for wetting phase cluster mobilization in reservoir systems, however, more realistic models that take into account contact angle hysteresis are considered necessary.

Appendix

Hydraulic and Morphological Properties of Microstructures

In analogy to what was done in [50, 78], pore-throat size distributions of computational unit cells are computed on the basis of a Delaunay triangulation of grain center points (Figure 9). The pore-throat size between two neighboring grains is considered equal to the length of the connecting Delaunay edge upon subtracting respective grain radii. Delaunay edges that intersect the system boundaries are excluded during generation of pore-throat size histograms. Resulting pore-throat size histograms and grain diameter histograms (Table 1) are subsequently fitted to the Gaussian distributions $G_T(x) := A_T \exp[-(x - m_T)^2 / (2v_T^2)]$ and $G_G(x) := A_G \exp[-(x - m_G)^2 / (2v_G^2)]$, respectively.

Data Availability

Simulation results and data used to generate figures are available upon request via e-mail to the first author.

Conflicts of Interest

The authors declare that there are no conflicts of interest.

Acknowledgments

Holger Steeb and Rakulan Sivanesapillai acknowledge the financial support from the German Science Foundation (DFG) through the Project STE 969/14-1, within the SPP 2005 “Opus Fluidum Futurum-Rheology of Reactive, Multiscale, Multiphase Construction Materials”.

Supplementary Materials

Animations showing WP and NWP distribution, normalized pressure, and velocity magnitude fields during the discussed numerical primary drainage experiments are available as online resources and accompany the electronic version of this manuscript. Animations show capillary fingering at $\log_{10}(\text{Ca}, M) = (-4, 0)$ in microstructures A–C (Online Resources 1–3), viscous fingering at $\log_{10}(\text{Ca}, M) = (-2, -1)$ in microstructures A–C (Online Resources 4–6), and stable displacement at $\log_{10}(\text{Ca}, M) = (-2, 1)$ in microstructures A–C (Online Resources 7–9). (*Supplementary Materials*)

References

- [1] R. Lenormand, E. Touboul, and C. Zarcone, “Numerical models and experiments on immiscible displacements in porous media,” *Journal of Fluid Mechanics*, vol. 189, pp. 165–187, 1988.
- [2] J. Bear, “Dynamics of Fluids in Porous Media,” *Soil Science*, vol. 120, no. 2, pp. 162–163, 1975.
- [3] G. R. Jerauld and S. J. Salter, “The effect of pore-structure on hysteresis in relative permeability and capillary pressure: pore-level modeling,” *Transport in Porous Media*, vol. 5, no. 2, pp. 103–151, 1990.
- [4] O. Van Genabeek and D. H. Rothman, “Macroscopic manifestations of microscopic flows through porous media: Phenomenology from simulation,” *Annual Review of Earth and Planetary Sciences*, vol. 24, pp. 63–87, 1996.
- [5] J. C. Muccino, W. G. Gray, and L. A. Ferrand, “Toward an improved understanding of multiphase flow in porous media,” *Reviews of Geophysics*, vol. 36, no. 3, pp. 401–422, 1998.
- [6] W. G. Gray and S. M. Hassanizadeh, “Averaging theorems and averaged equations for transport of interface properties in multiphase systems,” *International Journal of Multiphase Flow*, vol. 15, no. 1, pp. 81–95, 1989.
- [7] S. M. Hassanizadeh and W. G. Gray, “Mechanics and thermodynamics of multiphase flow in porous media including interphase boundaries,” *Advances in Water Resources*, vol. 13, no. 4, pp. 169–186, 1990.
- [8] S. Majid Hassanizadeh and W. G. Gray, “Toward an improved description of the physics of two-phase flow,” *Advances in Water Resources*, vol. 16, no. 1, pp. 53–67, 1993.
- [9] S. M. Hassanizadeh and W. G. Gray, “Thermodynamic basis of capillary pressure in porous media,” *Water Resources Research*, vol. 29, no. 10, pp. 3389–3405, 1993.
- [10] V. Joekar-Niasar, S. M. Hassanizadeh, and A. Leijnse, “Insights into the relationships among capillary pressure, saturation, interfacial area and relative permeability using pore-network modeling,” *Transport in Porous Media*, vol. 74, no. 2, pp. 201–219, 2008.
- [11] R. Hilfer, “Macroscopic equations of motion for two-phase flow in porous media,” *Physical Review E: Statistical Physics, Plasmas, Fluids, and Related Interdisciplinary Topics*, vol. 58, no. 2, pp. 2090–2096, 1998.
- [12] R. Hilfer and H. Besslerer, “Macroscopic two-phase flow in porous media,” *Physica B: Condensed Matter*, vol. 279, no. 1–3, pp. 125–129, 2000.
- [13] M. Fleischmann, D. J. Tildesley, and R. C. Ball, *Fractals in the Natural Sciences*, Princeton University Press, Princeton, 1990.
- [14] O. I. Frette, K. J. Måløy, J. Schmittbuhl, and A. Hansen, “Immiscible displacement of viscosity-matched fluids in two-dimensional porous media,” *Physical Review E: Statistical Physics, Plasmas, Fluids, and Related Interdisciplinary Topics*, vol. 55, no. 3, pp. 2969–2975, 1996.
- [15] M. Ferer, C. Ji, G. S. Bromhal, J. Cook, G. Ahmadi, and D. H. Smith, “Crossover from capillary fingering to viscous fingering for immiscible unstable flow: Experiment and modeling,” *Physical Review E: Statistical Physics, Plasmas, Fluids, and Related Interdisciplinary Topics*, vol. 70, no. 1, p. 7, 2004.
- [16] M. A. Theodoropoulou, V. Sygouni, V. Karoutsos, and C. D. Tsakiroglou, “Relative permeability and capillary pressure functions of porous media as related to the displacement growth pattern,” *International Journal of Multiphase Flow*, vol. 31, no. 10–11, pp. 1155–1180, 2005.
- [17] V. Berejnov, N. Djilali, and D. Sinton, “Lab-on-chip methodologies for the study of transport in porous media: Energy applications,” *Lab on a Chip*, vol. 8, no. 5, pp. 689–693, 2008.
- [18] C. Zhang, M. Oostrom, T. W. Wietsma, J. W. Grate, and M. G. Warner, “Influence of viscous and capillary forces on immiscible fluid displacement: Pore-scale experimental study in a water-wet micromodel demonstrating viscous and capillary fingering,” *ENERGY & FUELS*, vol. 25, no. 8, pp. 3493–3505, 2011.
- [19] M. M. Dias and A. C. Payatakes, “Network models for two-phase flow in porous media Part 1. Immiscible microdisplacement of non-wetting fluids,” *Journal of Fluid Mechanics*, vol. 164, no. 2, pp. 305–336, 1986.
- [20] M. J. Blunt and H. Scher, “Pore-level modeling of wetting,” *Physical Review E: Statistical, Nonlinear, and Soft Matter Physics*, vol. 52, no. 6, pp. 6387–6403, 1995.
- [21] J. F. Chau and D. Or, “Linking drainage front morphology with gaseous diffusion in unsaturated porous media: A lattice Boltzmann study,” *Physical Review E: Statistical, Nonlinear, and Soft Matter Physics*, vol. 74, no. 5, Article ID 056304, 2006.
- [22] A. Ferrari and I. Lunati, “Direct numerical simulations of interface dynamics to link capillary pressure and total surface energy,” *Advances in Water Resources*, vol. 57, no. 9, pp. 19–31, 2013.
- [23] H. Liu, Y. Zhang, and A. J. Valocchi, “Lattice boltzmann simulation of immiscible fluid displacement in porous media: Homogeneous versus heterogeneous pore network,” *Physics of Fluids*, vol. 27, no. 5, Article ID 052103, 2015.
- [24] A. Ferrari, J. Jimenez-Martinez, T. L. Borgne, Y. Méheust, and I. Lunati, “Challenges in modeling unstable two-phase flow experiments in porous micromodels,” *Water Resources Research*, vol. 51, no. 3, pp. 1381–1400, 2015.
- [25] P. Kunz, I. M. Zarikos, N. K. Karadimitriou, M. Huber, U. Nicken, and S. M. Hassanizadeh, “Study of Multi-phase Flow in Porous Media: Comparison of SPH Simulations with Micromodel Experiments,” *Transport in Porous Media*, vol. 114, no. 2, pp. 581–600, 2016.
- [26] T. Bultreys, W. De Boever, and V. Cnudde, “Imaging and image-based fluid transport modeling at the pore scale in geological

- materials: a practical introduction to the current state-of-the-art,” *Earth-Science Reviews*, vol. 155, pp. 93–128, 2016.
- [27] N. K. Karadimitriou and S. M. Hassanizadeh, “A review of micromodels and their use in two-phase flow studies,” *Vadose Zone Journal*, vol. 11, no. 3, 2012.
- [28] F. Moebius and D. Or, “Interfacial jumps and pressure bursts during fluid displacement in interacting irregular capillaries,” *Journal of Colloid and Interface Science*, vol. 377, no. 1, pp. 406–415, 2012.
- [29] R. T. Armstrong and S. Berg, “Interfacial velocities and capillary pressure gradients during Haines jumps,” *Physical Review E: Statistical, Nonlinear, and Soft Matter Physics*, vol. 88, no. 4, 2013.
- [30] D. Wildenschild and A. P. Sheppard, “X-ray imaging and analysis techniques for quantifying pore-scale structure and processes in subsurface porous medium systems,” *Advances in Water Resources*, vol. 51, pp. 217–246, 2013.
- [31] M. J. Blunt, B. Bijeljic, H. Dong et al., “Pore-scale imaging and modelling,” *Advances in Water Resources*, vol. 51, pp. 197–216, 2013.
- [32] S. Berg, H. Ott, S. A. Klapp et al., “Real-time 3D imaging of Haines jumps in porous media flow,” *Proceedings of the National Academy of Sciences of the United States of America*, vol. 110, no. 10, pp. 3755–3759, 2013.
- [33] T. Bultreys, M. A. Boone, M. N. Boone et al., “Real-time visualization of Haines jumps in sandstone with laboratory-based microcomputed tomography,” *Water Resources Research*, vol. 51, no. 10, pp. 8668–8676, 2015.
- [34] S. Schlüter, S. Berg, M. Rücker et al., “Pore-scale displacement mechanisms as a source of hysteresis for two-phase flow in porous media,” *Water Resources Research*, vol. 52, no. 3, pp. 2194–2205, 2016.
- [35] A. T. Krummel, S. S. Datta, S. Münster, and D. A. Weitz, “Visualizing multiphase flow and trapped fluid configurations in a model three-dimensional porous medium,” *AIChE Journal*, vol. 59, no. 3, pp. 1022–1029, 2013.
- [36] S. S. Datta, T. S. Ramakrishnan, and D. A. Weitz, “Mobilization of a trapped non-wetting fluid from a three-dimensional porous medium,” *Physics of Fluids*, vol. 26, no. 2, Article ID 022002, 2014.
- [37] P. Meakin and A. M. Tartakovsky, “Modeling and simulation of pore-scale multiphase fluid flow and reactive transport in fractured and porous media,” *Reviews of Geophysics*, vol. 47, no. 3, Article ID RG3002, 2009.
- [38] J. J. Monaghan, “Smoothed particle hydrodynamics,” *Reports on Progress in Physics*, vol. 68, no. 8, pp. 1703–1759, 2005.
- [39] A. M. Tartakovsky and P. Meakin, “A smoothed particle hydrodynamics model for miscible flow in three-dimensional fractures and the two-dimensional Rayleigh-Taylor instability,” *Journal of Computational Physics*, vol. 207, no. 2, pp. 610–624, 2005.
- [40] A. M. Tartakovsky and P. Meakin, “Pore scale modeling of immiscible and miscible fluid flows using smoothed particle hydrodynamics,” *Advances in Water Resources*, vol. 29, no. 10, pp. 1464–1478, 2006.
- [41] X. Y. Hu and N. A. Adams, “A multi-phase SPH method for macroscopic and mesoscopic flows,” *Journal of Computational Physics*, vol. 213, no. 2, pp. 844–861, 2006.
- [42] J. U. Brackbill, D. B. Kothe, and C. A. Zemach, “A continuum method for modeling surface tension,” *Journal of Computational Physics*, vol. 100, no. 2, pp. 335–354, 1992.
- [43] B. Lafaurie, C. Nardone, R. Scardovelli, S. Zaleski, and G. Zanetti, “Modelling merging and fragmentation in multiphase flows with SURFER,” *Journal of Computational Physics*, vol. 113, no. 1, pp. 134–147, 1994.
- [44] R. Sivanapillai, H. Steeb, and A. Hartmaier, “Transition of effective hydraulic properties from low to high Reynolds number flow in porous media,” *Geophysical Research Letters*, vol. 41, no. 14, pp. 4920–4928, 2014.
- [45] R. Sivanapillai, *Pore-scale study of non-darcian fluid flow in porous media using smoothed-particle hydrodynamics. Doctoral thesis [Doctoral, thesis]*, 2016.
- [46] J. Bonet and S. Kulasegaram, “Correction and stabilization of smooth particle hydrodynamics methods with applications in metal forming simulations,” *Int. J. Numer. Meth. Eng.*, vol. 47, pp. 1189–1214, 2000.
- [47] L. Cueto-Felgueroso, I. Colominas, G. Mosqueira, F. Navarri, and M. Casteleiro, “On the Galerkin formulation of the smoothed particle hydrodynamics method,” *International Journal for Numerical Methods in Engineering*, vol. 60, no. 9, pp. 1475–1512, 2004.
- [48] J. W. Swegle, D. L. Hicks, and S. W. Attaway, “Smoothed particle hydrodynamics stability analysis,” *Journal of Computational Physics*, vol. 116, no. 1, pp. 123–134, 1995.
- [49] P. S. Kurzeja and H. Steeb, “Variational formulation of oscillating fluid clusters and oscillator-like classification. I. Theory,” *Physics of Fluids*, vol. 26, no. 4, Article ID 042106, 2014.
- [50] R. Sivanapillai, N. Falkner, A. Hartmaier, and H. Steeb, “A CSF-SPH method for simulating drainage and imbibition at pore-scale resolution while tracking interfacial areas,” *Advances in Water Resources*, vol. 95, pp. 212–234, 2016.
- [51] A. Donev, S. Torquato, and F. H. Stillinger, “Neighbor list collision-driven molecular dynamics simulation for nonspherical hard particles. I. Algorithmic details,” *Journal of Computational Physics*, vol. 202, no. 2, pp. 737–764, 2005.
- [52] A. Donev, S. Torquato, and F. H. Stillinger, “Neighbor list collision-driven molecular dynamics simulation for nonspherical hard particles,” *Journal of Computational Physics*, vol. 202, no. 2, pp. 765–793, 2005.
- [53] L. Chen and T. C. G. Kibbey, “Measurement of air-water interfacial area for multiple hysteretic drainage curves in an unsaturated fine sand,” *Langmuir*, vol. 22, no. 16, pp. 6874–6880, 2006.
- [54] C. E. Schaefer, D. A. DiCarlo, and M. J. Blunt, “Experimental measurement of air-water interfacial area during gravity drainage and secondary imbibition in porous media,” *Water Resources Research*, vol. 36, no. 4, pp. 885–890, 2000.
- [55] M. L. Porter, D. Wildenschild, G. Grant, and J. I. Gerhard, “Measurement and prediction of the relationship between capillary pressure, saturation, and interfacial area in a NAPL-water-glass bead system,” *Water Resources Research*, vol. 46, no. 8, Article ID W08512, 2010.
- [56] F. P. Bretherton, “The motion of long bubbles in tubes,” *Journal of Fluid Mechanics*, vol. 10, pp. 166–188, 1961.
- [57] B. Widom, *Physics Today*, vol. 57, no. 12, pp. 66–67, 2004.
- [58] V. Starov, M. Velarde, and C. Radke, *Wetting and Spreading Dynamics. Surfactant Science Series*, CRC Press, Boca Raton, FL, USA, 2007.
- [59] G. F. Teletzke, H. T. Davis, and L. Scriven, “Wetting hydrodynamics,” *Revue de Physique Appliquée*, vol. 23, no. 6, pp. 989–1007, 1988.

- [60] P. G. Saffman and G. Taylor, "The penetration of a fluid into a porous medium or Hele-Shaw cell containing a more viscous liquid," *Proceedings of the Royal Society A Mathematical, Physical and Engineering Sciences*, vol. 245, no. 1242, pp. 312–329, 1958.
- [61] P. Meakin, "Diffusion-controlled cluster formation in 2 6-dimensional space," *Physical Review A: Atomic, Molecular and Optical Physics*, vol. 27, no. 3, pp. 1495–1507, 1983.
- [62] L. Paterson, "Diffusion-limited aggregation and two-fluid displacements in porous media," *Physical Review Letters*, vol. 52, no. 18, pp. 1621–1624, 1984.
- [63] R. Lenormand, "Liquids in porous media," *Journal of Physics: Condensed Matter*, vol. 2, no. S, pp. SA79–SA88, 1990.
- [64] M. Muradoglu and H. A. Stone, "Motion of large bubbles in curved channels," *Journal of Fluid Mechanics*, vol. 570, pp. 455–466, 2007.
- [65] T. C. Ransohoff and C. J. Radke, "Laminar flow of a wetting liquid along the corners of a predominantly gas-occupied noncircular pore," *Journal of Colloid and Interface Science*, vol. 121, no. 2, pp. 392–401, 1988.
- [66] J. M. Nordbotten, M. A. Celia, and S. Bachu, "Injection and storage of CO₂ in deep saline aquifers: Analytical solution for CO₂ plume evolution during injection," *Transport in Porous Media*, vol. 58, no. 3, pp. 339–360, 2005.
- [67] S. Yuster, "Some Theoretical Considerations of Tilted Water Tables," *Journal of Petroleum Technology*, vol. 5, no. 05, pp. 149–156, 2013.
- [68] M. Ayub and R. G. Bentsen, "Interfacial viscous coupling: a myth or reality?" *Journal of Petroleum Science and Engineering*, vol. 23, no. 1, pp. 13–26, 1999.
- [69] G. Jerauld, H. Davis, and L. Scriven, "Stability Fronts of Permanent Form in Immiscible Displacement," in *Proceedings of the SPE Annual Technical Conference and Exhibition*, Houston, Texas.
- [70] A. Riaz and H. A. Tchelepi, "Linear stability analysis of immiscible two-phase flow in porous media with capillary dispersion and density variation," *Physics of Fluids*, vol. 16, no. 12, pp. 4727–4737, 2004.
- [71] M. Rücker, S. Berg, R. T. Armstrong et al., "From connected pathway flow to ganglion dynamics," *Geophysical Research Letters*, vol. 42, no. 10, pp. 3888–3894, 2015.
- [72] S. E. Buckley and M. C. Leverett, "Mechanism of fluid displacement in sands," *Transactions of the AIIME*, vol. 146, no. 1, pp. 107–116, 2013.
- [73] S. Berg and H. Ott, "Stability of CO₂-brine immiscible displacement," *International Journal of Greenhouse Gas Control*, vol. 11, pp. 188–203, 2012.
- [74] S. Motealleh, M. Ashouripashaki, D. di Carlo, and S. Bryant, "Mechanisms of capillary-controlled immiscible fluid flow in fractionally wet porous media," *Vadose Zone Journal*, vol. 9, no. 3, pp. 610–623, 2010.
- [75] R. Holtzman and E. Segre, "Wettability Stabilizes Fluid Invasion into Porous Media via Nonlocal, Cooperative Pore Filling," *Physical Review Letters*, vol. 115, no. 16, Article ID 164501, 2015.
- [76] K. R. Mecke and D. Stoyan, *Statistical Physics and Spatial Statistics*, vol. 554, Springer Berlin Heidelberg, Berlin, Heidelberg, 2000.
- [77] K. Mecke and C. H. Arns, "Fluids in porous media: a morphometric approach," *Journal of Physics: Condensed Matter*, vol. 17, no. 9, pp. S503–S534, 2005.
- [78] M. Moura, E.-A. Fiorentino, G. Schäfer, and R. Toussaint, "Impact of sample geometry on the measurement of pressure-saturation curves: Experiments and simulations," *Water Resources Research*, vol. 51, no. 11, pp. 8900–8926, 2015.